Development and application of PICLas for combined optic-/plume-simulation of ion-propulsion systems

A thesis accepted by the Faculty of Aerospace Engineering and Geodesy of the University of Stuttgart in partial fulfilment of the requirements for the degree of Doctor of Engineering Sciences (Dr.-Ing.)

by

Tilman Binder

born in Helmstedt, Germany

Main referee:	Prof. Dr.-Ing. Stefanos Fasoulas
Co referee:	Prof. Dr. rer. nat. habil. Claus-Dieter Munz
Co referee:	Prof. Dr. Hans Leiter
Date of defense:	13.09.2019

Institute of Space Systems
University of Stuttgart

2019

Danksagung

An erster Stelle danke ich meinem Doktorvater, Herrn Stefanos Fasoulas, der meine Zeit als wissenschaftlicher Mitarbeiter am IRS ermöglicht und mich bei meinen Forschungstätigkeiten stets unterstützt hat. Vielen Dank Herrn Claus-Dieter Munz für seine Tätigkeiten als Mitberichter und auch stellvertretend für die Numerik-Forschungsgruppe am IAG, denn nur durch die institutsübergreifende Kooperation konnte *PICLas* den beeindruckenden Stand von heute erreichen. Ebenfalls danke ich meinen Betreuern und Ansprechpartnern bei der ArianeGroup GmbH in Lampoldshausen (namentlich Dieter Feyhl, Hans Leiter, Jan-Patrick Porst und Stefan Ziegenhagen). Der größte Dank gilt dabei Hans Leiter für die Übernahme des Mitberichts dieser Arbeit sowie für die fachlichen Diskussionen und Anregungen.

All die Jahre als Doktorand wären längst nicht so angenehm gewesen ohne die tollen Arbeitskollegen und unterstützenden Studenten. Vor allem die Zusammenarbeit mit den anderen *PICLas*-Entwicklern (Julian Beyer, Asim Mirza, Paul Nizenkov, Marcel Pfeiffer, Wladimir Reschke und Torsten Stindl vom IRS sowie Stephen Copplestone und Philip Ortwein vom IAG) ermöglichte erst die Arbeit in dieser Form. Dabei schätzte ich neben dem fachlichen Austausch auch die vielen unterhaltsamen Stunden, sei es morgendlich in der Kaffeeküche oder bei unseren alljährlichen „Events“ am Institut.

Ich danke der finanziellen Förderung durch das ArianeGroup-Graduiertenkolleg am IRS und durch die Deutsche Forschungsgemeinschaft (DFG). Die Rechenkapazitäten für die numerischen Simulationen wurden bereitgestellt am Bundes-Höchstleistungsrechenzentrum Stuttgart (HLRS) und am Steinbuch Centre for Computing (SCC) in Karlsruhe.

Ein besonderer Dank gilt meiner Familie für die moralische Unterstützung. Aber auch meinen Freunden gebührt dieser Dank, besonders meinen Studienfreunden sowie meiner Freundin Bea für ihre Geduld und Hilfe auf dem Endspurt.

Tilman Binder

Friedrichshafen, November 2019

Contents

Abstract **9**

Kurzfassung **11**

Nomenclature **13**

1 Introduction **19**
1.1 Motivation . . . 19
1.2 Point of departure . . . 22
1.3 Problem statement and outline . . . 25

2 Theoretical background **27**
2.1 Microscopic modeling of rarefied plasma flows . . . 27
2.2 Plasma physics . . . 28
2.2.1 Electromagnetic fields . . . 28
2.2.2 Categorization of plasmas . . . 29
2.2.3 Boltzmann relation and bounded plasmas . . . 30
2.3 Inter-particle collisions . . . 31
2.4 Ion thruster optics . . . 32
2.5 Monte Carlo Methods . . . 33
2.5.1 Inverse transform sampling . . . 34
2.5.2 Acceptance-rejection method . . . 35
2.6 Numerical simulation of rarefied, reactive plasmas . . . 35
2.6.1 Electromagnetic interactions . . . 35
2.6.2 Inter-particle interactions . . . 38
2.7 The Plasma Kinetic Code PICLas . . . 39
2.7.1 High order approach and spatial discretization . . . 40
2.7.2 PIC-related routines . . . 41
2.7.3 DSMC-related routines . . . 46
2.7.4 Necessary developments for the simulation of ion optics . . . 47

3 Numerical development **49**
3.1 Overview . . . 49
3.2 Temporal integration of particle motion in electrostatic PIC . . . 50
3.2.1 Euler scheme . . . 51

3.2.2 Midpoint method: Leapfrog scheme . . . 51
3.2.3 Runge-Kutta schemes . . . 52
3.3 Boundary conditions for particle distributions . . . 55
3.3.1 Inflow conditions . . . 56
3.3.2 Symmetry conditions and solid walls . . . 65
3.4 Boundary corrections for shape functions . . . 67
3.4.1 Layers of known distribution . . . 68
3.4.2 Outflowing re-emission . . . 68
3.4.3 Mirroring . . . 69
3.5 Electrostatic field solver . . . 71
3.6 Charge- and momentum-exchange interactions . . . 74
3.7 Speed-up of PIC-based ion optics simulations . . . 76

4 Verification and sensitivity analyses **79**
4.1 Smoothing algorithms for number of particle insertion . . . 79
4.2 Convergence studies on temporal integration schemes . . . 83
4.2.1 Exact initialization in volume . . . 84
4.2.2 Initialization via surface flux . . . 85
4.3 HDG-PIC for bounded, electrostatic plasmas . . . 86
4.4 Convergence studies on ion optics simulations . . . 87
4.4.1 Temporal order of convergence . . . 90
4.4.2 Influence of the field resolution . . . 92
4.5 Neutral-ion collisions . . . 94

5 Optic-/plume-simulations **97**
5.1 General simulation set-up . . . 98
5.2 Verification of applicability of the Boltzmann relation for electrons . . . 100
5.2.1 Simulation set-up . . . 101
5.2.2 Infinite aperture pattern . . . 102
5.2.3 Complete domain . . . 108
5.2.4 Preliminary, quantitative EBS evaluation and conclusion . . . 109
5.3 Validation by grid current simulations . . . 110
5.3.1 Simulation set-up . . . 111
5.3.2 Neutral gas distribution . . . 114
5.3.3 Sensitivity analysis of simulation parameters . . . 117
5.3.4 Results . . . 119
5.4 Application to changed grid geometries . . . 124
5.4.1 Simulation set-up . . . 125
5.4.2 Resulting beamlet deflections . . . 127
5.4.3 Resulting patterns of current density distribution . . . 127

6 Conclusion **131**
6.1 Summary 131
6.2 Outlook 133

Bibliography **139**

A Appendix **I**
A.1 Reservoir method as ARM for the flux velocity distribution I
A.2 Algorithms implemented in PICLas. II

Abstract

Electric propulsion systems are an efficient option for altitude/attitude control and orbit transfers of spacecraft. They raise the limited energy content of the on-board propellant by electrical means, increasing the payload mass or operating times compared to classical, chemical propulsion. One example is the gridded ion thruster which ionizes the propellant and accelerates the ions of the generated plasma by a biased, high-voltage grid system. This study deals with the numerical simulation of the plasma flow starting near the grid system in the ionization chamber and leaving the thruster with high velocity. These simulations give direct insight into the modeled, physical interrelationships and can be used to investigate questions arising in the industrial development process of ion propulsion systems. The required simulation method is challenging due to the high degree of flow rarefaction and the plasma state itself, including freely moving ions and electrons. Applicable simulation methods belong to a particle-based, gas-kinetic approach, such as Particle-In-Cell (PIC) for the simulation of electromagnetic interaction and the Direct Simulation Monte Carlo (DSMC) for inter-particle collisions. Many other publications deal with the simulation of the ion beamlet forming inside a single grid aperture, based on the assumption of an ideal, infinitely large system. However, the effects resulting from the finite size of a real system can only be investigated by simulating the complete, three-dimensional thruster geometry which requires a large and complex simulation domain. Acceptable simulation times are realized by using the already established framework of the coupled PIC-DSMC code *PICLas* in combination with high performance computing systems. As part of this study, *PICLas* is extended by a high-order electrostatic field solver. For the considered plasma states, the particle motion becomes the dominating time step defining characteristic. The accurate particle treatment at boundaries as well as the extension by charge and momentum exchange reactions are presented.

These new models are verified with different kinds of simulations. They prove the respective, correct implementation and show good agreement with reference solutions. Validation is achieved on the basis of ion optics simulations of ArianeGroup's RIT-μX EBB thruster. The applicability of the Boltzmann relation as an electron fluid model is verified even near the electron back-streaming limit. In addition, the influence of various simulation parameters including spatial and temporal discretization is analyzed. The PIC-DSMC simulations of the ion optics are in very good agreement with the experimental results, both qualitatively

in terms of expected erosion patterns and quantitatively with regard to measurable grid currents. Best agreement is achieved for a scattering-based collision model and a neutral gas temperature of reasonable 300 K. Subsequently, the validated simulation set-up is applied to changed grid geometries. Here, the influence of misaligned aperture positions is investigated, resulting in deflected beamlets. The consideration of the complete grid geometry makes it possible to show for the first time by means of numerical simulation that the deflection angles depend not only on the misalignment shift but also directly on the respective position inside the grid pattern. The deflection increases with radial position, being at its largest for edge apertures due to the positively charged beamlets repelling each other on the downstream side of the grids. That influence also reflects itself in a displaced erosion pattern of the second grid.

Kurzfassung

Elektrische Raumfahrtantriebe stellen eine effiziente Lösung für die Lage- und Bahnregelung sowie Orbit-Transfers von Raumfahrzeugen dar. Sie erhöhen den begrenzten Energieinhalt des Bordtreibstoffs auf elektrische Weise, wodurch die Nutzlast oder die Betriebszeiten im Vergleich zu klassischen chemischen Antrieben erhöht werden können. Ein Beispiel sind Gitter-Ionenantriebe, die den Treibstoff ionisieren und die Ionen des erzeugten Plasmas mit einem Hochspannungs-Gittersystem beschleunigen. Diese Arbeit beschäftigt sich mit der numerischen Simulation der Plasmaströmung, die nahe des Gittersystems in der Ionisationskammer beginnt und das Triebwerk mit hohen Geschwindigkeiten verlässt. Diese Simulationen geben einen direkten Einblick in die modellierten physikalischen Zusammenhänge und können verwendet werden, um Fragen nachzugehen, die sich im industriellen Entwicklungsprozess von Ionenantriebssystemen ergeben. Aufgrund des hohen Grads der Strömungsverdünnung und des Plasmazustands mit frei beweglichen Ionen und Elektronen, ist die erforderliche Simulationsmethode eine große Herausforderung. Anwendbare Simulationsmethoden basieren auf einem partikelbasierten, gaskinetischen Ansatz, wie Particle-In-Cell (PIC) zur Simulation elektromagnetischer Wechselwirkungen und Direct Simulation Monte Carlo (DSMC) für Kollisionen zwischen den Partikeln. Viele andere Veröffentlichungen befassen sich, unter der Annahme eines idealen, unendlich großen Systems, mit der Simulation des Ionen-Einzelstrahls („Beamlet“), der sich innerhalb einer einzelnen Gitteröffnung bildet. Die Auswirkungen der endlichen Größe eines realen Systems können hingegen nur durch Simulation der vollständigen, dreidimensionalen Triebwerksgeometrie untersucht werden, die jedoch einen großen und komplexen Simulationsbereich erfordert. Relativ kurze Simulationszeiten werden erreicht, indem das bereits bestehende Framework des gekoppelten PIC-DSMC-Codes *PICLas* in Kombination mit Höchstleistungscomputersystemen verwendet wird. Im Rahmen dieser Arbeit wird *PICLas* um einen elektrostatischen Feldlöser hoher Ordnung erweitert. Für die betrachteten Plasmazustände wird die Partikelbewegung zur dominierenden, Zeitschritt definierenden Eigenschaft. Die genaue Partikelbehandlung an den Rändern sowie die Erweiterung um Ladungs- und Impulsaustauschreaktionen werden dargestellt.

Diese neuen Modelle werden mit verschiedenen Simulationen verifiziert. Dadurch wird die jeweils korrekte Implementierung belegt und die zugehörigen Ergebnisse zeigen eine gute Übereinstimmung mit Referenzlösungen. Die Validierung wird anhand von Ionenoptik-

Simulationen des RIT-μX EBB Triebwerks der ArianeGroup GmbH erreicht. Die Anwendbarkeit der Boltzmann-Beziehung als Fluidmodell für Elektronen wird sogar nahe der Grenze des „Electron Backstreaming“ nachgewiesen. Zusätzlich wird der Einfluss verschiedener Simulationsparameter einschließlich räumlicher und zeitlicher Diskretisierung analysiert. Die PIC-DSMC-Simulationen der Ionenoptik stimmen sehr gut mit den experimentellen Ergebnissen überein, sowohl hinsichtlich der erwarteten Erosionsmuster als auch quantitativ angesichts der messbaren Gitterströme. Die beste Übereinstimmung wird für ein Scattering-basiertes Kollisionsmodell und einer Neutralgastemperatur von realistischen 300 K erreicht. Anschließend wird die validierte Simulationskonfiguration auf veränderte Gittergeometrien angewendet. Hierbei wird der Einfluss von fehlausgerichteten Gitteröffnungspositionen untersucht, was zu abgelenkten Beamlets führt. Die Betrachtung der vollständigen Gittergeometrie ermöglicht es, erstmalig durch numerische Simulation zu zeigen, dass die Ablenkwinkel nicht nur von dem Gitterversatz abhängen, sondern auch direkt von der jeweiligen Position innerhalb des Gittermusters. Die Ablenkung nimmt mit der radialen Position zu und ist bei Randöffnungen am größten, da sich die positiv geladenen Beamlets auf der stromabwärtigen Seite der Gitter gegenseitig abstoßen. Dieser Einfluss spiegelt sich auch in einem verschobenen Erosionsmuster des zweiten Gitters wider.

Nomenclature

Symbols

Sign	Unit	Description
A	$[-]$	Coefficient for differential update in LSERK scheme
$\tilde{A}$	$[-]$	Constant stage multiplier for second state of velocity
$\vec{A}$	$\left[\mathrm{m\,s^{-2}}\right]$	Second (register) state of velocity
$\vec{a}$	$\left[\mathrm{m\,s^{-2}}\right]$	Acceleration, $\vec{a} = (a_x, a_y, a_z)^{\mathrm{T}}$
a	$[-]$	Speed ratio
$\vec{B}$	$[\mathrm{T}]$	Magnetic field
B	$[-]$	Coefficient for state update in LSERK scheme
C	$[-]$	Coefficient for time update in LSERK scheme
$\vec{D}$	$\left[\mathrm{C\,m^{-3}}\right]$	Electric displacement field
$\vec{E}$	$\left[\mathrm{V\,m^{-1}}\right]$	Electric field
$\mathcal{F}$	$[-]$	State derivative
$\vec{F}$	$[\mathrm{N}]$	Force
f	$\left[\mathrm{s^3\,m^{-6}}\right]$	Particle distribution function
$\vec{F}_L$	$[\mathrm{N}]$	Lorentz force
g_{12}	$\left[\mathrm{m\,s^{-1}}\right]$	Relative velocity between two particles
I	$[\mathrm{A}]$	Current
$\vec{j}$	$\left[\mathrm{A\,m^{-2}}\right]$	Current density
M	$[-]$	Number of stages
m	$[\mathrm{kg}]$	Particle mass
m_{dry}	$[\mathrm{kg}]$	Dry mass of spacecraft
m_{prop}	$[\mathrm{kg}]$	Propellant mass
$\mathcal{N}$	$[-]$	Normal (Gaussian) distribution
N	$[-]$	(Particle) number, amount
n	$\left[\mathrm{m^{-3}}\right]$	Number density
$\dot{N}$	$\left[\mathrm{s^{-1}}\right]$	Particle flow
N_{geo}	$[-]$	Polynomial degree of element mapping
P	$[-]$	Probability
p	$[-]$	Polynomial degree
q	$[\mathrm{C}]$	Particle charge
R	$[-]$	Random number, $R \in [0;1]$
r	$[\mathrm{m}]$	Radius

Sign	Unit	Description
T	$[\mathrm{K}]$	Temperature
Δt	$[\mathrm{s}]$	Time step
t	$[\mathrm{s}]$	Time
unif	$[-]$	Uniform distribution
$\mathcal{U}$	$[-]$	State
$\tilde{\mathcal{U}}$	$[-]$	Second (register) state
$\vec{V}$	$\left[\mathrm{m\,s^{-1}}\right]$	Second (register) state of position
V	$\left[\mathrm{m^3}\right]$	Volume
Δv	$\left[\mathrm{m\,s^{-1}}\right]$	Delta-v of mission
$\vec{v}$	$\left[\mathrm{m\,s^{-1}}\right]$	Velocity, $\vec{v} = (u,v,w)^{\mathrm{T}}$
$\vec{v}_{eff}$	$\left[\mathrm{m\,s^{-1}}\right]$	Effective exhaust velocity
$\hat{v}$	$\left[\mathrm{m\,s^{-1}}\right]$	Most probable velocity
$v_{\perp}$	$\left[\mathrm{m\,s^{-1}}\right]$	Perpendicular velocity component
w	$[-]$	Weighting factor, $w = N_{\mathrm{real}}/N_{\mathrm{simu}}$
$\vec{x}$	$[\mathrm{m}]$	Position, $\vec{x} = (x,y,z)^{\mathrm{T}}$

Greek Symbols

Sign	Unit	Description
α	$[-]$	Shape function exponent (half of polynomial degree)
β	$[^\circ]$	Deflection angle of beamlet
δ	$[-]$	Kronecker delta
ε_r	$[-]$	Relative permittivity
ε	$\left[\mathrm{A^2\,s^2\,N^{-1}\,m^2}\right]$	Permittivity
Γ	$\left[\mathrm{s^{-1}\,m^{-2}}\right]$	Particle flux
λ	$[\mathrm{m}]$	Mean free path
λ_D	$[\mathrm{m}]$	Debye length
μ	$[-]$	Mean value
ρ	$\left[\mathrm{C\,m^{-3}}\right]$	Charge density
σ	$\left[\mathrm{m^2}\right]$	Particle cross section
σ	$[-]$	Standard deviation
Θ	$[-]$	Clausing factor (transmittance)
ϕ	$\left[\mathrm{J\,C^{-1}}\right]$	Electrostatic potential
Ω	$[\mathrm{sr}]$	Solid angle
ω_{pe}	$\left[\mathrm{s^{-1}}\right]$	Electron plasma frequency
$\vec{\xi}$	$[-]$	Position in reference space

Indices

Sign	Description
α	Particle species
accel	Acceleration (grid)
beam	(Ion) beam
chem	Chemical reaction
coll	Collision
e^-	Electron
el	Elastic with scattering
ion	Ion
imp.	Impinging
in	Incoming, inflow
j	Index of stage
n	Index of iteration
out	Outflowing
p	Plasma
part	Particles
ref	Reference
relax	Relaxation (of inner DOF)
screen	Screen (grid)
SF	Shape function
stage	Index of (reconstructed) stage
Xe	Xenon (neutral)
Xe^+	Xenon ion
$'$	Post-collisional or post-reaction values

Constants

Sign	Value	Description
c_0	$299792458\,\mathrm{m\,s^{-1}}$	Speed of light
ε_0	$8.8543 \cdot 10^{-12}\,\mathrm{A^2\,s^2\,N^{-1}\,m^2}$	Vacuum permittivity
k_B	$1.38064852 \cdot 10^{-23}\,\mathrm{J\,K^{-1}}$	Boltzmann constant
q_e	$1.6022 \cdot 10^{-19}\,\mathrm{C}$	Elementary charge

Acronyms and Abbreviations

ARI Aerospace Research Institute, Tehran
ARM Acceptance-Rejection Method

ARTEMIS Advanced Relay Technology Mission
BC Boundary Condition
BGG Background Gas
BGK Bhatnagar Gross Krook
BOUN Bogazici University Istanbul
BR Boltzmann Relation
BUAA Beijing University of Aeronautics and Astronautics
CEX Charge Exchange Reaction
CFD Computational Fluid Dynamics
CFL Courant Friedrichs Lewy
CSC Culham Science Centre
CSU Colorado State University
DG Discontinuous Galerkin
DOF Degree of Freedom
DSMC Direct Simulation Monte Carlo
EBS Electron Back-Streaming
EOC Experimental Order of Convergence
EP Electric Propulsion
ESA European Space Agency
FEM Finite Element Method
FK Fully kinetic
FMF Free Molecular Flow
GIT Gridded Ion Thruster
HDG Hybridizable Discontinuous Galerkin
HIT Harbin Institute of Technology, Shenzhen
HLRS High Performance Computing Center Stuttgart
IAG Institute of Aerodynamics and Gas Dynamics
IFE Immersed Finite Element
IOM Leibniz-Institut für Oberflächenmodifizierung
IRS Institute of Space Systems
JAXA Japan Aerospace Exploration Agency
JPL Jet Propulsion Laboratory
KeRC Keldysh Research center
KIT Karlsruhe Institute of Technology
LSERK Low Storage Explicit Runge-Kutta
MCC Monte Carlo Collision
MEX Momentum Exchange Reaction
MHD Magnetohydrodynamics
MPI Message Passing Interface
NAL National Aerospace Laboratory, Chofu
NASA Glenn John H. Glenn Research Center at Lewis Field

NPU Northwestern Polytechnical University
NSS Natural Sample Size
PIC Particle-in-Cell
RIT Radio frequency Ion Thruster
THM Technische Hochschule Mittelhessen
TMU Tokyo Metropolitan Institute of Technology
UM University of Michigan
UT University of Tennessee
UTokyo University of Tokyo
VDF Velocity Distribution Function
VHS Variable Hard Sphere
VT Virginia Polytechnic Institute and State University

1 Introduction

1.1 Motivation

The importance of Electric Propulsion (EP, short for electrically powered spacecraft propulsion) for spacecraft design has significantly increased in recent decades. Although the first conceptional ideas were already formulated in 1906 [42] and the first in-space demonstration was conducted in 1964 [31], the first commercial satellite using EP did not start until 1993. Between then and 2017, a further 248 satellites with EP systems were launched [67].

Motivation for the development of EP is to raise the limited energy content of the stored propellant and, hence, its defined maximum achievable effective exhaust velocity $\vec{v}_{eff}$ out of the thruster. By increasing $\vec{v}_{eff}$, the propellant mass m_{prop} required for a mission with defined total impulse can be reduced, which in turn results in an increased payload mass (as part of the dry mass m_{dry}) or operating time (by providing a higher Δv). This relationship is described by the well-known Tsiolkovsky rocket equation:

$$\Delta v = \vec{v}_{eff} \ln\left(\frac{m_{dry}+m_{prop}}{m_{dry}}\right) \quad \Leftrightarrow \quad \frac{m_{prop}}{m_{dry}} = \exp\left(\frac{\Delta v}{\vec{v}_{eff}}\right) - 1\,. \tag{1.1}$$

For EP, the approach in increasing $\vec{v}_{eff}$ is based on raising the energy for thrust production from the outside by electrical means, e.g., generated by photovoltaics. In an engineering context, two points need to be addressed: first, the way of energy coupling from the generator into the propellant; and secondly, the conversion method into kinetic energy. The topic of this study is the gridded ion thruster (GIT), which ionizes the propellant and accelerates the ions electrostatically by a high-voltage grid system, usually consisting of two or three biased electrodes with up to several thousand concentric apertures through which the ions are extracted. Their resulting very high velocities of several 10000 m/s produce the thrust. A special step for EP, and in particular GIT, was the launch of the Advanced Relay Technology Mission (ARTEMIS) spacecraft in 2001, a geostationary earth orbit satellite, whose mission was saved only by the availability of an ion thruster on-board. After it was launched into an orbit much lower than planned due to a failure in the upper stage of the rocket, a GIT was used for final orbit raising by a continuous operation of 10 months instead of the originally intended function for station keeping with much shorter thrust intervals [59].

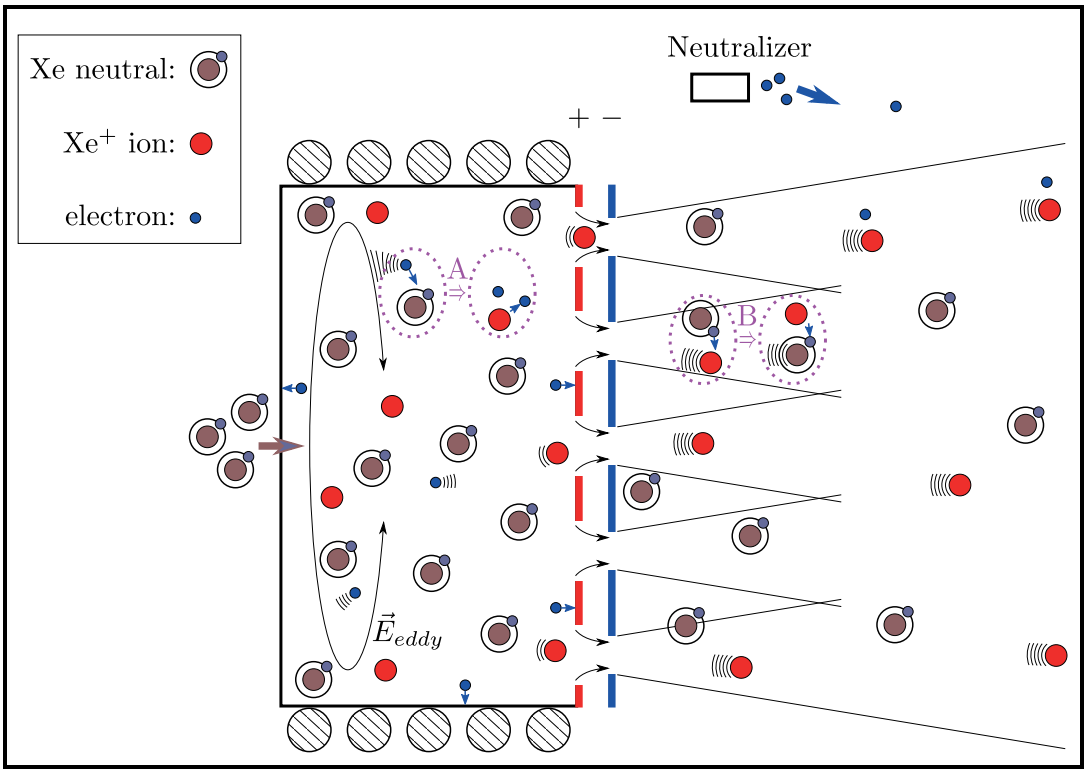

Figure 1.1: RIT schematic (A: ionization, B: charge exchange).

One specific kind of GIT is the so-called radio frequency ion thruster (RIT). It has been in development since the 1960s in Germany [70], currently also by ArianeGroup GmbH. RIT systems have many advantages. One such advantage relevant to this study is their good scalability allowing the operation of miniaturized thrusters [66]. The schematic of a RIT is shown in Fig. 1.1. The depicted discharge chamber includes on its left hand side a neutral gas inflow (here Xenon) and the alternating current inside the surrounding coil generates an axial magnetic field, which in turn induces an eddy electric field within the plasma. The freely moving electrons are accelerated and the plasma acts analogously to a secondary coil of an electrical transformer. This inductive energy coupling into the plasma enables electron impact ionization ("A") on the neutral gas, by which more electrons and ions are generated. The region adjacent to the ionization chamber, directly around the grids, is called "ion optics" and creates individual "beamlets" per aperture. A neutralizer emits electrons into the plume so that a quasi-neutral plasma forms again further downstream. This prevents a negative charging of the spacecraft by the remaining electrons, otherwise the ions would be attracted back and any thrust eliminated. Other inter-particle interactions besides the ionization process inside the ionization chamber include the so-called charge exchange reaction (CEX), which can transfer an electron from one of the slow neutral atoms to a fast, already accelerated ion ("B"). This CEX creates slow ions inside the plume, which are prone to the electric field back to the second grid and cause significant erosion.

The research in EP and plasma technology in general has been utilizing numerical simulation on computers already for several decades. However, the simulation of plasmas as present in EP systems is not trivial. One difficulty lies in the degree of flow rarefaction by which the continuum assumptions from Computational Fluid Dynamics (CFD) and Magnetohydrodynamics (MHD) methods are not applicable. The other difficulty lies in the plasma state itself because of freely moving ions and electrons. The interdependence of flow dynamics, applied electromagnetic fields, and the self-fields of the charged species causes complex physical phenomena. Applicable simulation methods belong to a particle-based, gas-kinetic approach by which the particle distribution function of ions, neutrals and electrons is modeled via representative simulation particles moving through a computational domain.

The main objectives of EP simulations are performance optimization and the estimation of recommended operating points dissociated from possibly occurring failure modes. Additionally, simulations can give direct insight into physical interrelationships, since all simulated values such as plasma state and fields can be evaluated at any position inside the simulation domain, which is in contrast to available measurements in the context of an experiment. Another advantage over experiments is that once a numerical model is set-up, it can be easily modified to simulate different conditions. Nevertheless, experimental measurements are crucial for the development of numerical simulation since their comparison validates the models and assumptions behind the simulation.

In the application of GIT, simulations can focus on the ionization chamber, the ion optics, or the total plume leaving the thruster. Since the ionization chamber differs in its simulation requirements from the other domains and is also already the focus of a team at the University of Gießen [48], the subject of this study is the adjacent part, starting with the ion optics. An important topic of ion optics simulations deals with the grid currents, caused by ions (e.g. from the already mentioned CEX interactions) hitting the surfaces of the grid system, which eventually erode and limit the life time of a thruster. One goal of this study shall be to reproduce the measured currents of a complete, albeit miniaturized, GIT for validation. Since a relatively large computational domain is required for this task, including both the whole radial extent of the grids and a sufficient distance in downstream direction, the corresponding simulations can be seen as the first steps towards a combined optic-/plume-simulation. Also other questions arising from thruster development can be addressed only when considering a complete, but finite pattern of grid apertures, such as effects dependent on the actual aperture position inside the pattern which will be the application case of the validated simulation set-up.

1.2 Point of departure

The simulation of ion optics goes back to so-called gun models, first developed in the 1960s for electron trajectory calculations in the field of particle accelerator research (i.e., the *SLAC Electron Trajectory Program* software [49], well-known over decades and developed at the Stanford Linear Accelerator Center[1]). In the same years, similar codes were also already applied to the axisymmetric simulation of ion thruster optics [17, 45]. The basis of those simulation methods for trajectories inside space-charge-defined fields is the decoupling of particle motion and the calculation of the electric fields, by which only the steady state solution is of interest and dynamic or transient processes are not considered. Here, a large number of particles starting at an inflow boundary are traced from time step to time step through the computational domain until all of them have left it. Subsequently, the charges corresponding to all total trajectories are interpolated onto the computational mesh, on which an updated electric field and the next trajectories' calculations are based. This iteration is repeated until the trajectories (or fields) have converged into a steady solution. The application of those gun (also called "flux-tube") models is versatile and, just in regard to the application to ion thrusters, a large amount of examples were published during the last decades. The same simulation approach is used by the Particle-in-Cell (PIC) [16, 54] method, including the same parts of particle tracking, field solver, and charge/field interpolations, which will be further described in 2.6.1. In contrast to the gun models, PIC is time-accurate. The fields are updated after each time step and are defined by the actual particle positions and not by steady trajectories. That enables simulating plasma phenomena with higher accuracy and less restrictions, including their dynamic characteristics such as the realistic electron motion as oscillation around the much heavier ions. However, it requires a much larger amount of simulation particles (and, thus, a higher computational cost) for approximating a smooth charge distribution.

Table 1.1 shows an overview of ion optics codes published since the early 1990s when the US, Japan, and European Space Agency (ESA) started new development campaigns for GIT. The distinctive features of each code include its type in terms of gun model vs. PIC and the utilized spatial discretization in terms of axisymmetric two-dimensional ("2D"), three-dimensional with azimuthal symmetry ("3D polar"), or full 3D. If it is not a standard finite difference scheme, the kind of field solver is also defined (e.g., finite element method (FEM) or immersed finite element (IFE) method). The coupling of the ion beam formation to the assumed discharge plasma can be achieved either by a self-consistent extraction from a corresponding plasma sheath or from a simplifying emission surface. When neutral gas

[1] Based on its more modern derivates, the commercial codes *EGUN* and *IGUN* [8], it is still used and also applied in the context of ion thruster optics [114].

Table 1.1: Overview of ion optics codes, sorted by publishing institute (see list of acronyms for full institute names) and year. Non-specified data included as "?". Erosion models distinguished between static erosion rate ("S") or dynamic grid change ("D").

Institute	Year of first publication	Name of code	Subsequent extensions	Type	Spatial discretiz.	Coupling to plasma	Distribution of neutrals	Model for CEX	Erosion model
NAL (Japan)	1990 [46]	?		gun	3D-FEM	sheath	-	-	-
UT (USA)	1991 [90]	?	1993: 3D [89]	PIC	2D/3D	sheath	via DSMC	MCC	S
UTokyo/JAXA (Japan)	1991 [2]	*opt/JIEDI*	1995: dynamic erosion [104]	gun	2D	surface	via FMF	MCC	D
			1996: 3D [3]		3D		via FMF		S
			2008 [80]: det. erosion model	both	3D-FEM	sheath	via DSMC		D
CSC (UK)	1995 [19]	*SAPPHIRE*		PIC	2D	sheath	via FMF	MCC	S
UM (USA)	1999 [30]	*ERODE*	2005 [33]: miscellaneous	PIC	2D	sheath	via DSMC	DSMC	D
KeRC (Russia)	1999 [79]	*GASEL*		gun	2D	sheath	via BGK	MCC	S
	2015 [102]	*IOS-3D*			3D		via FMF		
IOM (Germany)	1999 [112]	*IGUN* [8]	2008 [114]: detailed validation	gun	2D	sheath	via FMF	MCC	D
	2002 [113]	*KOBRA3* [105]			3D		-	-	-
JPL (USA)	2002 [97]	*CEX2D/3D*	2008 [119]: dynamic erosion	gun	2D	sheath	analytical	MCC	D
			2004 [1]: 3D		3D-FEM				S
			2018 [26]: PIC	PIC					
CSU (USA)	2001 [118]	*igx*		gun	3D (polar)	surface	analytical	MCC	S
	2003 [37]	*ffx*	2007 [35]/2010 [36]: misc.		3D				D
TMU (Japan)	2001 [87]	*IBEX-T*	2003 [86]: 3D	PIC	2D/3D	sheath	-	-	-
VT (USA)	2003 [57]	*(HG-)IFE-PIC*	2004 [56, 58]: hybrid grid (HG)	both	3D-IFE	sheath	via FMF	MCC	?
HIT (China)			2015 [23]: collab. with China	PIC			via DSMC		?
NASA Glenn (USA)	2004 [73]	*MICHELLE*		gun	3D-FEM	sheath	?	MCC	?
BUAA (China)	2008 [69]	?		PIC	3D	sheath	?	MCC	S
NPU (China)	2010 [111]	?	2018 [27]: 3D	PIC	2D/3D	sheath	constant	MCC	?
BOUN (Turkey)	2014 [115]	?		PIC	3D (polar)	sheath	via DSMC	DSMC	?
THM (Germany)	2017 [100]	?		gun	3D	sheath	-	-	-
ARI (Iran)	2018 [122]	?		PIC	2D	sheath	-	-	-

was included when considering CEX interactions with ions, the distribution of neutrals was simulated separately by DSMC, a free molecular flow (FMF) model, or a BGK model; whereas the CEX collisions themselves are modeled via DSMC with species-dependent particle weights or MCC (see subsection 2.6.2). Additionally, when the published codes included an erosion model via sputtering yield data, they either had a static erosion rate or a dynamic grid change.

One of the most noteworthy codes is the *opt* code from JAXA. After having been extended to 3D, a FEM field solver and a detailed erosion model, it was later incorporated into the *JIEDI* tool [39], in the course of which PIC routines were also added to the gun model. Several simulation results using *JIEDI* were published, including fully kinetic electrons, or most recently, the simulation of multi-aperture ion optics with an inhomogeneous inflow [81]. The counterpart on the US side is the *CEX2D/3D* tool from JPL. Its latest edition also includes a PIC module which models the charge of CEX ions self-consistently and, therefore, prevents their non-physical trapping within the plume [26]. It is important to distinguish between (gun) tools optimized for small computational cost and high fidelity PIC codes. The former, such as *igx* and *ffx* from the Colorado State University (CSU), may include several simplifications, but they allow very short simulation times by which geometrical optimization approaches also become feasible [36]. Nevertheless, Tab. 1.1 shows that the trend is leaning towards three-dimensional PIC models with more capabilities compared to classical gun models and more complex application cases, which is accompanied by the continuously increasing available computing power. An example is the *IFE-PIC* code from Kafafy, which includes a highly sophisticated PIC method, but nevertheless has reasonable computational cost due to its various optimizations. It also includes an optional gun model for efficient optics simulations, but due to its generic structure, it can be also used for other PIC applications such as ion thruster plume-spacecraft interaction [56]. The promising approach of this flexible (IFE-)PIC code is in addition emphasized by its further development in collaboration with the Harbin Institute of Technology (HIT) in China [23, 72].

A similarly flexible PIC-code named *PICLas* is being developed at the University of Stuttgart. At the Institute of Space Systems (IRS), the heritage of the numerical simulation of rarefied flows can be traced back to the work of Fasoulas [38] and Laux [63] and their implementation of a two-dimensional DSMC code named *LasVegas*. The Direct Simulation Monte Carlo (DSMC) method is a particle-based, gas-kinetic approach like PIC; however, it models the physical and chemical nature of inter-particle collisions instead of the electromagnetic interaction inside a plasma (further described in 2.6.2). The first steps towards the simulation of rarefied, reactive plasma flows were established by a cooperation between the IRS, the Institute of Aerodynamics and Gas Dynamics (IAG), the Karlsruhe Institute of Technology (KIT), the High Performance Computing Center (HLRS) in Stuttgart, and the German Research School of

RWTH Aachen. Here, the DSMC-modules of *LasVegas* were extended [91] and the coupling with an electromagnetic PIC code [82, 99, 109] was prepared, giving *PICLas* its name as a combination of PIC and a derivative of *LasVegas*. In connection with the development of a new field solver framework named *Flexi*, the whole coupling scheme and DSMC routines were re-implemented and several improvements and new routines added [75, 83, 92, 107], which are further described in section 2.7.

1.3 Problem statement and outline

The aim of this study is to prepare and apply *PICLas* for the simulation of the combined optic/plume region of a complete, miniaturized GIT. A representative simulation set-up shall be established that can be used to investigate questions arising in the industrial development process of ion propulsion systems. The most severe difficulties in the corresponding simulations are both the large number of required time steps due to the different particle velocities inside the plasma and the relatively large and complex simulation domain when considering a complete, although miniaturized, thruster. Therefore, the very efficient and already established framework of *PICLas* is an attractive approach to realize reasonable simulation times on high performance computing systems. Furthermore, by the utilization of a flexible PIC code instead of a tailor-made solution only applicable for ion optics, the possibility for future extensions is given, such as an enlargement of the simulation region and extended physical models, as needed for a coupling with the discharge chamber or a consideration of further downstream plume regions including the actual neutralization process.

First, the required theoretical background is explained in chapter 2, including the physical theory as well as the description of already existing and required models in *PICLas*. Chapter 3 deals with the own numerical development by the author in terms of describing the implemented, new routines which are verified in chapter 4. Finally, chapter 5 presents the simulations of the RIT-μX EBB (elegant breadboard) of ArianeGroup GmbH, including validation studies with comparisons between simulation results and experiments, as well as the application to changed geometries. The conclusions drawn from the study are set out in chapter 6, together with an overview of possible next steps.

2 Theoretical background

2.1 Microscopic modeling of rarefied plasma flows

A plasma is defined as (partly) ionized gas with freely moving ions and electrons, exhibiting a collective behavior under the influence of electromagnetic fields. Its kinetic behavior can be modeled by the Boltzmann equation that describes the development of the particle distribution function $f_\alpha = f_\alpha(\vec{x},\vec{v},t)$ depending on position $\vec{x}$, velocity $\vec{v}$, and time t:

$$\frac{\partial f_\alpha}{\partial t} + \vec{v}_\alpha \frac{\partial f_\alpha}{\partial \vec{x}_\alpha} + \frac{\vec{F}}{m_\alpha}\frac{\partial f_\alpha}{\partial \vec{v}_\alpha} = \left(\frac{\delta f}{\delta t}\right)_{Coll}. \tag{2.1}$$

Here, $\vec{F}$ is an external volume force acting on the particles of species α with mass m and $\left(\frac{\delta f}{\delta t}\right)_{Coll}$ is the so called collision integral describing the change of f by inter-particle collisions. The second term on the left hand side represents the change by diffusion and the third term by external forces. Under the assumption of Boltzmann's "Stosszahlansatz" [18], the collision integral can be described for binary collisions between distribution functions f_1 and f_2 with post-collisional values $()'$, relative velocity g_{12}, collision cross section σ, and solid angle Ω as:

$$\left(\frac{\delta f}{\delta t}\right)_{Coll} = \int_{\vec{v}_1}\int_{\Omega}\left(f_1 f_2 - f_1' f_2'\right) g_{12}\sigma \mathrm{d}\Omega \mathrm{d}\vec{v}_1 . \tag{2.2}$$

In a continuum flow, the frequent number of collisions relaxates f towards the thermodynamic equilibrium defined by the well-known Maxwell-Boltzmann distribution [14]. For the case of rarefied flows, however, the limited number of collisions results in a deviation from equilibrium and for increasing rarefaction, a continuum approach of flow description needs to model more statistical moments of f to describe the deviation with sufficient accuracy. Eventually, for a general (even free molecular) flow a macroscopic description is not applicable because f can become of arbitrary kind. Hence, a microscopic approach becomes necessary, such as a statistical modeling by representative simulation particles.

In this particle approach, the particle distribution function f is discretized in time as well as in physical and velocity space. Typically, a temporal first order approach is utilized that advances f linearly in time by small time steps Δt from $f(\vec{x},\vec{v},t)$ to $f(\vec{x},\vec{v},t+\Delta t)$. This allows a decoupling of the movement (based on diffusion and external forces) from the collision

process during a single time step. Furthermore, f is approximated as the linear combination of N_{part} individual particles, which are, as mathematical interpretation, δ-functions at positions $\vec{x}_k$ and velocities $\vec{v}_k$:

$$f(\vec{x},\vec{v},t) \approx \sum_{k=1}^{N_{part}} w\delta(\vec{x}-\vec{x}_k(t))\,\delta(\vec{v}-\vec{v}_k(t)) \,. \tag{2.3}$$

The weighting factor w defines the number ratio of real, physical particles N_{real} to simulation particles N_{sim} and assumes that N_{sim} is still large enough to model the same statistical behavior as the real plasma flow. From the microscopic description of Eq. 2.1, an interpretation of macroscopic values can be achieved via the statistical moments of f. With Boltzmann constant k_B, they are defined for number density n_{cell}, macroscopic flow velocity $\langle\vec{v}\rangle_{cell}$, and translational temperature T_{cell} within the volume of a computational cell V_{cell} as:

$$n_{cell} = \frac{w\langle N_{cell}\rangle}{V_{cell}}\,, \quad \langle\vec{v}\rangle_{cell} = \langle\vec{v}_{cell}\rangle\,, \quad T_{cell} = \frac{m_\alpha\left(\langle\vec{v}_{cell}^{\,2}\rangle - \langle\vec{v}_{cell}\rangle^2\right)}{3k_\mathrm{B}}\,. \tag{2.4}$$

2.2 Plasma physics

2.2.1 Electromagnetic fields

The definition of the force $\vec{F}$ is crucial for the correct modeling of the plasma physics via the Boltzmann equation (Eq. 2.1). For the considered plasma flows, this force equals the Lorentz force $\vec{F}_L$, based on particle charge q, electric field $\vec{E}$, particle velocity $\vec{v}$ and magnetic field $\vec{B}$:

$$\vec{F}_L = q\vec{E} + q\vec{v}\times\vec{B}\,. \tag{2.5}$$

The force defines the change in momentum $m\vec{v}$ and in the most general case, $m\vec{v}$ needs to be treated relativistically, with rest mass m_0 and speed of light c_0:

$$\vec{F}_L = \frac{\mathrm{d}(m\vec{v})}{\mathrm{d}t} \quad , \qquad m\vec{v} = \frac{m_0\vec{v}}{\sqrt{1-|\vec{v}|^2/{c_0}^2}}\,. \tag{2.6}$$

Equation 2.5 shows the important role of $\vec{E}$ and $\vec{B}$ in plasma dynamics. Their evolution in time t and space is described by the well-known Maxwell's Equations, consisting in their presented form of: Ampère's circuital law in Eq. 2.7, the Maxwell-Faraday equation in Eq. 2.8,

as well as Gauss's laws for magnetism in Eq. 2.9 and for electrostatics in Eq. 2.10:

$$\frac{\partial \vec{E}}{\partial t} - {c_0}^2 \nabla \times \vec{B} = -\frac{\vec{j}}{\varepsilon_0}, \tag{2.7}$$

$$\frac{\partial \vec{B}}{\partial t} + \nabla \times \vec{E} = 0, \tag{2.8}$$

$$\nabla \cdot \vec{B} = 0, \tag{2.9}$$

$$\nabla \cdot \vec{E} = \frac{\rho}{\varepsilon_0}. \tag{2.10}$$

Those equations define the coupling of electromagnetic fields with the distribution of charge density ρ and current density $\vec{j}$ of a plasma with vacuum permittivity ε_0. The assumption of an irrotational electric field (i.e., $\nabla \times \vec{E} = 0$) defines the case of electrostatics with $\frac{\partial \vec{B}}{\partial t} = 0$ for which a magnetic field can exist but its temporal development must be quasi-steady. Together with the definition of an electric potential ϕ by $\vec{E} = -\nabla\phi$, this yields the describing equation of electrostatics, the Poisson equation:

$$\Delta\phi = -\frac{\rho}{\varepsilon_0}. \tag{2.11}$$

2.2.2 Categorization of plasmas

The plasma inside a RIT can be described as cold[1], low pressure discharge with the characteristics of electron temperatures[2] in the range of $T_{e^-} \approx 1 - 10\,\mathrm{eV}$ together with ion and electron number densities of $n_{ion} \approx n_{e^-} \approx 1 \cdot 10^{14} - 1 \cdot 10^{19}\,\mathrm{m}^{-3}$ [68].

For most cases, the same amount of electrons and ions exist inside an ideal, unbounded plasma and their charges cancel each other out in a macroscopic perspective. Additionally, a plasma screens itself from internal and external fields by a resulting distribution of ions and electrons that compensates the imposed potential difference. The length scale of that screening is defined by the Debye length λ_D which is the distance at which the local potential inside a plasma decreases to $1/e$:

$${\lambda_D}^{-2} = \frac{n_{e^-} {q_e}^2}{\varepsilon_0} \left(\frac{1}{k_\mathrm{B} T_{e^-}} + \frac{1}{k_\mathrm{B} T_{ion}} \right). \tag{2.12}$$

At significantly greater distances, the plasma seems to be "quasi-neutral". Nevertheless, there still exists charge separation at the smaller lengths due to the dynamic electron behavior: In

[1] Plasmas are categorized into hot plasmas with similar temperatures for ions and electrons and cold plasmas with the ions being much colder than the electrons [68]

[2] The temperature definition in eV instead of K is based on the corresponding energy $E = k_\mathrm{B} T^{[\mathrm{K}]} = q_e T^{[\mathrm{eV}]}$, with Boltzmann constant k_B and elementary charge q_e resulting in a conversion factor of $q_e/k_\mathrm{B} = 11604.5\,\mathrm{K/eV}$.

the time scale of the electrons, the large mass ratio between ions and electrons results in ions seeming to be at rest and electrons themselves oscillate around them with displacements based on the thermal electron movement. The time scale of that phenomenon is characterized by the electron plasma frequency:

$$\omega_{pe} = \sqrt{\frac{{q_e}^2 n_{e^-}}{\varepsilon_0 m_{e^-}}}. \tag{2.13}$$

2.2.3 Boltzmann relation and bounded plasmas

In a macroscopic perspective, however, the described electron dynamics might not be of interest, especially for electrostatic cases. Due to their very small mass, electrons have a much higher mobility than ions and can be assumed to be in thermodynamic equilibrium (see section 2.1) for most cases. That allows to model the electrons as fluid for plasma states in which the ions are defined by their microscopic behavior, but the electron plasma frequency does not have to be resolved. A well-known electron fluid model is the Boltzmann relation (BR) which assumes that the electrons are isothermal, their inertia can be neglected in momentum conservation (i.e., the electron drift velocity is negligible), and the electron pressure follows the ideal gas law [25]. For the given assumptions, the electron number density n_{e^-} can be described as function of the local potential ϕ:

$$n_{e^-}^{\mathrm{BR}}(\vec{x},t) = n_{e^-,ref} \exp\left[\frac{q_e}{k_\mathrm{B} T_{e^-}}(\phi(\vec{x},t) - \phi_{ref})\right], \tag{2.14}$$

with a reference potential ϕ_{ref} at the location $\vec{x}_{ref}$ with $n_{e^-}(\vec{x}_{ref}) = n_{e^-,ref}$. In other words, the number density of electrons decreases exponentially towards a lower electric potential. The definition of the reference point of ϕ_{ref} and $n_{e^-,ref}$ is mostly based on the quasi-neutral assumption $n_{e^-} = n_{ion}$ at a known location.

Large potential differences can occur in bounded plasmas, i.e., when the plasma is bordered by a solid wall. Here, the charges accumulate or recombine, and can be externally controlled by an applied electric potential. Based on the charge balance of ions of electrons, their flows onto the confining walls must be equal in steady state, which is also known as “ambipolar diffusion” [25]. Since the flux of electrons is much higher than for ions (due to their higher temperature and smaller mass, see also subsection 3.3.1), a positive plasma potential ϕ_p forms inside the plasma with respect to the wall potential. Now, the decreasing potential towards the wall shields the electrons according to Eq. 2.14 inside a so-called “sheath” region between plasma and wall. An one-dimensional sheath model will be described in section 4.3.

2.3 Inter-particle collisions

In the Boltzmann equation, the effect of collisions between particles is described by the collision integral (see section 2.1). The collision process can result in various phenomena such as momentum and energy transfer as well as ionization. The degree of collisionality is defined by the mean free path λ describing the distance that a particle covers in average inside the gas with number density n_g before colliding with the next particle:

$$\lambda = \frac{1}{n_g \sigma}. \tag{2.15}$$

The cross section σ depends on the type of collision and the particle characteristics. During elastic collisions (in contrast to inelastic collisions), the internal particle energies do not change and, thus, the resulting scattering process conserves both total kinetic energy and total momentum. A simple model is the one of hard, elastic spheres with radius a_1 and a_2 which collide if both of their centers are inside a radius of $a_{12} = a_1 + a_2$, as depicted in Fig. 2.1 together with the scattering angle θ and impact parameter b. This hard-sphere model yields a cross section of $\sigma = \pi a_{12}^2$. There also exist several other models which reproduce the physical fluid behavior more accurately, such as the VHS model [14] with σ dependent on the relative velocity between the particles. For collisions between two charged particles ("Coulomb collisions"), other models are required, but it has been already shown [30] that the corresponding collisions are not required for the modeling of ion thruster optics.

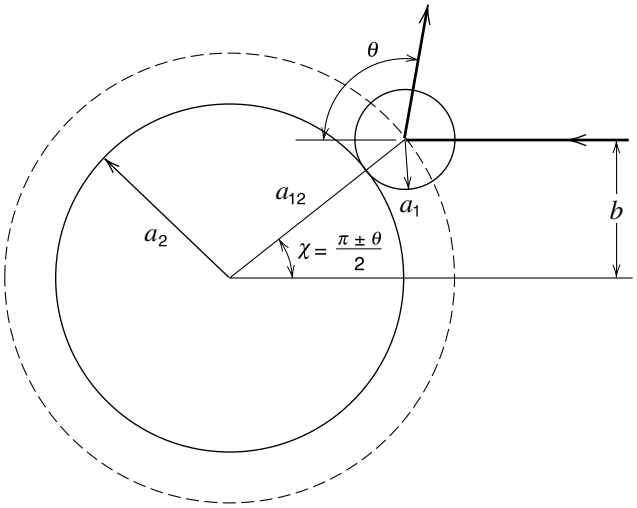

Figure 2.1: Hard-sphere scattering [68].

2.4 Ion thruster optics

Ion thruster optics consist of an assembly of biased grids with up to several thousand apertures (see also section 1.1) through which the ions are extracted and accelerated out of the discharge chamber at potential ϕ_{dis}. As described in section 2.2.3, sheaths form around structures inserted into a plasma with a decreasing voltage of ϕ_p towards the wall that repels the electrons, but also accelerates the ions. For the case that the potential behind the wall (e.g. the far field in space at ϕ_∞) is lower than the wall potential and it reaches through apertures into the plasma, it can be already imagined that not all ions impinge on the wall but a certain fraction is directed through the apertures, whereas the electrons are kept inside. To prevent any screening effect of the plasma (see subsection 2.2.2), the diameter of the apertures must be smaller or in the order of λ_D [43]. Assuming a negligible initial ion velocity, their end velocity is defined by the energy conservation as $v_\infty = \sqrt{2q_e U_{tot}/m_{ion}}$ with the total acceleration voltage $U_{tot} = \phi_{dis} - \phi_\infty$.

A high U_{tot} voltage results in a high thrust, but the potential drop towards the bounding grid should be limited so that the velocity of non-extracted (i.e., impinging) ions is still small to reduce any corresponding erosion effects. The resulting 2-grid design consists of, first, a "screen" grid at ϕ_{screen} and, secondly, an acceleration ("accel") grid at ϕ_{accel}, with both potentials lower than ϕ_{dis}. In respect to ϕ_{dis}, the ϕ_{screen} is basically defined by charge conservation via a "floating" ϕ_p, whereas the even lower ϕ_{accel} defines the acceleration voltage that highly effects the actual extraction characteristic, as shown in Fig. 2.2: If ϕ_{accel} is also only defined by ϕ_p, the plasma (including both ions and electrons) simply passes around both grids, shielded by individual sheaths, as shown in (a). With a certain acceleration voltage, all electrons are shielded from the acceleration aperture, as depicted in (b), and keeps them inside the discharge chamber for even higher voltages (i.e., lower ϕ_{accel}), as shown in (c) and (d). In those two figures, it can also be seen how a meniscus-shaped sheath forms at the screen apertures that defines the trajectories of ions extracted from the plasma. Only at a sufficiently high acceleration voltage, a well-focused beamlet forms that reaches directly through the apertures. With respect to ϕ_∞, the accel potential ϕ_{accel} is at a negative voltage to prevent downstream electrons from the neutralizer reaching the discharge chamber ("electron back-streaming", see also section 5.2) [43]. Slow charge exchange (CEX) ions are attracted by the negative potential of the screen grid, impinge on it, and can cause significant erosion. Therefore, 3-grid systems exist with a deceleration ("decel") grid at a potential near to ϕ_∞, by which the downstream face of the accel grid is protected from CEX erosion even at very high negative ϕ_{accel}. However, the third grid adds an additional complexity to the system, by which 2-grid systems can be seen as baseline design.

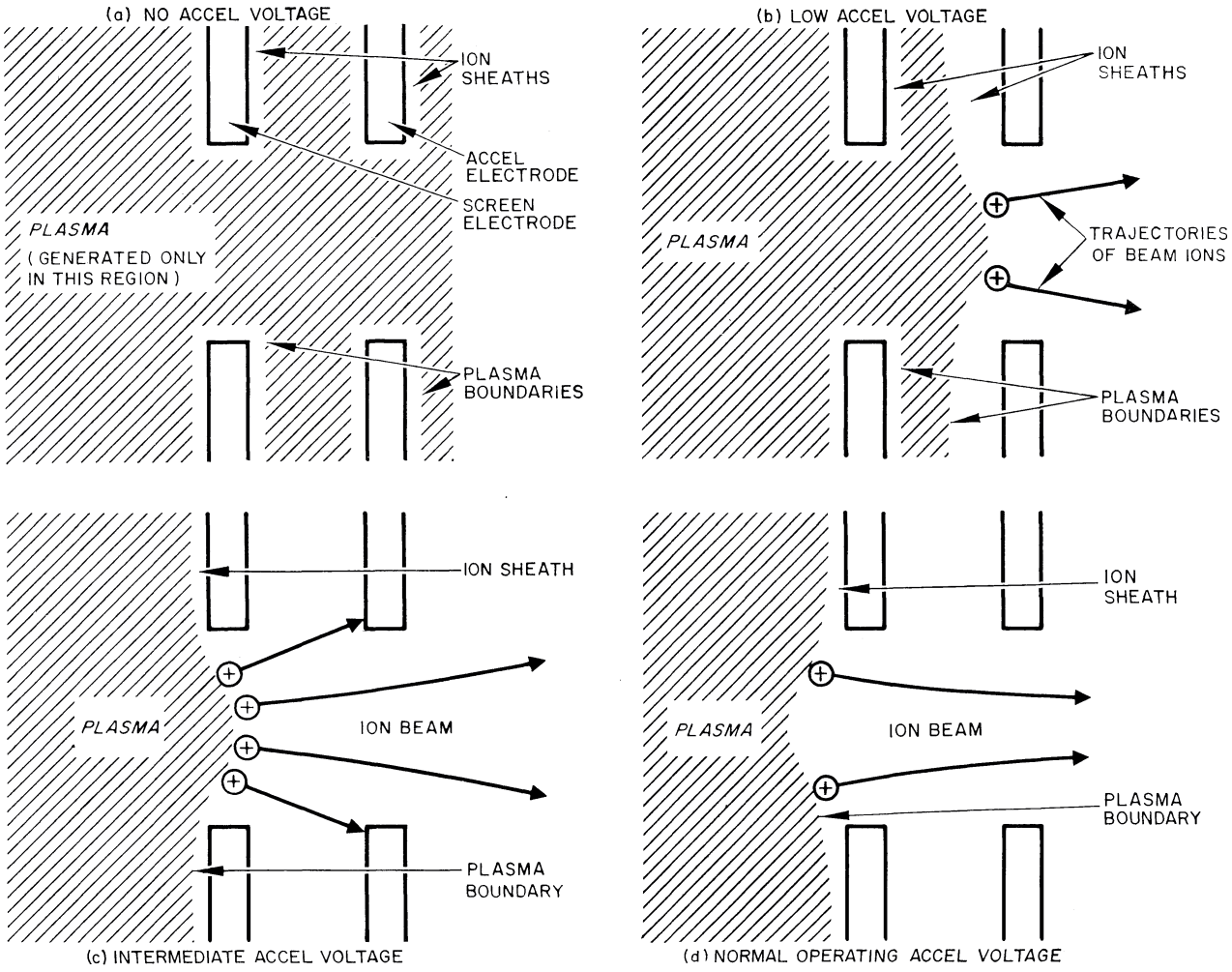

Figure 2.2: Illustration of the variation of the plasma sheath as the accel voltage is varied in ion thruster optics. [21].

2.5 Monte Carlo Methods

Amongst a multitude of other applications, particle methods can be interpreted as so called Monte Carlo simulations. Its background is the law of large numbers, stating that the statistical moments from samples of a random experiment converge with increased sample size towards the theoretical expected value. Starting point is the initialization of samples according to a given distribution. Next, each sample follows modeled rules and finally the results of all trials are combined to deduce the global result.

A very common example is the approximation of π by initializing points randomly by a uniform distribution of x- and y-coordinates inside a square with $x, y \in [0,1)^2$. The determination of π is now based on a circle with radius 1 around $x = y = 0$ and all points within the circle ($r = \sqrt{x^2 + y^2} < 1$) are accepted. The expected value E of the ratio of accepted points to

all initialized points is the same as the area ratio of the quarter circle to the whole square $E = {}^{A_{circle}}/_{4A_{square}} = {}^{\pi}/_{4}$. Thus, the simulated ratio multiplied with 4 will converge towards π with increasing number of total points.

For the previous example, the known distribution that the initial samples followed was a simple 2-D uniform distribution, the only modeled rule was to accept points inside the circle and the evaluated statistical result was the number of accepted points. In more complex Monte Carlo simulations, the initial distribution might differ from uniformity and the total result can depend on the statistical evaluations of all sample states. Furthermore, the modeled rules can be an interdependent sequence instead of single decisions and might include further random events which generate an own "history" for each individual sample [32]. Consequently, every particle-based simulation that approximately solves the Boltzmann equation can be considered as Monte-Carlo method. The initial distribution f is randomly sampled, afterwards propagated in space over time by the modeled physics and, eventually, the resulting distribution is evaluated. Here, the initial distribution functions can be of arbitrary kind. However, the pseudo-random numbers generators commonly available in a programming context only create uniform distributions unif$(0,1)$. The following question is how to convert a sampled $X \in \text{unif}(0,1)$ into $f(X)$. Basically, there are two different mathematical methods that can be also combined or further optimized and are briefly described below.

2.5.1 Inverse transform sampling

To perform an inverse transform sampling from the targeted probability density function $f(X)$ of the random variable X, the corresponding cumulative density function $F(X) = \int_{-\infty}^{X} f(x)$ needs to be known which also defines the scaling of f via $\lim_{X\to\infty} F(X) = 1$. Based on a given uniformly distributed $R \in \text{unif}(0,1)$, X can be calculated by inverting $F(X)$:

$$F(X) = \int_{-\infty}^{X} f(x)\,\mathrm{d}x \stackrel{!}{=} R \quad \Rightarrow \quad X = F^{-1}(R) \tag{2.16}$$

This method is particularly suited if F^{-1} can be explicitly expressed, such as for the example of the exponential distribution Exp(λ) with parameter λ:

$$\begin{aligned} f_\lambda(X) &= \begin{cases} \lambda e^{-\lambda X} & ,X \geq 0 \\ 0 & ,X < 0 \end{cases} \\ F_\lambda(X) = 1 - e^{-\lambda X} \quad &\Rightarrow \quad X = F_\lambda^{-1}(R) = -\frac{1}{\lambda}\ln(1-R) = -\frac{1}{\lambda}\ln(\tilde{R}) \end{aligned} \tag{2.17}$$

Here, it was utilized that when $R \in \text{unif}(0,1)$ also $1 - R = \tilde{R} \in \text{unif}(0,1)$.

2.5.2 Acceptance-rejection method

The inverse transform sampling becomes inefficient when an explicit inversion from $F(X)$ to $F^{-1}(R)$ is not possible and Eq. 2.16 needs to be solved numerically, e.g., by a Newton method. Then, a version of the so-called acceptance-rejection method (ARM) is mostly used instead. The ARM makes use of an envelope probability density function $g(X)$ from which can be easily sampled (e.g., directly by G^{-1}) and of a constant k ensuring $k \cdot g(X) \geq f(X)$ [76].

Figure 2.3b shows the general scheme. First, $g(X)$ is sampled as X_1 by the random number R_1. However, this X_1 is only accepted if a second random number R_2 is smaller than the ratio of f and $k \cdot g$, both evaluated at X_1. Figure 2.3a illustrates this for the targeted probability density function $f(X) = \mathrm{Exp}(\lambda = 1)$ (see Eq. 2.17) and $g(X) = \mathrm{unif}(0, X_{max})$ as uniform distribution[3]. The intervals of $g(X)$ are chosen because the lower boundary of zero matches the one of $f(X)$ and at $X_{max} = 14$ the target distribution has already dropped, in this example, below 10^{-6}. The factor $k = f^{max} \cdot X_{max}$ ensures that $k \cdot g(X)$ equals the maximum value $f^{max}_{\lambda=1} = 1$.

In Fig. 2.3a, $X_1 = G^{-1}(R_1) \approx 1.39$ was sampled and the resulting evaluated values are $f(X_1) = 0.25$ and $k \cdot g(X_1) = 1$. Hence, the probability of acceptance when comparing with R_2 is 25%. The number of expected acceptances decreases even more with increasing X which motivates the utilization of envelopes $k \cdot g(X)$ which progress along $f(X)$ more closely, e.g., with the same asymptotic behavior at high X. The example of sampling the velocity distribution function for a particle inflow condition will be described in section 3.3.1.

2.6 Numerical simulation of rarefied, reactive plasmas

2.6.1 Electromagnetic interactions

PIC

Nowadays, with its origins going back to the late 1950s and 1960s [16, 54], the PIC method is considered as standard approach for the simulation of rarefied plasmas. It does not assume any continuum assumptions, instead the plasma is modeled in phase space via the Boltzmann equation, as described by Eqs. 2.1 and 2.3. Under the assumption of a negligible collision integral on the right hand side, the Boltzmann equation is also known as Vlasov equation [117]. The temporal development of f is represented by the movement of particles. That movement, however, is defined by the forces resulting from the electromagnetic waves propagating in

[3] Note that also $g(X)$ is normalized (i.e., $\lim_{X\to\infty} G(X) = 1$), thus: $\mathrm{unif}(0, X_{max}) = \begin{cases} 1/X_{max} & , X \geq 0 \\ 0 & , X < 0 \vee X > X_{max} \end{cases}$

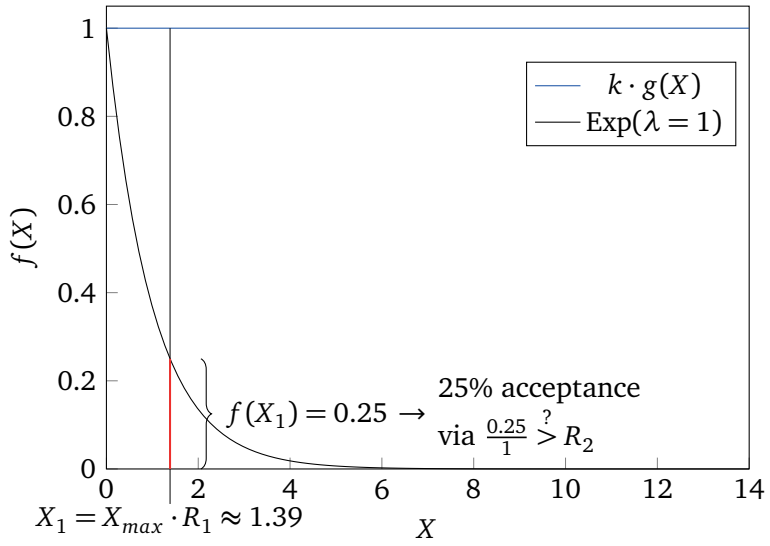

(a) Example for distribution function $f(X)$ and envelope $k \cdot g(X)$.

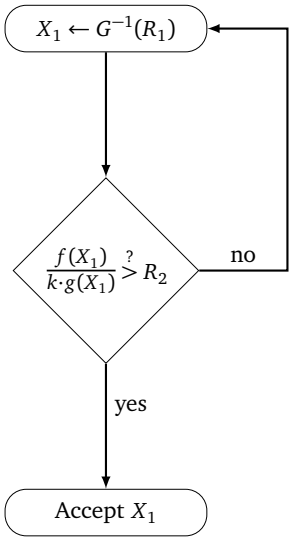

(b) General calculation scheme.

Figure 2.3: Acceptance-rejection method based on random numbers $R \in \text{unif}(0,1)$.

an Eulerian manner through the domain, which in turn depend on the particle distribution. Thus, the general PIC method is a coupled particle-mesh approach with mixed Lagrangian (as particles) and Eulerian (as fields) framework.

Figure 2.4 depicts a typical scheme of an electrodynamic PIC method. Besides the spatial discretization by particles and mesh cells, f is discretized in time, i.e., propagated by individual time steps Δt. At a given simulation time t, all N_{part} simulation particles are distributed within the domain, each including a position and velocity information $\vec{x}$ and $\vec{v}$, respectively. Additionally, the fields $\vec{E}(\vec{x})$ and $\vec{B}(\vec{x})$ are defined in each of the N_{cell} cells. The transition to the next time step is performed by a temporal integration of the corresponding derivatives: a "push" for the particles and the "propagation" of electromagnetic waves. Both advancements in time also account for boundary conditions encountered in the spatial domain such as reflective walls. The acceleration values as derivative of particle velocities result from the Lorentz force $\vec{F}_L$ (see Eq. 2.5) at the respective particle positions, whereas the derivatives of the electromagnetic fields are the result of the numerical solution of Maxwell's equations (see subsection 2.2.1) including the charge and current density distributions ρ and $\vec{j}$. Hence, before the temporal integration is performed concurrently for particles and fields, an "Interpolation" of $\vec{E}$ and $\vec{B}$ from cells to particle positions is required as well as a "Deposition" of the particle information onto the mesh. The actual, individual calculation procedures relevant for this study will be described in section 2.7 in terms of their implementation in *PICLas*.

The discretization requirements of the PIC method are based on aspects of both accuracy and numerical stability. The temporal integration of the hyperbolic Maxwell equations requires

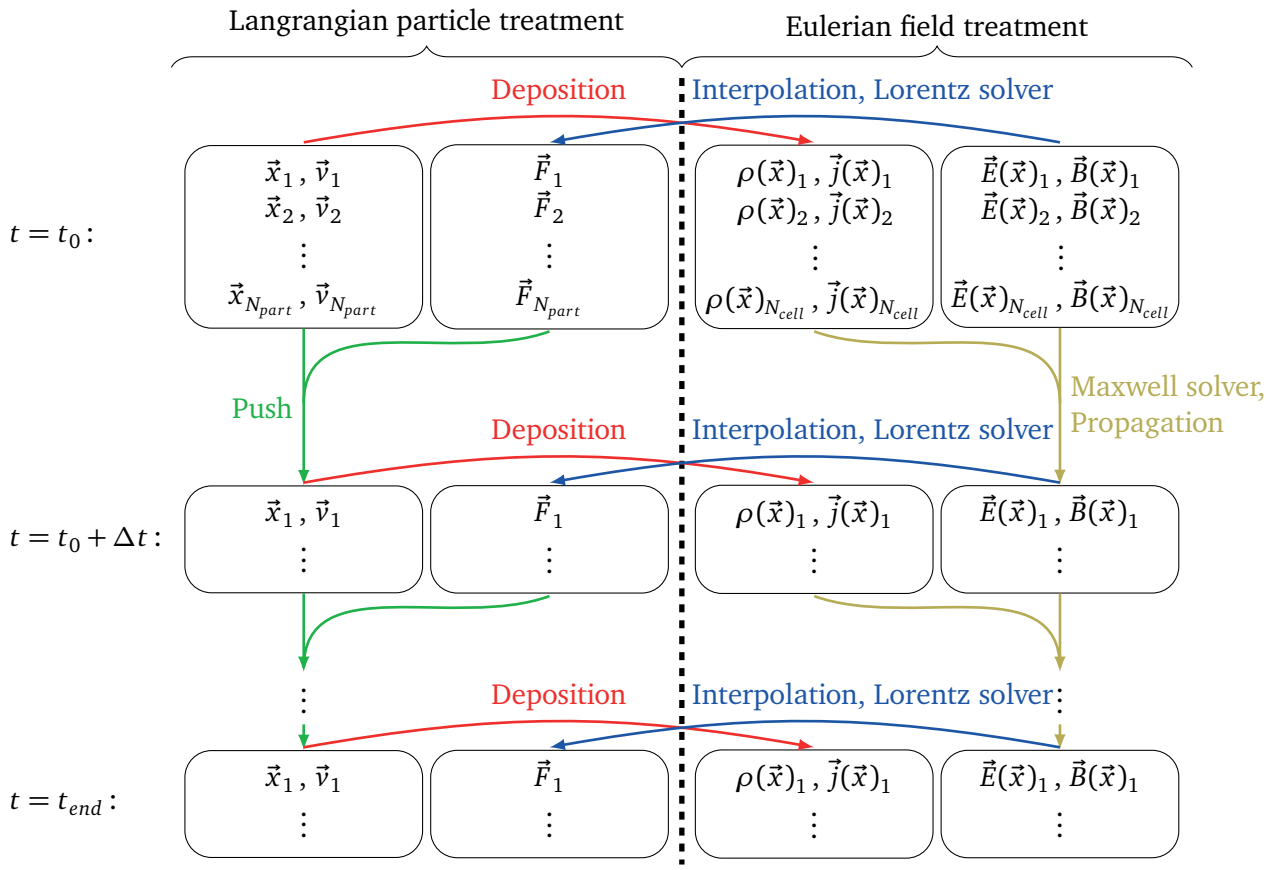

Figure 2.4: Electrodynamic PIC scheme.

the time step Δt to fulfill the Courant Friedrichs Lewy (CFL) condition for the speed of light to ensure the stability of the field solver. The time step also defines the accuracy when temporally integrating the particle paths across fields gradients. Furthermore, plasma oscillations (see Eq. 2.13) need to be resolved, limiting Δt to a certain fraction of the oscillation period [16]. The same applies for the spatial discretization which needs to resolve the Debye length (Eq. 2.12), otherwise the charge separation between electrons and ions cannot be reproduced in a physically correct manner.

Alternatives to PIC

There exist a multitude of simulation approaches for rarefied plasmas. The “right” choice depends on the actual application and is defined by a trade-off between accuracy and computational cost. PIC-based methods can be seen as method of choice for the current study. Nevertheless, other possible methods are briefly summarized. Continuum-based methods can be excluded for ion optics simulations, mostly due to the nearly free-molecular flow regime

and strong charge separation. Other mesh-only approaches are discrete velocity models in which the velocities are discretized and propagated via corresponding advection equations. The required 6-dimensional mesh, however, makes it computationally very intensive [22, 103]. An alternative in which the particle-mesh coupling is avoided, too, are grid-free methods [28] such as the Barnes-Hut tree [7] or the Fast Multipole Method [44]. These so-called treecode methods were already investigated in their usage for ion optics simulations [33], but their application to complex, realistic applications and the implementation of electron models pose severe difficulties.

2.6.2 Inter-particle interactions

DSMC

Similarly to the PIC approach (see 2.6.1), DSMC is a particle method that models the Boltzmann equation in phase space (see Eqs. 2.1 and 2.3) and goes back to the 1960s, introduced by G. A. Bird [14]. In addition to their positions and velocities, the simulation particles can carry information about their internal energy state through the computational domain. Under the assumption of negligible forces, collision process and particle movement are decoupled in a first order approach by calculating the change of each particle state blurred over a single time step. The collisions are handled in a probabilistic manner with phenomenological models. The actual implementation in *PICLas* will be described in 2.7, but the general aspects are described below.

Figure 2.5 depicts a typical DSMC cycle during a single time step. Particle movement and localization inside the computational mesh including the treatment of boundary conditions are the equivalent of the "push" included in 2.6.1. Possible particle pairs (with individual velocities v_{p1} and v_{p2}) are chosen and the corresponding collision probabilities P_{coll} calculated. P_{coll} also considers approximated macroscopic, local number densities n_{mesh}. Based on random

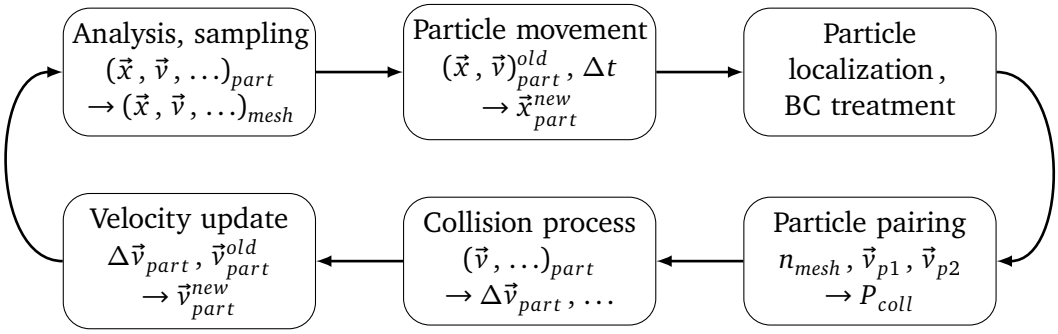

Figure 2.5: Typical DSMC cycle.

numbers and further probabilities, the type of an occurring collision is determined. The change of particle velocities and internal energy states is calculated as part of the collision process. In contrast to PIC, the velocities are not continuously changed by field-based forces but by discrete changes ("velocity update") as result of the collisions decoupled from the movement. Numerical resolution requirements for DSMC are defined by the collisions process. The time step and the spatial discretization between possible particle pairs must resolve the collision frequency and the mean free path, respectively.

Alternatives to DSMC

A very common alternative to DSMC for the coupling with PIC is the so called Monte Carlo Collision (MCC) approach. MCC assumes a temporally constant "background cloud" of collision partners. By that, every simulation particle is directly checked for a collision (instead of an actual pairing) and the collision partner is created only for the collision process itself. This assumes that the collisions do not affect the background cloud, which is the case if its number density n_{bg} is much higher than the one of the actual simulation particles. Similarly to DSMC, the decision for an occurring collision is based on a probability P_{coll} which is compared to a random number. Birdsall [15] proposes a P_{coll} that is exponentially dependent on the ratio of traveled particle distance (with relative velocity g_{12} during Δt) to mean free path λ and is by its definition always limited to an interval between 0 and 1:

$$P_{coll}^{MCC} = 1 - \exp\left(-\frac{g_{12}\Delta t}{\lambda}\right). \tag{2.18}$$

Under the assumption of negligible velocities of the background particles and a corresponding collision cross section σ, the probability becomes $P_{coll}^{MCC} = 1 - \exp(-n_{bg}\sigma g_{12}\Delta t)$.

As for PIC, discrete velocity models are a possible, but computationally intensive, alternative. Different corresponding implementations of the collision integral exist, such as Bhatnagar Gross Krook (BGK) models [9]. Those BGK approaches can also be implemented into particle-based methods, essentially replacing the particle pairing and collision process [93]. However, transitional flows on the edge to the free molecular regime pose severe difficulties in the correct modeling of the collision integral by BGK.

2.7 The Plasma Kinetic Code PICLas

The plasma kinetic code *PICLas* is a tool for the simulation of rarefied gases and plasmas. It has been cooperatively developed by the IAG and the IRS at the University of Stuttgart [78]. The

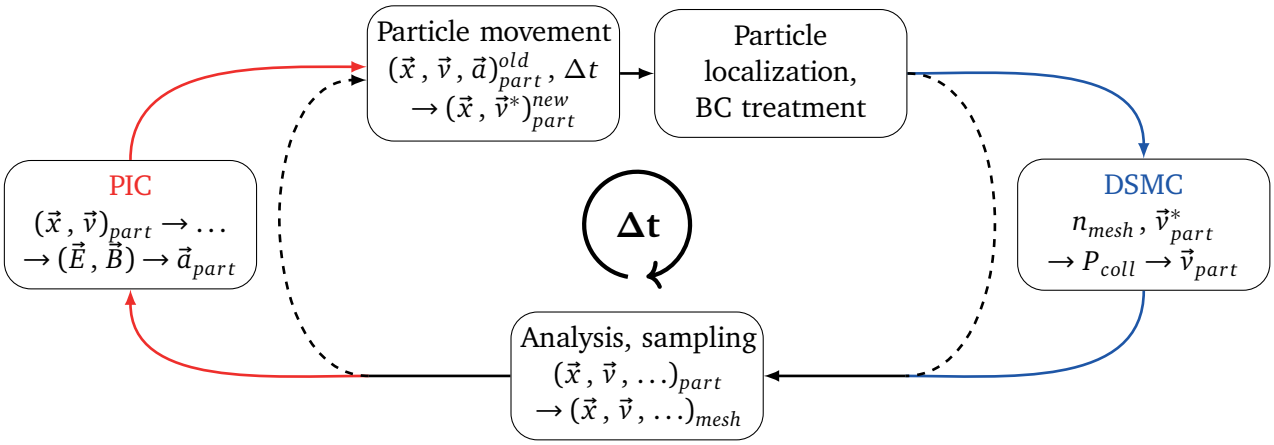

Figure 2.6: Coupled PIC-DSMC cycle of *PICLas*.

origin of *PICLas* lies, on its DSMC part, in the simulation of dilute, non-equilibrium flows, such as present in atmospheric entries and thruster plume expansion; and, on its (Maxwell-)PIC part, in the simulation of electromagnetic heating devices [110]. With the coupling of both approaches, the simulation of reactive, rarefied plasma flows becomes possible.

Figure 2.6 depicts the coupled simulation cycle within *PICLas*. The PIC part determines the acceleration of the individual particles due to electromagnetic fields (see 2.6.1). Afterwards, the particles are accordingly moved through the computational domain and consider possible boundary conditions. After the final particle positions $\vec{x}_{part}$ and temporary velocities $\vec{v}^*_{part}$ have been determined, the final velocities $\vec{v}_{part}$ are calculated by DSMC (see 2.6.2). A time step Δt resolving the collision frequency by DSMC is typically much higher than the PIC-related time step (see 2.6.1). This ensures in most cases a sufficient temporal discretization when using a single Δt based on PIC requirements. Nevertheless, sub-cycling approaches are also implemented. Eventually, analysis and sampling routines are called, e.g., for the evaluation of cell-based mean flow values. PIC and DSMC are coupled in a modular manner, which also enables simulations without any forces or inter-particle collisions (see black, dashed lines). *PICLas* includes several special features. On the following pages, those relevant for this study are described and, in the end, the additionally required models are discussed.

2.7.1 High order approach and spatial discretization

Main characteristic of *PICLas* is its part of the Discontinuous Galerkin (DG) framework that is developed at the IAG, named *Flexi* [47, 52] in its current version. This framework includes the description of the computational mesh and of the field solutions. The latter consist of piecewise polynomials, which are (giving DG its name) discontinuous at mesh cell interfaces.

More precisely, the implementation in *Flexi* and *PICLas* is a spectral element method which uses a tensor product basis and hexahedral cells with a collocation of integration and interpolation points [61, 62]. The mesh cells are of unstructured type, internally ordered along a Hilbert curve due to its clustering property [77]. The localization procedure of *PICLas* (i.e., the assignment of a general particle position to a specific cell) is accelerated by a Cartesian background mesh to reduce the possibilities in the searching algorithm. Each polynomial, curvilinear mesh cell with element nodes $\hat{\vec{x}}_{mno}$ defines a mapping from coordinates in reference space $\vec{\xi} = (\xi^1, \xi^2, \xi^3) \in [-1,1]^3$ to physical space $\vec{x}$, based on a Lagrange interpolation polynomial of degree N_{geo}:

$$\vec{\xi} \mapsto \vec{x} \,:\, \vec{x}(\vec{\xi}) = \sum_{m,n,o=0}^{N_{geo}} \hat{\vec{x}}_{mno} \ell_m(\xi^1) \ell_n(\xi^2) \ell_o(\xi^3)\,. \tag{2.19}$$

This high order approach in *PICLas* has several advantages. In the context of the Maxwell solver, it is motivated by the low dispersion and diffusion characteristics in the numerical approximation of wave propagation over long distances or time. But also in the context of parallel efficiency, there are additional advantages. *PICLas* is parallelized by domain decomposition and communication between the processes via the Message Passing Interface (MPI), which includes an exchange of particle data between shared cell layers. The DG approach is highly cell-local, meaning that the explicit field solver requires to communicate surface data only between direct cell neighbors. Additionally, the high order approach allows a sub-cell resolution by which the field solutions are of high accuracy even on coarse meshes [50]. Consequently, by the usage of curvilinear, body-fitted high-order meshes, the amount of required mesh cells can be significantly reduced which can improve not only the parallel efficiency, but also reduces the cost of the particle tracking since less cell changes occur.

2.7.2 PIC-related routines

All PIC-related routines in *PICLas* are designed to retain the higher order approach of the field solver described in the previous subsection. If one part corresponds to a lower order method, the accuracy of the total approach must be assumed to decrease accordingly. The implemented temporal integration schemes as well as the field solver itself will be presented in the context of the new electrostatic PIC approach in chapter 3. In the following paragraphs, the remaining parts of Deposition and Interpolation are described.

Deposition

As described in 2.6.1, the deposition part saves the particle information onto the mesh. Mathematically, the delta-distributions from particle positions and velocities, as defined in Eq. 2.3, must be interpolated to the cell-specific, polynomial field solutions in terms of densities of charge and current as source term of the field solver.

The deposition methods implemented in *PICLas* include:

- cell mean value,
- nearest interpolation point,
- B-splines based on a Cartesian background mesh,
- polynomial shape functions.

Here, a quick overview of those methods is given, a more detailed description including their application can be found in [108].

The cell mean value method is the fastest, but least accurate approach by which all charges are averaged to a single cell value. In the nearest interpolation point approach, the cell volume is subdivided into separate parts around each interpolation point to which, again, the corresponding constant value is assigned. Due to the subdivision, a sub-cell resolution is achieved, depending on the polynomial degree. However, the resulting discontinuous distribution within a cell can lead to large gradients and a very disturbed polynomial approximation of the source field, especially for a small particle number per cell [78]. Therefore, the particle distribution needs to be smoothed, ideally across several cells. That is achieved by interpreting each simulation particle as particle cloud of constant shape. The B-splines approach uses a polynomial shape with defined degree and deposits the charges onto a Cartesian background mesh and from there to the interpolation points [107]. This approach is computationally efficient, but the requirement of several neighboring cell layers for a higher order deposition and the underlying interpolation into fix Cartesian directions makes it very difficult to account for a correct deposition at domain boundaries. Hence, the higher order method of choice are polynomial shape functions [55, 110] which deposit the charge to all interpolation points within a user-defined radius. For several cases, the influence of boundaries can be considered, as described in section 3.4. The fundamentals are described below.

Deposition via polynomial shape functions The interpretation of each particle as shape function is defined as spherical cloud with radially decreasing charge density. At a defined radius r_{SF}, where the density drops to zero, the function is cut off. Figure 2.7a shows a 2D

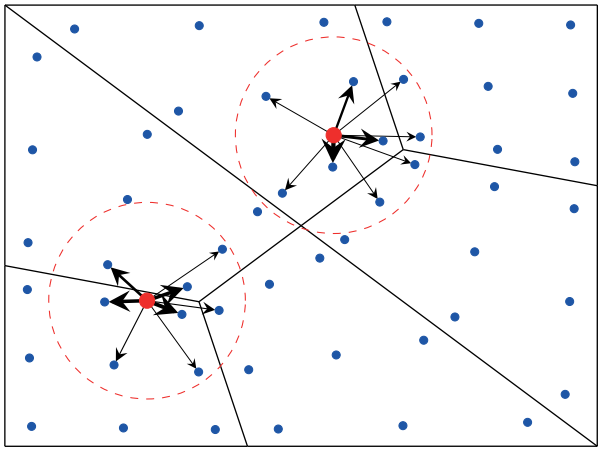

(a) Interpolation from particle onto DOF within r_{SF}.

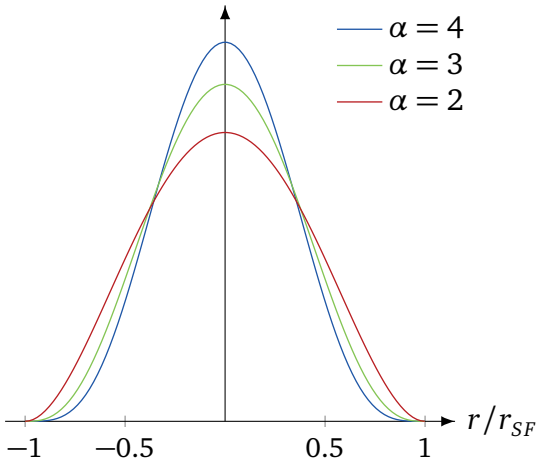

(b) Density function in 1D for different α.

Figure 2.7: Deposition by polynomial shape function.

computational mesh (black lines) with its corresponding Gauss-Legendre interpolation points (degree of freedom (DOF), shown as blue points). For all charged particles (the 2 red dots in this figure), each DOF in range is evaluated by Eq. 2.20 with scaling constant C ensuring the given, theoretical integral value. For a larger exponent α, the shape becomes more weighted towards the actual particle position, as shown in Fig. 2.7b.

$$\rho(r=|\vec{x}_{part}-\vec{x}_{DOF}|)=\begin{cases} Q_{part}C\left(1-\frac{r^2}{r_{SF}^2}\right)^{\alpha} & ,r<r_{SF} \\ 0 & ,r\geq r_{SF} \end{cases}, \quad \iiint_V \rho(r)\,\mathrm{d}V = Q_{part} \tag{2.20}$$

The characteristics for an 1D shape function are depicted in Fig. 2.8. With an r_{SF} that always spans the entire considered space, all individual particle shape functions create a superposed polynomial function $\rho(\vec{x})_{tot}$ of degree $p_{shape}=2\alpha$, as shown in Fig. 2.8a. The DOFs act as supporting points of the cell polynomials $\rho(x)_{interp.}$. The latter are identical to the respective $\rho(\vec{x})_{tot}$ if $p_{mesh}\geq p_{shape}$, as shown in Fig. 2.8c. But at distances r_{SF} from the particle positions (such as at $x=x_A+r_{SF}=-0.5$ and $x=x_B-r_{SF}=-0.25$ in Fig. 2.8b), $\rho(\vec{x})_{tot}$ is subdivided into a piecewise polynomial. For those considered x-intervals inside which shape functions are cut off, an identical cell-global $\rho(x)_{interp.}$ does not exist and, thus, it is only an approximation even for the same degree. The approximation becomes better with increasing p_{mesh} for which the number of DOF within a shape function sphere increases when the cell sizes are kept the same. This situation can also be seen in Fig. 2.8c–2.8e: Without cut-off, the interpolated polynomial converges with higher p_{mesh} fast towards the exact function and differs for $p_{mesh}\geq p_{shape}=8$ only by machine accuracy; whereas for the case with cut-off, the error is still larger but decreasing. Nevertheless, for realistic application cases, there are a multitude of superposed

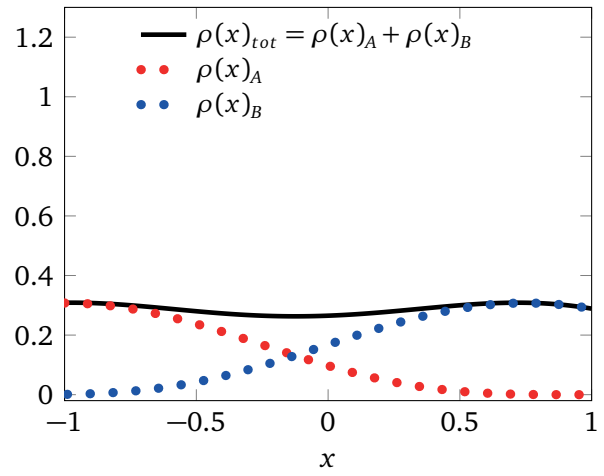

(a) Superposition of $\rho_A + \rho_B$ without cut-off ($r_{SF} = 2$).

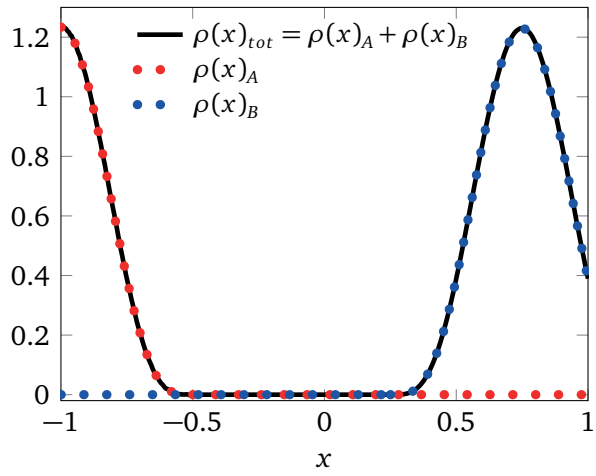

(b) Superposition of $\rho_A + \rho_B$ with cut-off ($r_{SF} = 0.5$).

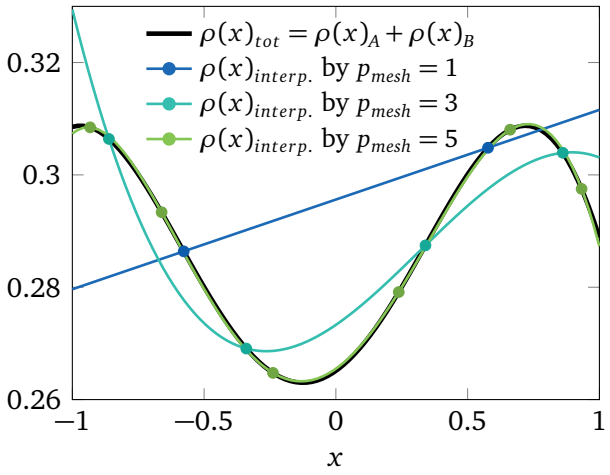

(c) Interpolated $\rho(x)_{interp.}$ without cut-off ($r_{SF} = 2$).

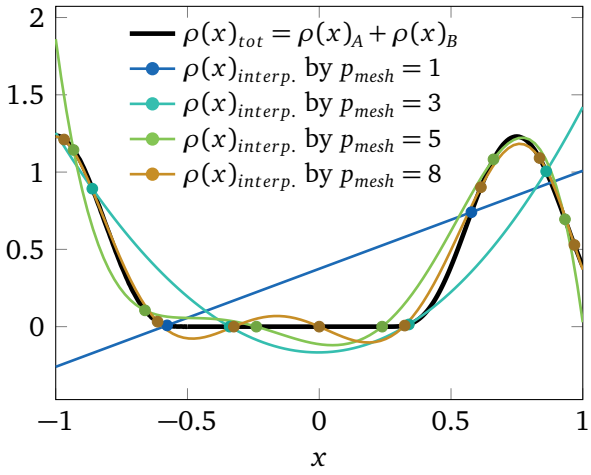

(d) Interpolated $\rho(x)_{interp.}$ with cut-off ($r_{SF} = 0.5$).

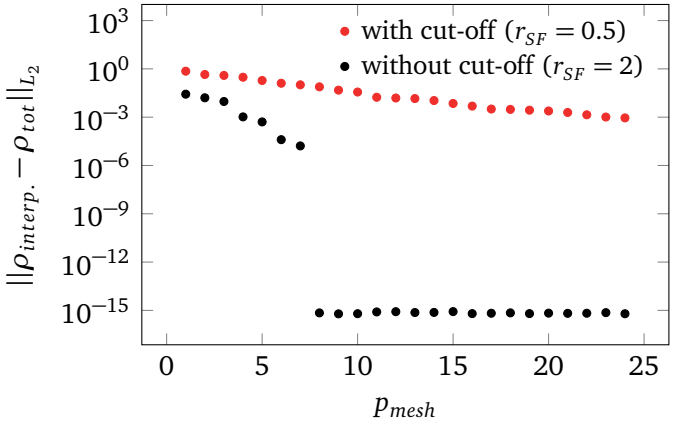

(e) L_2 error $\sqrt{\int (\rho(x)_{interp.} - \rho(x)_{tot})^2 \, dx}$ of by p_{mesh}-interpolated $\rho(x)_{interp.}$.

Figure 2.8: Deposition of particles (x_A =-1 , x_B =0.75) by 1D shape function with $\alpha = 4$.

particle functions deposited onto the cell DOFs, which results in a more continuous total density distribution that can be well interpolated also by smaller p_{mesh}.

Interpolation and Lorentz solver

In the DG scheme of *PICLas*, the fields are given as cell-local polynomials. Hence, the high order approach can be retained in the interpolation process by simply evaluating the corresponding tensor product. Due to the spectral collocation (see 2.7.1), this is implemented in a particularly efficient way. The cell polynomial is defined by the field values at the interpolation points. Therefore, an evaluation at a particle position takes all values within the respective cell into account, as shown in Fig. 2.9a.

It can be shown that the interpolation procedure should be an exact inversion of the actual deposition routine to prevent any mesh-related artificial acceleration [16]. For the cell mean value and nearest interpolation point method, the inverse function is implemented in a straightforward manner. However, for deposition approaches reaching across a large amount of interpolation points within several cells, such as shown in Fig. 2.9b for a corresponding inverse shape function, this is computationally intensive. But due to the higher order approximation and similarly to the deposition approach, it can be assumed that the polynomial evaluation yields a very similar result compared with the superposition of corresponding (inverse) shape functions.

Once the fields are evaluated at the particle positions, the respective Lorentz force is calculated, as defined in Eq. 2.5 together with its definition as temporal derivative of the particle

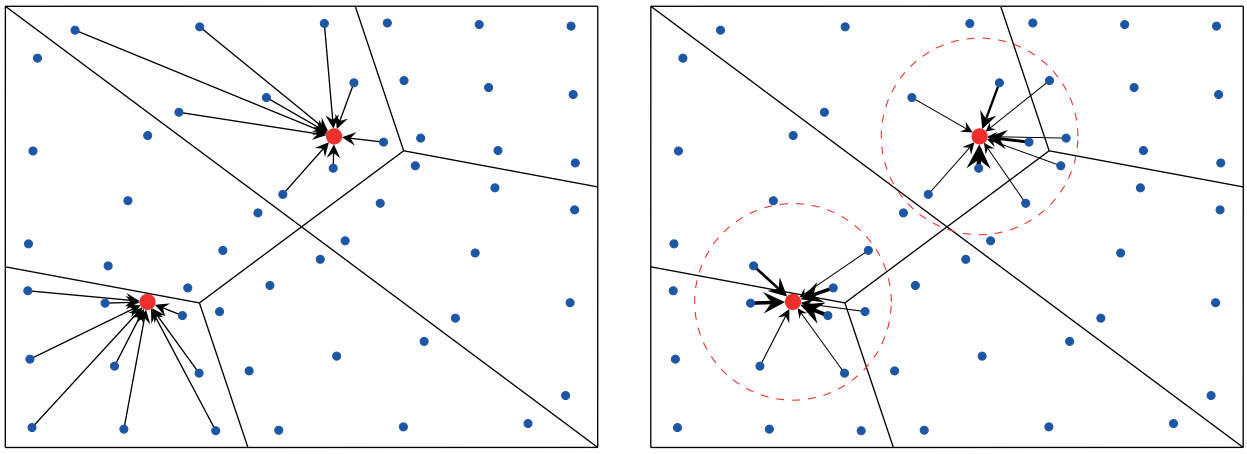

(a) Interpolation from cell polynomial onto particle. **(b)** Interpolation by inverse shape function.

Figure 2.9: Comparison of interpolation by polynomial evaluation and inverse shape function.

momentum $m\vec{v}$. The Lorentz solver calculates the corresponding acceleration $\vec{a} = \mathrm{d}\vec{v}/\mathrm{d}t$, which becomes trivial for the non-relativistic case with constant m.

2.7.3 DSMC-related routines

Main features of the DSMC-related routines in *PICLas* are, first, the approximately grid-free approach, which optionally decouples DSMC in its spatial discretization from PIC [95]; and, secondly, the extent of high-fidelity physical models, even considering polyatomic molecules [84, 96]. Furthermore, a DSMC-based background gas approach similar to MCC is implemented.

Like the PIC module of *PICLas*, also the DSMC routines feature a sub-cell resolution. This allows the utilization of coarse computational meshes with additional, module-specific, spatial discretization for the coupled PIC-DSMC approach. Classical DSMC uses a random pairing among all particles within one cell, by which the cell dimensions must resolve the local mean free path [14]. *PICLas* avoids this requirement by a recursive octree division into eight sub-cells per mesh cell. Besides the resulting higher resolution, the octree also optimizes the approximate implementation of a nearest neighbor search for the particle pairing, which further reduces the associated grid-dependence [95].

The collision scheme of *PICLas* is depicted in Fig. 2.10. Up to three probabilities are calculated and compared to unit random numbers: P_{coll} for entering the collision process at all, P_{chem} for chemical reactions, and P_{relax} for a relaxation of inner DOF. This scheme is executed for N_{pair} possible particle pairs out of the N_{part}^{cell} particles inside the respective cell.

The support of the nearest neighbor approach, however, complicates the usage of Bird's

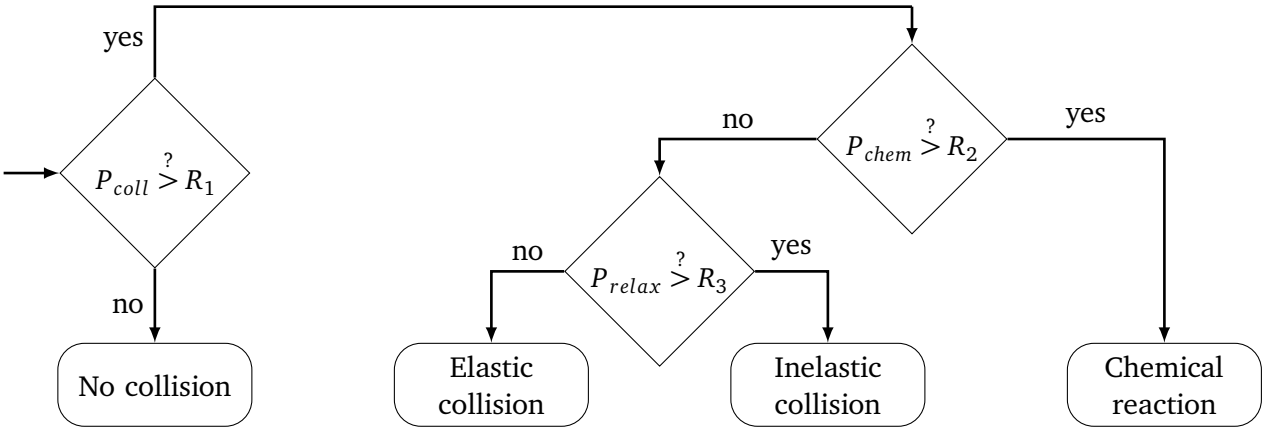

Figure 2.10: Collision scheme in *PICLas*: probabilities P are compared with generated random numbers $R \in \mathrm{unif}(0,1)$.

Constrained Probability method that defines N_{pair}. Instead, *PICLas* uses the so-called Natural Sample Size (NSS) model [6] in which N_{pair} depends only on N_{part}^{cell}. The NSS also defines the collision probability for a particle pair with species a and b to be [63]:

$$P_{coll} = \frac{N_a^{cell} N_b^{cell}}{1+\delta_{ab}} \frac{w}{N_{pair} V_{cell}} g_{12} \sigma \Delta t \,, \tag{2.21}$$

with cell volume V_{cell}, relative velocity g_{12} between the pair, collision cross section σ, and the Kronecker delta δ_{ab} (which is 1 for identical species a and b, otherwise 0). The collision cross sections are implemented in *PICLas* via the Variable Hard Sphere (VHS) model (see section 2.3) with isotropic scattering angles.

Under the assumption that the collision partner b belongs to a species not affected by the collisions (i.e., its number density $n_{bg} = N_b^{cell} w / V_{cell} \gg n_a$), the background gas (BGG) approach [92] becomes applicable. Here, every occurring collision is assumed to be between a and the BGG. That yields $N_{pair} = N_a^{cell}$ and Eq. 2.21 can be simplified to $P_{coll}^{BGG} = n_{bg} g_{12} \sigma \Delta t$. It should be noted that P_{coll}^{BGG} equals the exponential factor of the collision probability P_{coll}^{MCC} from the MCC approach (see 2.6.2) and, thus, $P_{coll}^{BGG} \approx P_{coll}^{MCC}$ holds for a sufficiently small Δt due to the Taylor series expansion of $\exp(x) = 1 + x + O(x^2)$.

2.7.4 Necessary developments for the simulation of ion optics

Compared to previous applications of *PICLas*, the efficient simulation of ion optics exhibits several essential differences which required further numerical development. Most crucial was the implementation and testing of the new electrostatic field solver, since the ion optics can be assumed to be of purely electrostatic nature.

Consequently, the particle motion is the dominating, time step defining dynamic characteristic instead of the propagation of electromagnetic waves as in Maxwell-PIC. Furthermore, electrostatic problems can be directly reduced to smaller simulation domains by symmetry conditions in terms of zero normal gradients for the electric potential. Hence, *PICLas* required an accurate particle treatment at boundaries, which also include open boundaries with optionally applied inflow conditions. These inflows require to allow relatively large time steps and reservoir states near to a free molecular flow state instead of transitional, hypersonic conditions. Last but not least, collisions between ions and neutral atoms needed to be implemented.

The most important code developments for this study are described in the following chapter. However, it should be noted that there were a multitude of other extensions required which will not be further described, but for the sake of completeness, briefly summarized.

Besides the participation in the general maintenance of *PICLas* and the development of several pre- and post-processing tools, those extensions include:

- an inhomogeneous, cell-dependent background gas approach based on macroscopic evaluations of preceding DSMC simulations;
- sampling routines, such as for particle distribution functions with increased sample size and for surface currents;
- fully-kinetic electron simulations as restart from the Boltzmann relation;
- radial-dependent inflow conditions;
- particle tracking and localization routines for non-planar mesh-sides;
- load balancing and distribution strategies for efficient parallel simulations;
- first steps in floating wall potentials for additional (not included) verification studies.

3 Numerical development

3.1 Overview

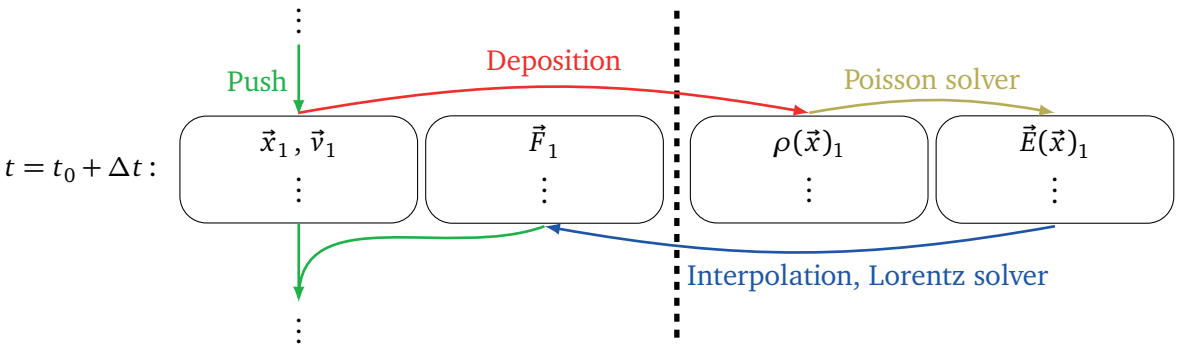

Figure 3.1: Electrostatic PIC scheme.

The described approach of a fully electrodynamic PIC changes significantly when the magnetic field $\vec{B}$ can be neglected. For the Maxwell PIC in Fig. 2.4, particles and fields were advanced in time separately from each other, linked only by the preceding (but between each other independent) Deposition and Interpolation steps. For the electrostatic case, however, the distribution of $\vec{E}$ is not actually propagated anymore. This allows considerably increased time step sizes, not anymore dependent on the speed of light. Instead, $\vec{E}$ results directly from ρ in the Poisson equation (Eq. 2.11) and all calculation steps are now sequentially linked with each other, as shown in Fig. 3.1. Hence, the cycle of Push, Deposition, Poisson solver, and Interpolation performs an update of particle and field information, both corresponding to the current simulation time.

Besides their creation by chemical reactions, new simulation particles are initialized at simulation start inside the computational domain according to $f(\vec{x},\vec{v},t_0)$ and each time step near the domain boundaries. In most cases, an initial distribution according to the Maxwell-Boltzmann velocity distribution is assumed, i.e., inside an infinitesimal volume $\mathrm{d}x\mathrm{d}y\mathrm{d}z$ each velocity component v_i follows the normal distribution $\mathcal{N}(\mu,\sigma^2)$ with mean μ and standard deviation σ:

$$f_{\mathcal{N}(\mu,\sigma^2)}(v_i) = \frac{1}{\sqrt{2\pi\sigma^2}}\exp\left(-\frac{(v_i-\mu)^2}{2\sigma^2}\right), \quad \mu = \langle v_i \rangle , \quad \sigma^2 = \frac{k_\mathrm{B}T}{m}. \tag{3.1}$$

Elaborated algorithms based on coordinate transformations are used for sampling from $\mathcal{N}(\mu,\sigma^2)$, such as the Marsaglia polar or Box Muller method [76]. Both are implemented in *PICLas* because the direct inverse transform sampling (see subsection 2.5.1) would include a computationally intensive inversion of the Gauss error function:

$$\mathrm{erf}\left(\frac{v_i-\mu}{\sqrt{2\sigma^2}}\right) \stackrel{!}{=} R \in \mathrm{unif}(-1,1). \tag{3.2}$$

Once the particles are initialized inside the computational domain, they move from time step to time step according to their respective velocity and acceleration values in terms of temporally integrating their equations of motion. The corresponding algorithms implemented in *PICLas* are described in the following section 3.2. During their push, the particles can cross boundary conditions (BC) and new particles need to be inserted in emptied regions near open boundaries which is subject of section 3.3. The subsequent subsections deal with the points of Deposition and the electrostatic field solver. Finally, the DSMC-specific routines relevant for the simulation of ion optics are covered, as well as general options for the speed-up of the coupled PIC-DSMC simulations.

3.2 Temporal integration of particle motion in electrostatic PIC

In *PICLas*, the particle motion is temporally integrated in a discretized manner. The equation of motion for a single particle is an initial value problem of state $\mathcal{U}$ evolving with time t:

$$\frac{\mathrm{d}\mathcal{U}}{\mathrm{d}t} = \mathcal{F}\left[t,\mathcal{U}(t)\right] \quad , \qquad \mathcal{U}(t=0) = \mathcal{U}_{t=0}\,. \tag{3.3}$$

The state $\mathcal{U}$ represents the position $\vec{x}$ and velocity $\vec{v}$ of each individual simulation particle. Thus, the state derivative $\mathcal{F}$ from Eq. 3.3 consists of $\vec{v}$ and acceleration $\vec{a}$:

$$\mathcal{U} = \begin{pmatrix}\vec{x}\\ \vec{v}\end{pmatrix} \quad , \qquad \mathcal{F} = \begin{pmatrix}\vec{v}\\ \vec{a}\end{pmatrix}. \tag{3.4}$$

Three different numerical integration schemes are used for the electrostatic modes of *PICLas*, each with different order, but corresponding complexity. Figure 3.2 illustrates their basic differences in terms of utilized derivatives, i.e., slopes for an 1D case of $\mathcal{U}(t)$. The simplest approach, the Euler method, is first order accurate and uses the derivative at each time step. The midpoint method is of similar complexity but of second order and uses a time-centered $\mathcal{F}$. The last, and most accurate approach, is a Runge-Kutta scheme (here with 5 stages) that uses several evaluations of the derivative between the actual time steps.

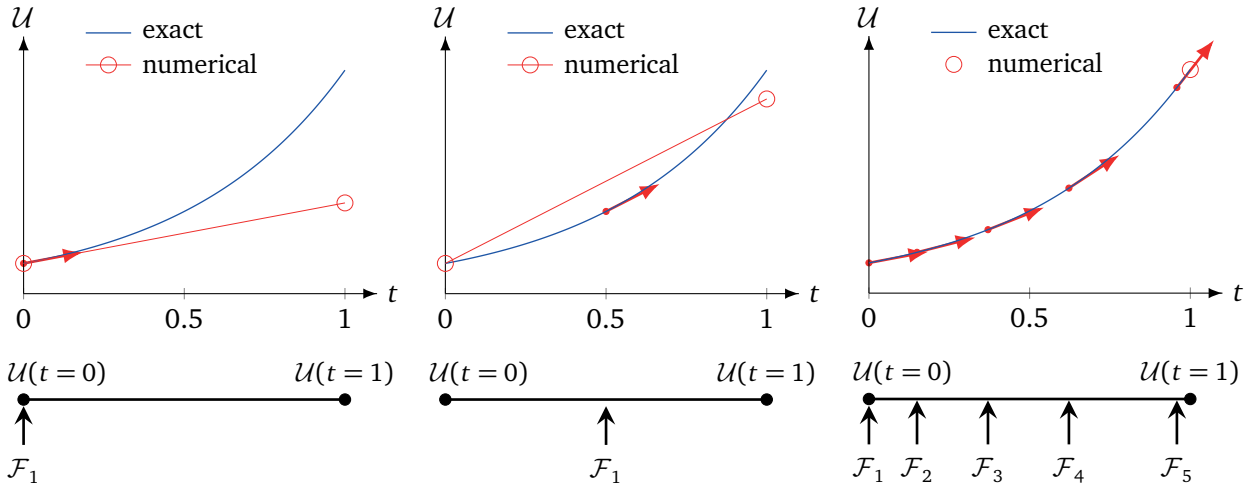

(a) Euler method. **(b)** Midpoint method. **(c)** 5 stage Runge-Kutta.

Figure 3.2: Approaches and utilized derivatives for the explicit numerical solution of $\frac{\mathrm{d}\mathcal{U}}{\mathrm{d}t} = \mathcal{F}$.

3.2.1 Euler scheme

The realization of the Euler method in *PICLas* is straightforward, since the cycle shown in Fig. 3.1 can be directly implemented. The particles are at state $\mathcal{U}$, which yields the charge density deposited onto the mesh. Next, the Poisson equation is solved and the resulting field is interpolated back to particle positions where the resulting forces define the acceleration values. The latter, in turn, constitute together with the velocities the derivative $\mathcal{F}$ (see Eq. 3.4) and the next state is:

$$\mathcal{U}_{n+1} = \mathcal{U}_n + \Delta t \mathcal{F}_n \,. \tag{3.5}$$

3.2.2 Midpoint method: Leapfrog scheme

Due to the first order characteristic of the Euler method, very small time steps are required to attain results of acceptable accuracy. Additionally, it can be shown that for fields resulting in a harmonic oscillation, the Euler method is inherently unstable and can never reach complete energy conservation [54]. For PIC simulations, the most common solution is to utilize the so-called leapfrog scheme, which is basically a midpoint method (see Fig. 3.2b).

Here, particle velocities $\vec{v}$ (as derivative of $\vec{x}$) and positions $\vec{x}$ (defining, via ρ, the acceleration values $\vec{a}$ as derivative of $\vec{v}$) are shifted in their "local" time by $\Delta t/2$. In other words, as shown in Fig. 3.3, each saved particle $\vec{x}$ belongs to time steps $t_0, t_1, ..., t_{end}$ whereas the velocities belong to $t_{-\frac{1}{2}}, t_{\frac{1}{2}}, ..., t_{end} - \frac{\Delta t}{2}$.

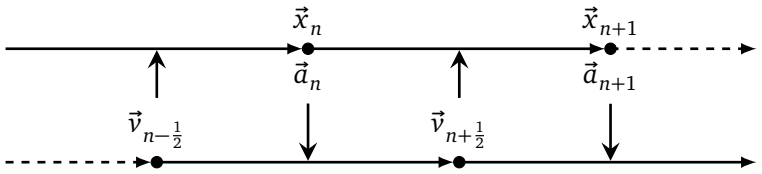

Figure 3.3: Temporal integration in electrostatic PIC via leapfrog method.

The push to the next time step (equivalent to Eq. 3.5 of the Euler method) is defined by Eq. 3.6. The implemented PIC cycle from Fig. 3.1 is unchanged for the leapfrog scheme.

$$\begin{pmatrix} \vec{x}_{n+1} \\ \vec{v}_{n+\frac{1}{2}} \end{pmatrix} = \begin{pmatrix} \vec{x}_n \\ \vec{v}_{n-\frac{1}{2}} \end{pmatrix} + \Delta t \begin{pmatrix} \vec{v}_{n-\frac{1}{2}} \\ \vec{a}_n \end{pmatrix} \tag{3.6}$$

In contrast to a Maxwell PIC scheme, where also the velocities are required for the calculation of $\vec{a}$, the shifted nature of the velocities is unproblematic, as long as the following points are considered:

- At t_n, particles are created with $\vec{x}_n$ and $\vec{v}_n$, i.e., $\vec{v}_{n-\frac{1}{2}}$ does not exist. Therefore, the velocities of new particles need to be initially shifted to $\vec{v}_{n-\frac{1}{2}} = \vec{v}_n - \Delta t\,\vec{a}_n/2$.
- When the time step size is variable, the velocities need to be updated to the new midpoint by $\vec{v}_{n+\frac{1}{2}} = \vec{v}_{n-\frac{1}{2}} + (\Delta t_{n-1} - \Delta t_{n+1})\,\vec{a}_n/2$.
- At analyze procedures of $\mathcal{U}$, the $\vec{v}$ values must be synchronized in time with $\vec{x}$.

It should be mentioned that all "synchronization" steps of $\vec{v}$ cannot be done with a time-centered $\vec{a}$ and, thus, an Euler push is performed instead of a midpoint method. However, it was found that those few $\Delta t/2$ steps do not influence the accuracy for the simulation cases of interest. Furthermore, it can be argued that particle positions and velocities need to be synchronized for a DSMC coupling. But based on the stochastic, first order nature of DSMC, by which the particle motion is decoupled from the collision and, therefore, blurred within the actual time steps, it seems to be irrelevant.

3.2.3 Runge-Kutta schemes

The higher order schemes for temporal integration in *PICLas* include a so called low storage explicit Runge-Kutta (LSERK) scheme with a discretization into time steps Δt between times t^n and t^{n+1}, each consisting of M stages. Its special characteristic is that, in addition to the actual state in phase space of each particle (first "register"), only one further register has to be saved. That lowers the memory demand and is in contrast to classical Runge-Kutta schemes, for which the derivatives need to be saved for all M stages during the entire Δt.

For the general initial value problem of Eq. 3.3, the used LSERK algorithm [24] is:

$$\begin{aligned} \mathrm{d}\mathcal{U}_j &= A_j \mathrm{d}\mathcal{U}_{j-1} + \Delta t \mathcal{F}(\mathcal{U}_j) \\ \mathcal{U}_j &= \quad \mathcal{U}_{j-1} + B_j \mathrm{d}\mathcal{U}_j \quad , \quad j = 1, \ldots, M \,. \end{aligned} \tag{3.7}$$

Here, j is the stage index, $\mathrm{d}\mathcal{U}$ is the differential of the state $\mathcal{U}$, and A and B are optimized parameters. Equation 3.7 shows how the two state vectors $\mathrm{d}\mathcal{U}$ and $\mathcal{U}$ have to be kept in memory from one to the next stage, but not the prior ones. At each new time step (i.e., $j = 1$) at time t^n, the initial state $\mathcal{U}_0$ corresponds to $j = M$ of the last time step, whereas the $\mathrm{d}\mathcal{U}_0$ is irrelevant due to $A_1 = 0$ which makes this algorithm "self-starting". Besides A and B, a third stage-specific parameter C defines time-dependent values at the stage time t_j according to:

$$t_j = t_n + C_j \Delta t \,. \tag{3.8}$$

For $M = 5$, Carpenter and Kennedy [24] derived the following optimized coefficients which yield an integration scheme of 4$^{\text{th}}$ order:

Table 3.1: Coefficients for implemented 5-stage LSERK algorithm of 4$^{\text{th}}$ order [24].

j	A	B	C
1	0	0.1496590219993	0
2	-0.4178904745	0.3792103129999	0.1496590219993
3	-1.192151694643	0.8229550293869	0.3704009573644
4	-1.697784692471	0.6994504559488	0.6222557631345
5	-1.514183444257	0.1530572479681	0.9582821306748

Implementation in PICLas

Dividing the first line of Eq. 3.7 by Δt, the integration scheme becomes together with Eq. 3.4:

$$\begin{aligned} \tilde{\mathcal{U}}_j &= A_j \tilde{\mathcal{U}}_{j-1} + \begin{pmatrix} \vec{v}_{j-1} \\ \vec{a}_j \end{pmatrix} = \begin{pmatrix} \vec{V}_j \\ \vec{A}_j \end{pmatrix} \\ \begin{pmatrix} \vec{x}_j \\ \vec{v}_j \end{pmatrix} &= \begin{pmatrix} \vec{x}_{j-1} \\ \vec{v}_{j-1} \end{pmatrix} + B_j \Delta t \tilde{\mathcal{U}}_j \,. \end{aligned} \tag{3.9}$$

Here, also the actual second register $\tilde{\mathcal{U}} = \mathrm{d}\mathcal{U}/\Delta t$ is introduced which is evaluated prior to the update of the state vectors, i.e., with $\vec{v}_{j-1}$ and $\vec{a}_j$ at $\vec{x}_{j-1}$. This stage-specific push is performed M times as part of the whole cycle from Fig. 3.1. Therefore, all steps (including Deposition, Poisson solver, etc.) are respectively repeated for advancing $\mathcal{U}_n$ to $\mathcal{U}_{n+1}$. Once the updated,

PIC-specific state is calculated, the remaining steps such as the DSMC module and analyze routines (see Fig. 2.6) are executed. Again, a higher order implementation of DSMC would not give any benefit due to its first order decoupling between particle motion and collisions.

One additional difficulty arises, when particles are created during the individual stages of a time step. This situation results from ensuring the self-consistency of the approach, for which besides the fields also the stage-specific particles state $\mathcal{U}_j$ needs to be updated in terms of a push. During this push, particles can interact with boundary conditions which can result into effectively new particles. These new particles, however, do not have the required values of the previous stage $j-1$. Assuming that a new particle has been created with known $\vec{x}_{j-1}$ and $\vec{v}_{j-1}$, the only undefined variable in Eqs. 3.9 is $\tilde{\mathcal{U}}_{j-1}$, depending on the values of the previous stages $1,...,j-2$. Thus, a recursive reconstruction with initial assumptions needs to be performed. A useful approximation turned out to assume that the forces from previous stages were constant and equal the one at $\vec{x}_{j-1}$, i.e., $\vec{a}_{stage<j} = \vec{a}_j$. This makes the reconstruction of $\vec{A}_{stage<j}$ trivial due to $A_1 = 0$. From Eqs. 3.9 results (recursively from $\vec{A}_1$ to $\vec{A}_{j-1}$) the calculation of the constant stage multiplier $\tilde{A}_{stage}$ that defines $\vec{A}_{stage} = \tilde{A}_{stage}\vec{a}_j$:

$$\tilde{A}_1 = \cancel{A_1}\overset{0}{\cancel{\tilde{A}_0}} + 1 \quad , \quad \tilde{A}_{stage} = A_{stage}\tilde{A}_{stage-1} + 1\,. \tag{3.10}$$

Next, $\vec{v}_{stage<j-1}$ can be reconstructed recursively from $\vec{v}_{j-2}$ to $\vec{v}_0$:

$$\vec{v}_{stage-1} = \vec{v}_{stage} - B_{stage}\Delta t\vec{A}_{stage}, \tag{3.11}$$

which finally sets the $\vec{V}_{stage<j}$ recursively from $\vec{V}_1$ to $\vec{V}_{j-1}$:

$$\vec{V}_1 = \cancel{A_1}\overset{0}{\cancel{\vec{V}_0}} + \vec{v}_0 \quad , \quad \vec{V}_{stage} = A_{stage}\vec{V}_{stage-1} + \vec{v}_{stage-1}\,. \tag{3.12}$$

Equations (3.10) to (3.12) define the missing single second register $\tilde{\mathcal{U}}_{j-1}$ by which the corresponding particle can be treated normally afterwards.

The approaches for stage reconstruction are only an approximation since a constant, particle-specific acceleration is assumed for the reconstructed stages. This results in a discontinuity in the acceleration profile which cannot be represented by the polynomial interpolation of the used higher order RK scheme. At least, the assumption of $\vec{a}_{stage<j} = \vec{a}_j$ prevents a jump as it would be the case for $\vec{a}_{stage<j} = 0$. Furthermore, the simulation time during the stages (as defined by Eq. 3.8) is not of physical nature by which all time-dependent functions are only first order accurate [24].

3.3 Boundary conditions for particle distributions

As described in the previous sections, particles are initialized in the computational domain and afterwards pushed from time step to time step. The particle distribution is affected by boundary conditions, such as open BCs (deleting all crossing particles) or reflective walls. The state of the distribution function can be depicted for single $\vec{v}$- and $\vec{x}$-components in phase diagrams, such as in Fig. 3.4 for v_x and x. In this example, not the actual values of f are displayed but just the maximum extent of the particle populations in phase space, e.g., within v_{min} and v_{max} as well as x_{min} and x_{max}. Three spatially adjacent populations, which could correspond to computational mesh cells, are depicted. Each starts at $t = t_0$ inside an x-interval of $x_{i+1} - x_i$ with velocities between $-v_{max}$ and v_{max}. Thus, their initial extents are (the blue/green/red dashed) rectangles in the diagram. After a single time step Δt, the population extents shift in phase space towards (solid) parallelograms, because regions with positive velocities move downstream to greater x, those with negative velocities upstream to smaller x, and the lines with $v_x = 0$ stay constant. Now, Fig. 3.4 illustrates the problem of domains with open boundaries at which the crossing flow is deleted. The interval around x_0 is surrounded by the other cells and, consequently, $f(x_0)$ does not change if $f(x_{-1},t_0) = f(x_0,t_0) = f(x_1,t_0)$ was met, since the regions moving up- and downstream are exactly compensated by the regions coming from the neighbor intervals. However, this compensation does not apply for the boundary cells (around x_{-1} and x_1), where the shaded parts of f are missing after Δt. Those "emptied" regions in phase space need to be dealt with by proper particle boundary conditions.

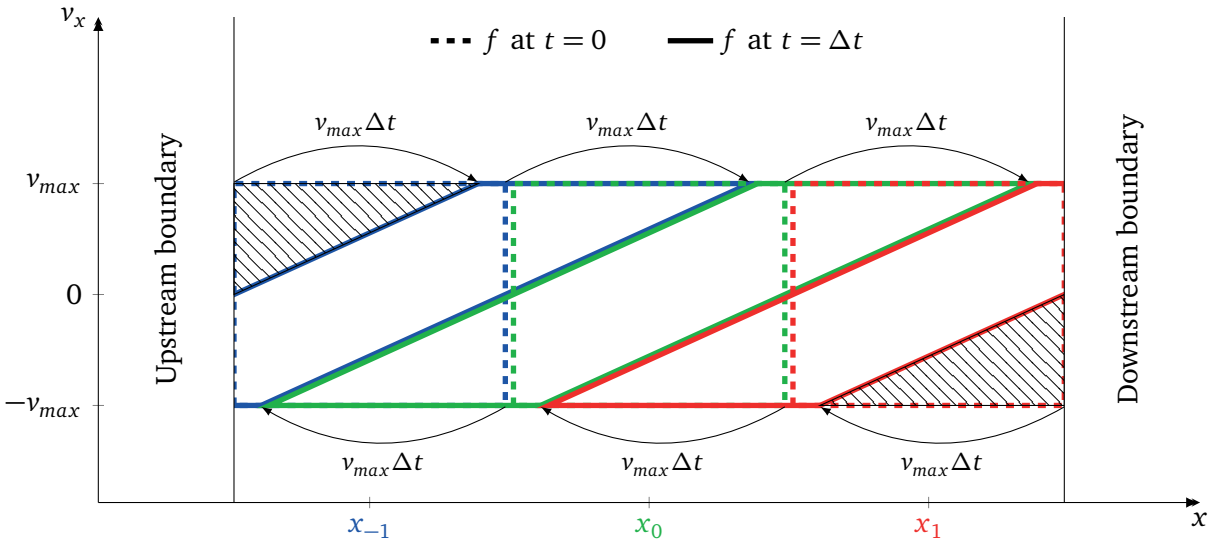

Figure 3.4: Temporal development of f in v_x and x with open, deleting boundaries.

3.3.1 Inflow conditions

As illustrated in Fig. 3.4, inflow conditions must balance the missing contribution of the particles which move from the boundaries into the domain. A constant inflow condition is considered in terms of an assumed infinite reservoir (with $\langle\vec{v}_{in}\rangle$, T_{in}, and n_{in}) that adjoins the domain at the boundary and compensates the missing neighbor cells. In general, the amount of inflow particles N_{in}^{real} during one time step Δt can be calculated based on the respective particle flux Γ_{in}, inflow area A_{in}, and time step Δt:

$$N_{in}^{real} = \Gamma_{in} A_{in} \Delta t\,, \quad N_{in}^{simu} = N_{in}^{real}/w\,. \tag{3.13}$$

For constant individual particle velocities (i.e., $T_{in} = 0\,,\ \langle\vec{v}_{in}\rangle = \vec{v}_{in}$), this can be implemented in a straightforward manner because the velocity-extent in the phase diagram collapses to zero and the problem becomes one-dimensional in the spatial direction perpendicular to the domain boundary (x in Fig. 3.4). Here, the inflow flux becomes $\Gamma_{in} = n_{in} v_{\perp in}$ with $v_{\perp in} = \vec{n}_{BC} \cdot \vec{v}_{in}$ and $\vec{n}_{BC}$ as normal vector of the boundary directed into the domain. In other words, domain layers with thickness $v_{\perp in}\Delta t$ are filled up near the boundaries with new particles at velocity $\vec{v}_{in}$.

For realistic gases with $T > 0$ however, this approach is just an approximation and its quality depends on the specific flow state. The actual inflow flux is the one of those particles with $v_{\perp in} > 0$ and crossing a perpendicular section inside the reservoir:

$$\Gamma_{in} = n_{in} \int_0^\infty v_{\perp in} f_{\mathcal{N}(\mu,\sigma^2)}(v_{\perp in})\,\mathrm{d}v_{\perp in} = \frac{n_{in}\sigma}{\sqrt{2\pi}} \left(e^{-a^2} + \sqrt{\pi} a \left[1 + \mathrm{erf}\,(a)\right]\right)\,,\ a = \frac{\mu}{\hat{v}}\,. \tag{3.14}$$

The speed ratio a relates the mean velocity to the most probable velocity

$$\hat{v} = \sqrt{2}\sigma = \sqrt{2 k_\mathrm{B} T_{in}/m} \tag{3.15}$$

and is linked by ξ as degrees of freedom of the individual gas molecule to the Mach number $M = a \cdot {}^{2\xi}\!/\!_{\xi+2}$. The integral in Eq. 3.14 can be interpreted as average flux velocity v_Γ with the following limits for hypersonic ($a \to \infty$) and stationary ($a = 0$) flows:

$$v_\Gamma = \Gamma_{in}/n_{in}\,, \quad v_\Gamma^{a\to\infty} = \mu = \langle v_{\perp in}\rangle\,, \quad v_\Gamma^{a=0} = \sigma/\sqrt{2\pi} = \sqrt{k_\mathrm{B} T_{in}/2\pi m}\,. \tag{3.16}$$

The reduction from μ for finite a is due to the existing negative particle velocities even at arbitrarily high a. But already for $a = 3$, the deviation $\mu - v_\Gamma$ is below $1 \cdot 10^{-6} \cdot v_\Gamma$. This explains that the procedure for $T = 0$ is also a good approximation for hypersonic flows, at least for calculating the particle number. Additionally, when the difference between maximum and minimum particle velocities is relatively small compared to μ, the compensated inflow-regions

in phase space can be approximated by rectangles, corresponding to re-filling layers $v_\Gamma \Delta t$ with the inflow distribution $f(\vec{v}_{in})$. The remaining deviation from the actual desired distribution is smoothed for collisional flow conditions by the inter-particle collisions, which relaxate the total f again towards the Maxwell-Boltzmann distribution.

Nevertheless, this approach is not an option for dilute, slower inflows. The exact number of particles across the boundary must be determined and exactly the missing regions of f as emphasized in Fig. 3.4 must be compensated.

The most demonstrative interpretation of this problem is to actually model the adjoined reservoir, as illustrated in Fig. 3.5a. When allowing to neglect the part of f with $v > v_{max}$ (e.g., with v_{max} resulting from $R = 1 - \varepsilon$ in Eq. 3.2 and an acceptable small ε), the reservoir can be limited to an extent of $x = -L = -v_{max}\Delta t$, by which also the fastest particles could reach a position inside the domain arbitrarily near the boundary after Δt.[1]

This direct reservoir or "virtual pre-inserting" approach used as inflow condition contains the following steps:

1. Fill reservoir region randomly with particles positions according to unif$(-L, 0)$, velocities to $\mathcal{N}$, and number to n_{in}.
2. Move each reservoir particle by respective $\vec{v}\Delta t$.
3. For the simulation, accept only particles that have reached $x > 0$, reject remaining ones.

The described reservoir approach is very easy to implement, however, it exhibits the disadvantages that:

- although the particles lie with their final positions inside the domain with respect to the inflow boundary, they might have already crossed other BCs during their push into the domain. Thus, all other BCs must have a distance of at least $v_{max}\Delta t$ from the inflow.
- The full reservoir is filled up with (temporary) particles, but only a small fraction might reach the domain,
- separate inflow reservoirs can overlap each other at domain corners, a multiple insertion corresponding to the same inflow must be prevented,
- and the random, final positions are not known a priori, thus, they might be located in the domain of another process which creates additional MPI communication.

[1] Particles with $v > v_{max}$ (if v_{max} only defines L) would be missing inside the interval $x \in [0, (v - v_{max})\Delta t]$.

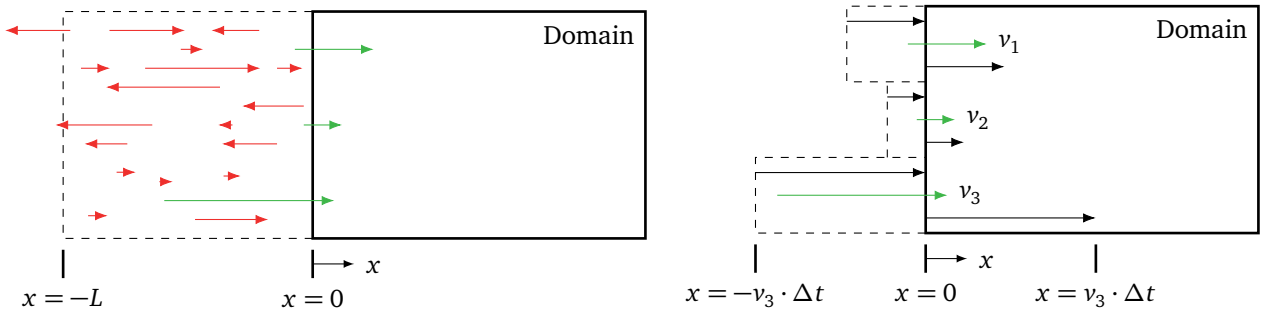

(a) Reservoir method: same length for all velocities, full Maxwell-Boltzmann distribution is inserted in reservoir.

(b) Surface flux: respective reservoir length depends on velocity, all sampled particles reach the domain.

Figure 3.5: Inflow reservoir attached to open boundary of domain.

Surface flux as inflow condition

All previously stated disadvantages of the direct reservoir approach can be eliminated by the usage of an approach called “surface flux” in *PICLas* by which:

- only those particles that reach the domain are actually sampled,
- the push from the inflow boundary into the domain is handled by the default tracking routine that also checks the path for additional BC intersections,
- the approach is cell-side specific and, thus, the corresponding initial mesh cell is known,
- and there is no virtual reservoir that might overlap with others from the same inflow.

The actual procedure of the flux insertion results from randomly setting the virtual positions x_{-1} in unif$(-L,0)$ inside the reservoir. The number of pre-inserted particles is based on the product of n_{in} and the spatial volume of the insertion interval. Now however, the length L that includes only particles reaching the domain is proportional to the specific particle velocity that is inserted (see velocities v_1 to v_3 in Fig. 3.5b). For particles with velocity $v_\perp$, the reservoir needs to be only of length $L(v_\perp) = v_\perp \Delta t$, because particles virtually starting at greater distances within the reservoir could not reach the domain. Thus, also the number of inserted particles is scaled with $v_\perp$.

In other words, with regard to the reservoir distribution function $f_{\mathcal{N}(\mu,\sigma^2)}(v_{\perp in})$ and considering the inflow velocities of $v_{\perp in}$, the particles would start at $x_{-1} = (R-1)L(v_{\perp in}) = (R-1)v_{\perp in}\Delta t$ and finally move to the domain at $x_0 = x_{-1} + v_{\perp in}\Delta t = v_{\perp in}R\Delta t$ with $R \in$ unif$(0,1)$. Hence, first, the inflow particles can be placed directly at $x = 0$ and, secondly, they are only partially moved by $R\Delta t$ during their first push. This ensures a continuous inflow, with a maximum reachable distance at $x_0^{max}(v_{\perp in}) = v_{\perp in}\Delta t$, see Fig. 3.5b. As described, the number of inserted particles with $v_{\perp in}$ now follows $f_{flux}(v_{\perp in}) \propto v_{\perp in} f_{\mathcal{N}(\mu,\sigma^2)}(v_{\perp in})$ instead of $f_{\mathcal{N}(\mu,\sigma^2)}(v_{\perp in})$.

That flux velocity distribution function f_{flux} is the one of all particles that cross the inflow boundary and can be also deduced by an interpretation of the reservoir method as ARM, as shown in A.1. When scaling besides $\mu = \langle v_{\perp in} \rangle$ (resulting in speed ratio a, see Eq. 3.14) also the sample velocity $v_{\perp in}$ by $\hat{v}$, we finally get for the properly normalized f_{flux}:

$$f_{flux}(\tilde{v}) = \frac{2}{e^{-a^2} + \sqrt{\pi} a \left[1 + \mathrm{erf}(a)\right]} \cdot \tilde{v} e^{-(\tilde{v}-a)^2}, \quad \tilde{v} = \frac{v_{\perp in}}{\hat{v}}. \tag{3.17}$$

As shown in A.1, the reservoir method as ARM with envelope $g_{\mathcal{N}(\mu,\sigma^2)}(v)$ can be expected to be efficient for large speed ratios only. Therefore, as better alternative, there exist individual envelopes which are optimal for a specific a interval [40] and all of them are implemented in the surface flux routine of *PICLas*. However, two trivial cases exist. The first for constant particle velocities ($T = 0$, $\hat{v} = 0$, $a \to \infty$) yields $f_{flux}^{T=0}(\tilde{v}) = \delta(\tilde{v} - a)$ and the second, for stationary flows ($a = 0$), is the directly invertible (see 2.5.1) Rayleigh distribution shown in Eq. 3.18. Please note, that the mentioned optimal sample procedures [40] create $z^* = a - \tilde{v}$ by which $v = \hat{v}(a - z^*)$.

$$f_{flux}^{a=0}(\tilde{v}) = 2\tilde{v}e^{-\tilde{v}^2} \Rightarrow \tilde{v}(R) = \sqrt{-\ln(R)}, \quad R \in \mathrm{unif}(0,1) \tag{3.18}$$

The actual surface flux routine is depicted in algorithm 1 in appendix A.2. For each side, the inwards normal vector $\vec{n}_{BC}$ and two orthogonal tangential vectors $\vec{t}_{1,BC}$ and $\vec{t}_{2,BC}$ have been initially stored. A mean velocity vector $\vec{v}_{in}$ with arbitrary orientation towards $\vec{n}_{BC}$ is implemented. The normal component is treated by the approach previously described (in terms of velocity distribution and inserted particle number), whereas the tangential components directly get their corresponding final velocity values because they are independent from the following partial push. The two subroutines `RoundingRoutine` and `placeOnSide` of algorithm 1 are important parts of the surface flux procedure. Their characteristics are described in the following sections.

Integer number of inserted particles

The speed ratio of the velocity component that is perpendicularly directed into the domain (a_{side} in algorithm 1) determines the flux through a side (Γ_{in} from Eq. 3.14), which in turn defines the average number of simulated inflow particles through the considered area (see Eq. 3.13). In a numerical context with constant particle weights w, however, N_{in}^{simu} needs to be an integer value. A straightforward solution is to directly round the floating point value corresponding to a side in a statistical manner so that the theoretical value $N_{part}(i_{side})$ is reached in average. In other words, a discrete probability distribution is sampled for each

side and its statistical expected value must yield $E \stackrel{!}{=} N_{part}(i_{side})$. The easiest approach for that is the stochastic rounding in Eq. 3.19. Here, the floor function is evaluated at $X+R$ with X as desired expected (floating point) value.

$$\text{round}(X) = \lfloor X+R \rfloor, \quad R \in \text{unif}(0,1) \quad \Rightarrow \quad \text{round}(X) = \begin{cases} \lfloor X \rfloor & , X - \lfloor X \rfloor + R < 1 \\ \lfloor X \rfloor + 1 & , X - \lfloor X \rfloor + R \geq 1 \end{cases} \tag{3.19}$$

The random value R is equally distributed between 0 and 1 and the value $P_1 = 1 - (X - \lfloor X \rfloor)$ is the threshold between producing the result of either $\lfloor X \rfloor$ or $\lfloor X \rfloor + 1$. Thus, the probability for the first case is P_1 and $1 - P_1$ for the second case. The evaluation of the expected value proves an average value of X itself:

$$\begin{aligned} E(\text{round}(X)) &= P_1 \cdot \lfloor X \rfloor + (1 - P_1) \cdot (\lfloor X \rfloor + 1) \\ &= (1 - X + \lfloor X \rfloor) \cdot \lfloor X \rfloor + (X - \lfloor X \rfloor) \cdot (\lfloor X \rfloor + 1) = X \end{aligned} \tag{3.20}$$

Even though it is very simple to implement, there are two disadvantages for this direct stochastic rounding.

First, it can create anomalous correlations producing numerical non-equilibrium effects [116]. This can be circumvented by using a Poisson distribution instead, again with $E(X) \stackrel{!}{=} N_{part}(i_{side})$. In most cases, as also for the applications within this study, that is, however, not necessary because the non-equilibrium effects appear only in the high precision of the statistical moments. Please note that for stochastic rounding the deviation from the theoretical value of each instance is always ≤ 1 (rounding up or down), but for the Poisson distribution any integer value can be the result.

Secondly, the stochastic rounding of the particle flow through each individual element side produces a significant statistical noise in the simulation because the defined flow rate is only ensured in average and the error can accumulate over all sides. Therefore, to reduce the artificial noise in the simulation (e.g., of number density) several smoothing approaches were implemented. The first step is to reduce the fluctuation of total inserted particles during a time step. This is achieved by calculating the rounded integer value for a larger amount of sides as a whole (e.g., for all sides of the respective inflow) and subsequently splitting that value into parts for the included sides, which limits the accumulated deviation from the average. The implemented procedure is depicted in algorithm 2 in appendix A.2 and splits the given total integer number N_{part}^{total} into individual $N_{part}(i_{side})$, based on the given expected values as weights $W_{side}^{total} \propto E(N_{part}(i_{side}))$. It is ensured that the deviation from average is as small as possible for each side by at least assigning the floor value of the corresponding part. The further increment of $N_{part}(i_{side})$ ensures to retain the given total integer number and is

based on the remaining weights W_{side}^{remain}, interval thresholds X_{side}, and random numbers.

The second step, in addition to noise reduction during a time step, is to smooth the inserted particle number over several time steps by which the deviation from the theoretical average is stored and included in the next time step as correction. However, it is important to prevent any artificial periodicity. The verification of the implemented smoothing routines will be described in section 4.1.

Placement on sides and extension to curved meshes

The routine `placeOnSide` of algorithm 1 is considered to determine a random position on the respective side. It is important that each infinitesimal area dA within the side can be chosen with the same probability, as it is the case for a parallelogram spanned by vectors $\vec{a}$ and $\vec{b}$ and sampling the position by Eq. 3.21. But the mesh sides for *PICLas* can be of arbitrary shape defined by 4 vertices located within a general polynomial surface and connected by corresponding edges.

Planar, linear inflow sides A planar inflow side that is bordered by straight edges can be split up into two triangles for which the position sampling can be based on the parallelogram approach shown in Fig. 3.6.

Therefore, the described $N_{part}(i_{side})$-partitioning of the surface flux over N_{part} sides is subdivided into $2N_{part}$ triangles. For each triangle, the particles are randomly distributed in a supporting parallelogram (see Fig. 3.6b):

$$\vec{x}_{samp} = R_1\vec{a} + R_2\vec{b}, \quad R_i \in \text{unif}(0,1)\,. \tag{3.21}$$

Two additional vectors are defined: $\vec{c} = (\vec{a}+\vec{b})/2$ and the outwards directed normal vector $\vec{n}$ of unity length, perpendicular to the vector of the third triangle edge $\vec{a}-\vec{b}$. For the case of

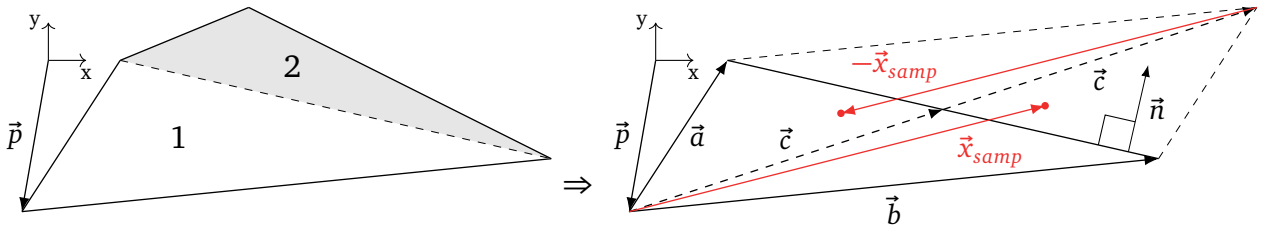

(a) Splitting of side into triangles 1 and 2.

(b) Position sampling inside triangle 1.

Figure 3.6: Particle placement in planar, linear side.

$\vec{n} \cdot (\vec{x}_{samp} - \vec{c}) > 0$, the sampled position is not inside the actual triangle and it is swapped into the right one by $\vec{x}_{swap} = 2\vec{c} - \vec{x}_{samp}$. Since the position sampling is performed with respect to a base point at position $\vec{p}$, the final coordinates are shifted accordingly.

Arbitrary sides The previous approach is not applicable for sides which cannot be split into two triangles, such as non-planar sides or when their edges are curved. Regarding the placement onto the side, the approach implemented in *PICLas* is based on the coordinates in reference space (ξ,η, see 2.7.1) by sampling $R_\xi \in \text{unif}(-1,1)$ and $R_\eta \in \text{unif}(-1,1)$. A direct assignment of $\xi \leftarrow R_\xi$ and $\eta \leftarrow R_\eta$, however, would result in an inhomogeneous distribution within physical space, corresponding to the area differential $\mathrm{d}A = \mathrm{d}x\mathrm{d}y$. This possible inhomogeneity is illustrated in the exemplary element side of Fig. 3.7, for which the ratio $\mathrm{d}A_{max}/\mathrm{d}A_{min}$ is greater than 6. The area differential is determined in terms of the first fundamental form with m_{ij} as scalar product of the physical coordinate vector $\vec{x}$ differentiated with respect to the corresponding coordinates (i, j) in reference space:

$$\mathrm{d}A = \sqrt{m_{\xi\xi}m_{\eta\eta} - m_{\xi\eta}^2}\,\mathrm{d}\xi\mathrm{d}\eta\,, \quad m_{\xi\xi} = \frac{\mathrm{d}\vec{x}}{\mathrm{d}\xi}\cdot\frac{\mathrm{d}\vec{x}}{\mathrm{d}\xi}\,, \quad m_{\eta\eta} = \frac{\mathrm{d}\vec{x}}{\mathrm{d}\eta}\cdot\frac{\mathrm{d}\vec{x}}{\mathrm{d}\eta}\,, \quad m_{\xi\eta} = \frac{\mathrm{d}\vec{x}}{\mathrm{d}\xi}\cdot\frac{\mathrm{d}\vec{x}}{\mathrm{d}\eta}\,. \tag{3.22}$$

In *PICLas*, each element side is represented as polynomial Bézier basis [88], by which the numerical differentiation is easily implemented [34]. The actual insertion procedure consists of the following two parts.

First, similarly to the subdivision into two triangles, each side is now "super-sampled" by $N_{sub} \times N_{sub}$ sub-sides, equidistantly distributed in reference space, as shown as white lines in Fig. 3.7. Figure 3.8 depicts for the same exemplary side the relative deviation $(\mathrm{d}A_{max} - \mathrm{d}A_{min})/\mathrm{d}A_{min}$ among the 4 values of the area differential calculated for the vertices of a single sub-side. For $N_{sub} > 1$, the values were evaluated as minimum, maximum and arithmetic average of

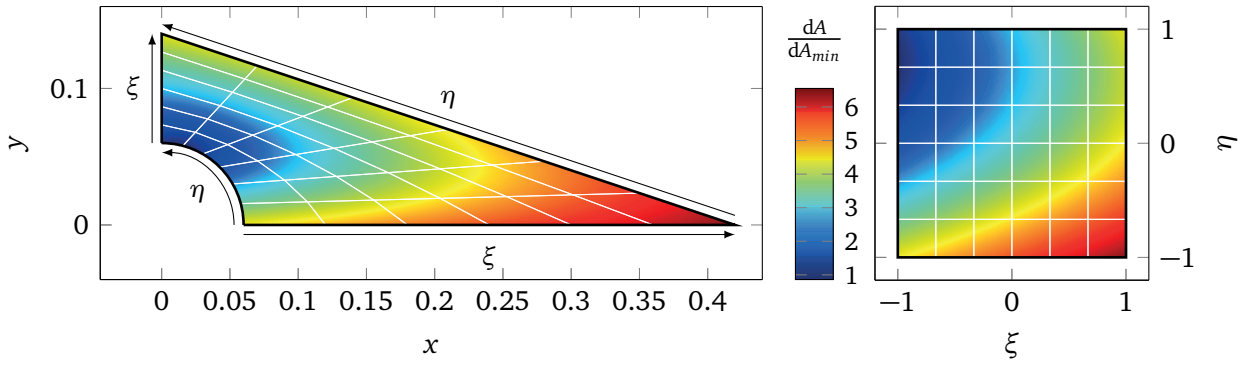

(a) Single element side in physical space with curved edge at ξ_{min}. **(b)** Side in reference space.

Figure 3.7: Mapping of physical to reference space and distribution of area differential $\mathrm{d}A$.

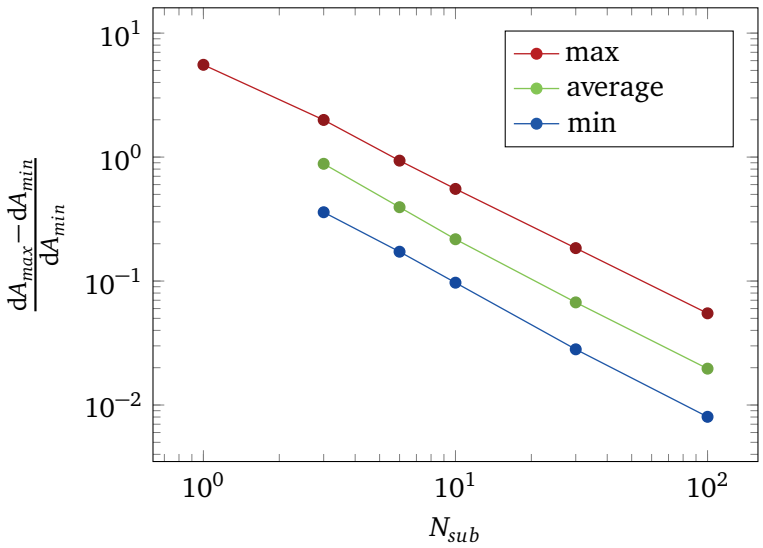

Figure 3.8: Deviation of area differential in sub-sides for different super-sampling numbers.

all individual sub-side deviations, whereas for $N_{sub} = 1$, the result is a single (in this case maximum) deviation. It can be seen that the inhomogeneity of dA within a single sub-side decreases with the super-sampling number N_{sub}. Hence, also the error associated with an equal distribution in reference space decreases accordingly.

The second part of the insertion procedure represents an ARM with respect to the area differential by the maximum sub-side value as constant envelope (see 2.5.2). Since the maximum value, including the coordinates of the respective position, is unknown a priori for an arbitrary side, each sub-side is initially further sampled by a defined amount of ξ,η and statistically evaluated by the corresponding maximum dA value which is used later.[2]

The previously described approach for the placement onto an arbitrarily shaped side assumes that the flux is constant within a considered (sub-)side i_{side} so that the total number of inflow particles through i_{side} is proportional to $\Gamma_{in}(i_{side}) \cdot \iint_A dA(i_{side})$. However, that is not applicable for curved sides because $v_{\perp in}$ from Eq. 3.14 depends on the local normal vector at the respective position. Therefore, the described ARM must be extended to $\Gamma_{in}(\xi,\eta) \cdot dA(\xi,\eta)$ instead of $dA(\xi,\eta)$ to be exact. But since the inflow conditions (temperature and mean velocity) might change during the simulation by which the computationally intensive initialization of the constant envelope needs to be performed each time, only an approximation was implemented in *PICLas*.

Basically, it is assumed that each one of the $N_{sub} \times N_{sub}$ sub-sides is planar instead of curved which, again, improves in its accuracy with increasing super-sampling number. Both for the total area and dA_{max} calculation, the surfaces are projected towards the normal vector at

[2]For linear elements, only the 4 vertices ($N_{sub} = 1$) need to be evaluated since dA is proportional to ξ and η.

the reference space origin of the respective sub-side. The same vector is also used for $v_{\perp in}$, but the insertion at the sampled ξ and η is performed on the actual, curved surface. This approximation becomes exact for the special case of a perpendicularly directed inflow. Here, the mean velocity vector is always identical with the local normal vector of the side. Thus, a projection (as well as a super-sampling) is not necessary and Γ_{in} is constant again. In this case, however, the local normal vector as well as both orthogonal tangential vectors $\vec{t}_{1,BC}$ and $\vec{t}_{2,BC}$ need to be evaluated at the actual position on the surface for the final calculation of the sampled velocity vector (see algorithm 1). Since for a stationary flow ($a = 0$), the mean velocity vector can be assumed to be arbitrarily directed, that approach enables an exact inflow also over curved sides at least for $a = 0$.

Influence of higher order temporal integration schemes on inflow conditions

Subsections 3.2.2 and 3.2.3 already dealt with the state initialization of new particles, such as the $\Delta t/2$-shift of velocities and stage reconstruction for leapfrog and LSERK, respectively. The background is that the temporal integration highly depends on the given initial values. When particles are already starting at a wrong point in phase space, the associated error might accumulate with time. Special care needs to be taken when the particle push does not take place at the actual, current t_n, but at a randomly shifted t_{BC} corresponding to the time when a new surface flux particle crosses the inflow side (see 3.3.1). This shifted time needs to be merged with the additional fractions resulting from the $\vec{v}$-shift of the leapfrog or stage-specific time.

Several initialization algorithms are possible [60], referred to as 0^{th} order when simply assuming $t_{BC} = t_n$ and 1^{st} order when synchronizing with partial Euler pushes. More accurate schemes utilize derivatives of higher order, if necessary, approximated by derivatives from more previous time steps.

Leapfrog scheme Since the field cannot be evaluated beyond the boundary, it is calculated at $\vec{x}_{BC}$ instead. Thus, the surface flux procedure is called after the field solver but before the interpolation step. Next, the push is performed, that utilizes the resulting acceleration $\vec{a}_{BC}$. The implemented leapfrog-specific algorithm for initialized surface flux particles is a combination of 2^{nd} order approach for $\vec{x}$ and 1^{st} order for $\vec{v}$. It does not require any states previous to the currently saved one:

$$\begin{pmatrix} \vec{x}_j \\ \vec{v}_j \end{pmatrix} = \begin{pmatrix} \vec{x}_{BC} \\ \vec{v}_{BC} - \frac{\Delta t}{2}\vec{a}_{BC} \end{pmatrix} + R\Delta t \begin{pmatrix} \vec{v}_{BC} + \frac{R\Delta t}{2}\vec{a}_{BC} \\ \vec{a}_{BC} \end{pmatrix}. \tag{3.23}$$

Runge-Kutta schemes When considering new particles inserted by the surface flux approach for the utilization of the Runge-Kutta schemes of *PICLas*, the stage reconstruction (see 3.2.3) has to be modified. First, the actual particle push is performed only by a random fraction, i.e., Eq. 3.9 becomes:

$$\begin{pmatrix}\vec{x}_j\\ \vec{v}_j\end{pmatrix} = \begin{pmatrix}\vec{x}_{BC}\\ \vec{v}_{BC}\end{pmatrix} + B_j R \Delta t\, \tilde{\mathcal{U}}_j \quad , \quad R \in \text{unif}(0,1)\,. \tag{3.24}$$

$\tilde{\mathcal{U}}_j$ includes the now unknown velocity $\vec{v}_{j-1}$ as well as $\vec{a}_j$ at position $\vec{x}_{j-1}$. Similarly to the leapfrog, the acceleration is evaluated at $\vec{x}_{BC}$ and now assumed to be the same in previous stages. Secondly, also the counterpart of Eq. 3.24 which results in the particle state $j-1$ needs to be calculated, but here only the already mentioned $\vec{v}_{j-1}$ is of interest, which inserts an additional initial step to Eq. 3.11:

$$\vec{v}_{j-1} = \vec{v}_{BC} - B_j (1-R) \Delta t \tilde{A}_j \vec{a}_{BC} \quad , \quad R \in \text{unif}(0,1)\,. \tag{3.25}$$

3.3.2 Symmetry conditions and solid walls

The opposite of open boundaries are reflective walls. Their main physical parameters are the energy and momentum accommodation which range from 0 (for perfectly specular reflection) to 1 (for a fully diffuse interaction) [63]. For partial accommodation, corresponding statistical blending algorithms are implemented in *PICLas*, which however were irrelevant for the application within this study.

Main application for specular reflection are symmetry conditions for which it is assumed that behind a planar symmetry BC exactly the same, but mirrored, flow field exists with even the same corresponding samples (i.e., simulation particles) of the distribution function. Thus, when a particle leaves the domain through such a boundary, it can be assumed that at the same time the mirrored identity enters the domain. For that, all original vector values just need to be mirrored into normal direction of the BC, as shown in Fig. 3.9.

Here, $\vec{p}$ is the coordinate vector towards a point on the reflective wall and $\vec{n}$ is a normal vector directed into the domain. The position vector relative to the wall $\vec{x}-\vec{p}$ and the velocity $\vec{v}$ are now mirrored with respect to $\vec{n}$ to replace the original particle by the mirrored one. Figure 3.9b shows that for an orthonormal $\vec{n}$ (i.e., $|\vec{n}| = 1$) a general vector $\vec{o}$ is mirrored to $\vec{m}$ by:

$$\vec{m} = \vec{o} - 2\vec{n}\,(\vec{o}\cdot\vec{n})\,. \tag{3.26}$$

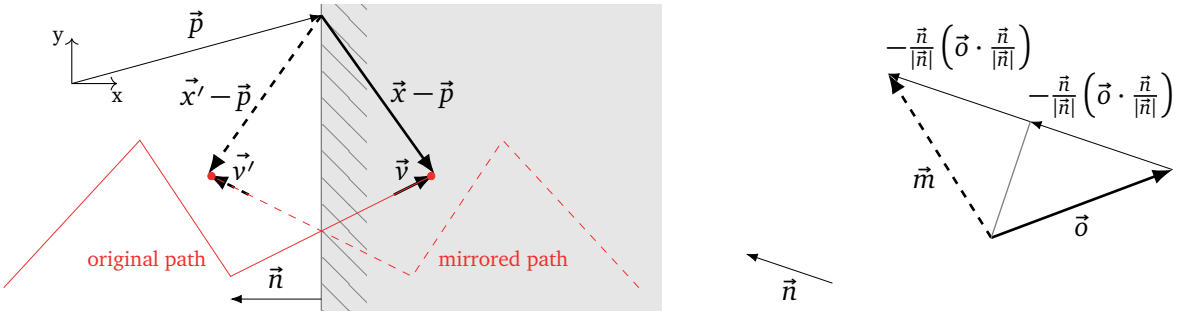

(a) Position and velocity vectors in front of/behind wall. **(b)** General mirroring at normal vector.

Figure 3.9: Specular reflection as symmetry condition.

In contrast, fully diffuse BCs can be applied for walls such as physical surfaces. Here, it is assumed that the reflected flow accommodates with its energy to the wall temperature and its momentum to the wall velocity. The latter is zero for the considered applications. Hence, a Maxwellian flow with $\mu = 0$ and $\sigma^2 = k_B T_{wall}/m$ is created. This approach is identical to the surface flux procedure of the special case $a = 0$ and leads to a Rayleigh velocity distribution (see 3.3.1). Number of particles, starting positions at the wall and time step fractions of the wall interaction, however, are resumed from the original particles.

Influence of higher order temporal integration schemes on outflow conditions

When the time derivatives of particle states change during time (i.e., by acceleration due to fields), the actual time of wall intersection must be implemented into the field evaluation and temporal integration scheme to retain the order of convergence [64]. For the application within this study, however, that is not of importance due to the following reasons:

- Symmetry conditions are also applied for the field solver in terms of a zero normal gradient Neumann boundary condition. This leads to vanishing forces into normal wall direction by which the mirroring of all vectorial particle states (including the second register for the LSERK scheme) is exact.
- Although wall boundaries can have non-zero fields de- or accelerating particles towards the surface, charged species are deleted at walls in all considered applications. Thus, a higher order temporal reconstruction is not necessary.

3.4 Boundary corrections for shape functions

As described in the overview of chapter 3, the derivatives from the particle motion are based on the solution of the field solver, which in turn needs the spatial distribution of charged particles as source term. This interpolation step from particle to mesh information was already introduced in 2.7.2 as the "deposition" step of PIC in terms of its implementation in *PICLas*. To consistently retain the higher order approach, the shape function approach was chosen as method of choice within this study.

Continuous distributions are highly affected by the mesh boundaries. Figure 3.10 depicts a total (dimensionless) charge of $Q = 1$, equally distributed in (dimensionless) x via 5 simulation particles inside a cell of interval $x \in [-1, 1)$. In this 1D example, the actually continuous charge density is $\rho = Q/(x_{max} - x_{min}) = 0.5$. It is well approximated by the superposed ρ_{tot} with the chosen $\alpha = 2$ and $r_{SF} = 1.3$, provided that also the surrounding cells contain the assumed particle distribution at least within $x \in [-1 - r_{SF}, 1 + r_{SF}]$, as depicted in Fig. 3.10a. However, in the case that the cell boundaries represent the limit of the domain and particles do not exist beyond (see Fig. 3.10b), ρ_{tot} will decrease towards the boundaries, as also does the interpolated cell polynomial.

To compensate for the particles that would exist beyond the domain boundaries, several correction approaches were implemented in *PICLas* for specific cases. In addition to compensate the lack of particles outside of the domain, it is also possible to assume that each particle

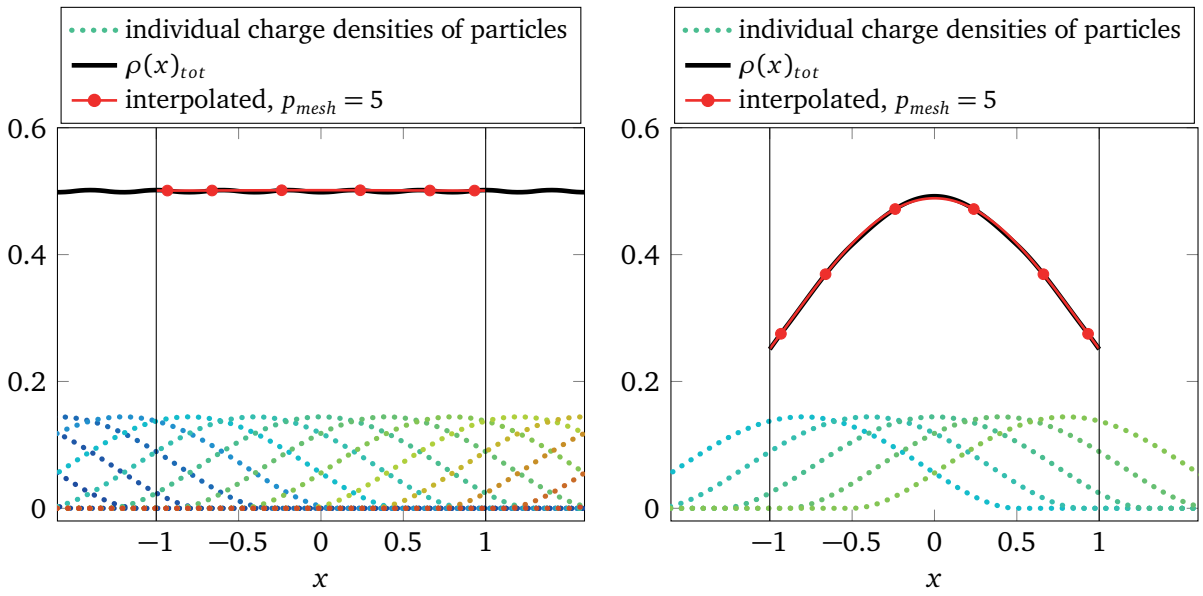

(a) Unlimited particle distribution.

(b) Distribution limited to cell interval.

Figure 3.10: Influence of domain boundaries on deposition via shape function.

must completely deposit its charge somewhere inside the domain. With shape functions exceeding the boundaries, their charge distribution is cut-off at a value greater than zero and therefore total charge is missing. Based on this thought, the utilization of anisotropic shape functions that do not cross the respective cell extent and, thus, deposit all of their charge within the domain might appear appropriate. However, the general preservation of equal distributions such as in Fig. 3.10a would pose severe difficulties. Therefore, the following correction approaches were developed:

- Layers of known distribution
- Outflowing re-emission
- Mirroring

3.4.1 Layers of known distribution

At domain boundaries beyond which a known, homogeneous state exists, such as for inflow boundaries, the obvious solution is to assume an adjacent "ghost" layer according to the assumed state. Layers with rectangular and circular bases of area A_{layer} and thickness r_{SF} (corresponding shape functions at greater distances would not reach any DOF) were implemented in *PICLas* and are filled with $N_{layer} = n_{inflow} A_{layer} r_{SF} / w_{layer}$ temporary particles, randomly distributed within the volume. Those particles are treated by the same deposition routines as the ones inside the domain, but their related statistical noise can be reduced by choosing a smaller w_{layer}. The increased computational cost is kept to a minimum by saving the resulting integral value for each applicable DOF as constant value by which the insertion is only initially required. The theoretical limit of an infinite particle number ($w_{layer} \to 0$) would correspond to an analytical integration of the homogeneous state over the shape function part outside the domain for each DOF. Also this analytical approach would be possible, at least in 1D, but it becomes highly non-trivial in 3D, particularly combined with the influence of other domain boundaries. Hence, the actual creation of temporary particles was chosen, which can be interpreted as Monte Carlo integration of the respective integrals.

3.4.2 Outflowing re-emission

In contrast to inflow boundaries, outflow BCs cannot be assumed to be homogeneous. For example, an outflowing ion beam can have an arbitrary (e.g. radial) density distribution. Nevertheless, if the outflow is at hypersonic state, information travels downstream only and the corresponding distribution can be directly rebuilt from the flux over the sides. For the case

of negligible further de-/accelerating outside, the leaving particles would simply remain on their prolonged paths. This results in an approach similar to the previously described layers. In *PICLas*, it was implemented that for a specified BC and species, the intersection positions $\vec{x}_{re}$ and velocities $\vec{v}_{re}$ are saved in an array containing all crossing particles.[3]

After a given sampling time interval (or the read-in of an already created file), the sampled total particle flow $\dot{N}_{re}$ as well as minimum velocity $v_{re}^{min} = \min\left(-\vec{n}_{BC} \cdot \vec{v}_{re}^{part}\right)$ are set for the next sample interval. Additionally, the array of crossed particles can be reduced in its particle number, since a higher sample can be of interest for analysis purposes, but is not necessary for the re-emission. During the deposition, particles are now randomly chosen from the array and temporarily placed at:

$$\vec{x}_{re}^{depo} = \vec{x}_{re} + R\Delta t_{re}\vec{v}_{re}\,, \quad R \in \mathrm{unif}(0,1)\,, \quad \Delta t_{re} = r_{SF}/v_{re}^{min}\,. \tag{3.27}$$

The number of inserted temporary particle results from $\dot{N}_{re}\Delta t_{re}$. This also illustrates the restriction to hypersonic outflows, since the scalar product of $\vec{v}_{re}^{part}$ with the outwards direct normal $-\vec{n}_{BC}$ must be > 0 and even better $\gg 0$ for reasonably small Δt_{re} based on which the whole layer height r_{SF} is filled.

3.4.3 Mirroring

With both previous correction approaches, a continuous flow through a domain can be simulated via shape functions. The corrections prevent unphysical fields at in- and outflow, resulting from locally too low charge densities. Remaining BCs to be addressed are surfaces at which the charge distribution follows its defined physical characteristics. Due to their simplicity, two extreme cases were implemented. First, a boundary with the parallel field component set to zero (i.e., $\vec{E}_{BC} \times \vec{n}_{BC} = 0$, as it is the case at electrically perfectly conducting walls) and, secondly, a boundary representing a symmetry plane with exactly the same, but mirror-symmetric, distribution assumed on the other side.

Individual BC planes

Both cases can be realized by an actual mirroring of all particles at the respective boundary. That approach can be only implemented for planes, since an infinite number of mirror particles would be required at curved faces. An assignment of the same charge as the original one corresponds to a symmetry condition, whereas the negative charge results in $\vec{E}_{BC} \times \vec{n}_{BC} = 0$.

[3] A flux sampling of new inflow particles instead of the outflow results in the corresponding velocity distribution described in section 3.3.1. Again, a random partial push is required to create a volume distribution.

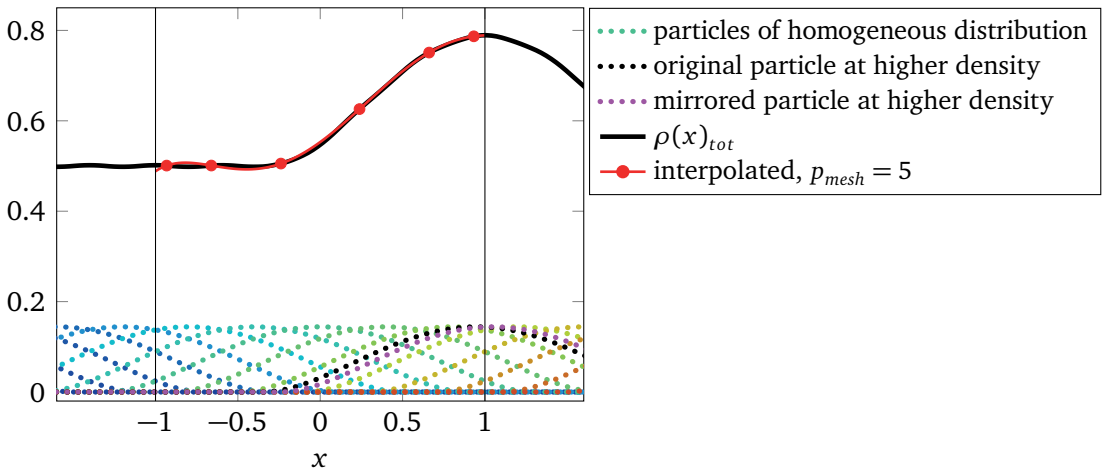

Figure 3.11: Correction of shape function via symmetry plane.

The mirroring calculation itself is the same as illustrated in Fig. 3.9, including a supporting and normal vector. Only particles inside the domain within a distance less than r_{SF} to the boundary plane are considered because the ones further inside would be mirrored to positions at distances greater than r_{SF} to all DOF.

Again, an ion beam with a radial density profile can be used as example. A symmetry plane is placed in its center where the charge density is assumed to be the highest. Figure 3.11 depicts how the distribution could be in direction perpendicular to the symmetry plane: Compared to the previously described 1D homogeneous distribution, there exists an additional simulation particle at $x = 0.95$ near the symmetry axis ($x = 1$). The particle is mirrored to $x = 1.05$. It can be seen that the resulting total distribution is symmetric as expected and is also well approximated by the interpolated polynomial.

Corners of BC planes

For planar symmetry conditions, two individual BC planes A and B are allowed to intersect, provided that their normal vectors $\vec{n}_A$ and $\vec{n}_B$ are located in the same plane (corresponding to a domain corner in 2D) and that they divide 180° into an integer number of:

$$n_{180} = \frac{\pi}{\arccos(-\vec{n}_A \cdot \vec{n}_B)} \,. \tag{3.28}$$

The background is that besides the original particle also all mirrored identities must be further mirrored at the other symmetry plane. In the implemented algorithm 3 in appendix A.2, the particle identity I is, first, deposited itself and, next, $n_{180} - 1$ times recursively mirrored, alternating at B and A. The actual `depositOnDOFs` routine interpolates the applicable particle

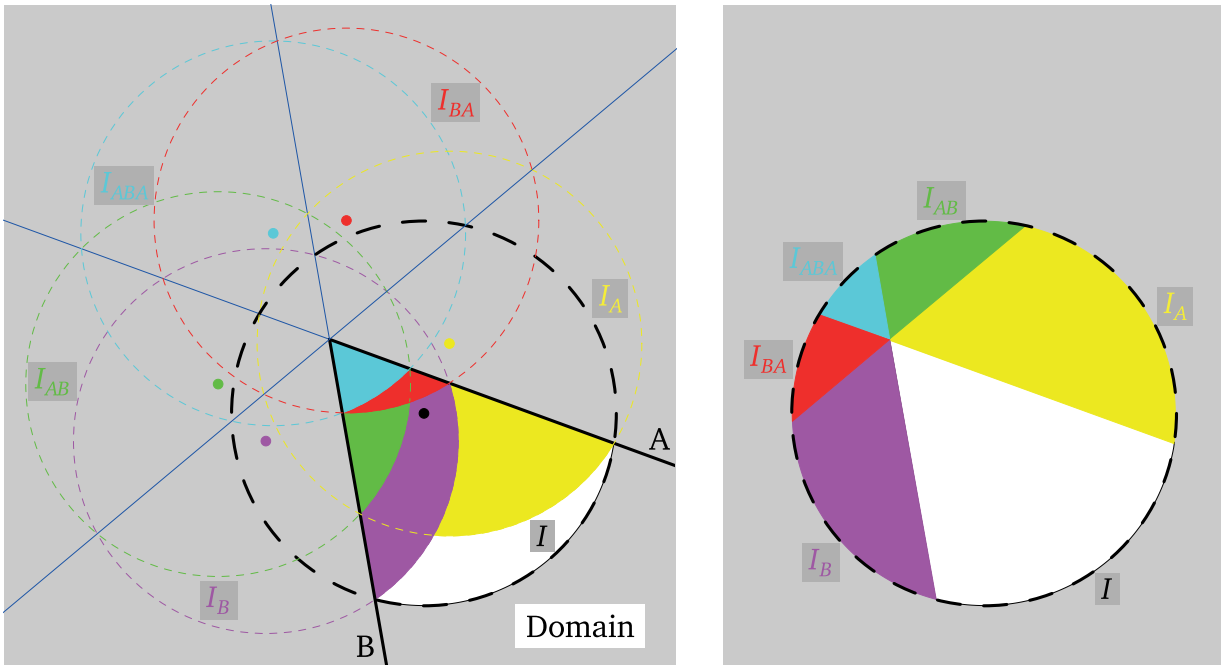

(a) Recursive mirroring of I and I_A.

(b) Rebuild of shape function circle.

Figure 3.12: Correction of shape function for intersecting symmetry boundaries A and B.

values onto the DOFs of the mesh, again provided that the comparison of the resulting distances to A and B with r_{SF} does not eliminate the influence on any DOF. The same is performed for the identity mirrored once at A, resulting in $2 \cdot n_{180}$ depositions for each "link" i_{link} of $A(i_{link})$ and $B(i_{link})$. Afterwards, but not included in the shown algorithm, I is additionally mirrored and deposited based on the remaining BC planes which were not already included by a link. Based on the interpretation that each particle must completely deposit its charge somewhere inside the domain, the mirroring is performed until the complete shape function sphere (or circle in 2D) is rebuilt inside the domain, as depicted in Fig. 3.12 for $n_{180} = 3$. As described in algorithm 3, the identity I is mirrored at A and, eventually, both I and the resulting I_A are recursively mirrored $n_{180} - 1 = 2$ times: First at B (giving I_B and I_{AB}) and, next, at A (giving I_{BA} and I_{ABA}). The individual parts reaching the domain between A and B are shown for the mirrored shape functions as colored patterns. Figure 3.12b illustrates how they can be rearranged to the complete shape function circle to prove charge conservation.

3.5 Electrostatic field solver

Crucial part of the new electrostatic PIC of *PICLas* is the corresponding field solver. Its detailed description and analysis have already been published [94]. Therefore, here, it is presented only briefly. For more details about the implementation, the theoretical derivation of the

numerical method, and additional test cases for verification and validation (including a dielectric sphere and a point source in a dielectric medium), please refer to the original publication.

Based on the high order approach of *PICLas* (see 2.7.1), the Hybridizable Discontinuous Galerkin (HDG) method [29] was identified as compatible method for solving the Poisson equation in *PICLas*. This field solver is able to handle complex geometries by using unstructured curved meshes and also allows the simulation of jumps in permittivity from different dielectrical materials. The latter feature, however, is not utilized in the following simulations from this thesis.

A significant advantage of HDG is its reduction of number of globally coupled unknowns involved in the field solver by a transformation from volume to surface states. In a classic 3D-DG frame of spatial order p_{mesh} with a number of N_{cells} cells, the total number of DOF in the system is $N_{cells}(p_{mesh}+1)^3$. In the HDG method, each DOF is unique on element interfaces, by which the total number is approximately $3N_{cells}(p_{mesh}+1)^2$. Therefore, the system size is reduced with HDG for $p_{mesh} > 2$. Additionally, the HDG was combined with the spectral element method [61] of *PICLas*, where integration and interpolation points are collocated, yielding sparse tensor-product operators and diagonal mass matrices.

As part of the actual implementation, also the interaction between electric fields and linear materials was taken into account by considering the displacement field $\vec{D} = \varepsilon\vec{E}$, with the relative permittivity of the material ε_r defining $\varepsilon = \varepsilon_0\varepsilon_r$. This generalizes the Poisson equation (Eq. 2.11) to:

$$\nabla\cdot\vec{D} = \nabla\cdot\left(\varepsilon\vec{E}\right) = -\nabla\cdot(\varepsilon\nabla\Phi) = \rho\,. \tag{3.29}$$

If the Boltzmann relation (Eq. 2.14) is used for the electrons, the right-hand side becomes nonlinear due to $\rho = \rho(\Phi)$ and the problem is solved iteratively with the Newton method. In each Newton iteration step n, the source term is linearized using a first order Taylor expansion resulting in

$$\rho(\Phi^{n+1}) = \rho(\Phi^n) + (\rho_\Phi)^n(\Phi^{n+1}-\Phi^n)\,, \quad (\rho_\Phi)^n = \left.\frac{\mathrm{d}\rho}{\mathrm{d}\Phi}\right|_{\Phi^n}. \tag{3.30}$$

Hence, Eq. 3.29 becomes

$$(\rho_\Phi)^n\Phi^{n+1} + \nabla\cdot(\varepsilon_0\nabla\Phi^{n+1}) = r^n\,, \quad r^n = \rho_I - \rho(\Phi^n) + (\rho_\Phi)^n\Phi^n\,, \tag{3.31}$$

which is iterated until the residual r is smaller than a defined tolerance.

The numerical scheme for solving Eq. 3.31 is derived by the variational form of the problem, which utilizes the test functions for the electric field and its potential $\bar{E}, \bar{\Phi}$ as well as an integration over the domain. The computational domain Ω is subdivided into n_K non-overlapping and conforming hexahedral elements K_i, $i = 1, 2, \ldots, n_K$. With regard to a single element K and reducing the equation system to a system solely depending on the solution at each element interface e, the additional unknown λ is introduced, which is unique on each element interface, together with its test function $\bar{\lambda}$.

After making the local DG hybridizable (LDG-H) ansatz [29], setting the numerical traces on the element interfaces based on a stabilization parameter $\tau > 0$, and the assumption of a constant permittivity per element ε_K, we get

$$\begin{aligned} \frac{1}{\varepsilon_K}\left\langle \vec{D}, \bar{D} \right\rangle_K - \left\langle \Phi, \nabla \cdot \bar{D} \right\rangle_K + \sum_{e \in \partial K} \left\{ \lambda \bar{D} \cdot \vec{n} \right\}_e = 0 \\ -\left\langle \nabla \cdot \vec{D}, \bar{\Phi} \right\rangle_K + \left\langle \rho_\Phi \Phi, \bar{\Phi} \right\rangle_K - \sum_{e \in \partial K} \left\{ \tau \Phi \bar{\Phi} \right\}_e + \sum_{e \in \partial K} \left\{ \tau \lambda \bar{\Phi} \right\}_e = \left\langle r, \bar{\Phi} \right\rangle_K, \end{aligned} \tag{3.32}$$

with the Neumann boundary condition defined by:

$$\sum_{e \in K, K'} \left(\left\{ \vec{D} \cdot \vec{n} \bar{\lambda} \right\}_e + \left\{ \tau \Phi \bar{\lambda} \right\}_e - \left\{ \tau \lambda \bar{\lambda} \right\}_e \right) = \sum_{e \in \Omega_{\text{Neu.}}} \left\{ \vec{D} \cdot \vec{n} \bar{\lambda} \right\}_e . \tag{3.33}$$

For Dirichlet boundaries, λ can be specified directly, and for inner interfaces, the right-hand side of Eq. 3.33 is set to zero.

Finally, a transformation of the integrals and derivatives to the reference space (see Eq. 2.19) and applying the spectral element ansatz result in a symmetric linear equation system, where all degrees of freedom are assigned to a vector that consists of the element unknowns $\underline{D}$ and $\underline{\Phi}$ as well as the unknowns on the element interfaces $\underline{\lambda}$:

$$\begin{bmatrix} \underline{\underline{\mathcal{A}}} & \underline{\underline{\mathcal{B}}}^T & \underline{\underline{\mathcal{C}}}^T \\ \underline{\underline{\mathcal{B}}} & \underline{\underline{\mathcal{D}}} & \underline{\underline{\mathcal{E}}}^T \\ \underline{\underline{\mathcal{C}}} & \underline{\underline{\mathcal{E}}} & \underline{\underline{\mathcal{F}}} \end{bmatrix} \begin{bmatrix} \underline{D} \\ \underline{\Phi} \\ \underline{\lambda} \end{bmatrix} = \begin{bmatrix} 0 \\ \underline{r} \\ \underline{D}_N \end{bmatrix}. \tag{3.34}$$

Equation 3.34 can be reduced even further to a symmetric system for the unknowns on the element interfaces only. This reduced $\underline{\lambda}$-system is solved with an iterative conjugate gradient solver, using either a diagonal or block-Jacobi preconditioner. Once the solution λ at the element interfaces is known, the evaluation of the potential and the electric field is a post-processing step based on Eqs. 3.32.

3.6 Charge- and momentum-exchange interactions

Besides the elastic collisions inside the neutral gas, also the interactions between ions and neutral gas are particularly important for the ion optics simulations of this study. In contrast to the neutral gas collisions, however, the cross sections σ for charge- and momentum-exchange cannot be accurately modeled by the VHS approach (see 2.7.3), but instead by a logarithmic relation [74]:

$$\sigma = A \cdot \log(g_{12}) + B, \tag{3.35}$$

with collision type-specific constants A and B. For the state as present inside the ion optics, the ions I are moving with much higher velocity through the neutral gas N, which is approximately at rest. The majority of occurring collisions are at small deflection angles by which the ions are slightly deflected but keep most of their magnitude of velocity:

$$I_{fast} + N_{slow} \rightarrow I_{fast} + N_{slow}, \tag{3.36}$$

which is commonly named momentum exchange reaction (MEX). Besides Eq. 3.35, the second difference to neutral-neutral collisions is that, additionally, an electron can be transferred from an ion to a neutral particle, by which the singly ionized I_{fast} becomes a neutral and the neutral N_{slow} an ion:

$$I_{fast} + N_{slow} \rightarrow N_{fast} + I_{slow}, \tag{3.37}$$

which is commonly named charge exchange (CEX). The created slow ions I_{slow} are prone to the electric fields towards surfaces inside the ion optics and can cause significant erosion by the resulting ion impingement (see section 2.4).

Basically, two different approaches can be found in literature for modeling charge and momentum exchange interactions. The first (“simple model”, hereinafter) assumes MEX as isotropic scattering and CEX as simple species swap without any exchange of momentum [85], which results from the assumption that CEX occurs only at large distances between the collision partners (i.e., with negligible deflection angles). However, it was shown [41] that the simple model over-predicts the creation of ions with high-angle scattering and a non-isotropic model can reproduce experimental results more accurately. That second (“scattering-based”) model reproduces the theoretical differential cross sections instead of an isotropic scattering and combines MEX and CEX into one single scattering process. Thus, also CEX can occur with an exchange of momentum, i.e., scattering. The implementation of Araki [4] was chosen, which is a combination of classical scattering by ab initio spin-orbit free potentials [20] and

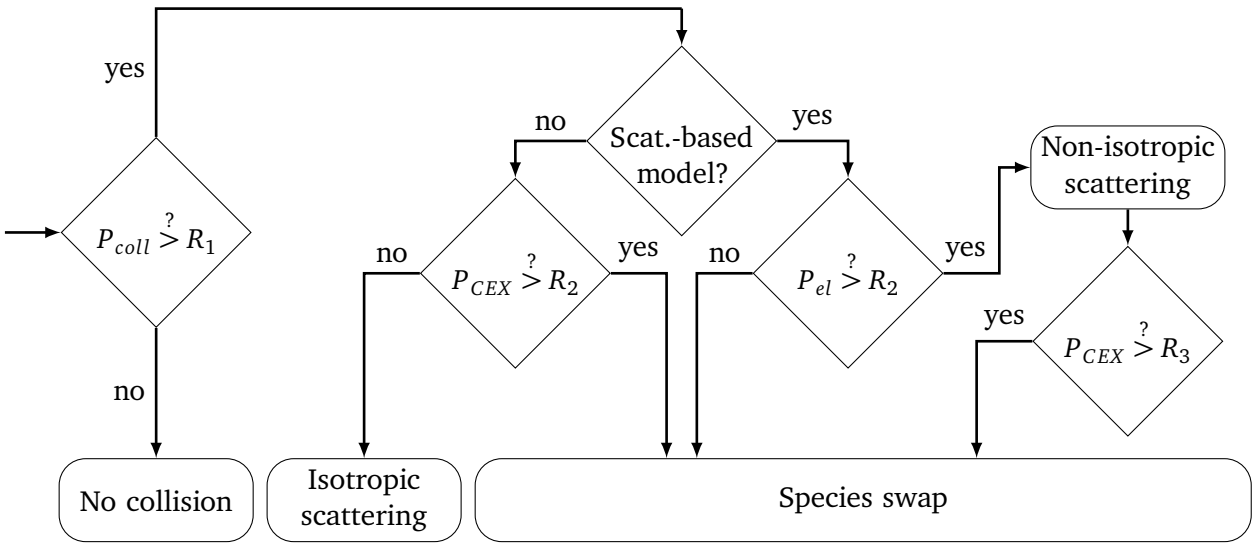

Figure 3.13: Implemented scheme for charge and momentum exchange interactions.

the VHS model. Deflection angles are interpolated from a pre-computed lookup table by the collision energy and a sampled impact parameter [5].

Both the simple and the scattering-based model were implemented in the collision routines of *PICLas*. Consistently with the other collision types, a collision is assumed to occur based on P_{coll} from Eq. 2.21, with a total cross section

$$\sigma_{tot} = \sigma_{CEX} + \sigma_{MEX} = P_{CEX}\sigma_{tot} + (1 - P_{CEX})\sigma_{tot}\,, \tag{3.38}$$

based on Eq. 3.35 and $P_{CEX} = \sigma_{CEX}/\sigma_{tot}$, which is usually set to 0.5 [20]. Based on a minimum deflection angle threshold (e.g., 1°) and the corresponding impact parameter, the value of σ_{tot} can be further sub-divided for the scattering-based model into a part $P_{el} = \sigma_{el}/\sigma_{tot}$ with scattering and a part without ($\sigma_{\chi\approx 0} = \sigma_{tot} - \sigma_{el}$):

$$\sigma_{tot} = P_{CEX}(\sigma_{el} + \sigma_{\chi\approx 0}) + (1 - P_{CEX})(\sigma_{el} + \sigma_{\chi\approx 0}) = \sigma_{CEX,el} + \sigma_{CEX,\chi\approx 0} + \sigma_{MEX,el} + \sigma_{MEX,\chi\approx 0}\,. \tag{3.39}$$

Since the MEX part with negligible exchange of momentum does not change any particle state, it can be simply excluded by setting $\sigma_{MEX,\chi\approx 0} = 0$, which results in a decreased effective cross section of $\sigma_{tot} = \sigma_{CEX} + (1 - P_{CEX})\sigma_{el}$ and can save a large amount of unnecessary scattering calculations [5].

In contrast to Fig. 2.10, the path for $P_{coll} > R_1$ goes directly to a new elastic collision routine, corresponding to the actual MEX or CEX process. It either performs the scattering process (isotropic or non-isotropic) or skips any exchange of momentum. To distinguish between the

actual type of collision, the respective probabilities are compared with additional random numbers: $P_{el} \overset{?}{>} R_2$ and $P_{CEX} \overset{?}{>} R_3$, as shown in Fig. 3.13. For the case of $P_{CEX} \leq R_3$, the collision scheme ends with the non-isotropic scattering, otherwise an additional species swap is performed. The verification of the implemented routines will be presented in section 4.5.

3.7 Speed-up of PIC-based ion optics simulations

In time-accurate PIC, the dynamic source terms result in a strong coupling between particles and field solver, which demands for each temporal discretization step to deposit the charge density ρ, update the field and move the particles accordingly to their interpolated accelerations. A large number of simulation particles is required to ensure a sufficiently smooth, approximated ρ and makes time-accurate PIC computationally intensive. But for cases in which a steady state can be reached and dynamic effects do not need to be resolved, further simplifications are possible, such as an under-relaxation of ρ.

In this optional speed-up method implemented in *PICLas*, the charge density is considered from time step $n-1$ to n as exponential moving average with a relaxation factor $\alpha \in [0,1]$:

$$\rho^n = \alpha\rho(t) + (1-\alpha)\rho^{n-1}\,. \tag{3.40}$$

By that, the effective particle sample size of ρ^n, as used as source term for the field solver, is increased and a larger particle weight w can be used, which decreases the number of simulation particles. Additionally, the resulting field solution is blurred in time. This allows to restrict the field update to every N_{HDG} time steps, but removes the time-accuracy of the simulation approach, i.e., it delays the steady state towards later simulation times. For early simulation times with particle distributions of highly unsteady nature, N_{HDG} must be kept small, since otherwise the field solver might not converge as continuation of the previous iteration steps. But after the initial time steps, N_{HDG} can be increased, which drastically reduces the computational cost per Δt. The actual benefit, however, depends on the specific application, defining the steady state and required sample sizes of time-averaged results.

As a matter of fact, this approach is very similar to implementations of the gun models for ion trajectory calculations (see section 1.2); but instead of initially single ion layers, the simulation particles are simultaneously distributed along their complete trajectories. Additionally, instead of depositing fixed-field trajectories, the under-relaxation is pseudo-dynamic in terms of a temporally blurred deposition during the actual motion along the trajectories. In gun-type simulations, the achievement of steady state is not fully self-consistent and can result in non-physical, “trapped” populations of slow CEX ions [26]. Those ions can influence the simulated

erosion characteristics, despite of their very small part of the charge density distribution. The trapping is expected to be prevented by considering the dynamic behavior of the plasma and as simplification also by the pseudo-dynamic approach. Furthermore, gun models with single ion layers are disadvantageous for a parallelization via domain decomposition since they result in a highly local particle distribution, in contrast to the more evenly distributed computational load for the PIC-based approach.

4 Verification and sensitivity analyses

4.1 Smoothing algorithms for number of particle insertion

As described in 3.3.1, several rounding algorithms are implemented in *PICLas* for the side-specific determination of N_{in}, defining the integer number of inserted particles per time step for the surface flux. A higher fluctuation of N_{in} can increase the statistical noise of the total particle number N_{domain}^{tot} that is reached after steady state inside the computational domain with a balanced in- and outflow. This fluctuation results in a generally decreased accuracy of the particle simulation.

The easiest rounding method is to calculate the theoretical real number for each insertion side and convert it directly into an integer number, either by a Poisson distribution with the corresponding real number as expected value ("side-specific Poisson") or by stochastic rounding ("side-specific random", see Eq. 3.19). An additional smoothing can be achieved by, first, determining the total number over all inflow-sides and, subsequently, subdividing it for the individual sides, based on algorithm 2. The total integer number is determined by stochastic rounding, either separately for each time step ("global random") or with additional smoothing over several time steps ("temporally smoothed"). Next, all 4 approaches are compared with each other. Additionally, the influence of time step size, side areas and velocity distribution is investigated.

The simulations utilize the computational mesh depicted in Fig. 4.1, with symmetry conditions in x and y as well as open sides in z. The discretizations in Δx_1 and Δx_2 were varied, resulting in cell numbers N_{cell} of [2; 200; 101] and individual side areas of [$0.5\,\mathrm{m}^2$; $0.5\cdot10^{-2}\,\mathrm{m}^2$; both mixed], respectively. The insertion procedure via triangles was used, which divides the actual inflow areas further in half. Both cases of either a constant velocity distribution ($a\to\infty$) or a hypersonic inflow with $a=4$ were considered. Essentially, all inflow particles (in z) have velocities $v_{\perp in}>0$ and $v_\Gamma=\mu=\langle v_{\perp in}\rangle$ holds (see Eq. 3.16 in subsection 3.3.1). The number density of the inflow was set to $n=2\cdot10^6\,\mathrm{m}^{-3}$ so that the total volume of $0.5\,\mathrm{m}^3$ gives, for a weighting factor of $w=1$, a mean particle number of $\left\langle N_{domain}^{tot}\right\rangle=1\cdot10^6$ in steady state. The mean velocity of $\langle v_{\perp in}\rangle=7378.647\,\mathrm{m/s}$ and time step of either $1\cdot10^{-8}\,\mathrm{s}$ or $1\cdot10^{-6}\,\mathrm{s}$ yield N_{in} particle insertions per time step and insertion triangle of 0.36898, 36.898, or 3689.8.

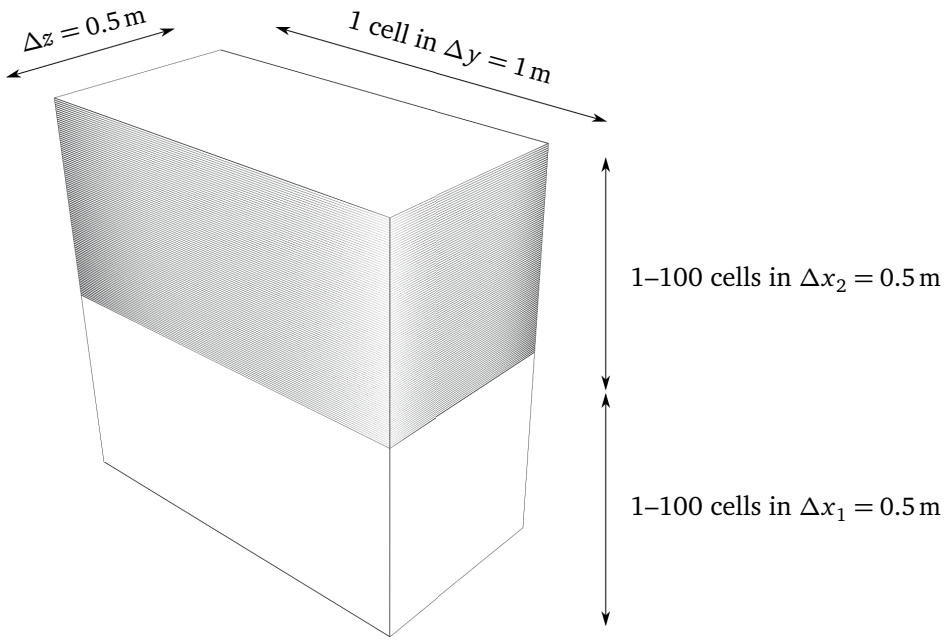

Figure 4.1: Box with cell subdivision in x and inflow in z direction.

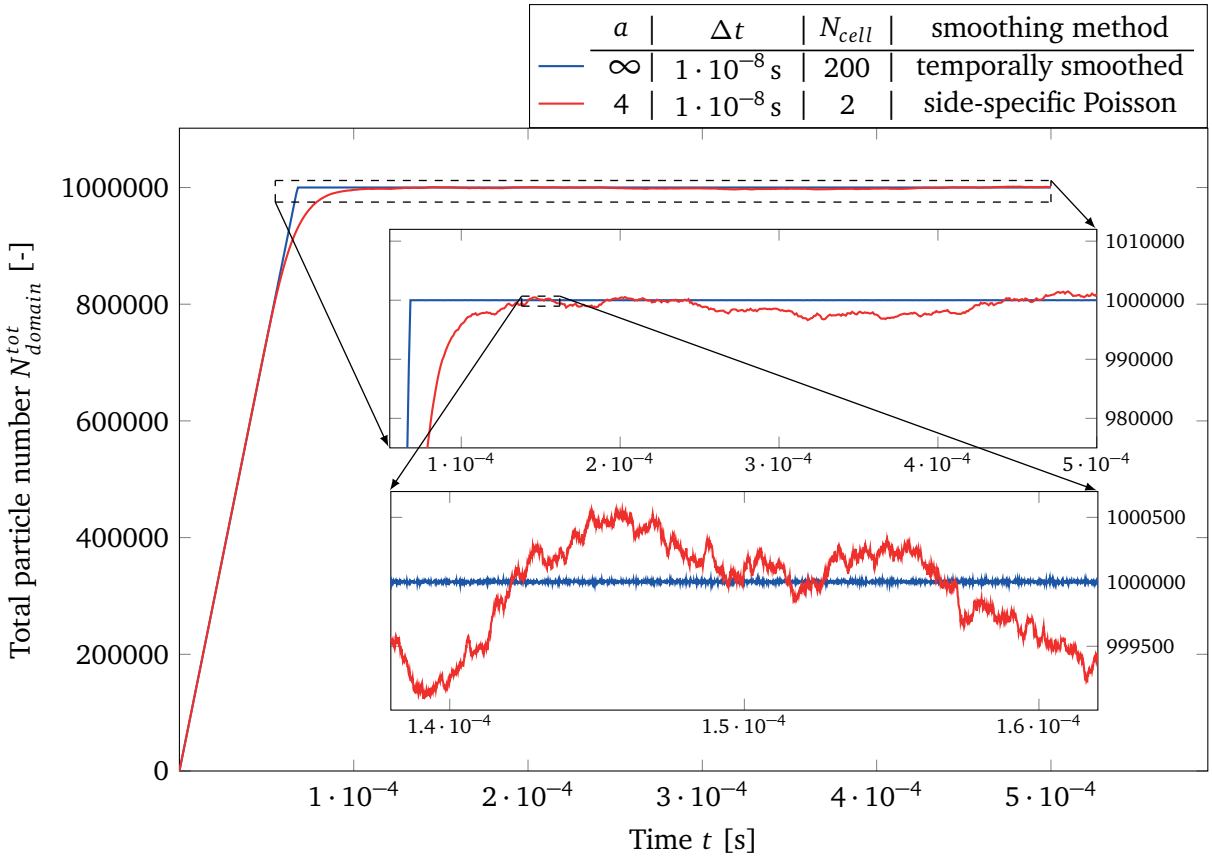

Figure 4.2: Development of $N^{tot}_{domain}(t)$ for cases with minimum and maximum fluctuation.

To illustrate the strong dependence of the statistical noise of N^{tot}_{domain} on the varied parameters, Fig. 4.2 depicts the corresponding temporal development for two exemplary cases. The shown parameter set with small fluctuation is an inflow with constant velocity distribution, small time step, and temporal smoothing. The one with large fluctuation is with Maxwellian inflow, small time step, side-specific Poisson rounding, and small cell number. Both cases reach the expected mean particle number of $\left\langle N^{tot}_{domain} \right\rangle = 1 \cdot 10^6$. The difference in the time at which steady state is reached is mostly based on the fact that for a constant velocity distribution, all particles are inserted into a layer of width $L = v_{\perp in} \Delta t$ adjacent to the inflow boundary and move exactly the same distance in each time step. This determines that the layer inserted at $t = 0$ reaches the outflow boundary exactly after the steady state time at $t^{a \to \infty}_{steady} = \Delta z / v_{\perp in} \approx 6.78 \cdot 10^{-5}\,\mathrm{s}$. For the Maxwellian distribution, however, the particles slower than $\langle v_{\perp in} \rangle$ reach the outflow later, resulting in a delayed steady state.[1] Furthermore, particles are not assigned to a certain, initial layer of width L, but they mix accordingly to their velocities. Hence, there exists an additional statistical noise for $N^{tot}_{domain}(t)$, depending on the discrete sampling of velocity space besides the physical space.

Figure 4.3 illustrates the actual interdependence between all varied parameters in terms of the resulting fluctuation. The noise is evaluated as standard deviation σ of N^{tot}_{domain}, calculated over $n_{\Delta t} = 251$ equidistant time steps between $t_{steady} = 2.5 \cdot 10^{-4}\,\mathrm{s}$ and $t_{end} = 5 \cdot 10^{-4}\,\mathrm{s}$ by:

$$\sigma^2 = \frac{1}{n_{\Delta t} - 1} \sum_{i=1}^{n_{\Delta t}} \left(N^{tot}_{domain}(t_i) - \left\langle N^{tot}_{domain} \right\rangle \right)^2 . \tag{4.1}$$

After t_{steady}, all simulations reached the mean total number $\left\langle N^{tot}_{domain} \right\rangle$. Summarized, it can be seen that with decreasing smoothing of N_{in} (starting with global "temporally smoothed", over time step specific "global random" and "side-specific random" to "side-specific Poisson") the standard deviation increases or stays approximately constant, which verifies the different approaches. Please note that simulations resulting in $N_{in} = 3689.8$ were not conducted with Poisson rounding. Reason is the numerical implementation of sampling from a Poisson distribution by an evaluation of $\exp(-N_{in})$, which is subjected to the limitations of floating-point arithmetic. The temporal smoothing is shown to be most effective for the three cases with constant velocities and small time steps. With decreasing smoothing, σ is the smallest for large cell side areas (i.e., small cell numbers). That is particularly important for side-specific methods, for which the noise of N_{in} accumulates over the individual sides. Comparing the small time steps (blue and pink lines) with larger ones (red lines) it can be seen that the temporal smoothing performs better for a small Δt, with which the inflow particle number

[1] Here, t_{steady} depends on the actually occurring, minimum particle velocity. As mentioned in 3.3.1, the part of velocities $v_\perp < 0$ is less than $1 \cdot 10^{-6}$ for $a = 3$ and, thus, the same negligible part is below $\hat{v} = 1844.662\,\mathrm{m/s}$ for $a = 4$. With respect to the particle part with larger or equal velocities, this yields $t^{a=4}_{steady} \approx 2.5 \cdot 10^{-4}\,\mathrm{s}$.

can be adapted more often. But for side-specific methods, the cases with large Δt (red) or small cell number (pink) perform better, since the individual N_{in} values are larger and, thus, the relative rounding deviation is smaller. All mentioned relations are expected to hold for the cases with Maxwellian inflow, too. However, the statistical fluctuation associated with the insertion smoothing is superposed with the one based on the discrete sampling of velocity space. Consequently, the fluctuation cannot be reduced with further smoothing because the corresponding value ($\sigma \approx 250 - 500$ for the simulated cases with $a = 4$) seems to be equal or greater than the part resulting from the side-specific random rounding. Nevertheless, the temporal smoothing can be used in all simulations since it does not result in any significant additional computational cost.

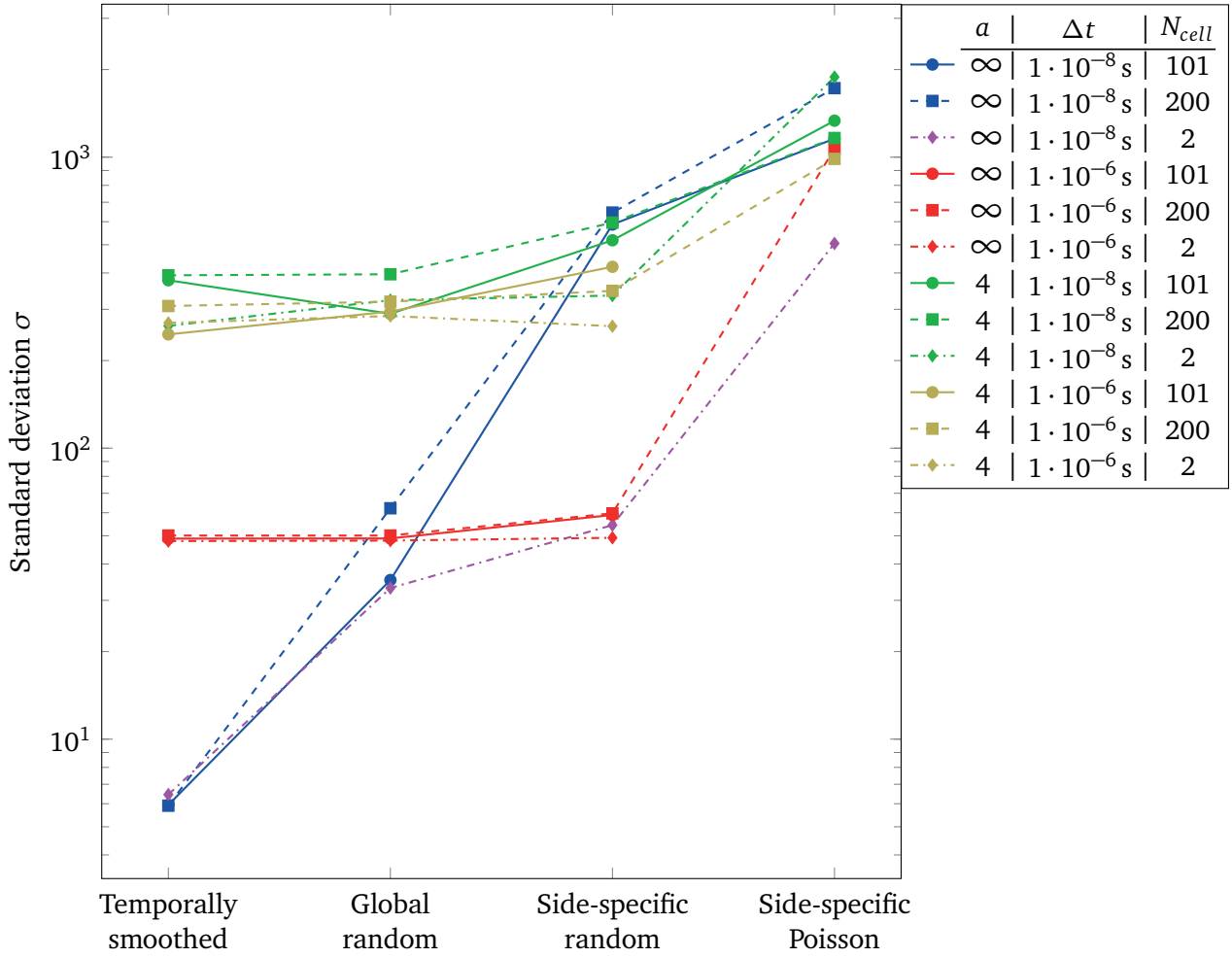

Figure 4.3: Standard deviation of N^{tot}_{domain} during steady state for different smoothing methods.

4.2 Convergence studies on temporal integration schemes

Section 3.2 described the temporal integration schemes implemented for the new electrostatic PIC. In this section, they are verified in terms of an experimental order of convergence (EOC). An 1D, temporally constant, but spatially varying electrostatic field in x-direction is assumed. More precisely, the acceleration $a(x)$ at a particle position x is determined by:

$$a(x) = x''(t) = -c_2^2(x + c_3)\,. \tag{4.2}$$

By c_3, a particle already has an initial acceleration of $a(x=0) \neq 0$. The $c_3 = -x(t=0)$ and $c_1 = x'(t=0)$ define the integration constants of $\iint x''\,\mathrm{d}t$ and, thus, the exact solution:

$$x_{exact}(t) = \frac{c_1}{c_2}\sin(c_2 t) - c_3 \quad , \qquad x'_{exact}(t) = v_{exact}(t) = c_1\cos(c_2 t)\,. \tag{4.3}$$

Solving $x_{exact}(t)$ in Eq. 4.3 for the time t yields $t(x)$ of Eq. 4.4, which also defines the initial particle-specific time t_0 for a particle at $x = 0$ and moving according to Eq. 4.2:

$$t(x) = c_2^{-1}\arcsin\left[\frac{(x+c_3)c_2}{c_1}\right] \quad , \qquad t_0 = c_2^{-1}\arcsin\left[\frac{c_3 c_2}{c_1}\right]\,. \tag{4.4}$$

Particles are continuously inserted across $x = 0$ and move until $t \leq t_{end}$. This yields, for each particle, the temporal development of $x_{exact}(t)$ and $v_{exact}(t)$ depicted in Fig. 4.4. Here, the constants were set according to Tab. 4.1, by which the initial velocity at $t_0 \approx 1.609 \cdot 10^{-7}\,\mathrm{s}$ becomes $v(t_0) = 32000\,\mathrm{m/s}$ and decreases to $v(t_{end}) \approx 15107\,\mathrm{m/s}$ at $x_{max} \approx 0.00326\,\mathrm{m}$.

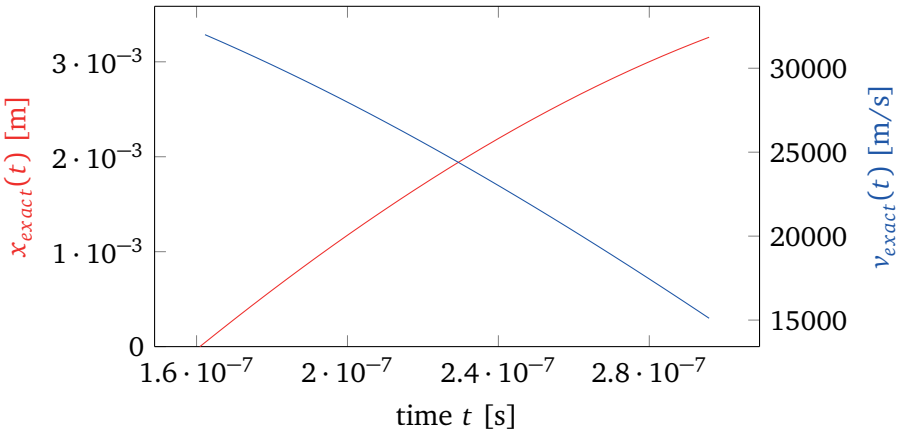

Figure 4.4: Exact reference solutions in particle-specific framework.

Table 4.1: Simulation parameters.

$t_{end} - t_0$	c_1	c_2	c_3
$1.35 \cdot 10^{-7}\,\mathrm{s}$	$4 \cdot 10^4\,\mathrm{m/s}$	$4 \cdot 10^6\,\mathrm{s}^{-1}$	$6 \cdot 10^{-3}\,\mathrm{m}$

Particles are propagated through the domain by a direct evaluation of Eq. 4.2 instead of the sequence of deposition, field solver and interpolation. Based on the inflow through $x = 0$, the domain is filled with an increasing number of N_{part} simulation particles, each with its specific time t_i according to Eq. 4.4. The chosen computational domain of $x \in [0; 0.004\,\mathrm{m}]$ ensures that all particles stay inside the domain. After t_{end}, all $N_{part} = 9000$ resulting particles are compared in their individual position x_i and velocity v_i with the exact solution from Eq. 4.3. The total deviation is calculated by Eq. 4.5 which can be interpreted as Monte Carlo integration of the L2-norm of the entire trajectory. In the case of the leapfrog scheme, $s = 1$ applies for considering the respective, different times for position and velocity; whereas for the other schemes $s = 0$ holds.

$$||x||_{L_2}^2 = \sum_{i=1}^{N_{part}} \left(x_i - x_{exact}(t_i)\right)^2 , \quad ||v||_{L_2}^2 = \sum_{i=1}^{N_{part}} \left(v_i - v_{exact}(t_i - s\Delta t/2)\right)^2 \tag{4.5}$$

4.2.1 Exact initialization in volume

First, simulations with an exact initialization are investigated. Each time step, a layer between $x = 0$ and $x(t = t_0 + \Delta t)$ is randomly filled by an equal distribution and the particle values $t_i = t(x_i)$ and $v_i = v(t_i)$ are set by their exact solution. In the case of the LSERK scheme, particles are inserted only after the last stage for avoiding any stage reconstruction.

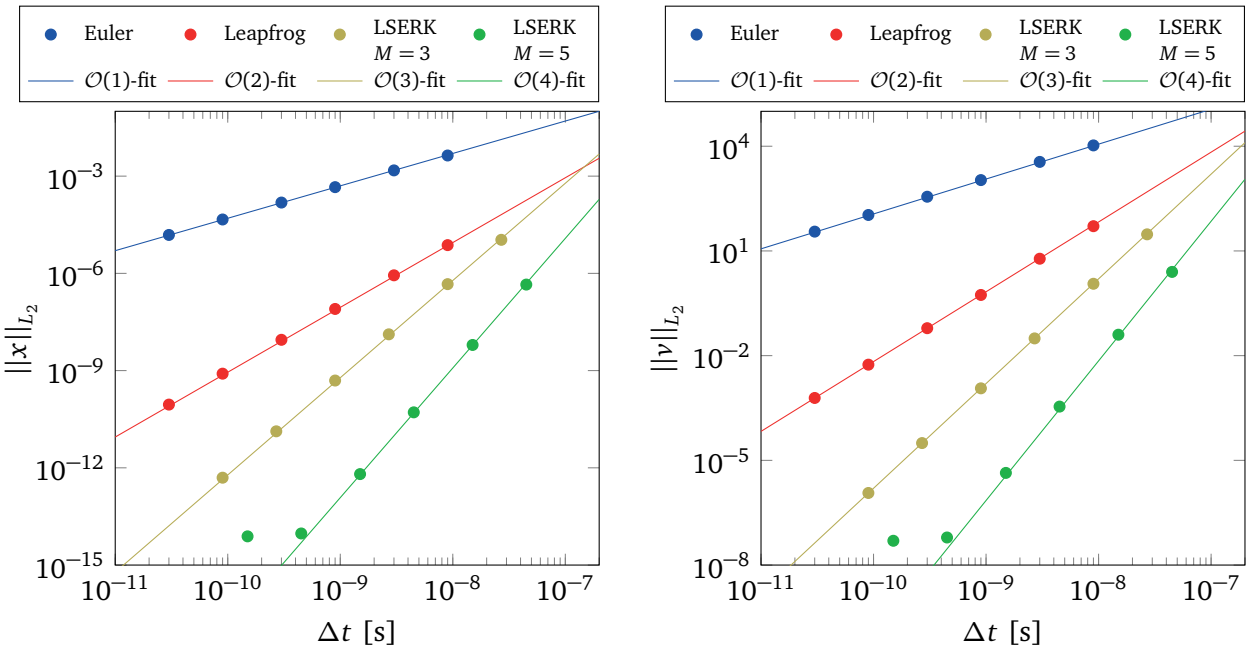

(a) Deviation in physical space x.

(b) Deviation in velocity v.

Figure 4.5: Experimental order of convergence with exact initialization in volume.

The results from the simulations are depicted in Fig. 4.5. For the determination of the actual EOC, also fits of type $A \cdot (\Delta t)^B$ with respective order $O(B)$ are included. It can be seen that all expected orders are reproduced: $O(1)$ for the Euler push, $O(2)$ for the leapfrog, as well as $O(3)$ and $O(4)$ for the respective LSERK scheme. The 5-stage LSERK levels out at a very low deviation threshold due to the reached machine accuracy.

4.2.2 Initialization via surface flux

When particles are initialized via surface flux (see 3.3.1), their initial values of x_i and v_i are based on the (random) partial time step $R_i \Delta t$, velocity $v(x=0) = 32000\,\mathrm{m/s}$, and $a(x=0) = -9.6 \cdot 10^{10}\,\mathrm{m/s^2}$. Hence, there can already be an initial shift from the exact solution that accumulates during the simulation. As can be seen in Fig. 4.6, the Euler push is nearly unchanged compared with the exact initialization, but the accuracy of the other schemes is deteriorated. The leapfrog keeps its $O(2)$ characteristic, but also the LSERK schemes decrease to $O(2)$ due to the lower order stage reconstruction. Hence, when a plasma state is mostly defined by inflows with significant applied forces, a temporal integration of higher order might not be of any benefit. Therefore, the actual influence in the application of ion optics simulations will be further analyzed in section 4.4. The integration schemes themselves, however, can be seen as verified, also including the surface flux-specific routines.

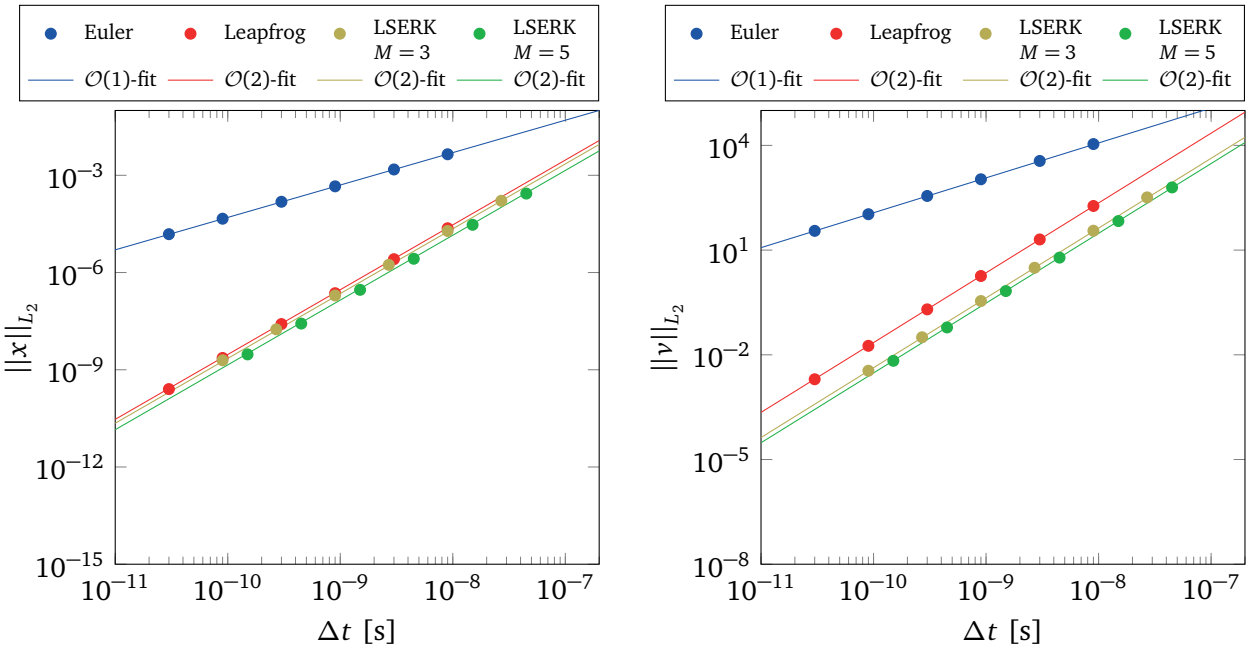

(a) Deviation in physical space x.

(b) Deviation in velocity v.

Figure 4.6: Experimental order of convergence with initialization via surface flux.

4.3 HDG-PIC for bounded, electrostatic plasmas

The new electrostatic field solver (see 3.5) and its detailed verification as HDG-PIC has already been published [94]. Due to the particularly important role of plasma sheaths in the bounded, electrostatic plasmas of ion optics from this thesis, the corresponding verification is presented. For an unmagnetized, collisionless plasma, the resulting 1D sheath in x-direction can be described under the assumption of the Boltzmann relation (BR) as differential equation for $\Phi(x)$ with $\chi = -q_e\Phi/(k_\mathrm{B}T_{e^-})$, $\chi' = -q_e\partial_x\Phi/(k_\mathrm{B}T_{e^-})$ and $\vartheta = v_{ion}/\sqrt{k_\mathrm{B}T_{e^-}/m_{ion}}$ [101] by:

$$\frac{1}{2}\chi'^2 = \vartheta^2\left[\left(1+\frac{2\chi}{\vartheta^2}\right)^{1/2}-1\right]+\mathrm{e}^{-\chi}-1\,. \tag{4.6}$$

This can be used as reference for the simulation results. The numerical set-up includes:

- a pseudo 1D mesh with polynomial degree $p = 4$ and periodic boundary conditions;
- one cell in y and z with a dimension of $3\cdot10^{-3}\,\mathrm{m}$ and 20 cells in $x \in [0, L = 0.03\,\mathrm{m}]$;
- boundary conditions for the potential of $\Phi(x=0) = 0\,\mathrm{V}$ and $\Phi(x=L) = -0.18011\,\mathrm{V}$;
- open boundary conditions for particles at $x = 0$ and $x = L$;
- ions ($m_{ion} = 1.673\cdot10^{-27}\,\mathrm{kg}$) entering the sheath at $x = 0$ with $v_{ion} = 11492.19\,\mathrm{m/s}$;
- BR electrons with quasi-neutral inflow ($n_{e^-,ref} = n_{ion,in} = 1\cdot10^{12}\,\mathrm{m}^{-3}$ with $\Phi_{ref} = 0\mathrm{V}$);
- an electron temperature $T_{e^-} = 1000\,\mathrm{K}$, which equals the inflow ion temperature;
- 4^{th}-order shape functions ($r_{SF} = 1.5\cdot10^{-3}\,\mathrm{m}$) as deposition method;
- a temporal integration using the leapfrog scheme with $\Delta t = 1\cdot10^{-7}\,\mathrm{s}$;
- a weighting factor of $w = 1$, resulting in $2.67\cdot10^5$ ions after $7.5\cdot10^{-6}\,\mathrm{s}$ simulation time.

The domain is limited by two boundaries which need to be considered for the shape functions, since otherwise, artificial drops of charge density occur near the boundaries, as described in section 3.4. At $x = 0$, an inflow layer can be inserted and at $x = L$, as second boundary, the field component parallel to the boundary plane can be forced to zero by mirroring the charges with their negative sign, corresponding to an electrically perfectly conducting wall.

Figure 4.7 compares the simulation results with the reference solution, which was numerically solved by the ordinary differential equation solver LSODE [53] of GNU Octave. Three different cases for shape function corrections were considered: Only an inflow layer, both an inflow layer combined with a perfectly conducting wall, or no correction at all. They show very good agreement for the most positions, thus, verifying the HDG field solver of *PICLas*. When comparing the solutions, it should be noted that the applied Dirichlet conditions set Φ always

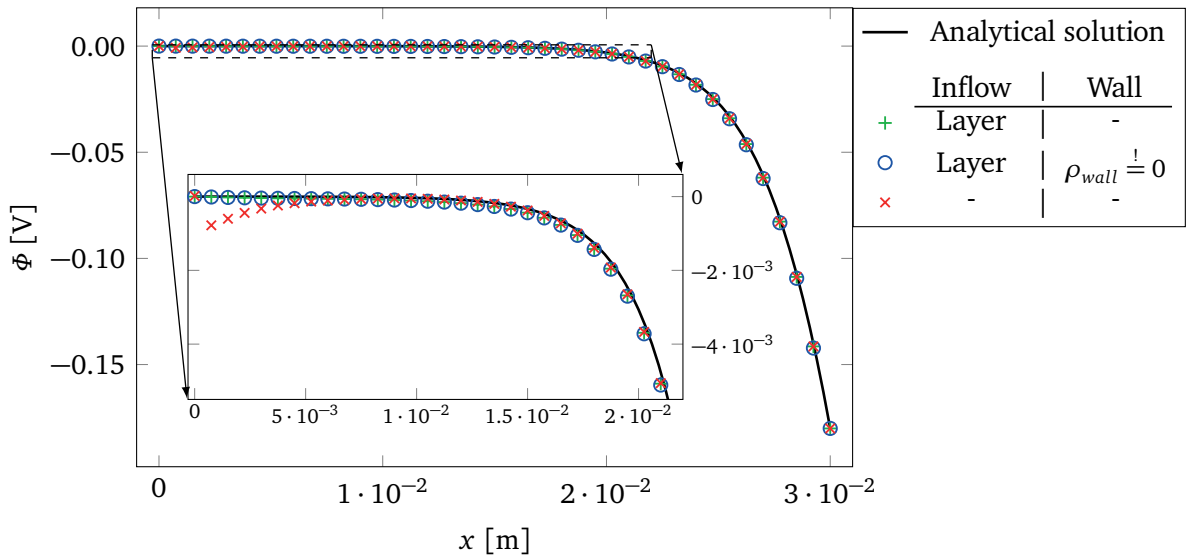

Figure 4.7: Plasma sheath results of the BR model compared with the analytical solution.

to the respective boundary value. Hence, only the shape of $\Phi(x)$ towards the boundary is of interest. It can be seen that the drop towards the wall is always quite accurate, which drastically simplifies the simulation of complex wall geometries, since a charge correction seems not to be required at walls. On the inflow side, however, a potential drop towards the artificially decreased, deposited charge density can be identified when no correction is applied. This would create a false acceleration of inflow ions into the domain which would affect especially the higher order temporal integration schemes, as described in section 4.2.

4.4 Convergence studies on ion optics simulations

Now, with the temporal integration schemes and field solver separately verified, they are combined to further analyze their characteristics in applications related to ion optics simulations. Similarly to the application cases presented in the published HDG-PIC verification [94], the simulation set-up is based on ion optics simulations of the full 2-grid system of the RIT-μX EBB from ArianeGroup GmbH, as it will be presented in chapter 5. Here, we want to keep the geometrical complexity while the domain size is reduced by assuming two different simplified domains, both representing an effectively infinite pattern of grid apertures taken from the full simulation setup.

In the more realistic simplification, the computational domain ('A' in Fig. 4.8) spans both grids and electrons are included via the BR model. A quasi-neutral state is assumed at the 'inflow A' plane that turns into a plasma sheath towards the lower potentials of the grid system. The second domain ('B' in Fig. 4.8) is limited to an extent from which the low potentials would

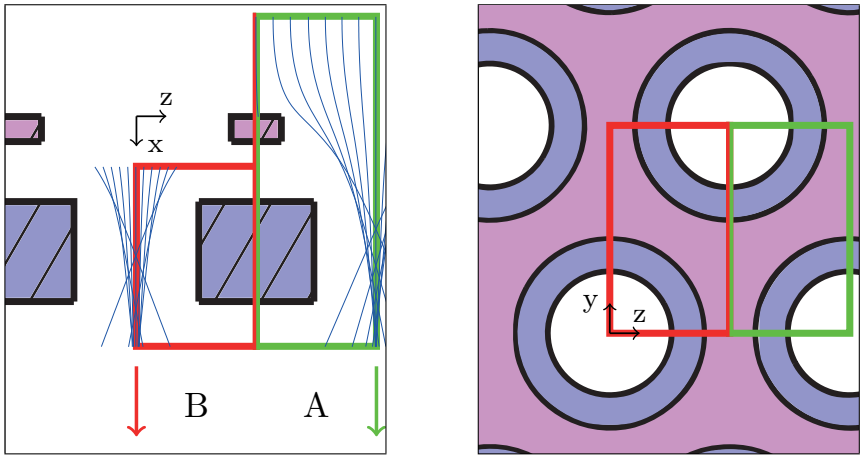

Figure 4.8: Simplified domains (red and green), left with ion trajectories (blue).

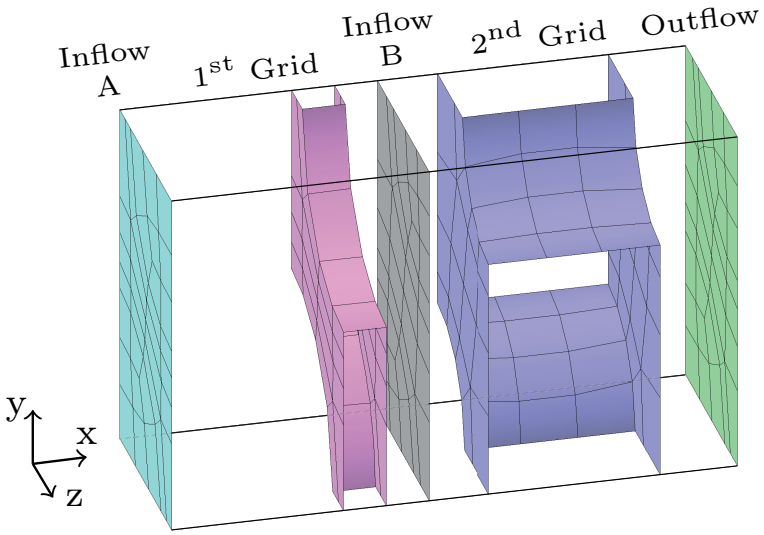

Figure 4.9: Surface mesh.

repel all electrons. Therefore, electrons can be completely excluded from the B simulations and only ions are considered. The upstream 'inflow B' plane between first and second grid (see Fig. 4.9) matches the equi-potential plane at 500 V from the full simulation. The boundary conditions for the field solver are equi-potential at the inflow and zero normal gradient at the outflow. Additional zero gradient conditions in x-y and x-z planes reduce the topology to two quarter apertures.

Figure 4.9 depicts the surface mesh where boundary conditions (BCs) are applied, with corresponding definitions in Table 4.2. For particles, open BCs remove crossing particles from the simulation, whereas symmetry conditions perform specular reflection. For domain 'A', a mesh with 2416 cells (22 cells along the x-axis) was considered, domain 'B' consists of 928 cells (10 cells along the x-axis). The curvilinear boundaries are represented by polynomials of $N_{geo} = 2$ and, unless otherwise specified, field polynomials are of degree $p = 4$. In the

Table 4.2: Boundary conditions for simplified ion optics domains.

Name	Field-BC	Particle-BC
Inflow A	$\Phi = 1315\,\mathrm{V}$	open, Xe^+ inflow
1st Grid	$\Phi = 1300\,\mathrm{V}$	open
Inflow B	$\Phi = 500\,\mathrm{V}$	open, Xe^+ inflow
2nd Grid	$\Phi = -300\,\mathrm{V}$	open
Outflow	$\frac{\partial \Phi}{\partial \vec{n}} = 0$	open
Symmetry	$\frac{\partial \Phi}{\partial \vec{n}} = 0$	reflective

inflow region of domain 'A', the upstream quasi-neutral state has an assumed bulk velocity of 2500 m/s, ion temperature of 450 K, and electron temperature of 3.5 eV. For domain 'B', truncated ion beams were considered as inflow and, therefore, a pre-defined radial velocity profile was imposed including a mean velocity of 34700 m/s. The inflow flux was set to match a beam current of 5 mA for the full thruster with 37 apertures.

Next, simulation results are compared between each other. The three-dimensional charge density field was chosen as characteristic, because it is sensitive to the whole interaction between field solver and particle routines, independently of the actual effect of space charges onto the electric field. Due to the Monte-Carlo-based insertion scheme of simulation particles, their distribution is affected by a statistical noise. The deposition onto the mesh via 4^{th}-order shape functions represents a smoothing approach with a certain sample size of particles with a macro particle factor of $w = 500$. After having reached steady state, the sample size of the deposited charge density ρ can be further increased by arithmetically averaging over n_s time steps between t_1 and $t_{n_s} = t_1 + n_s \Delta t$ at each interpolation point $\vec{x}_j$ of the field solver:

$$\langle \rho \rangle (\vec{x}_j) = \sum_{i=1}^{n_s} \rho(\vec{x}_j, t_i)/n_s. \tag{4.7}$$

This averaged charge density $\langle \rho \rangle$ is used as comparative field based on which the deviations from a respective reference solution are evaluated. If not otherwise specified, $n_s = 250$ was used. The deviation is calculated as volumetric L_2 norm $|| \langle \rho \rangle - \langle \rho_{ref} \rangle ||_{L_2}$, but since an analytical solution does not exist, a simulation result $\langle \rho_{ref} \rangle$ with highest accuracy is used as reference. For the comparison and integration of the L_2 norm, all solutions were interpolated onto a mesh with equidistant interpolation points of degree $p_{ref} \cdot (p_{ref} + 1)$ to ensure an exact integration of the polynomial field norm by the corresponding Gaussian quadrature. Please note that for domain 'A', the integration was only performed for mesh cells downstream of the quasi-neutral inflow ($x > 0$ in Fig. 4.8), since the higher statistical uncertainty at $x < 0$ would need much larger sample sizes.

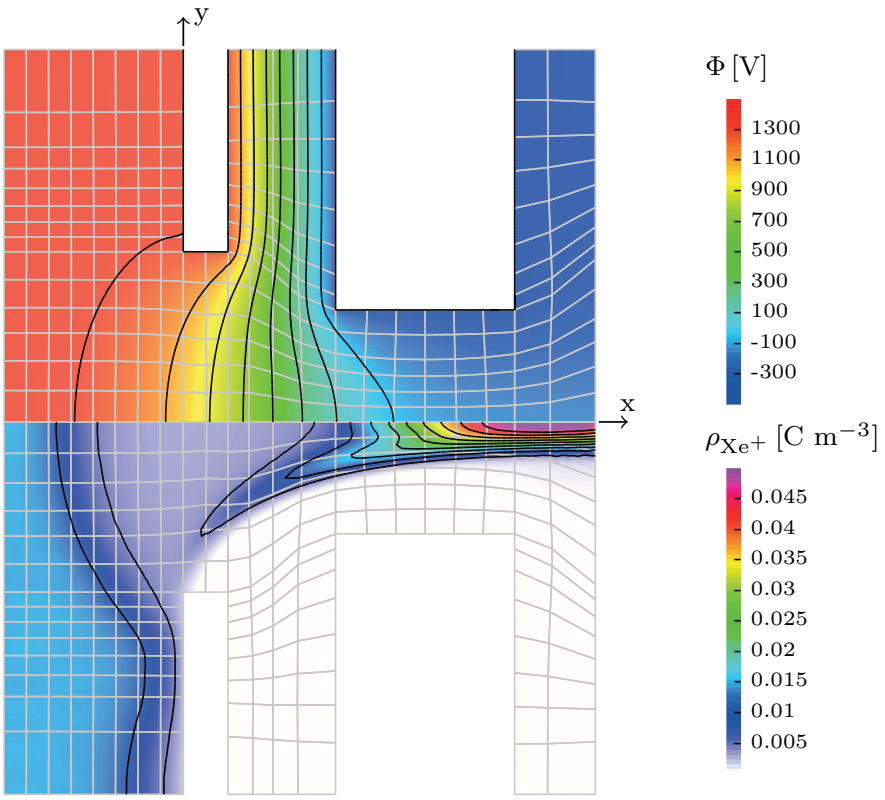

Figure 4.10: Electric potential (above) and charge density (below) for domain 'A'.

4.4.1 Temporal order of convergence

Similarly to section 4.2, the temporal integration was also analyzed for ion optics simulations to evaluate the efficiencies of the individual approaches.

Self-consistent ion extraction

First, the self-consistent ion extraction from a quasi-neutral state is modeled by ions and BR electrons inside the computational domain 'A'. By that, the inflow is placed at a position with very small potential gradients resulting in negligible forces for the surface flux related aspects of higher order temporal integration schemes. Figure 4.10 depicts the resulting contours of electric potential and ion charge density inside a symmetry plane through one grid aperture. In the inflow region with $\rho_{Xe^+} = 1.3826 \cdot 10^{-2}\,\mathrm{C/m^3}$, quasi-neutrality is reached since the Boltzmann relation is set to the same negative value for electrons at $\Phi_{in} = 1315\,\mathrm{V}$. About 350000 particles are simulated in steady state, mostly within the dense upstream region.

Figure 4.11 shows the result from the simulations with varied Δt. The averaged charge density field for $\Delta t = 5 \cdot 10^{-10}\,\mathrm{s}$ from the 3-stage LSERK was used as reference solution for

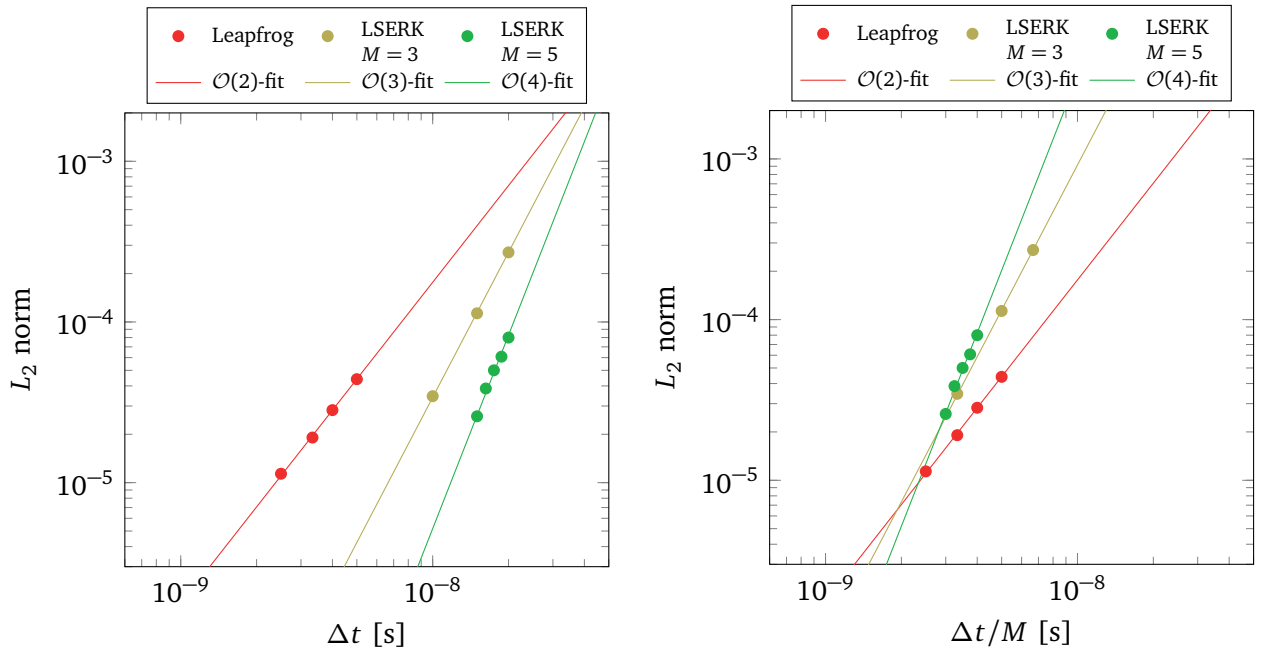

(a) L_2 norm $||\langle\rho\rangle - \langle\rho_{ref}\rangle||_{L_2}$ over time step size Δt. **(b)** L_2 norm $||\langle\rho\rangle - \langle\rho_{ref}\rangle||_{L_2}$ over average stage size.

Figure 4.11: EOC for domain 'A' (reference $\Delta t = 5 \cdot 10^{-10}$ s with 3-stage LSERK).

calculating the L_2 norm. It can be seen that the theoretical convergence orders are also reached for the complete PIC approach. However, when comparing the leapfrog with the LSERK schemes, it must be considered that the latter include M separate stages per time step and essentially all PIC routines are repeated in each stage. Hence, the actual computational cost per time step Δt is approximately M times higher, which was also verified by various representative simulations. Therefore, the different integration schemes are only comparable based on the same $\Delta t/M$, as chosen as horizontal axis in Fig. 4.11b. It shows that with respect to a similar computational cost, the highest accuracy is not anymore achieved with the highest temporal integration order. Instead, with a time step greater than $2 \cdot 10^{-9}$ s, the smallest L_2 norm is achieved with the leapfrog scheme due to its $M = 1$. Only for smaller $\Delta t/M$ ratios (corresponding to a Δt below $5 \cdot 2 \cdot 10^{-9}$ s $= 1 \cdot 10^{-8}$ s for the $M = 5$ scheme), the LSERK schemes can achieve higher accuracies. Thus, the optimal time step and temporal integration scheme depend on the actually desired accuracy.

Truncated ion beam insertion

Eventually, the truncated domain 'B' is considered which sets the inflow boundary at a position with a significant potential gradient and corresponding forces onto the inserted particles. Furthermore, the B domain enables to neglect all electrons inside the domain by which the

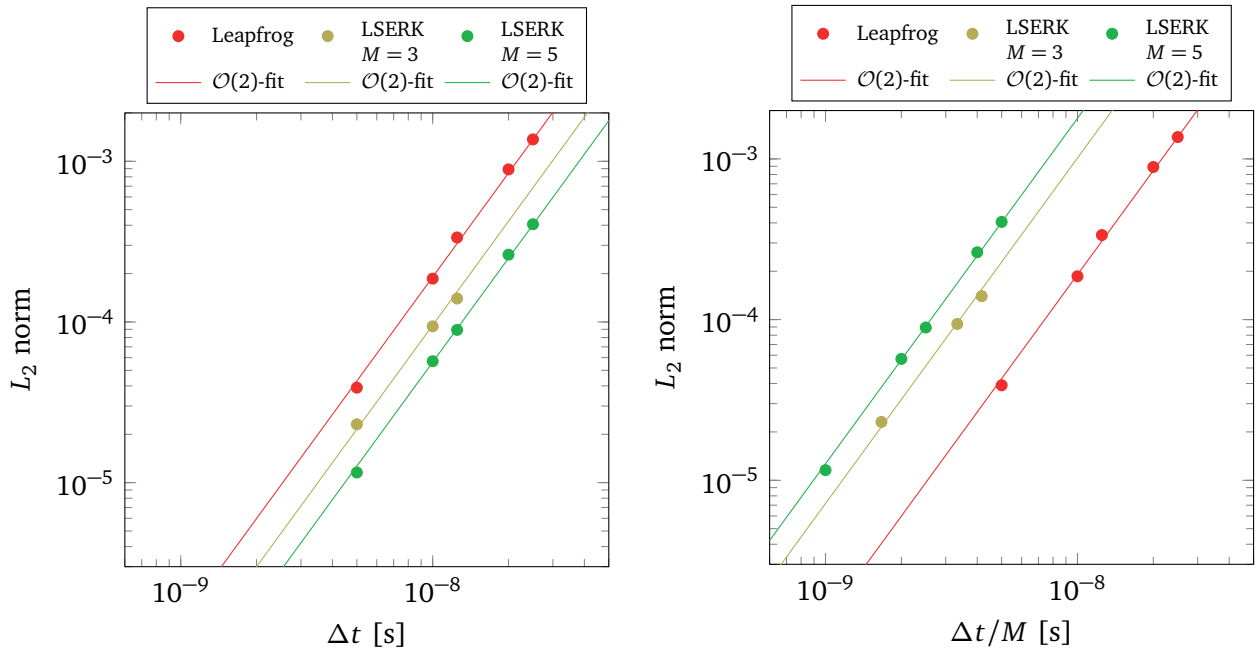

(a) L_2 norm $||\langle\rho\rangle - \langle\rho_{ref}\rangle||_{L_2}$ over time step size Δt. **(b)** L_2 norm $||\langle\rho\rangle - \langle\rho_{ref}\rangle||_{L_2}$ over average stage size.

Figure 4.12: EOC for domain 'B' (reference $\Delta t = 1.25 \cdot 10^{-10}$ s with 5-stage LSERK).

linear HDG can be used. After having reached steady-state with a simulation particle number of about 35000, the L_2 norm was integrated in the complete domain based on averaged charge densities and the solution from the 5-stage LSERK with $\Delta t = 1.25 \cdot 10^{-10}$ s was used as reference solution. As can be seen in Fig. 4.12, the acceleration at the inflow boundary affects the EOC in the same way as already shown in 4.2.2. The LSERK schemes are deteriorated towards a $O(2)$ characteristic and loose their benefit, as illustrated by Fig. 4.12b. Hence, if it is not guaranteed that the surface flux is applied at a force-free boundary, the utilization of the leapfrog seems to be the best choice. Of course, those circumstances change when the state is not anymore defined for the most part by the initial insertion of particles which are moved through an electric field with negligible temporal development. When the fields are highly unsteady, as in the case of kinetic electrons oscillating around the ions, the downside from surface flux-related routines in higher order integration schemes can be compensated.

4.4.2 Influence of the field resolution

The quality of the simulation results depends on all PIC-specific aspects: deposition, the accurate calculation of the electric field, and finally the field evaluation and temporal integration of particle motion. Besides the Δt-dependence of the latter, all these parts are additionally sensitive to the spatial discretization. Additional to the p-convergence of the field solver, this

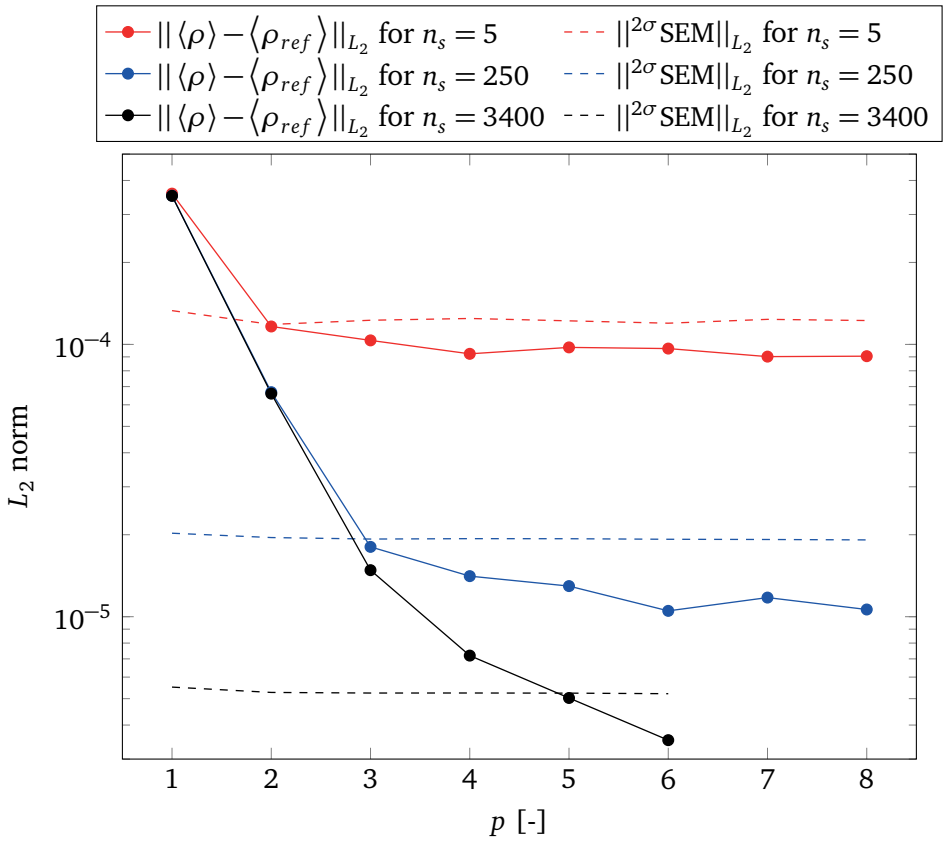

Figure 4.13: L_2 norm $||\langle\rho\rangle - \langle\rho_{ref}\rangle||_{L_2}$ for domain 'A' (reference $p_{ref} = 9;9;7$)

includes, e.g., also the shape functions used for deposition, which need to be interpolated by a sufficient number of DOF (see subsection 2.7.2). Therefore, the convergence behavior is evaluated for varied polynomial degree p, again based on the averaged charge density field. Additionally, the influence of the particle-based, statistical uncertainty was investigated, as also published as part of the HDG-PIC verification [94].

The simulations are restricted to the self-consistent ion extraction inside the computational domain 'A', with the same set-up as in 4.4.1. To ensure an accurate temporal integration, the 5-stage LSERK is used with $\Delta t = 5 \cdot 10^{-9}$ s. The convergence behavior is shown in Fig. 4.13 for three different sample sizes ($n_s = 5$, 250, and 3400 time steps). It can be seen that the L_2 norm levels out after having reached a certain polynomial degree. Thus, even an arbitrarily higher p would not result in a smaller deviation from the reference solution with p_{ref}. This must not be interpreted as a p-converged solution but rather as an integration of the statistical noise. It demonstrates that in the PIC application, there is a maximum reasonable discretization beyond which the error from the limited sample size exceeds the error based on the temporal or spatial resolution. Even with exactly the same numerical parameters, two solutions cannot agree beyond their uncertainty from different random numbers due the different particle positions.

To quantify this effect, the L_2 norms were not only calculated for the deviations of mean $\langle\rho\rangle(\vec{x}_j)$, but also for the corresponding 2-σ standard error of the mean (SEM) by Eq. 4.8 and can be interpreted as $||\langle\rho\rangle - \langle\rho_{ref}\rangle||_{L_2}$ with a reference solution that equals $\langle\rho\rangle$ but is shifted exactly by ${}^{2\sigma}\mathrm{SEM}(\vec{x}_j)$ at every $\vec{x}_j$.

$$||{}^{2\sigma}\mathrm{SEM}||_{L_2}^2 = \frac{\sum_{j=1}^{N_{cells}} \int_{V_j} \left({}^{2\sigma}\mathrm{SEM}(\vec{x}_j)\right)^2 dV_j}{V_{\mathrm{total}}}, \quad \left({}^{2\sigma}\mathrm{SEM}(\vec{x}_j)\right)^2 = \frac{2\sum_{i=1}^{n_s}(\rho_i(\vec{x}_j) - \langle\rho\rangle(\vec{x}_j))^2}{n_s(n_s-1)} \tag{4.8}$$

Those additional L_2 norms are included in Fig. 4.13 as dashed lines for all p and show their proportionality to $n_s^{-0.5}$ and independence on p. It can be seen that they are very similar to the respective convergence limits. With increasing sample size, the convergence limits decrease accordingly. After a $||\langle\rho\rangle - \langle\rho_{ref}\rangle||_{L_2}$ curve reaches the threshold, it simply fluctuates within the same order of magnitude as of the limit itself.

4.5 Neutral-ion collisions

A code-to-code comparison was conducted for the verification of the implemented CEX and MEX routines (see section 3.6). The simulation set-up corresponds to the one for the coupled PIC-DSMC code from the University of Michigan with published results [41] including a comparison of the simple and the scattering-based model. Background is an experiment conducted at the University of California in Los Angeles (UCLA) [120], in which an ion beam was injected into a test cell filled with neutral gas, as depicted in Fig. 4.14.

The volume within the inner cylinder, closed by a front and exit plate was used as computational domain. The currents onto the solid surface were experimentally measured and served as comparison values for the simulations. The full 3D domain was spatially discretized with curvilinear boundaries represented by polynomials of $N_{geo} = 2$ and cell sizes of approximately 1 mm in both axial and radial direction, as shown in Fig. 4.15. A case with unbiased voltages (i.e., all walls are at $\Phi = 0\,\mathrm{V}$ and orifices with zero normal gradient) and low neutral gas pressure was chosen as simulation point ("unbiased DSA" [41] with $p_{neutral} = 1.21 \cdot 10^{-4}\,\mathrm{Torr}$). The background gas approach (see 2.7.3) was used, since the number density of the neutral gas ($n_{neutral} = 3.8948 \cdot 10^{18}\,\mathrm{m}^{-3}$, $T_{neutral} = 300\,\mathrm{K}$, $\langle v_{neutral}\rangle = 0\,\mathrm{m/s}$) is approximately seven orders of magnitude larger than for the inflow ion beam ($n_{ion} = 4.2177 \cdot 10^{11}\,\mathrm{m}^{-3}$, $\langle v_{ion}\rangle = 46923\,\mathrm{m/s}$). The simulation particles are deleted at all boundaries, corresponding to a recombination of ions to neutral gas which, however, is not further considered. Neutral gas and ions are Xenon with $m_{\mathrm{Xe}} = 2.18 \cdot 10^{-25}\,\mathrm{kg}$ and a weighting factor of $w = 1$. The collision cross section used for CEX and MEX interactions are defined by Eq. 3.35 with $A_{cex} = -27.2\,\text{Å}$,

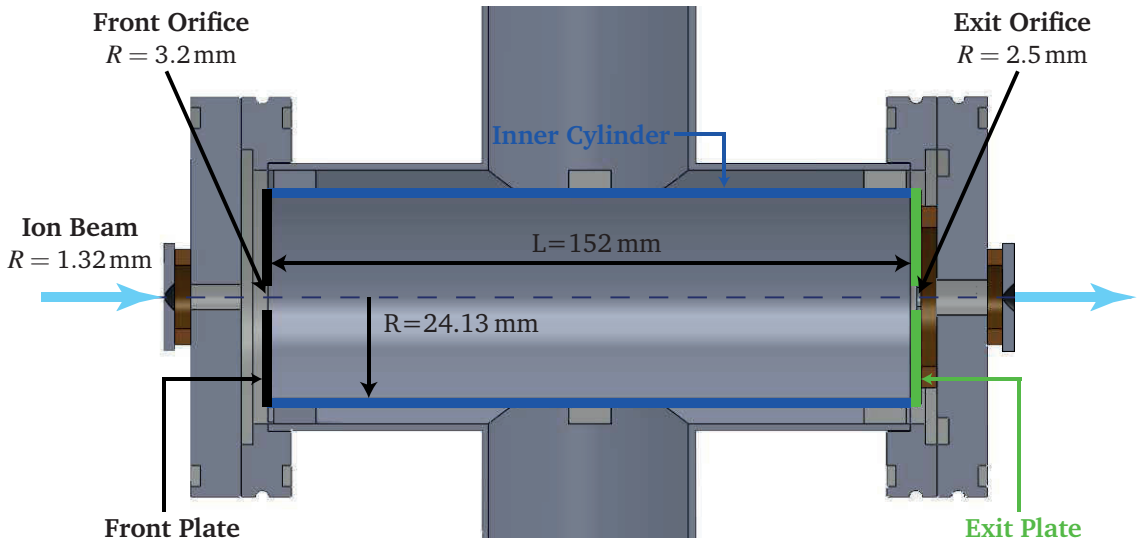

Figure 4.14: Schematic of test cell from experiment (based on [4, 41], courtesy of UCLA).

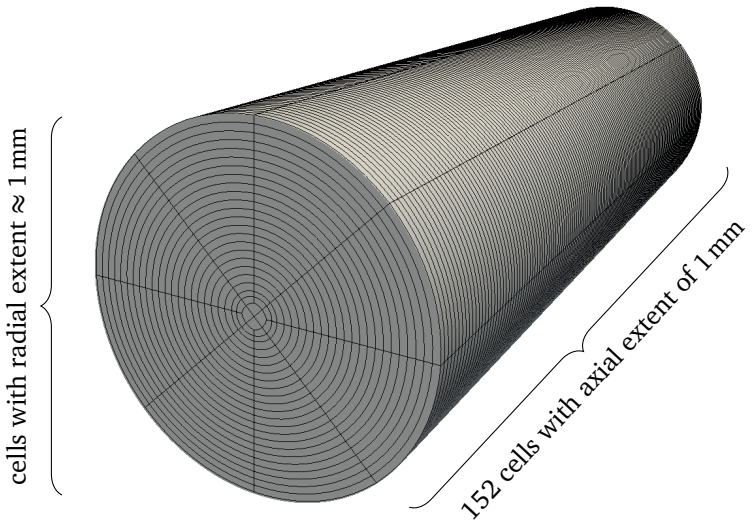

Figure 4.15: Computational mesh for verification study of neutral-ion collisions.

$B_{cex} = 175.269\,\text{Å}/\log_{10}(\text{m/s})$, $A_{el} = -26.8\,\text{Å}$, $B_{el} = 148.975\,\text{Å}/\log_{10}(\text{m/s})$, and $P_{cex} = 0.5$ [5]. For the lookup table of the scattering-based model, 200 samples for the impact parameter and 6000 for collision energy were used together with a minimum energy of $E_{min} = 30\,\text{eV}$ and maximum energy of $E_{max} = 3400\,\text{eV}$. The leapfrog scheme was used with a time step of $\Delta t = 2 \cdot 10^{-8}\,\text{s}$. Due to the high ion density in the axial center of the cylinder and the similar radial behavior of strongly decreasing ion density and azimuthally increasing cell extents,

the nearest interpolation point method was used for deposition. The spatial discretization utilized field polynomials of degree $p = 4$, which was verified by a negligible relative deviation ($< 0.5\,\%$) of evaluated wall currents compared with simulations of smaller degree.

Table 4.3 includes the simulation results in terms of time-averaged currents I onto inner cylinder (IC) and exit plate (EP). A direct comparison of each model between *PICLas* and the code from the University of Michigan shows deviations of less than $10\,\%$, which is a good agreement considering the uncertainty of $\pm 5\,\%$ from the readout of the published diagrams and several undefined simulation parameters. Also the results with *PICLas* come to the conclusion that the simple model over-predicts the creation of ions with high-angle scattering impinging on the inner cylinder and that the non-isotropic model can reproduce experimental results more accurately.

Table 4.3: Comparisons between *PICLas* and code from the University of Michigan.

	PICLas		Comparison [41]		
	Simple model	Scattering-based model	Simple model	Scattering-based model	Experiment
I_{IC} [nA]	6.40	4.11	6.48	3.75	3.49
I_{EP} [nA]	0.77	0.77	0.72	0.78	1.30

5 Optic-/plume-simulations

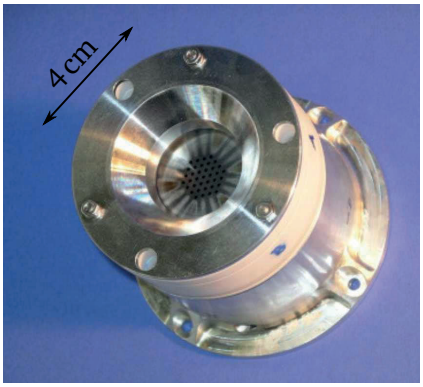

(a) Tested thruster assembly. [66]

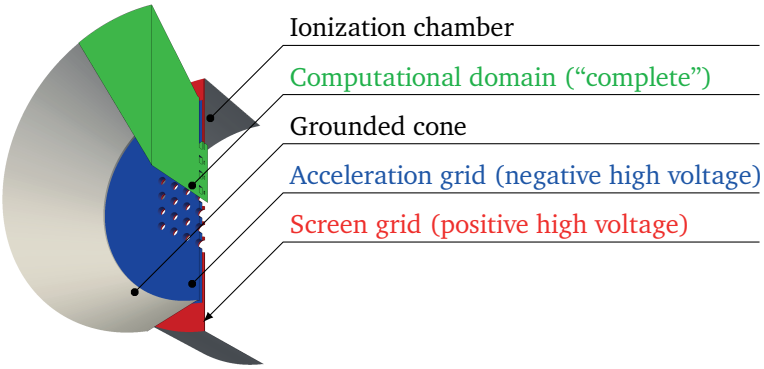

(b) Schematic of simulated ion thruster.

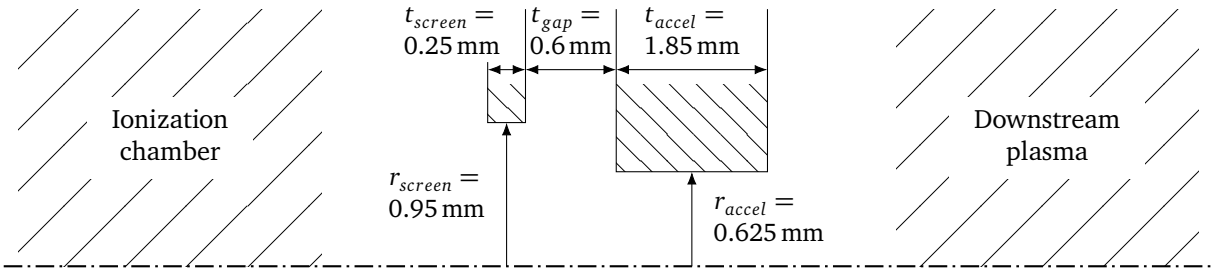

(c) Grid dimensions.

Figure 5.1: RIT-μX EBB.

Figure 5.1 depicts the considered RIT from this study, the RIT-μX EBB (elegant breadboard) of ArianeGroup GmbH [66]. Its discharge chamber of 40 mm diameter is closed by two grids with 37 apertures in a hexagonal pattern within a diameter of approximately 20 mm and a minimum distance of 2.4 mm between the aperture axes. In the experimental set-up, a diverging, grounded ring follows behind the grids. This thruster was chosen for the numerical simulations because the grid system is already a geometry of sufficient complexity so that its characteristics can be also transferred to larger thrusters. Furthermore, different types of measurement are available for that thruster which shall be reproduced by the numerical simulation as validation, i.e., to prove that the simulation results agree with reality. One type of measured values are currents onto the thruster grids, created by the flow of ions and electrons through the ion optics as it will be described in more detail in section 5.3. The comparison between simulation and experiments is twofold. On the one hand, validation

can be achieved and the assumptions of the simulation proven to be justified. On the other hand, once the numerical set-up is validated, it can give valuable insight into the physics and further simulations may even replace expensive tests and support the qualification process.

5.1 General simulation set-up

Two different domains were considered. One is the actual "complete" domain which starts in an undisturbed plasma state inside the discharge vessel, goes through the grid apertures and eventually expands along the attached ring of the thruster housing, as depicted in Figs. 5.1b and 5.2b. It is reduced by symmetry conditions to a 30° piece and the upstream section is restricted to distances from the apertures beyond which they do not influence the solution. The distance from inflow plane to the upstream edge of the screen grid ($x = 0$) is 1 mm and the further distance to the outflow plane is 17 mm. The other domain is the corresponding, effectively "infinite pattern" of apertures with symmetry conditions reducing the topology to two quarter apertures, as already utilized and described in section 4.4, but now with the same dimensions in x as the complete domain.

Fig. 5.2a depicts the surface meshes and nomenclature of the boundary conditions. For this visualization, parts of the frontal symmetry planes are cut away to show the hidden sides. The number of mesh cells for the complete and infinite pattern domain is 90758 and 5488, respectively. Linear mesh cells are used, because the approach based on a very coarse mesh with curvilinear elements (e.g., circles discretized by only 4 circumferential segments) is not applicable for the 30° domain. The hexahedral mesh topology[1] defines the minimum cell number and boundary approximation (32–48 linear segments per circle) which is assumed to already correspond to the actual manufacturing tolerance and, thus, a larger N_{geo} would not be of any benefit but increase the computational cost. If not otherwise stated, a polynomial degree of $p = 4$ was used for field solutions, i.e., each cell contains $5 \cdot 5 \cdot 5 = 125$ interpolation points. The deposition routine of PIC utilized the 4^{th}-order shape functions with $r_{SF} = 1.25 \cdot 10^{-4}$ m including all applicable boundary corrections. Table 5.1 summarizes the applied boundary conditions. The voltage between inflow and screen grid corresponds to the assumed plasma potential Φ_p, as described in section 2.4. Open BCs remove crossing particles from the simulation, for solid boundaries this assumes a recombination to neutral species, which are not considered afterwards. The upstream plasma density was iterated as inflow for each case so that the resulting total beam current matches the given I_{beam}. The considered operating points are summarized in Tab. 5.2.

[1] The pre-processing was conducted with the multiblock-structured mesh generator GridPro [98] and a subsequent conversion via HOPR [51].

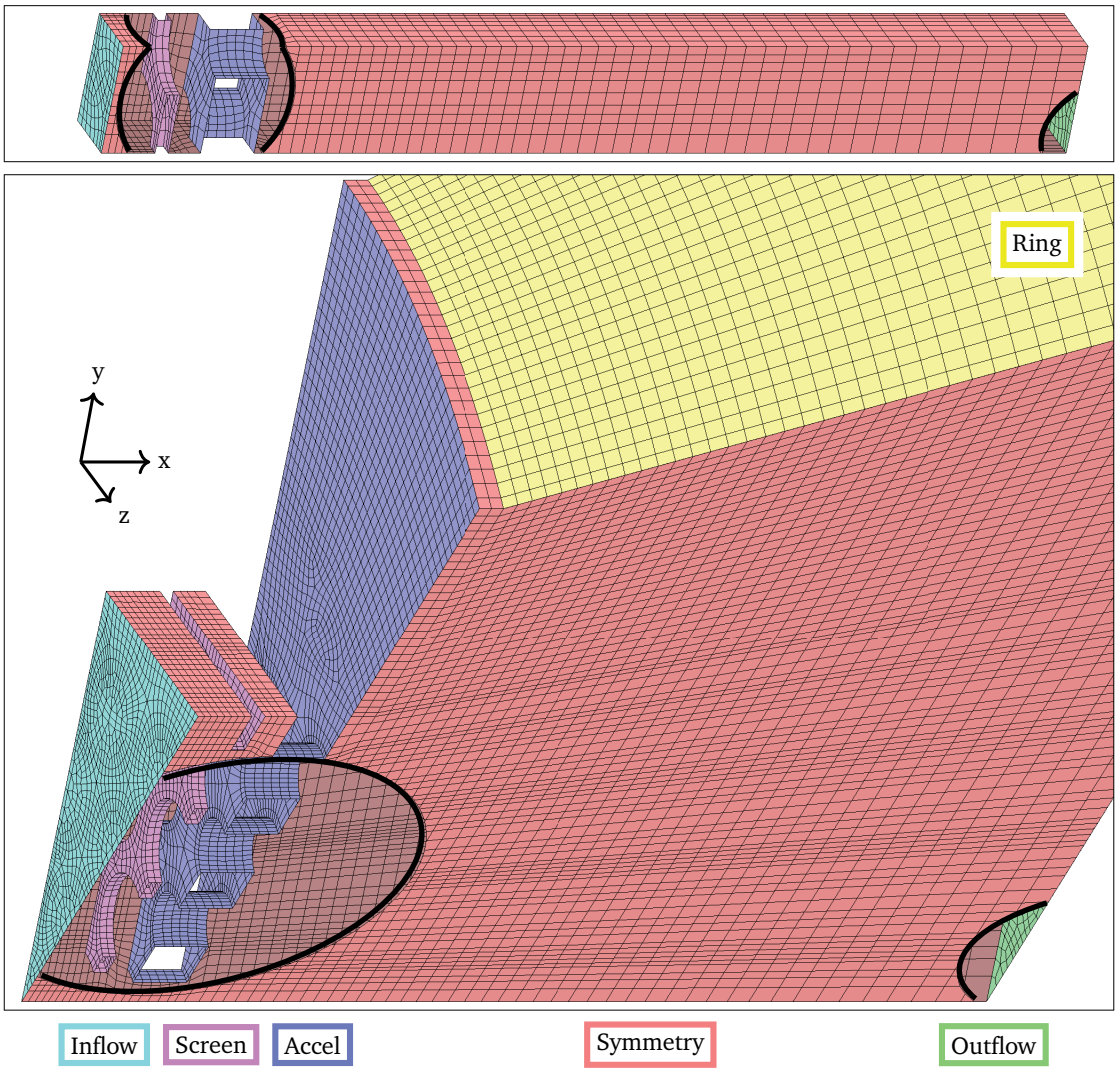

(a) Surface meshes and boundary conditions: “complete” (below) and “infinite pattern” (above).

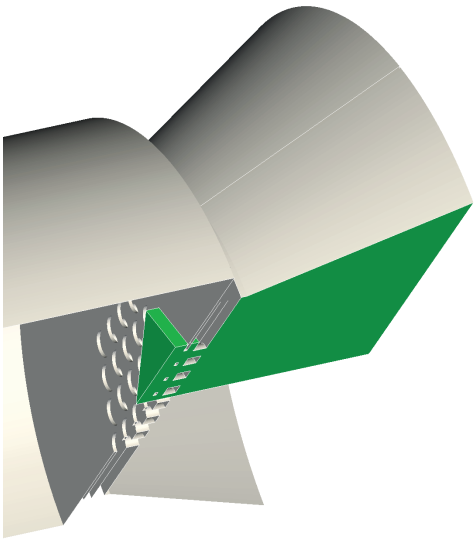

(b) Position of “complete” domain in thruster.

Figure 5.2: Utilized computational domains.

Table 5.1: Applied boundary conditions.

Name	Field-BC	Particle-BC
Inflow	$\Phi_{screen} + \Phi_p$	open, Xe^+ inflow
Screen grid	Φ_{screen}	open
Accel grid	Φ_{accel}	open
Symmetry	$\frac{\partial \Phi}{\partial \vec{n}} = 0$	reflective
Outflow (BR)	$\frac{\partial \Phi}{\partial \vec{n}} = 0$	open
Outflow (FK)	$\Phi_{out} = 0\,\mathrm{V}$	open, e^- inflow
Ring	$\Phi_{ring} = 0\,\mathrm{V}$	open

Table 5.2: Tested operating points.

I_{beam}	$\dot{N}_{Xe,in}\,[\mathrm{s}^{-1}]$	Φ_{screen}	Φ_{accel}
4 mA	$5.4106 \cdot 10^{16}$	1100 V	−250 V
5 mA	$5.4106 \cdot 10^{16}$	1300 V	−300 V
6 mA	$6.3124 \cdot 10^{16}$	1450 V	−300 V
7 mA	$7.6651 \cdot 10^{16}$	1550 V	−300 V
8 mA	$8.1160 \cdot 10^{16}$	1700 V	−300 V

Two individual electron populations exist in the domain, both physically separated by a potential well as result of the negative voltage of the acceleration grid. The axial position $x_{\Phi,min}$ of the minimum potential was estimated by preparatory simulations. Fluid electrons via the Boltzmann relation (BR) which correspond to the inflow were included for $x < x_{\Phi,min}$ and, if applicable, to the outflow for $x > x_{\Phi,min}$. For fully kinetic (FK) outflow-electrons, Φ_{out} is set to 0 V and includes an inflow of electrons as simulation particles.

5.2 Verification of applicability of the Boltzmann relation for electrons

Before dealing with the actual validation results, the applicability of simplifications serving as possible speed-up for the simulations is investigated. The most severe difficulties in the optic-/plume-simulations are, first, the different scales of heavy ions and very low mass electrons and, secondly, the relatively large geometries when considering more than a single beamlet. One possible solution for the first point is the utilization of electron fluid models such as the Boltzmann relation instead of the fully kinetic modeling of both ions and electrons. However, it must be assumed that the BR loses its applicability if the electrons are, for instance, part of a non-isothermal expansion or not even in thermodynamic equilibrium at all. This assumption is questionable in the downstream part of ion optics, i.e., inside the plume region. Fully kinetic ion optics simulations published in the past showed a significant deviation of electron densities in the neutralizing region of the beam compared to results assuming BR electrons, which the authors stated to be linked to non-Maxwellian velocity distributions of electrons [10]. These differences will be addressed by comparing FK with BR results considering both electron densities and velocity distribution functions. Another condition for a failure of the BR assumption is a non-negligible drift velocity of electrons. This occurs for sure when ion optics systems are operated near or beyond the electron back-streaming (EBS) limit, the critical failure mode for ion optics with the negative accel grid voltage becoming

too near to 0V. Here, an electron population with large drift velocity can pass across the associated minimum potential barrier. Therefore, the application of the following simulations consists of preliminary EBS investigations by using the PIC module of *PICLas*. Additional to the electron modeling, also the different simulation domains ("complete" vs. "infinite pattern") are compared. It should be noted that the presented results of this section were already published in the context of the IEPC 2017 [13].

5.2.1 Simulation set-up

For the following simulations, the operating point of $I_{beam} = 6\,\mathrm{mA}$ from Tab. 5.2 was chosen, together with a simulation particle weight of approximately 550. The essential simulation parameters are summarized in Tab. 5.3. Furthermore, a plasma potential of $\Phi_p = 15\,\mathrm{V}$ was assumed and the temporal integration utilized the 5-stage LSERK scheme. For infinite pattern simulations, the average ion density at the outflow plane was taken as reference, resulting in an electron number density of approximately $4.4 \cdot 10^{15}\,\mathrm{m}^{-3}$. For fully kinetic, complete thruster simulations, the value was determined adaptively, based on the averaged ion-densities inside the boundary-adjacent cells. By that, a quasi-neutral downstream-state is assumed and those electrons from the neutralizer travel upstream through the space charge of the beamlet until they are blocked by the negative voltage of the acceleration grid. To eliminate the (statistical) influence of kinetic electrons originating from the inflow BC on the solution, the upstream region of BR-electrons was also assumed for FK simulations, i.e., fully kinetic electrons are coming only from the outflow BC. This is justified by the already determined equality of BR- and kinetic electrons in the upstream region of ion optics simulations [10], but it was additionally verified by own simulations. FK simulations were continuations from BR simulations, since this allows to take an already fully expanded ion beam as initial condition and the time for reaching steady state is significantly decreased. Before the first time step of these continuation simulations, kinetic electrons were sampled in the downstream BR-region once, corresponding to the cell-average number density from Eq. 2.14 combined with a Maxwellian velocity distribution of the electron temperature.

Table 5.3: Simulation parameters.

Time-step	$\Delta t_{BR} = 5 \cdot 10^{-9}\,\mathrm{s}$, $\Delta t_{FK} = 5 \cdot 10^{-11}\,\mathrm{s}$
Velocity of inflow-Xe^+	$v_{Xe^+} = 2500\,\mathrm{m/s}$
Temperature of inflow-Xe^+	$T_{Xe^+} = 450\,\mathrm{K}$
Temperature of inflow-e^-	$T_{e^-}^{in} = 3.5\,\mathrm{eV}$
Temperature of outflow-e^-	$T_{e^-}^{out} = 2\,\mathrm{eV}$

5.2.2 Infinite aperture pattern

The following simulations utilize the “infinite pattern” domain and compare BR with FK. The chosen figure of merits are the spatial distributions of field values as well as the velocity distribution functions (VDF) of kinetic electrons. The value of Φ_{accel} was successively changed towards zero until significant EBS occurred which will be further described in 5.2.4. The shown results are for $\Phi_{accel} = -300\,\mathrm{V}$ as nominal operation and $-120\,\mathrm{V}$ as example for EBS.

Comparison of field values

Figure 5.3 depicts the line plots of electric potential and number densities along the axis through a beamlet. These field values are evaluations of the DG-polynomial on an equidistant visualization mesh and were averaged for several thousand time-steps during steady state for reducing the statistical noise, as already described in section 4.4. The number densities access

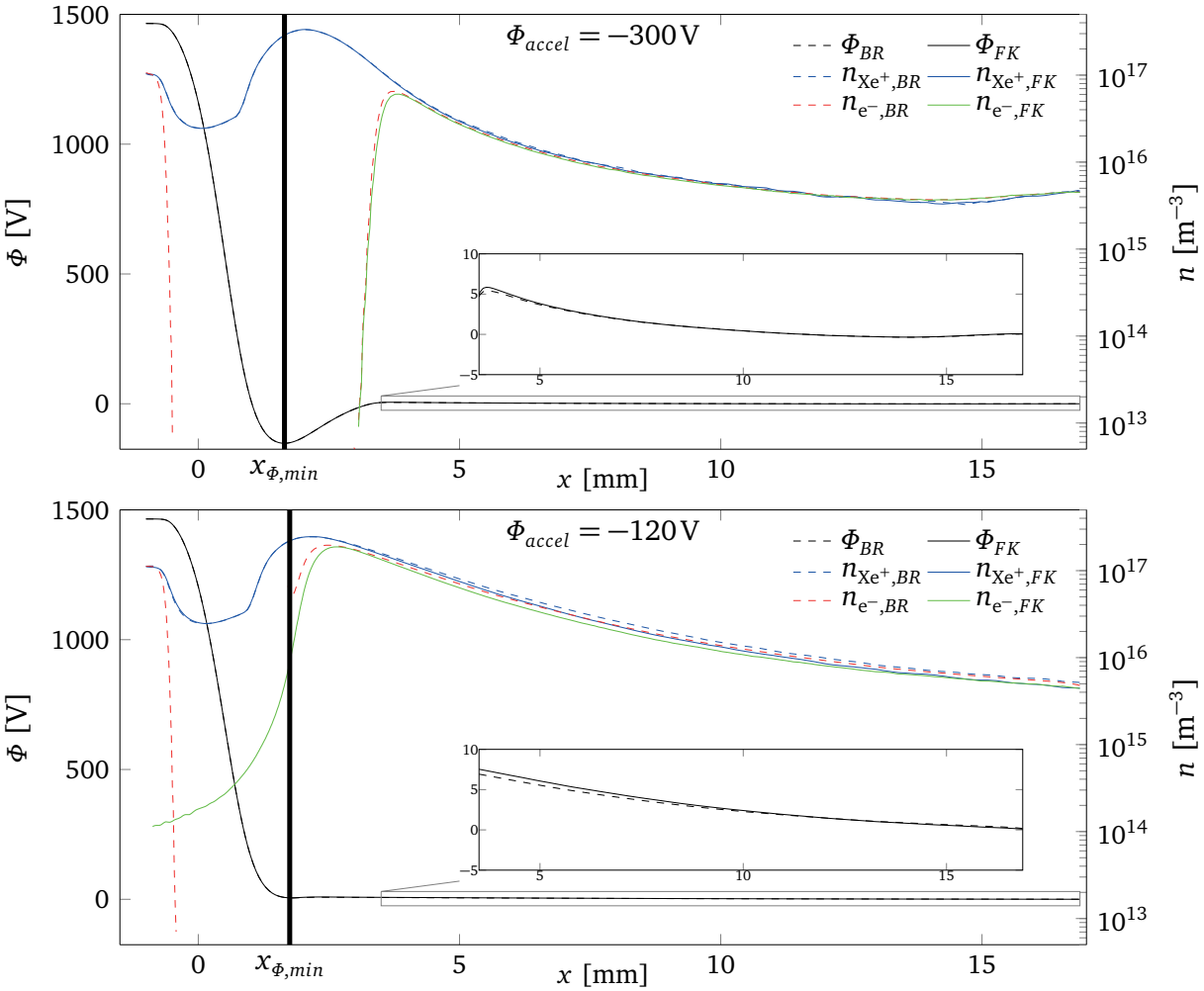

Figure 5.3: Axis plots through beamlets (infinite pattern).

the source term of the field solver. Basically, the curves of the potential Φ (black), ion number density n_{Xe^+} (blue), and electron number density n_{e^-} (green and downstream part of the red line) need to be compared. It can be seen that the FK simulations (solid lines) match the BR ones (dashed lines) well. For less negative Φ_{accel} the deviation increases, but it remains small. This deviation is strongly linked to the state at $x_{\Phi,min}$: If the corresponding potential is significantly lower than at the outflow plane (i.e., $\ll 0\,\mathrm{V}$), the density of BR electrons drops towards zero, as it is also the case for kinetic electrons. In this case, the increasing potential in upstream direction at $x < x_{\Phi,min}$ is insignificant, since no electrons pass the barrier, which motivates the described assumption of confined BR regions. Otherwise, the BR would predict a likewise increasing n_{e^-}. For a voltage at the EBS limit, however, electrons pass the barrier (see $\Phi_{accel} = -120\,\mathrm{V}$ in Fig. 5.3) and the electron density does not increase in FK simulations, since they are strongly accelerated towards the upstream direction so that the electron drift velocity cannot be neglected anymore. Here, the simulated number density of electrons deviates approximately with one order of magnitude at $x_{\Phi,min}$ when comparing FK and BR.

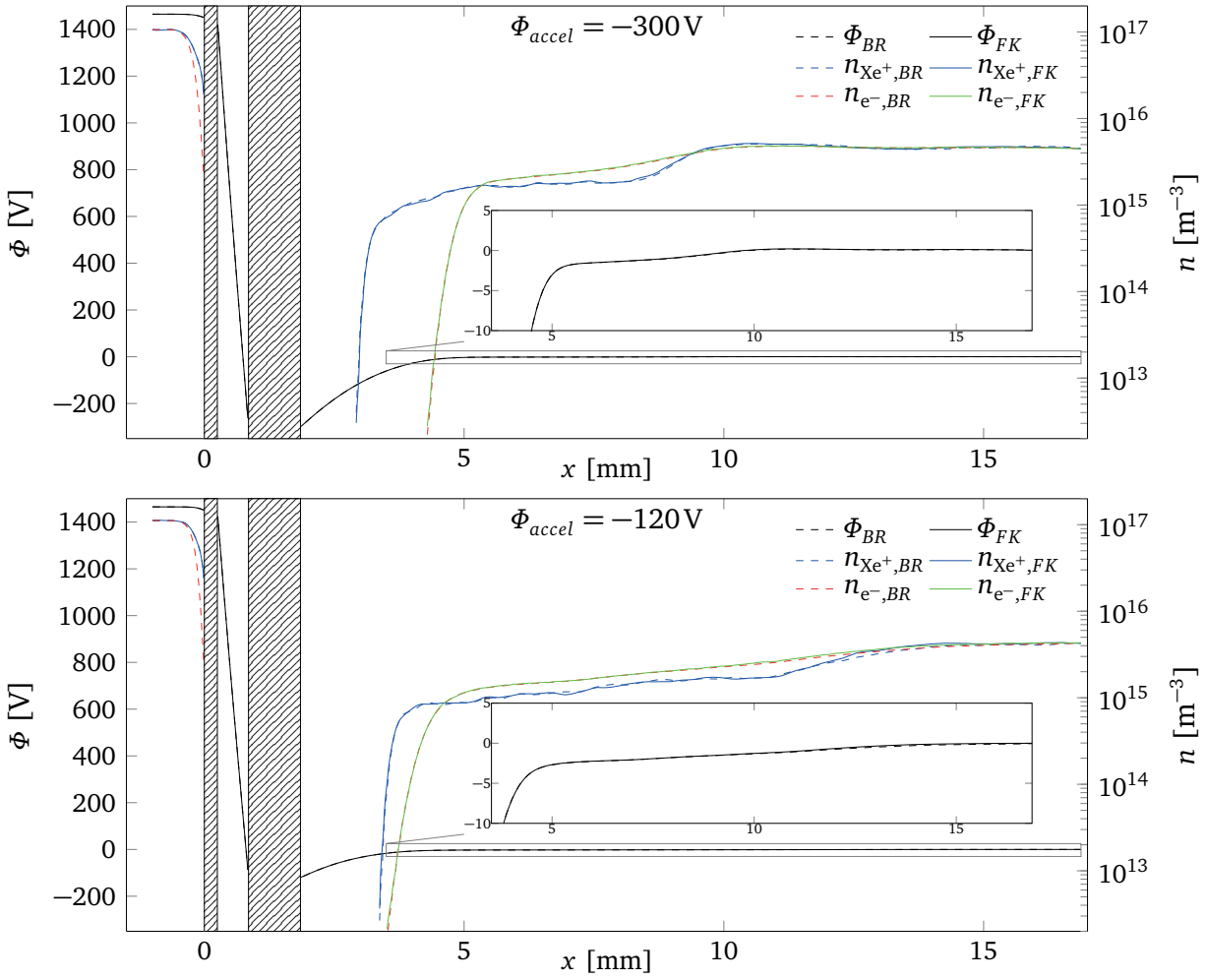

Figure 5.4: Center plots between beamlets (infinite pattern).

Figure 5.4 shows the lines equidistantly between the beamlets, intersecting the screen and accel grid (which are depicted by the shaded areas). The potential is always monotonically decreasing towards the accel grid, which shields the electrons and makes the deviations between FK and BR insignificant.

Evaluation of electron velocity distribution functions

Once steady state was reached, individual electron velocities inside defined volumes were saved for evaluating the VDF. For checking spatial homogeneity, the resulting histograms are shown for the three different reference volumes x_{min}, x_{max}, and y_{min}, illustrated in Fig. 5.5. Particle velocities are saved only every $l_{min}/(v_{min}\Delta t)$ time steps to ensure that the smallest electron velocity v_{min} has already crossed the minimum length l_{min} of the sampling volume.

Figures 5.6–5.8 depict the VDF at positions with decreasing x, together with the Maxwellian VDF of the specified $T_{e^-}^{out}$ and marker colors corresponding to the reference volumes. Figure 5.6 shows the distributions at $x = 15\,\text{mm}$ close to the boundary with kinetic inflow electrons ("Outflow" in Fig. 5.2a). It can be seen that the electron temperature of $T_{e^-}^{out} = 2\,\text{eV}$ is sustained for both grid voltages. The spatial homogeneity for the histograms is proven because all three colors describe the same curve. Also for the further upstream position at $x = 5\,\text{mm}$ in Fig. 5.7, the temperatures deviate only slightly from 2 eV. Between the beamlets, the electrons are in perfect equilibrium and isothermal, which is also in accordance with the matching results of FK and BR for the field values. The higher statistical noise results from the smaller sample size due to the decreased number density. Figure 5.8 depicts the VDF at and upstream of $x_{\Phi,min}$ where significant electrons exist only for $\Phi_{accel} > -130\,\text{V}$ and, thus, only the results for $-120\,\text{V}$ are shown. The histograms of the y_{min}-volume are excluded because the sample volume includes the entire radial extent. The electrons are in thermal equilibrium for v_y. In axial direction, however, the subsequent strong acceleration is visible.

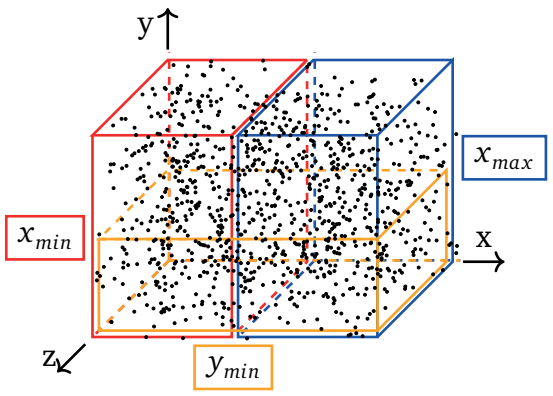

Figure 5.5: Sample volumes for histograms.

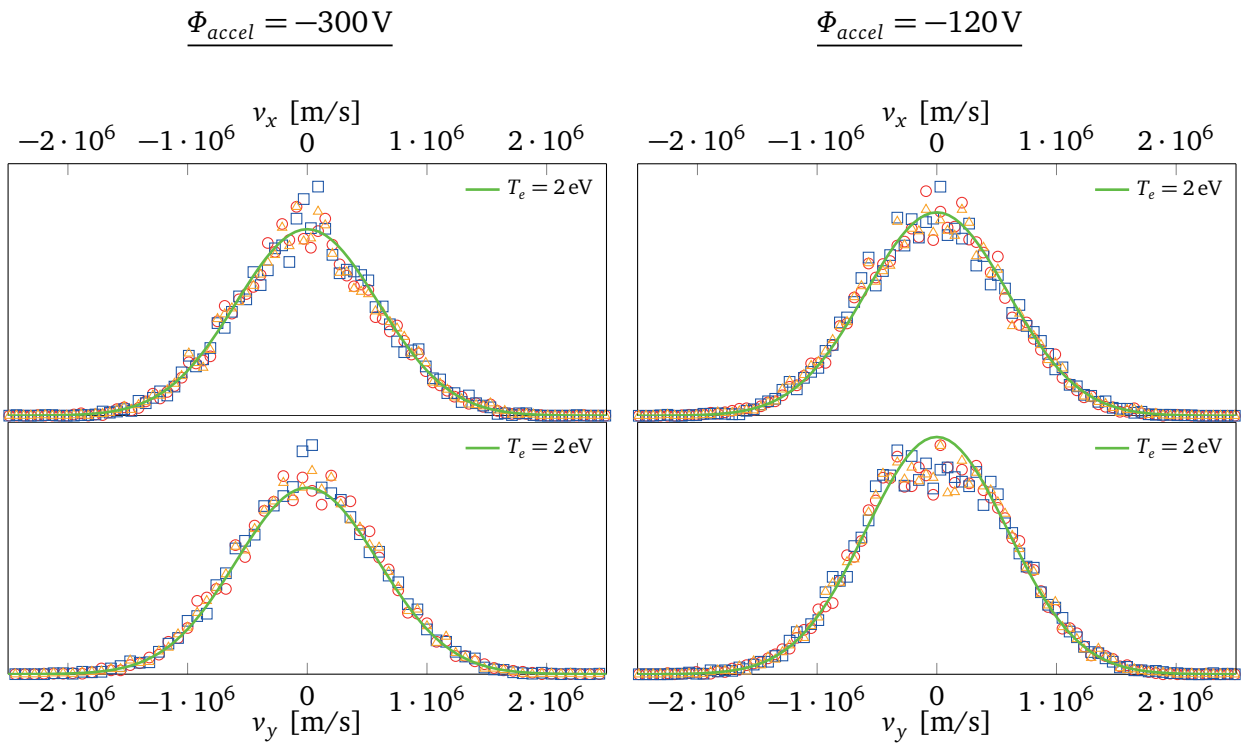

(a) In beamlet axis.

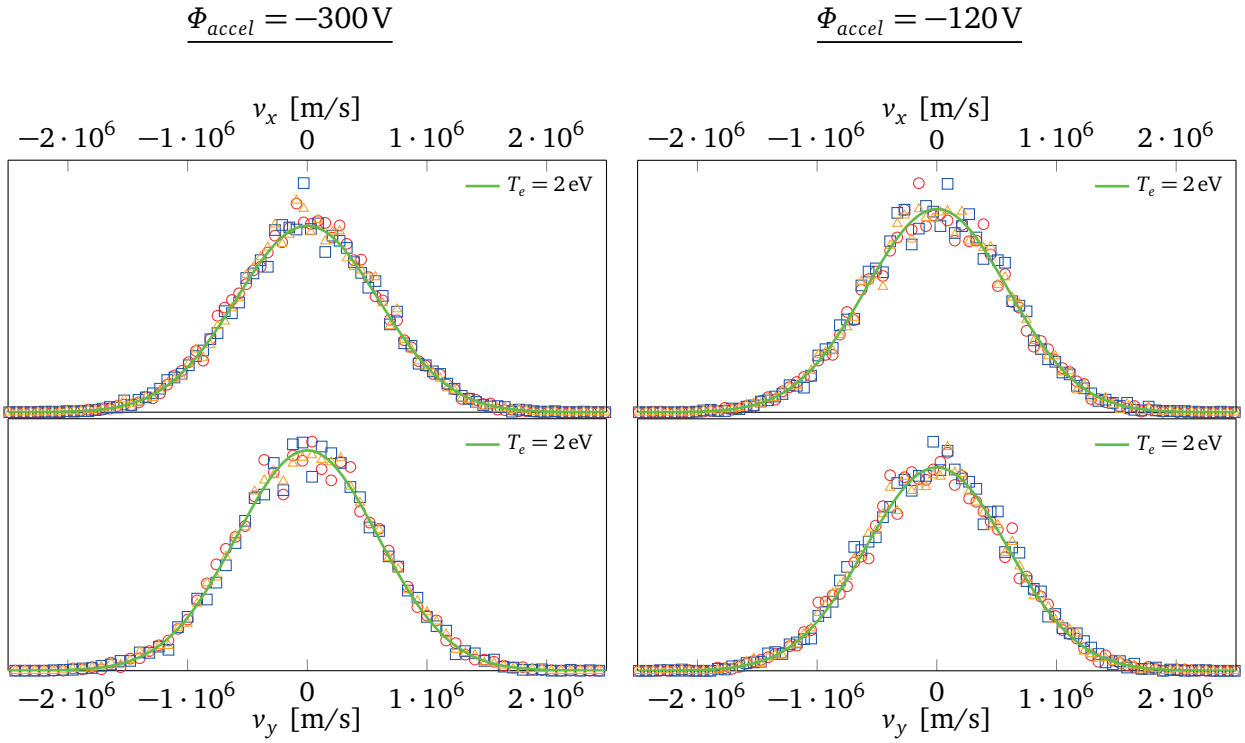

(b) Between beamlets.

Figure 5.6: VDF at $x = 15\,\mathrm{mm}$ (infinite pattern).

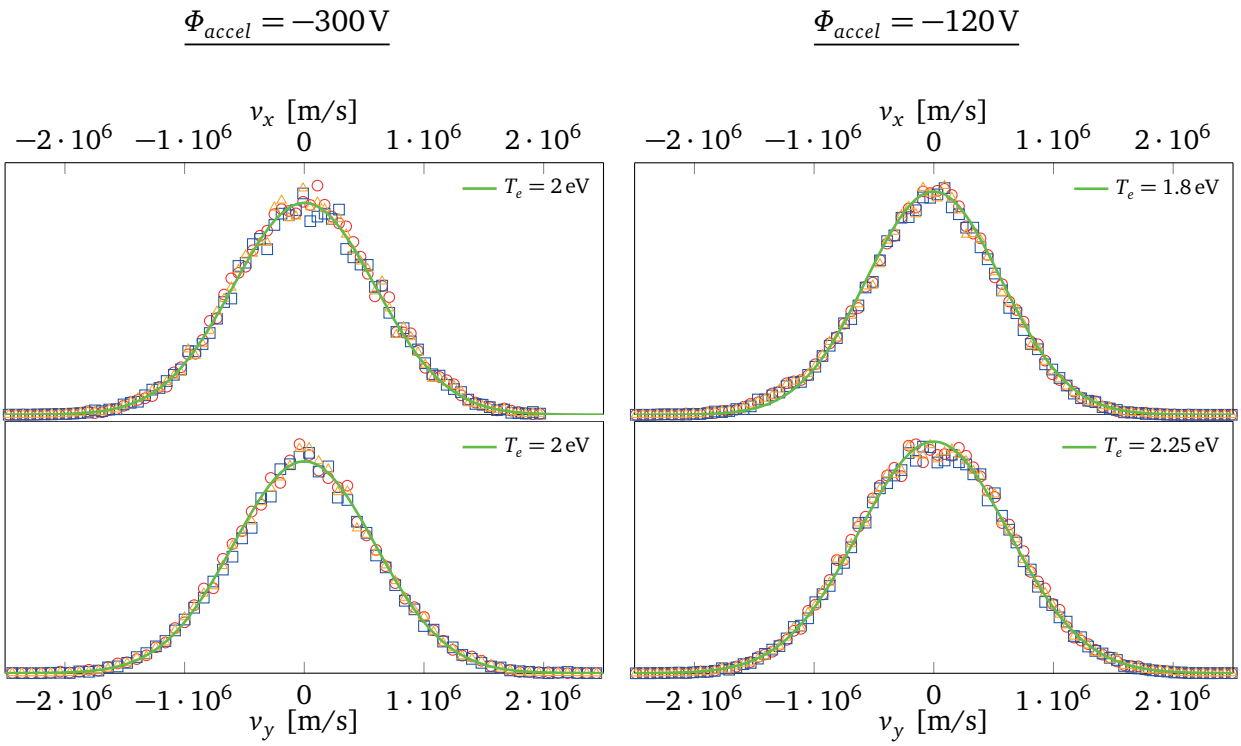

(a) In beamlet axis.

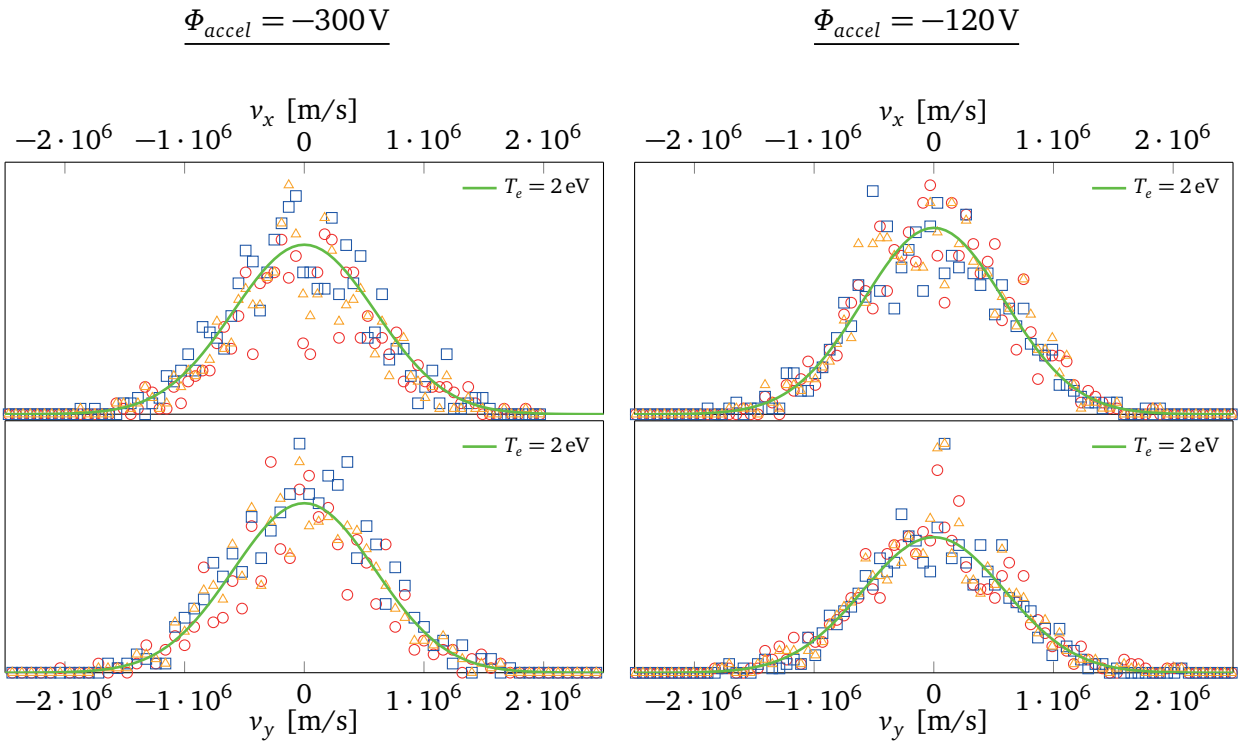

(b) Between beamlets.

Figure 5.7: VDF at $x = 5\,\mathrm{mm}$ (infinite pattern).

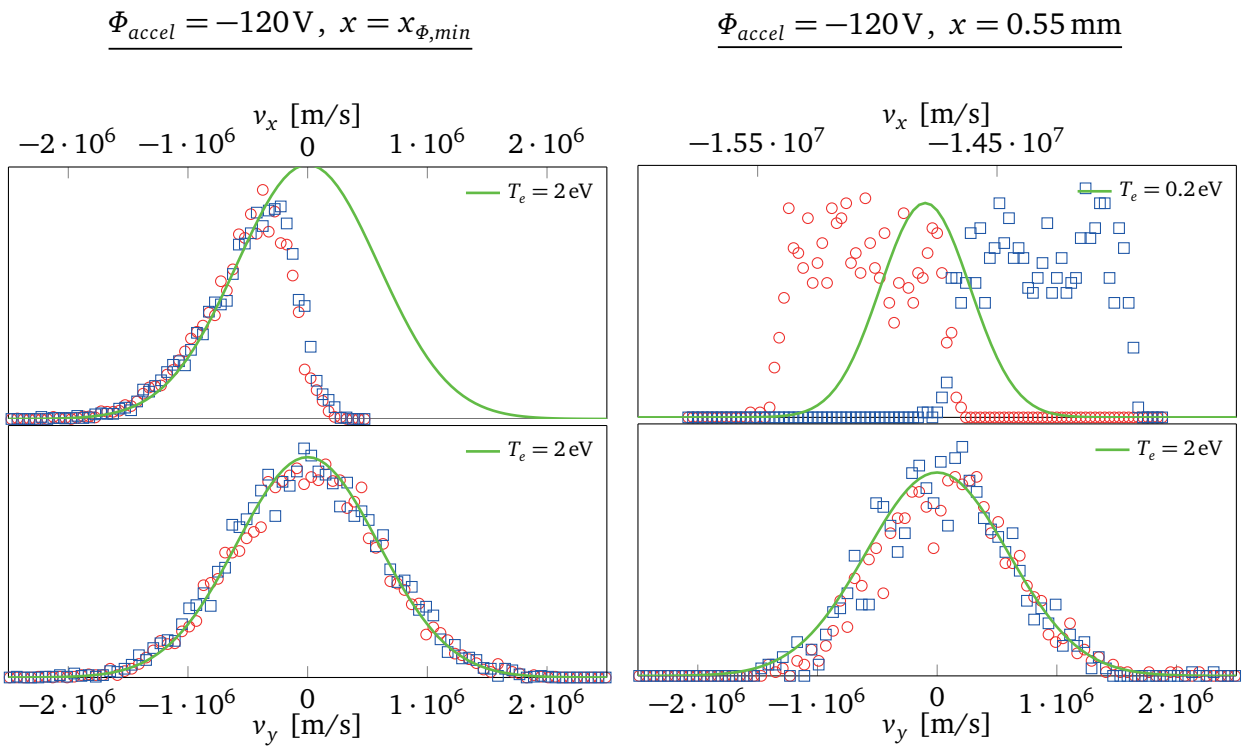

Figure 5.8: VDF in beamlet axis at/upstream of potential minimum (infinite pattern).

At $x_{\Phi,min}$ (plots on the left), electrons pass upstream but are further accelerated so that none oscillate back. Additionally, the number of electrons with less negative velocities is reduced which leads to a larger directed mean velocity into upstream direction. Further upstream at $x = 0.55\,\mathrm{mm}$, the strong potential gradient between the grids creates v_x of more than $1\cdot10^7\,\mathrm{m/s}$ into negative direction. The ongoing acceleration explains the spatial inhomogeneity in x that also broadens the depicted VDFs.

Strong non-Maxwellian velocity distributions of electrons [10] could not be identified for any final simulation result. Similar characteristics were observed only for non-steady, transient states, as well as for even less negative Φ_{accel} values of $-100\,\mathrm{V}$ and higher (not shown). The latter case, however, was found to be associated rather with limitations of the boundary conditions instead of a real physical background: Relative strong potential gradients between the beamlets form very near the outflow BC through which the neutralizing electrons are inserted. By the resulting force onto the inflow electrons, they are not able to create the local equilibrium state and, thus, they cannot be expected to follow the BR predictions.

In summary, the results for Φ and n agree well between FK and BR simulations and also the VDF corresponds at most positions to thermal equilibrium. The largest differences exist inside a beamlet at $x \leq x_{\Phi,min}$.

5.2.3 Complete domain

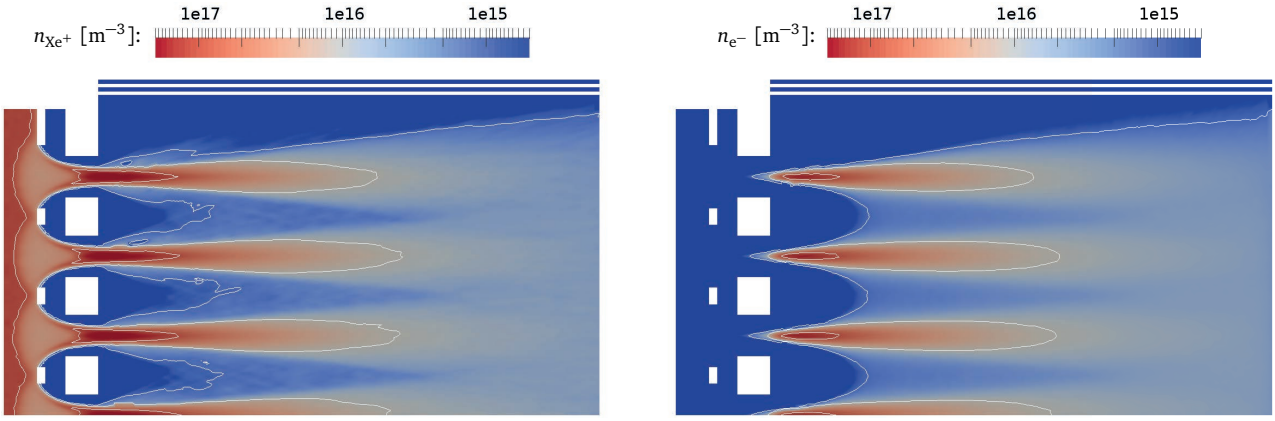

Figure 5.9: Number densities in symmetry plane of complete domain ($\Phi_{accel} = -120\,\mathrm{V}$).

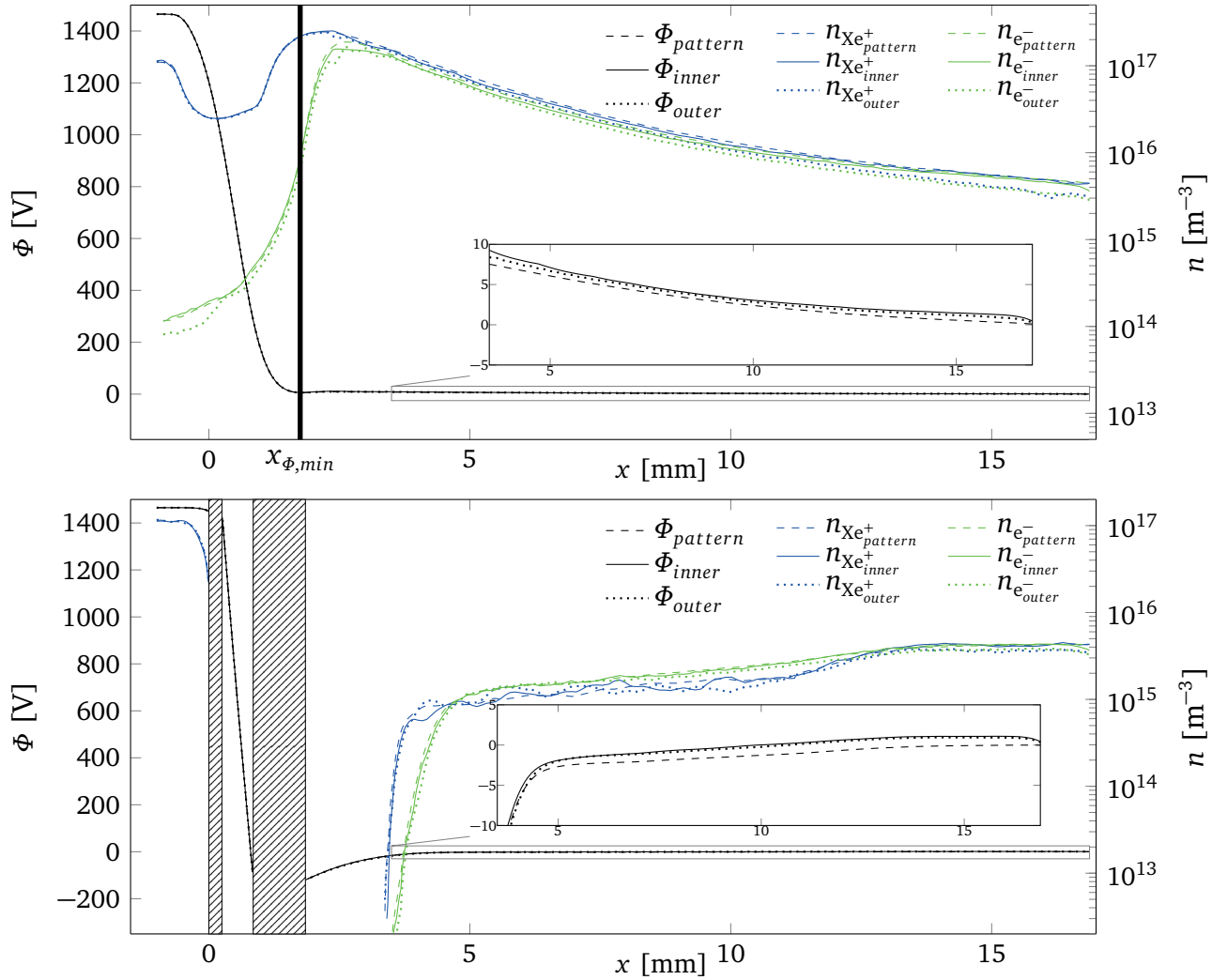

Figure 5.10: Comparison of inner/outer beamlets in complete domain with infinite pattern (above: along beamlet axis, below: centerlines between beamlets, both for $\Phi_{accel} = -120\,\mathrm{V}$).

The "complete" domain was simulated with fully kinetic electrons for $\Phi_{accel} = -120\text{V}$. Figure 5.9 depicts a contour plot of ion (left) and electron (right) number densities within a plane as part of the frontal symmetry plane in Fig. 5.2a. It can be seen that the individual beamlets are nearly identical. Only the most outer one deviates slightly, probably because it is influenced by the electrostatic forces from the positively charged inner plume region and the low voltage of ring and outer acceleration grid. The different locations are also compared between each other in Fig. 5.10, together with the results from the corresponding infinite pattern. The lines along an inner and outer beamlet axis are included in the figure above, whereas the inner and outer centerline between beamlets are shown below. It can be seen that the deviations are very small indeed. Please note that the averaging time for the complete thruster simulation was much shorter than for infinite pattern simulations which results in increased statistical noise.

5.2.4 Preliminary, quantitative EBS evaluation and conclusion

Having both FK and BR simulations, the actual back-streaming electron current can be calculated by two methods. First, for FK electrons, the particles crossing the upstream BC simply have to be counted. Secondly, for BR electrons, the thermal flux at $x = x_{\Phi,min}$ needs to be integrated [121]. The resulting values are summarized in Tab. 5.4, scaled with the beam current. It can be seen that BR and FK simulations agree very well also for these results. Since the flux is proportional to number density and directed mean velocity, the observed lower number densities at $x_{\Phi,min}$ for FK cases (see Fig. 5.3) are exactly compensated by the more negative mean velocity. This also agrees with the described VDF (see Fig. 5.8). With respect to the comparison between simulations of infinite pattern and full thruster, Tab. 5.4 shows that the difference is very small as well. Additionally, it was found that the maximum deviation in electron current between the individual beamlets of the thruster is around 20 %, slightly decreasing outwards.

The current density inside the discharge plasma of a RIT is relatively constant [71] and guarantees very similar beamlets along the radial extent of the grid system. Additional simulations

Table 5.4: Simulated EBS currents ratios.

Φ_{accel}	-300V	-150V	-140V	-130V	-120V	-100V
$I_{EBS,BR}^{inf.pattern}/I_{beam}$	$1.01\cdot10^{-35}$	$1.40\cdot10^{-6}$	$9.25\cdot10^{-5}$	$4.95\cdot10^{-3}$	$9.54\cdot10^{-2}$	$6.45\cdot10^{-1}$
$I_{EBS,FK}^{inf.pattern}/I_{beam}$	-	-	$6\cdot10^{-5}$	$4.0\cdot10^{-3}$	$9.7\cdot10^{-2}$	$6.82\cdot10^{-1}$
$I_{EBS,FK}^{thruster}/I_{beam}$	-	-	-	-	$9.5\cdot10^{-2}$	-

showed, however, that in contrast to the beamlet characteristics the resulting EBS current I_{EBS} is highly dependent on the individual plasma parameters such as electron temperatures and ion velocities at the inflow. Thus, I_{EBS} depends on the actual radial position with plasma parameters resulting from the discharge process inside the chamber. Since a corresponding coupling approach is beyond the scope of this study, only preliminary simulations with constant plasma parameters were conducted, which however were not applicable for verification purposes. Nevertheless, it can be already concluded that the results of BR and FK simulations agree very well. Even for cases at the EBS threshold, both field values and electrons VDFs show good agreement. Only near and upstream of the minimum potential deviations occur, but the evaluated values of EBS current are very similar again. The following points can be concluded, provided that a quasi-neutral downstream-state is assumed:

1. For operating points far from EBS, the Boltzmann relation is justified without limitation;
2. For a quantitative EBS evaluation with the same homogeneous inflow condition for all beamlets, BR simulations of an infinite pattern domain are a very good approximation.

5.3 Validation by grid current simulations

This section deals with the grid current validation, as is was also partly presented in the context of the RGD 2018 [12]. In the previous section it was shown that the BR is sufficient as electron fluid model. That enables extensive parameter studies in terms of comparing different numerical models and analyzing the dependence on undefined plasma parameters.

Background are the measured currents (i.e., flows of charged particles) onto the grids during thruster operation. Figure 5.11 illustrates flow balance in an ion optic with the assumption of time-averaged, steady state. The flow of neutral gas into the chamber $\dot{N}_{Xe,in}$ is divided into an unionized flow $\dot{N}_{Xe}$ and an ionized flow $\dot{N}_{e^-} = \dot{N}_{Xe^+}$. The latter leaves, as one part, the chamber through the apertures and, as other part, impinges on the first grid (screen)

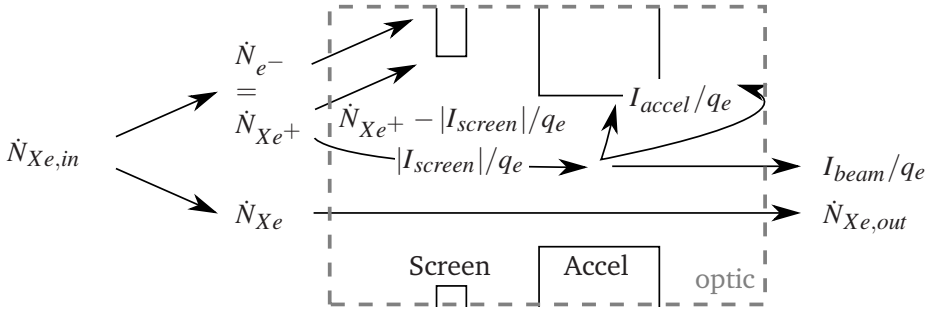

Figure 5.11: Flow balance at extraction grids.

where electrons and ions are absorbed or recombined. The electrons are repelled from the aperture region by the low "accel" potential that extends into the upstream plasma sheath of the screen grid. Thus, only ions leave the chamber through the apertures besides $\dot{N}_{Xe}$. The current onto the screen grid I_{screen} corresponds to the difference of impinging electrons and ions, whereby the ion flow $\dot{N}^{imp.}_{Xe^+}$ onto the grid is defined by Eq. 5.1.

$$\frac{|I_{screen}|}{q_e} = \dot{N}_{e^-} - \dot{N}^{imp.}_{Xe^+}, \quad \dot{N}_{e^-} = \dot{N}_{Xe^+} \quad \Rightarrow \quad \dot{N}^{imp.}_{Xe^+} = \dot{N}_{Xe^+} - \frac{|I_{screen}|}{q_e} \tag{5.1}$$

$$I_{beam} = |I_{screen}| - I_{accel}, \quad \dot{N}_{Xe,out} = \dot{N}_{Xe,in} - I_{beam}/q_e \tag{5.2}$$

This results in an ion flow through the screen apertures equal to the net current onto screen grid $|I_{screen}|/q_e$, which in turn is further reduced by I_{accel} onto the acceleration grid. The resulting I_{beam} of ions and $\dot{N}_{Xe,out}$ of neutral gas from Eq. 5.2 leave the thruster. For given conditions (I_{beam} and $\dot{N}_{Xe,in}$ together with ϕ_{screen} and ϕ_{accel}), the goal of the validation approach is to reproduce the corresponding I_{accel}, which is caused in normal operation mostly by the effect of scattered ions due to neutral gas interaction (see section 3.6) and requires to consider the complete ion optics with their unique neighborhood relations of the individual beamlets.

5.3.1 Simulation set-up

For the considered simulations, number densities of neutral gas and ions differ by more than approximately two orders of magnitude. This fact justifies to assume the neutral gas distribution to be independent from the ions. Hence, the background gas approach (see 2.7.3) was used for the following simulations. The total simulation approach of the ion optics can be divided into the following three steps:

1. The neutrals gas distribution corresponding to $\dot{N}_{Xe,out}$ is simulated separately by DSMC, only including neutral Xenon.
2. By PIC simulations of Xe^+ ions, the parameters (i.e., the number density of inflow ions) are iteratively determined so that the given I_{beam} value is reached.
3. In coupled PIC-DSMC simulations, the neutral collision partners are sampled from the DSMC results of step 1 for performing CEX and MEX interactions with the ions.

The only defined input values from the experiment were $\dot{N}_{Xe,in}$, Φ_{screen}, and Φ_{accel} for corresponding beam currents I_{beam} (see Tab. 5.2). All remaining parameters were calculated or varied as part of a sensitivity analysis, as shown in Tab. 5.5. Both the scattering-based and the simple model were used and compared with each other for CEX and MEX interaction, including the same parameters as in the verification study from section 4.5.

Table 5.5: Set-up of PIC(-DSMC) simulations.

Fix parameters:			
Time-step, time-accurate	$\Delta t_{O(2)}$	$=$	$2 \cdot 10^{-9}\,\mathrm{s}$
Time-step, under-relaxation	$\Delta t_{O(4)}$	$=$	$1 \cdot 10^{-8}\,\mathrm{s}$
Ion temperature, inflow	T_{Xe^+}	$=$	$450\,\mathrm{K}$
Varied parameters:			
Total ion beam current	I_{beam}	$=$	$4,5,6,7,8\,\mathrm{mA}$
Ion velocity, inflow	$v^{in}_{\mathrm{Xe}^+}$	$=$	$1.2 \cdot v_{Bohm}, 1.5 \cdot v_{Bohm}$
e^--temperature, inflow	$T^{in}_{e^-}$	$=$	$3.5\,\mathrm{eV}, 5\,\mathrm{eV}$
Neutralization potential	Φ_n	$=$	$0\,\mathrm{V}, 10\,\mathrm{V}$
Neutralization e^--temp.	$T^{n}_{e^-}$	$=$	$2\,\mathrm{eV}, 5\,\mathrm{eV}$
Chamber temperature	$T_{\mathrm{Xe}^{ch}}$	$=$	$300\,\mathrm{K}, 450\,\mathrm{K}$
Superposed BG pressure	p_{BG}	$=$	$0\,\mathrm{Pa}, 2 \cdot 10^{-4}\,\mathrm{Pa}$

In contrast to the previous sections, the plasma potential Φ_p with regard to Φ_{screen} was now calculated based on the common assumption of an equal wall flux of electrons and ions from the plasma sheath, which yields for the respective particle mass m:

$$|I^{wall}_{\mathrm{Xe}^+}| \stackrel{!}{=} |I^{wall}_{\mathrm{e}^-,BR}| \quad \Rightarrow \quad \Phi_p = -\frac{k_\mathrm{B} T^{[\mathrm{K}]}_{e^-}}{q_e} \ln\left(v^{in}_{\mathrm{Xe}^+} \sqrt{\frac{2\pi m_{e^-}}{k_\mathrm{B} T^{[\mathrm{K}]}_{e^-}}} \right) . \tag{5.3}$$

Furthermore, the inflow velocity $v^{in}_{\mathrm{Xe}^+}$ was considered as multiple of $v_{Bohm} = \sqrt{k_\mathrm{B} T^{[\mathrm{K}]}_{e^-} / m_{\mathrm{Xe}^+}}$. The temporal integration of particle trajectories was performed by the leapfrog-push for the time-accurate simulations, based on the results presented in 4.4.1. For the under-relaxation approach, however, the 5-stage, low-storage, explicit Runge-Kutta scheme of 4^{th} order was used because it showed to be more efficient, as will be shown in subsection 5.3.3. Time-accurate simulations utilized a weighting factor of $w_{PIC} = I_{beam} \cdot 100\,\mathrm{mA}^{-1}$, whereas the one for simulations with under-relaxation was 10 times larger. This resulted in simulated ion numbers of $\approx 5 \cdot 10^6$ and $\approx 5 \cdot 10^5$, respectively.

In the experiment, no dedicated neutralizer was used. Therefore, it is expected that the walls of the vacuum chamber acted as electron source, since otherwise the plume could not leave the thruster at all. With the Boltzmann relation as electron fluid, two unknowns need to be defined for the neutralizing electrons: their temperature $T^n_{e^-}$ and a reference point (see Eq. 2.14), such as $n_{e^-,ref}$ at $\Phi_{ref} = 0\,\mathrm{V}$, which can be interpreted based on the following reasoning. At sufficient distance downstream from the acceleration grid, a smooth,

radial flow state, i.e., without effects of the separate grid apertures, can be assumed. The Neumann condition $\frac{\partial \Phi}{\partial \vec{n}} = 0$ is applied at the particle outflow, which is justified at a sufficient distance from the grids, and also enforces the self-fields to be zero into normal direction. This results in local quasi-neutrality and neutralization potentials at the outflow, which ensure $n^{out}_{\mathrm{Xe}^+} = n^{out}_{\mathrm{e,BR}}$. In reality this describes the effect of the high potential inside the expanding ion beam attracting the electrons from the chamber walls which reduce the beam potential until the respective forces are canceled. Radially, the maximum outflow potential Φ_n is in the core of the plume where the number density, and thus the corresponding reference charge density, can be approximated by:

$$n^{out}_{\mathrm{Xe}^+} \approx \frac{I_{beam}/q_e}{37 A_{ap.,hex.} v^{out}_{\mathrm{Xe}^+}}, \quad v^{out}_{\mathrm{Xe}^+} \approx \sqrt{\frac{2q_e}{m_{\mathrm{Xe}^+}}(\Phi_{in} - \Phi_n) + \left(v^{in}_{\mathrm{Xe}^+}\right)^2}. \tag{5.4}$$

Here, $A_{ap.,hex.}$ is the area of the hexagonal region around a single aperture. The assumed value of Φ_n is now the unknown besides $T^n_{e^-}$ and can be interpreted as remaining maximum electric potential at the outflow BC due to the non-fully neutralized ion beam.

For the DSMC simulations of neutral gas ("step 1"), each I_{beam}-case had the neutral gas temperature $T_{\mathrm{Xe}^{ch}}$ as unknown, as result from the assumed inflow condition and full accommodation at all walls. A time step of $\Delta t_{DSMC} = 5 \cdot 10^{-8}\,\mathrm{s}$ and a particle weighting factor of $w_{DSMC} = 1 \cdot 10^6$ were used. The simulated Xenon atoms flow into the domain through the upstream BC without drift velocity and a number density corresponding to the particle flow of $\dot{N}_{Xe,out} = \dot{N}_{Xe,in} - I_{beam}/q_e$, as it will be described in the next subsection. To maintain the given value of $\dot{N}_{Xe,out}$, also the inflow boundary is set as fully diffuse wall which models the corresponding reflections at actually more upstream surfaces. Within the neutral species, the VHS model was assumed for collisions:

$$\sigma^{VHS}_{Xe} = \pi \left(5.74 \cdot 10^{-10}\,\mathrm{m}\right)^2 \left(\frac{273\,\mathrm{K}}{T}\right)^{0.35}. \tag{5.5}$$

Additionally, to prove that a so far neglected background pressure does not have any influence, it was considered for one case by increasing the number densities of neutral Xe in each cell by $p_{BG}/(k_\mathrm{B} T_{\mathrm{Xe}^{cell}})$, with p_{BG} as realistic pressure of the vacuum chamber. Furthermore, the results utilizing different domain sizes were compared with each other.

In the subsequent grid current simulations ("step 3"), the cell-mean values of the respective, steady DSMC solution, averaged over 100000 time steps, were used as n-, v-, T_x-, T_y-, and T_z-field for sampling the neutral collision partners in CEX and MEX interactions. To keep the assumed ideal plasma sheath as inflow condition in an undisturbed state, only ions with $v^{min}_{\mathrm{Xe}^+} > v^{screen}_{\mathrm{Xe}^+}$ were allowed for collisions, with $v^{screen}_{\mathrm{Xe}^+}$ as calculated maximum value at the

screen grid based on its potential and thermal ion velocity.

When coupling the collisions with PIC, steady state was shifted to a 10 times later physical time due to the slow Xe^{+}_{slow} ions within the plume (corresponding to I_{slow} in Eq. 3.37). By this, the computational effort of time-accurate PIC increased from around 1 h to 10 h on 2400 cores of a Cray XC40 and precluded any extensive parameter study. However, the under-relaxation approach described in section 3.7 enabled to delay the collision-independent (now unphysical) steady time towards the value of the scattered ions, but with much less intensive time steps and, thereby, a similar computational effort of around 1.5 h.

5.3.2 Neutral gas distribution

As described above, the distribution of neutral Xenon was simulated separately by DSMC. In reality, the full amount of gas ($\dot{N}_{Xe,in}$) is inserted through small orifices at the very upstream side of the ionization chamber which creates a reservoir state based on wall accommodation and balance of mass flows in steady state. The resulting neutral gas distribution is partly ionized. The creation of the ionized part is balanced by recombination at walls and the electrostatic extraction, but the remaining, non-ionized part ($\dot{N}_{Xe,out}$) leaves the chamber by thermal diffusion (i.e., speed ratio $a = 0$) through the grid system with an open area of the screen apertures of $A^{open}_{screen} = 37\pi r^2_{ap.,screen}$. The reservoir state is already created at positions very near the inflow orifices. Therefore, the orifices are not required to be simulated, but instead, any upstream cross section can be used as inflow. When the inflow section is located near the grid system, it is justified to assume that inside the considered domain no further ionization occurs and, thus, the neutral flow is already reduced to $\dot{N}_{Xe,out}$. However, the upstream boundary that imposes that flow into the domain cannot be placed arbitrarily near to the grids, since otherwise the local effects caused by the apertures are neglected. Therefore, the influence of different domain sizes was analyzed. In preparatory, preliminary simulations it was found that a distance from the first grid of $x_{in} = -5\,\text{mm}$ (instead of the $-1\,\text{mm}$ as used for the PIC simulations) is sufficient. Furthermore, the neutral gas domain should include the whole diameter of the chamber for the upstream region to ensure a realistic radial transition from the chamber wall towards the grid apertures.

Figure 5.12 depicts the resulting number density of neutral Xenon inside the described neutral gas domain for the case of $I_{beam} = 6\,\text{mA}$ and $T_{\text{Xe}^{ch}} = 450\,\text{K}$. The PIC domain boundaries are shown as green lines and, additionally, the "x-extended domain" is introduced, illustrated by the magenta lines. It can be seen how the reservoir state expands rapidly out of the chamber and that the individual parts from the grid apertures form a single, homogeneous neutral gas cloud already at short distance.

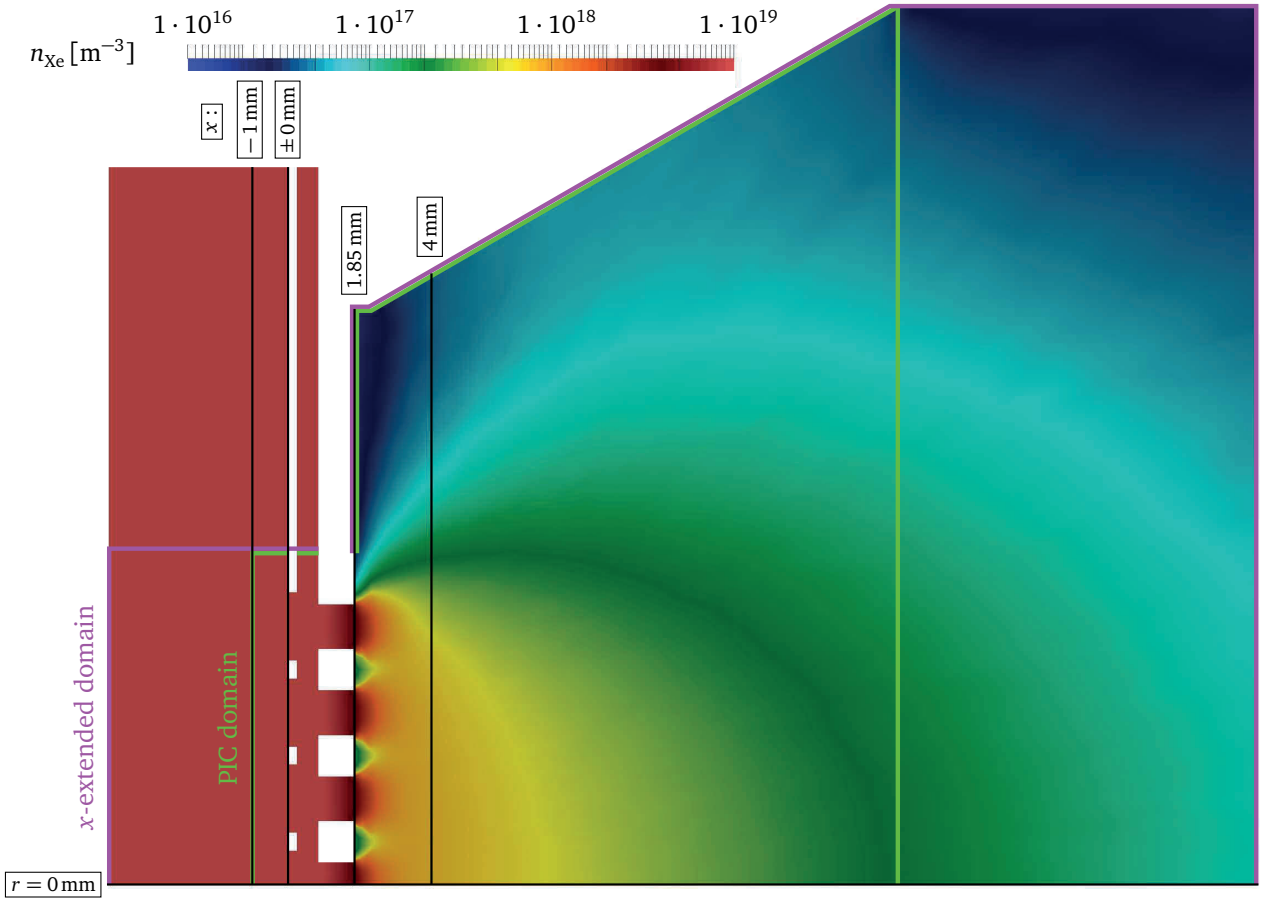

Figure 5.12: Xe number density in neutral gas domain ($I_{beam} = 6\,\text{mA}$, $T_{\text{Xe}^{ch}} = 450\,\text{K}$).

Together with the directed flux velocity $v_\Gamma^{a=0}$ (see subsection 3.3.1), the number density n_{ch} that is reached inside the chamber in steady state can be calculated by:

$$v_\Gamma^{a=0} = \sqrt{\frac{k_B T_{ch}}{2\pi m}} \quad , \qquad n_{ch} = \frac{\dot{N}_{Xe,out}}{v_\Gamma A_{screen}^{open} \Theta} = \sqrt{\frac{2\pi m}{k_B T_{ch}}} \frac{\dot{N}_{Xe,in} - I_{beam}/q_e}{A_{screen}^{open} \Theta}. \tag{5.6}$$

The factor Θ is the geometry-dependent transmission probability (also known as Clausing factor) [11] through the complete grid system. It is the ratio between the particle flow entering the entrance plane and the flow leaving through the exit plane directly at the grids. A particle can reach the exit (i.e., the plume region) directly from the entrance, or can be scattered along the walls before reaching the exit. However, a particle can also return back to the entrance (i.e., the ionization chamber). For the free molecular flow entering the ion optics without drift velocity ($a = 0$), the value of Θ is solely dependent on the grid geometry and species mass m, but not on the chamber temperature $T_{\text{Xe}^{ch}}$. Thus, Eq. 5.6 shows that the product $n_{ch}\sqrt{T_{\text{Xe}^{ch}}}$ is constant for one operating point defining $\dot{N}_{Xe,in}$ and I_{beam}.

Figure 5.12 includes 5 black lines, labeled with their corresponding position: Four at different

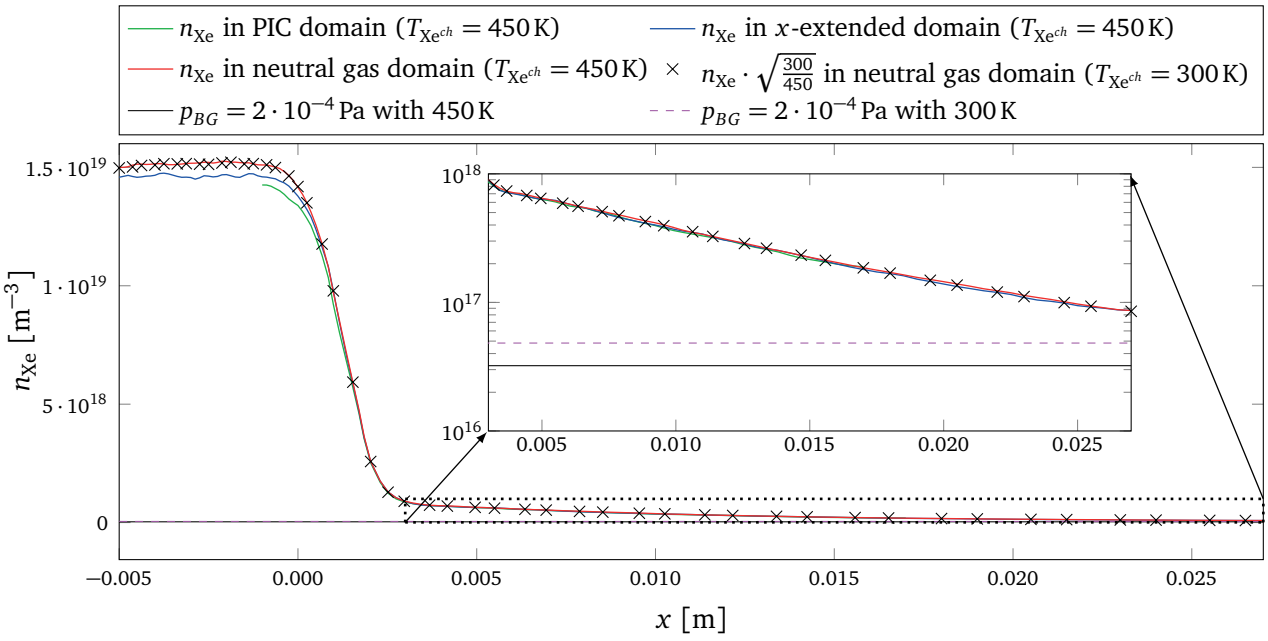

(a) Along center axis ($r = 0\,mm$).

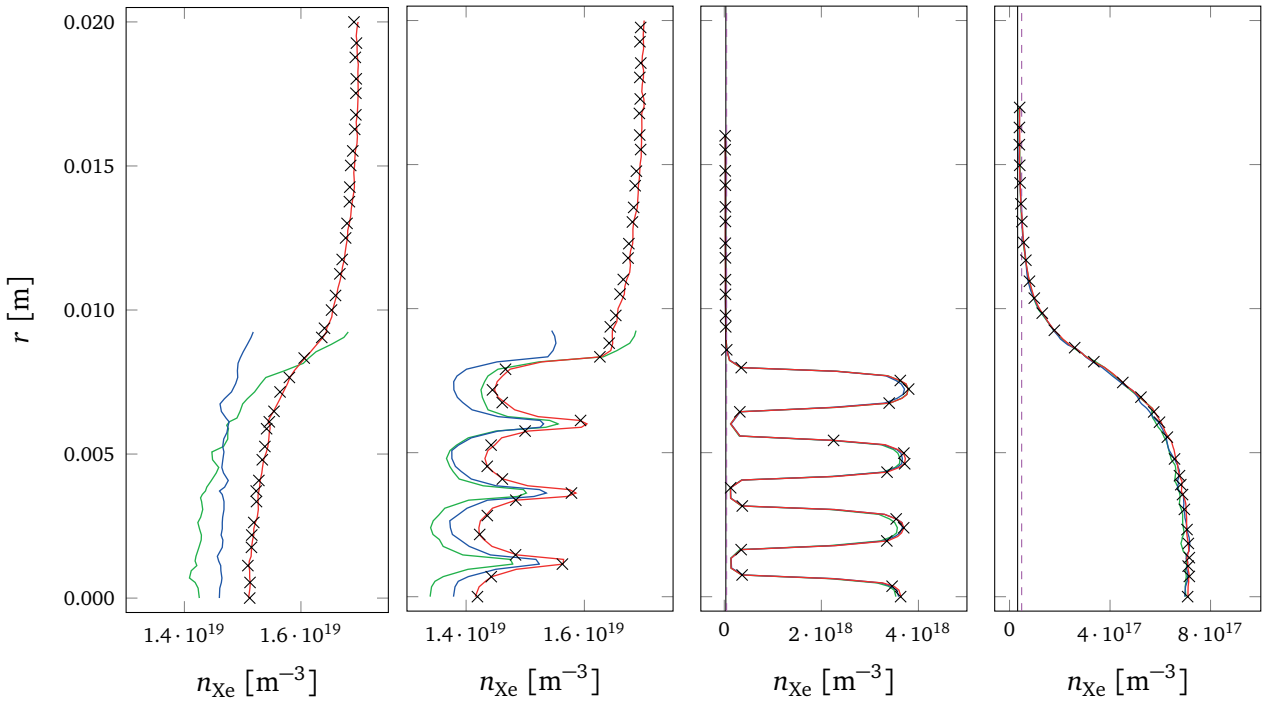

(b) $x = -1\,mm$. **(c)** $x = 0\,mm$. **(d)** $x = 1.85\,mm$. **(e)** $x = 4\,mm$.

Figure 5.13: Line plots of neutral number density ($I_{beam} = 6\,mA$).

x positions and one along the center axis ($r = \sqrt{y^2 + z^2} = 0\,mm$). The number density along those lines is depicted in Fig. 5.13 for all three domains. To prove the inverse proportionality of n_{ch} and $\sqrt{T_{Xe^{ch}}}$, also the line of $n\sqrt{\frac{300}{450}}$ is included as black crosses, with n as solution inside the neutral gas domain for $T_{Xe^{ch}} = 300\,K$. It can be seen that it matches the solution with

$T_{\mathrm{Xe}^{ch}} = 450\,\mathrm{K}$ (red lines) perfectly. When comparing the solutions by their computational domain, it is shown that the deviations are significant in the chamber region, but are negligible in the plume region. The higher statistical noise of the additional domain simulations is due to a reduced sample size. Furthermore, the number density for a background pressure of $p_{BG} = 2 \cdot 10^{-4}\,\mathrm{Pa}$ in the experimental vacuum chamber is shown for the two different temperatures, evaluated by $p = nk_{\mathrm{B}}T$ and yields $3.2191 \cdot 10^{16}\,\mathrm{m}^{-3}$ and $4.8286 \cdot 10^{16}\,\mathrm{m}^{-3}$, respectively. It can be seen that the number density of the effusing gas is much greater at most positions, at least one order of magnitude along the center axis.

5.3.3 Sensitivity analysis of simulation parameters

Similarly to section 4.4, an EOC was determined for both the polynomial degree p of the field solutions and the temporal discretization in terms of integration scheme and time step Δt. Now, however, the steady grid current I_{accel} that is averaged during the simulation is the value of most interest, since its comparison with the experiment serves as basis for the validation. For the EOC, the relative deviation $|I_{accel} - I_{accel}^{ref}|/I_{accel}^{ref}$ is used as approximate error value in reference to an accurate solution. For quantitative comparisons, also the statistical uncertainty of the determined I_{accel} is of particular importance. It was estimated by splitting the sampling duration $t_{end} - t_{steady}$ into 21 sub-intervals which are evaluated as averaged total value and the corresponding 2-σ standard error of the mean ${}^{2\sigma}\mathrm{SEM}(I_{accel})$ (see Eq. 4.8).

The result for different polynomial degrees p is shown in Fig. 5.14. An increased p can be interpreted as higher sub-cell resolution and, additionally, also the number of interpolation points inside a single deposition shape function is increased which reduces the associated error. The reference solution ($p = 6$) has a relative ${}^{2\sigma}\mathrm{SEM}(I_{accel})/I_{accel}$ of $\approx 0.45\,\%$, shown as horizontal black line. All relative deviations below this threshold can be seen as of equal quality, since the statistical noise prevents any further quantification, as also illustrated by the included error bars. It can be seen that already at $p = 3$, the relative deviation drops below the statistical uncertainty. Hence, $p = 4$ can be assumed to be of sufficient accuracy.

With p set to 4, Fig. 5.15 depicts the results for varied time steps. Both the leapfrog and the 5-stage LSERK scheme were investigated, shown as red and green line, respectively. The uncertainty of the two reference solutions ($\Delta t = 2 \cdot 10^{-10}\,\mathrm{s}$ for leapfrog and $\Delta t = 1 \cdot 10^{-9}\,\mathrm{s}$ for LSERK) is $\approx 0.4\,\%$ again. The EOC seems to be of first order for the considered time steps, as illustrated by the included fits. Considering that the LSERK scheme consists of $M = 5$ stages, it must be at least by a factor of 5 more accurate than the leapfrog scheme to be of any benefit. That applies, indeed, as also shown by the plots over average stage size $\Delta t/M$ in Fig. 5.15b. By choosing $\frac{\Delta t^{LSERK4-5}}{M} = \frac{1 \cdot 10^{-8}\,\mathrm{s}}{5} = 2 \cdot 10^{-9}\,\mathrm{s}$ instead of $\Delta t^{leapfrog} = 2 \cdot 10^{-9}\,\mathrm{s}$, the

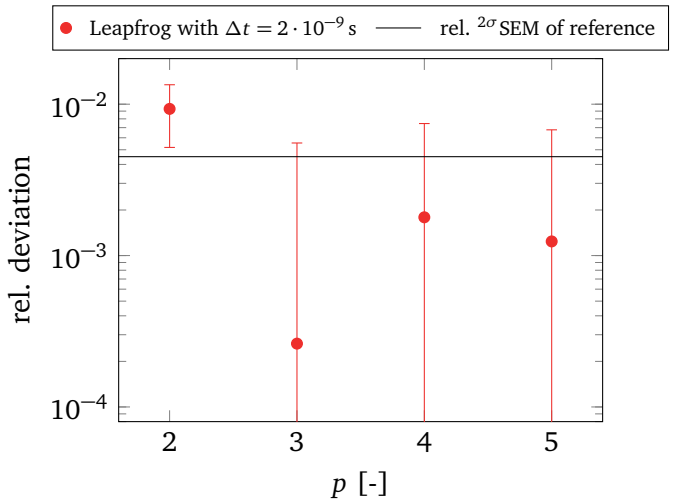

Figure 5.14: Relative deviation $|I_{accel} - I_{accel}^{ref}|/I_{accel}^{ref}$ over varied polynomial degree p (with reference solution from $p_{ref} = 6$, error bars by $^{2\sigma}$SEM).

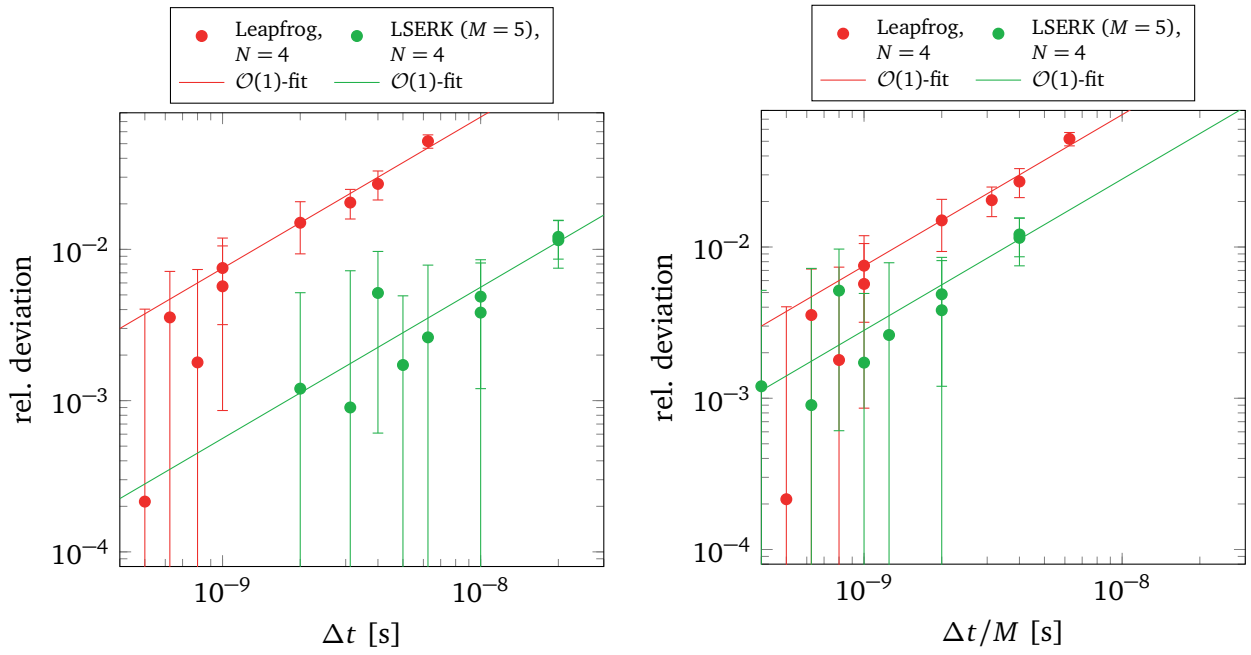

(a) Relative deviation of I_{accel} over time step size Δt. **(b)** Relative deviation of I_{accel} over average stage size.

Figure 5.15: EOC for temporal discretization (relative deviation from reference solution with $\Delta t_{ref}^{leapfrog} = 2 \cdot 10^{-10}$ s and $\Delta t_{ref}^{LSERK4-5} = 1 \cdot 10^{-9}$ s, error bars by $^{2\sigma}$SEM).

computational effort is approximately the same, but the accuracy is around 3 times higher and now exactly in the range of the statistical uncertainty. However, it should be noted that all those relations apply only for the utilized under-relaxation. It is expected that the LSERK integration benefits from the resulting very smooth charge densities.

In addition to p and the temporal discretization, also an enlarged domain ("x-extended" from

the previous subsection), the utilization of under-relaxation itself compared to time-accurate PIC, and the superposed pressure p_{BG} were analyzed in their influence on the simulated grid current. All relative deviations of I_{accel} compared with a reference were $\lesssim 1\,\%$, by which the chosen simulation parameters are verified for the following simulations.

5.3.4 Results

Figure 5.16 compares contour slices for ion charge density ρ_{Xe^+} of a PIC-only with a PIC-DSMC simulation for the case with $I_{beam} = 7\,\mathrm{mA}$ and $T_{Xe^{ch}} = 300\,\mathrm{K}$. It can be seen that without collisions (above) the separate, focused ion "beamlets" have well-defined boundaries towards vacuum and only a small part with two orders of magnitude lower ρ_{Xe^+} performs so-called overcrossing, resulting in the (green) region with larger divergence angles. In contrast, with collisions (below) additional ion populations are present near the acceleration grid: first, inside the whole cylindrical apertures as diffuse clouds around the beamlets, and secondly, at the downstream face in the middle between adjoining beamlets with decreasing intensity for more outwards located inter-beamlet positions. Both ion populations impinge on the grid and create the measurable current. Figure 5.17a depicts this current divided by the

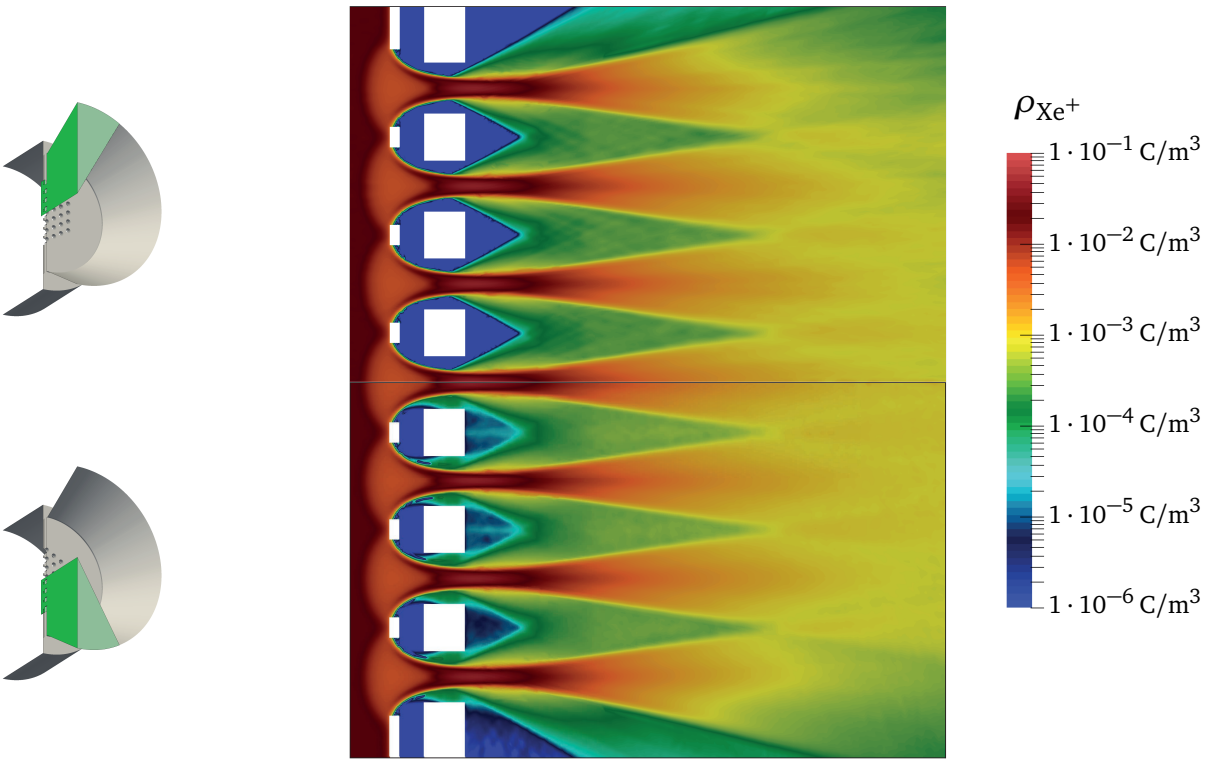

(a) Positions in domain.

(b) Charge densities of Xe^+ for $I_{beam} = 7\,\mathrm{mA}$ and $T_{Xe^{ch}} = 300\,\mathrm{K}$.

Figure 5.16: Results for PIC-only (above) and PIC-DSMC with scattering-based model (below).

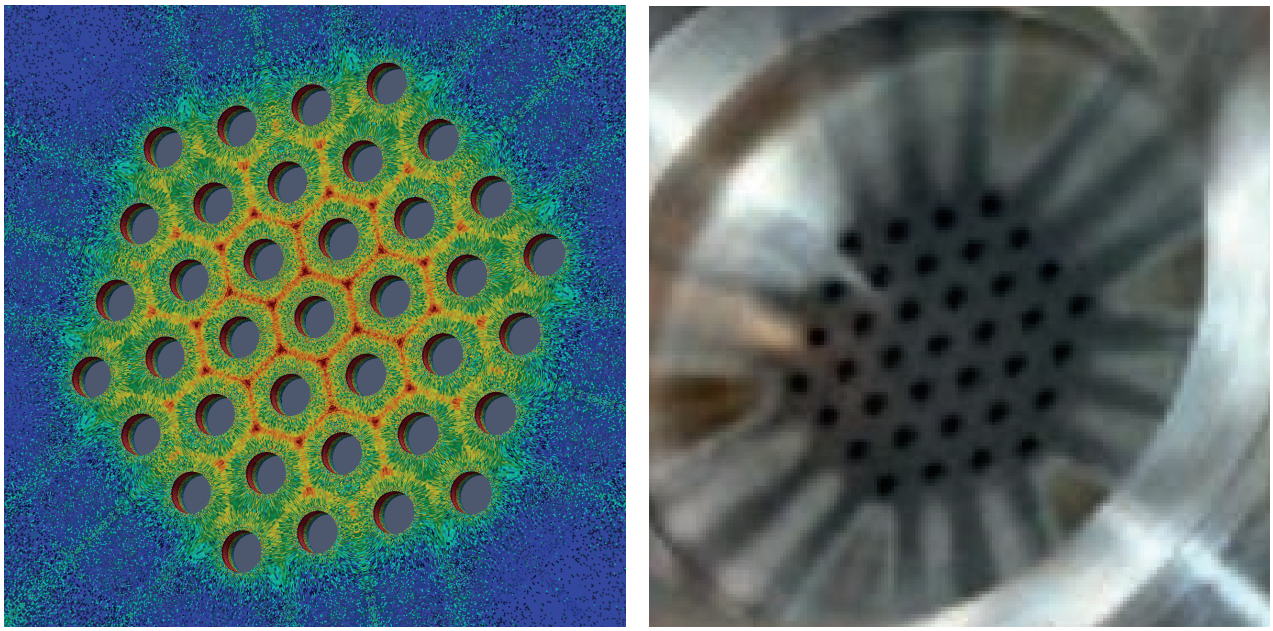

(a) Simulated current densities (30° mirrored to 360°). **(b)** Erosion pattern of thruster after experiment. [66]

Figure 5.17: Qualitative comparison of simulated grid current density to experiment.

respective sampling area as current density in logarithmic scale (green to dark red is a factor of ten). The described high inter-beamlet values are visible in the whole hexagonal aperture pattern, decreasing outwards which corresponds to the radially decreasing ρ_{Xe^+} in Fig. 5.16b. Outside of the actual pattern, the high value regions continue as radial rays. In addition to the simulation results, Fig. 5.17 also includes a picture of the thruster after experiment that shows the same characteristic erosion pattern, commonly known as “pits and grooves”. According to this, the simulation can be seen as validated, at least qualitatively. For a more quantitative validation, the total current values (i.e., the integrated densities) are considered in the following paragraphs.

The results for the remaining varied parameters, first $v^{in}_{Xe^+}$, $T^{in}_{e^-}$, Φ_n, and $T^{n}_{e^-}$, are summarized in Tab. 5.6 for 6 mA, $T_{Xe^{ch}} = 450\,\mathrm{K}$, and the scattering-based collision model. Please note, that the $n^{in}_{Xe^+}$ value was iterated to match the given I_{beam} in the PIC-only simulation (i.e., with $I_{accel} = 0$ as “step 2” from subsection 5.3.1) so that the same iteration was not required for each changed I_{accel}. Therefore, not the actual given beam current was simulated but $I_{beam} - I_{accel}$. Nevertheless, those operating conditions are still very similar to the given ones and, thus, the I_{accel}/I_{beam}-ratios are considered as good comparative values. The table shows that all four varied parameters have no significant influence on the simulated current ratio: all ratios are around 0.009. The relative deviations are $\lesssim 1\,\%$ and, thus, similar to the determined statistical uncertainty with a 2-σ-SEM of $0.3-0.5\,\%$.

Table 5.6: Simulated values for I_{accel}/I_{beam}-ratio and its sensitivity for varied parameters with $I_{beam} = 6\,\mathrm{mA}$, $T_{\mathrm{Xe}^{ch}} = 450\,\mathrm{K}$, and scattering-based collision model (bold parameter values are reference for respective relative deviations and used as default for the following simulations).

$\Phi_n = 10\,\mathrm{V}$, $T^n_{e^-} = 2\,\mathrm{eV}$				$T^{in}_{e^-} = 3.5\,\mathrm{eV}$, $v^{in}_{\mathrm{Xe}^+}/v_{Bohm} = 1.5$			
$v^{in}_{\mathrm{Xe}^+}/v_{Bohm}$ \ $T^{in}_{e^-}$	3.5 eV	5 eV	rel. dev. for $T^{in}_{e^-}$	$T^n_{e^-}$ \ Φ_n	0 V	10 V	rel. dev. for Φ_n
1.2	0.00901	0.00904	0.37 %	2 eV	0.00909	0.00903	0.71 %
1.5	0.00903	0.00906	0.33 %	5 eV	0.00895	0.00894	0.09 %
rel. dev. for $v^{in}_{\mathrm{Xe}^+}$	−0.23 %	−0.18 %		rel. dev. for $T^n_{e^-}$	−1.62 %	−1.01 %	

However, the remaining two parameters ($T_{\mathrm{Xe}^{ch}}$ and the collision model) have a significantly greater influence, as shown together with the experimental results in Fig. 5.18. It shows that both a smaller chamber temperature and the simple model produce much higher simulated grid currents. For the scattering-based model with an assumed $T_{\mathrm{Xe}^{ch}} = 300\,\mathrm{K}$, the simulations match the experiment well. It can be shown that for both pairs of curves using the same collision model, the curves lie on top of each other when scaling the current ratio with the respective $\sqrt{T_{\mathrm{Xe}^{ch}}}$. As for the number densities of neutral gas n_{Xe} (see subsection 5.3.2), this corresponds to an inverse proportionality of the simulated currents to $\sqrt{T_{\mathrm{Xe}^{ch}}}$, which is also expected since the collision probability is proportional to n_{Xe}. The current ratios of the simple model are by a factor of $X = 1.63$ too high for the $T_{\mathrm{Xe}^{ch}} = 300\,\mathrm{K}$ case and $X = 1.33$ for $T_{\mathrm{Xe}^{ch}} = 450\,\mathrm{K}$. Hence, it can be estimated that they would match the experiment at $X^2 T_{\mathrm{Xe}^{ch}} = 800\,\mathrm{K}$. Comparing now the values of 300 and 800 K and having in mind that both thruster before experiment and gas supply were at room temperature, the former value can be considered as reasonable assumption, whereas the latter is certainly too high. Consequently, the good quantitative agreement between experiment and simulation indicates the usefulness of the scattering-based model in its used parametrization.

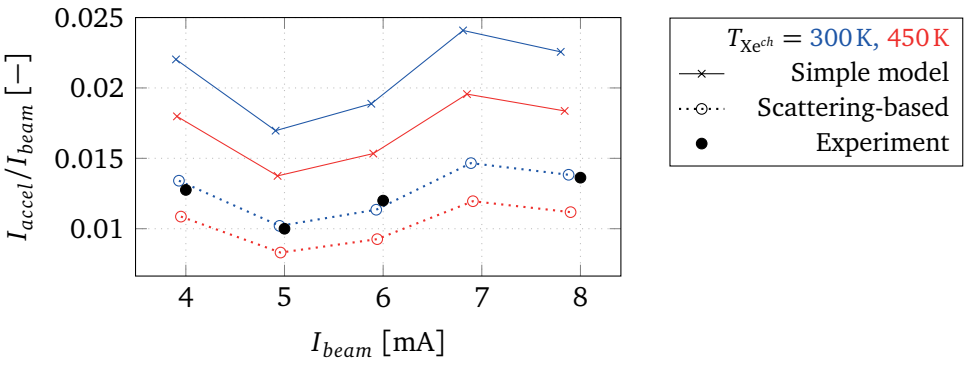

Figure 5.18: Simulated I_{accel}/I_{beam}-ratios for varied $T_{\mathrm{Xe}^{ch}}$ and collision model.

To further analyze the differences between both collision models in more detail, Fig. 5.19 subdivides the acceleration grid into separate regions. Figure 5.19b illustrates the individual region types. On the one hand, it can be distinguished if either the downstream face is impinged or the inner (cylindrical) surface of an aperture. On the other hand, there are 6 different aperture types, dependent on their distance from the thruster axis and its neighboring apertures. To each aperture, a hexagonal area of the downstream face can be assigned, the remaining area is referred to as “outer” region. Figure 5.19a includes the individual parts of current ratio by their corresponding impinged region for $I_{beam} = 7\,\mathrm{mA}$ and $T_{\mathrm{Xe}^{ch}} = 300\,\mathrm{K}$. The darkly colored bases of the bars are the values per single aperture, and the complete bars the values multiplied by the respective amount of region type as present in the whole grid. It can be seen that for the downstream face (green bars) the value per single aperture (dark bases) decreases from #1 to #6, thus, with increasing distance from the thruster axis. In contrast, they are exactly constant for the cylinder regions (red), but significantly higher. Furthermore, the diagram shows that the simple collision model compared with the scattering-based (bars with line pattern vs. without) has only small influence for the downstream regions, but a much greater one for the cylinders: For the downstream face, the value of the total current ratio on aperture regions is increased by 28 % from 0.00208 to 0.00266 and on the outer region by 35 % from 0.00139 to 0.00187; whereas for the cylinder region by 74 % from 0.01095 to 0.01902. This observation is consistent with the results of the verification study from section 4.5 showing that the simple model over-predicts the creation of ions with high-angle scattering, because mostly ions at large divergence angles result in impingement inside the short aperture cylinders.

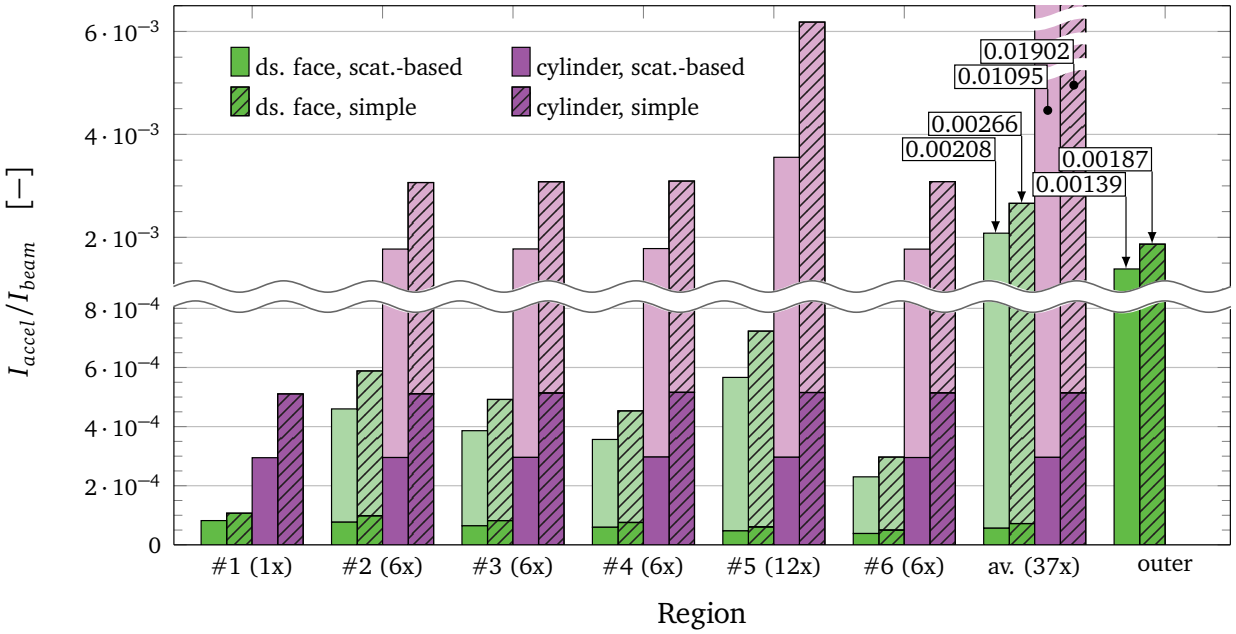

(a) Current ratio by region (total of all region types in 360°, dark color is per single aperture).

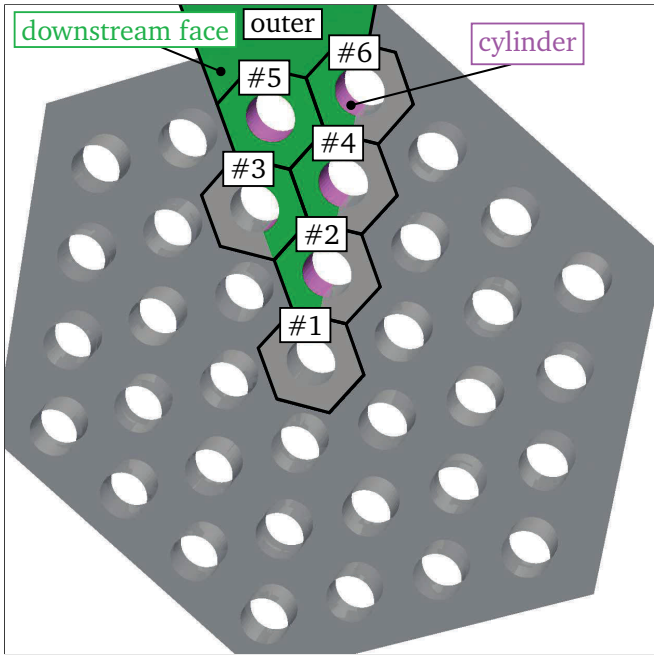

(b) Separate regions of impinged surfaces.

Figure 5.19: Parts of current ratio by impinged region for $I_{beam} = 7\,\text{mA}$ and $T_{\text{Xe}^{ch}} = 300\,\text{K}$.

5.4 Application to changed grid geometries

With the general set-up validated for grid-current simulations, it can be applied to varied geometries for further investigations. One subject of special interest is the influence of grid shifts, i.e., when the apertures of screen and acceleration grid are not perfectly aligned with each other. Background of this misalignment is that, especially for larger thrusters, the grid geometry is exposed to local deformations dependent on thrust level, temperature and specific operating point and, thus, compromises need to be accepted for thruster design [65].

Figure 5.20 shows how a shift Δr_{shift} between an aperture pair results in a deflection angle β of the beamlet. The direction is caused by the negative voltage of the second grid which attracts the positively charged ions. A correct alignment of the grids is crucial for the determination of operating points for maximum efficiency and minimized erosion, because a deflection has the following, obvious influences on thruster operation:

- The thrust vector changes.
- The limits of operating points without direct impingement are deteriorated.
- The deflected beamlet positions change both the creation places of CEX ions and the electric fields which alter the impingement positions at the downstream face.

Due to the described complex dependence of grid-deformation, a known relation between the actual grid shift and its influence in terms of deflection angle and erosion is very important. Furthermore, the “hot state design” (i.e., during operation) is inaccessible for direct measurements of the actual grid shift, but the resulting “pits and grooves” erosion pattern also remains after the experiment. Therefore, the question arises as to whether inferences can be drawn from the erosion pattern about the occurred grid shift.

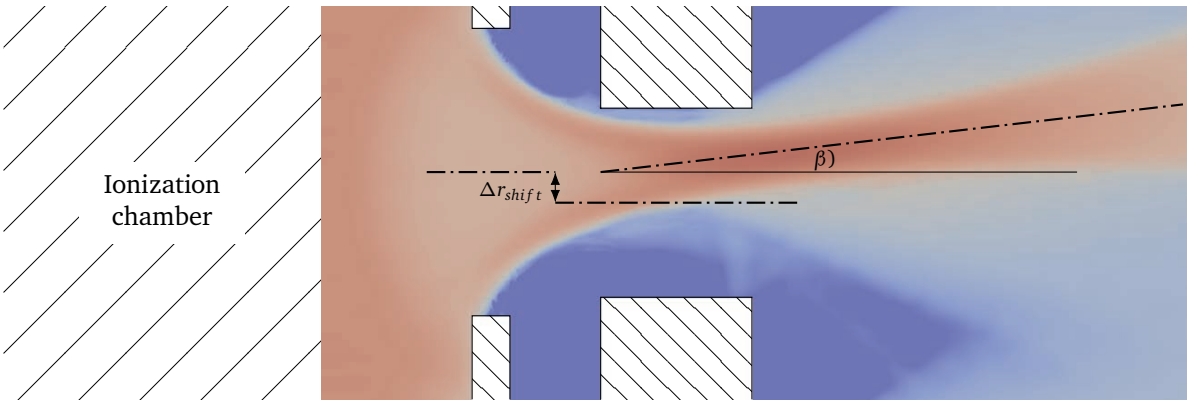

Figure 5.20: Shifted grid geometry.

Previous publications dealt with a mutual, constant shift inside an assumed infinite pattern of apertures, e.g., in the context for feasibility studies of an active thrust vectoring [86, 113]. Only Shagayda [102] also dealt with the resulting erosion pattern and the question about possible inferences, but again based on the infinite pattern approach. However, it is important to consider not only the influences of the inter-grid region (resulting from the grid shift) but also the deviations from the assumed infinite aperture pattern. This applies particularly in the downstream region of edge aperture positions, since the outer beamlets are repelled from the core of the positively charged total beam. So far, the influence of edge apertures on the erosion pattern from shifted grids was only considered as result from upstream inhomogeneities, such as variations in current densities and velocity inclinations [102].

5.4.1 Simulation set-up

The validated operating point with $I_{beam} = 6\,\mathrm{mA}$ and $T_{\mathrm{Xe}^{ch}} = 300\,\mathrm{K}$ was chosen with its baseline parameters but adapted geometry. All radial axis positions of the screen grid apertures at $r = \sqrt{y^2 + z^2}$ inside the hexagonal pattern were linearly scaled according to:

$$r_{axis,new} = r_{axis,old} f\left(r_{axis,old}\right), \quad f = r_{axis,old} C + 1\,. \tag{5.7}$$

The linear scaling function f with parameter C can be interpreted as homogeneous expansion of radial positions of the screen apertures[2] and ensures that the symmetry conditions of the domain still apply as well as $f\left(r_{axis,old} = 0\right) = 1$. Hence, the central aperture (#1 in Fig. 5.19b) is always without any shift: $\Delta r_{shift} = r_{axis,new} - r_{axis,old} = r_{axis,old}^2 C$.

To investigate the influence of both grid shift and its respective position inside the aperture pattern, three different C values were considered, as summarized in Tab. 5.7 together with the resulting shifts for apertures #1, #2, #4, and #6 from Fig. 5.19b. By those chosen scalings, the shift of $\Delta r_{shift} = 0.0225\,\mathrm{mm}$ can be analyzed both at apertures #2 and #4, whereas $\Delta r_{shift} = 0.09\,\mathrm{mm}$ both at apertures #4 and #6.

Table 5.7: Considered grid shifts.

C	Δr_{shift}(#1) at $r_{axis,old} = 0.0\,\mathrm{mm}$	Δr_{shift}(#2) at $r_{axis,old} = 2.4\,\mathrm{mm}$	Δr_{shift}(#4) at $r_{axis,old} = 4.8\,\mathrm{mm}$	Δr_{shift}(#6) at $r_{axis,old} = 7.2\,\mathrm{mm}$
0	0 mm	0 mm	0 mm	0 mm
$1/1024$	0 mm	0.005625 mm	0.0225 mm	0.050625 mm
$1/576$	0 mm	0.01 mm	0.04 mm	0.09 mm
$1/256$	0 mm	0.0225 mm	0.09 mm	0.2025 mm

[2] Only the axis positions are scaled, i.e., the apertures keep their cylindrical shape with unchanged radius.

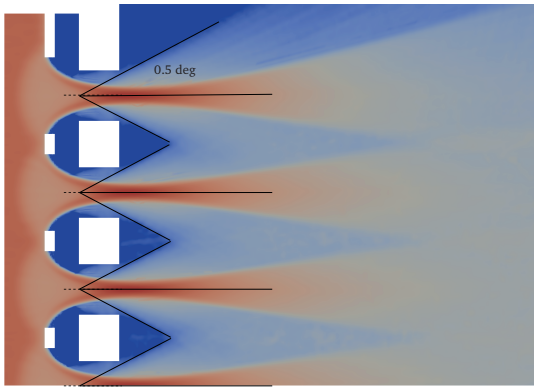

(a) Baseline geometry without shift.

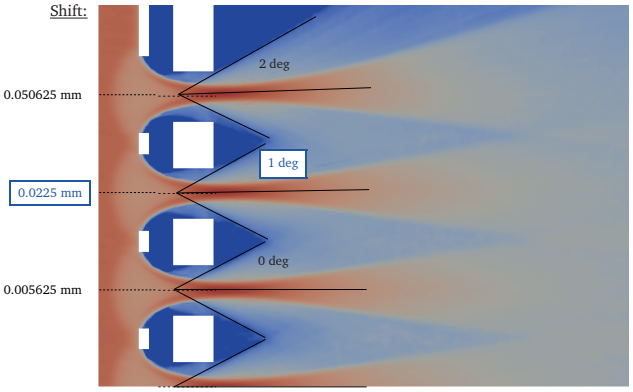

(b) Shift with $C = 1/1024$.

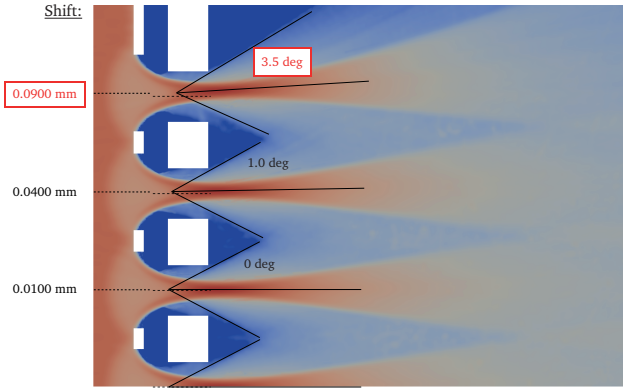

(c) Shift with $C = 1/576$.

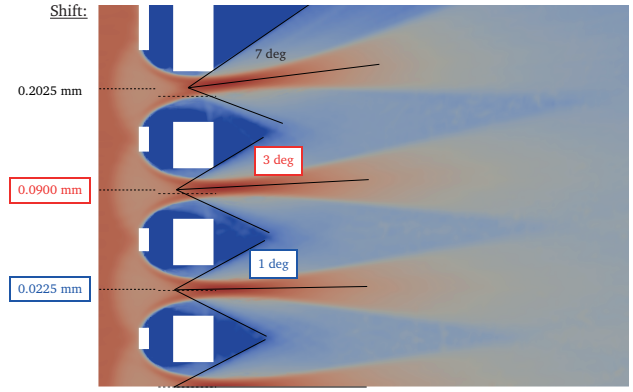

(d) Shift with $C = 1/256$.

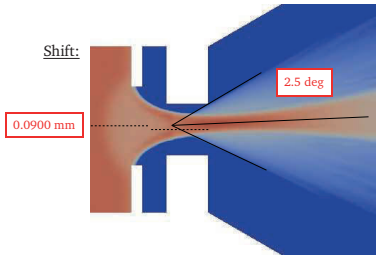

(e) Shift of 0.09 mm for single aperture.

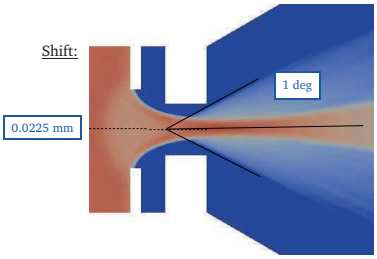

(f) Shift of 0.00225 mm for single aperture.

Figure 5.21: Varied, radially increasing shifts ($I_{beam} = 6\,\text{mA}$, $T_{\text{Xe}^{ch}} = 300\,\text{K}$, scat.-based model).

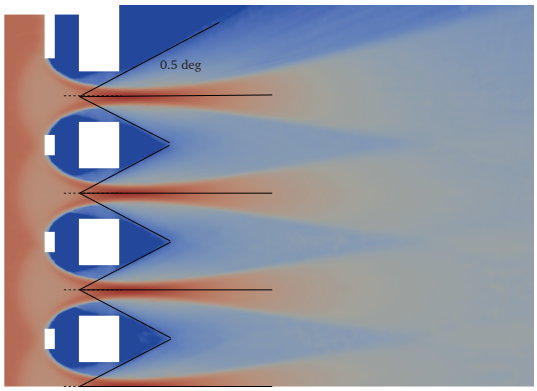

(a) Baseline geometry without shift.

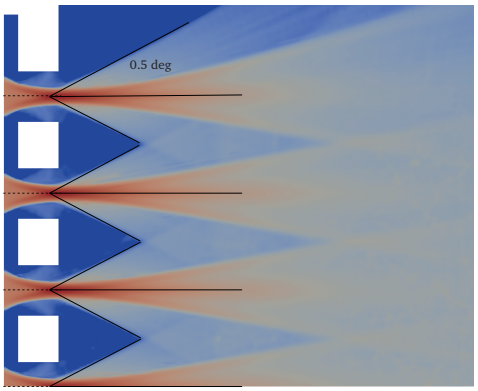

(b) Baseline geometry with truncated beamlets.

Figure 5.22: Influence of upstream plasma ($I_{beam} = 5\,\text{mA}$, $T_{\text{Xe}^{ch}} = 300\,\text{K}$, scat.-based model).

5.4.2 Resulting beamlet deflections

Figure 5.21 depicts the resulting beamlet deflections for the different C from Tab. 5.7. Additionally, single apertures without any neighboring beamlets are included by Figs. 5.21e and 5.21f. The deflection angle β increases with Δr_{shift}, but it also depends on the actual beamlet position inside the grid pattern. The shift of $\Delta r_{shift} = 0.09\,\text{mm}$ results in $\beta = 2.5°$ for the single aperture and with larger radial position it increases to $\beta = 3°$ and $\beta = 3.5°$ for beamlet #4 and #6, respectively. However, for a very small deflection such as for $\Delta r_{shift} = 0.0225\,\text{mm}$, the dependency is much less pronounced. The dependence of β on the beamlet position is also already evident in Fig. 5.21a with an edge aperture deflection of $\beta = 0.5°$ even for $\Delta r_{shift} = 0\,\text{mm}$. To exclude any influence from the upstream plasma, Fig. 5.22 compares for the case of $I_{beam} = 5\,\text{mA}$ without any grid shift the baseline simulation with an additional set-up utilizing the beamlet truncation from section 4.4. It can be seen that, again, the deflection angle of the edge aperture is $\beta = 0.5°$, which excludes any influence of a possibly asymmetric sheath meniscus due to the one-sided neighbors. Previous publications stated an approximation of beamlet deflection by linear optical theory with the screen and acceleration apertures interpreted as thin focusing and de-focusing lenses, which results in a predicted proportionality of $\tan(\beta)$ and Δr_{shift} [106]. Figure 5.23 shows that, also here, this proportionality applies as good approximation. For edge apertures (#6), it was assumed that a constant, additional deflection of 0.5° exists and, thus, the associated values were accordingly corrected for excluding the influence from the downstream plasma.

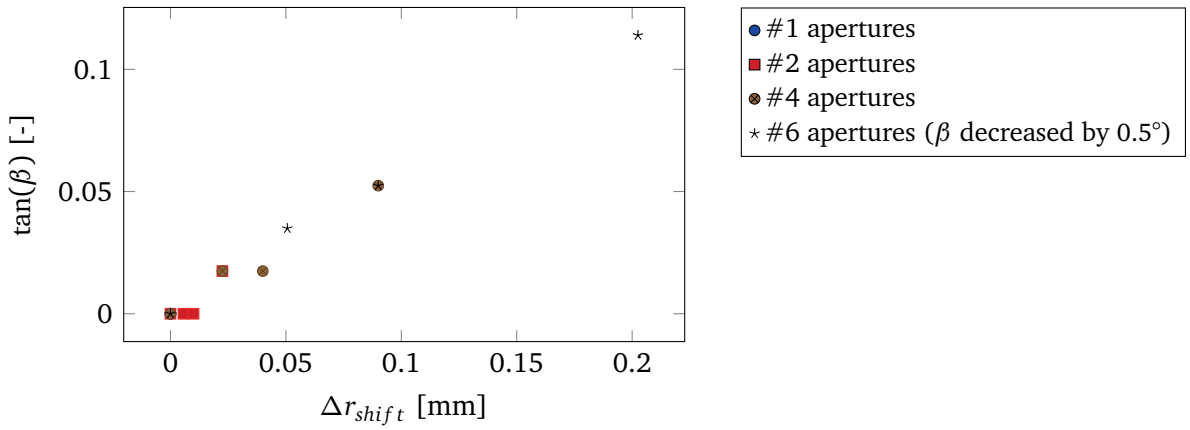

Figure 5.23: Deflection angle over grid shift.

5.4.3 Resulting patterns of current density distribution

Figure 5.24 shows the distributions of current density on the downstream face of the acceleration grid which correspond to the expected erosion patterns after operation. Additionally,

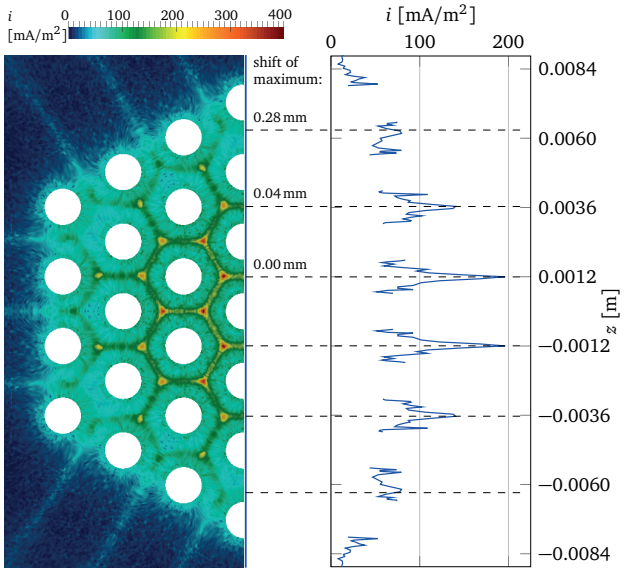

(a) Baseline geometry without shift.

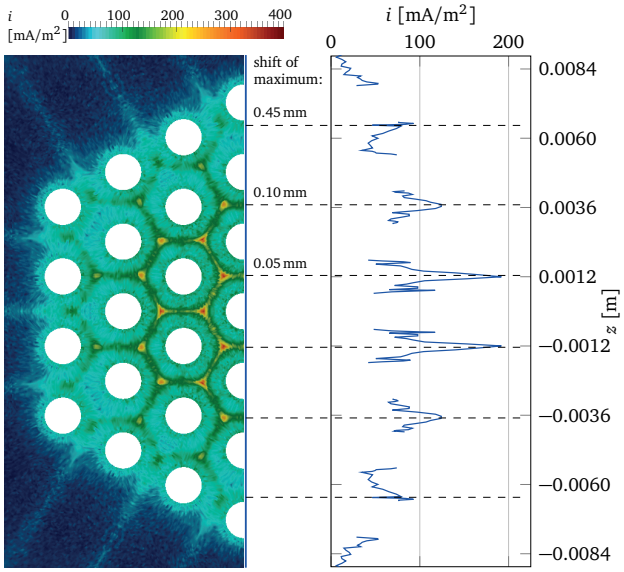

(b) Shift with $C = 1/1024$.

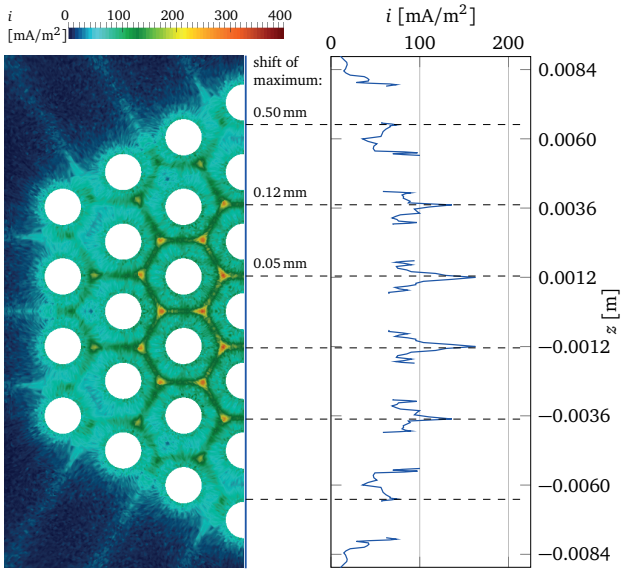

(c) Shift with $C = 1/576$.

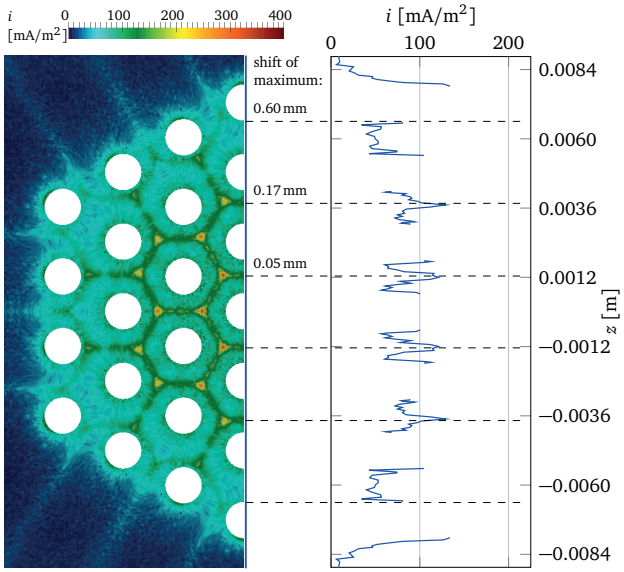

(d) Shift with $C = 1/256$.

Figure 5.24: Distributions of current density i on the downstream face of acceleration grid.

the displacements of the individual current density maxima ("shift of maximum") are shown with respect to the centers between two adjacent apertures. It can be seen that with the grid shifts and beamlet deflections, also the erosion pattern will be shifted into the same direction. Furthermore, the maximum values of current density onto the grid are reduced with increasing C which is expected to be caused by the larger total beam divergence and, thus, less overlapping beamlets. But the disadvantages of a grid shift are expected to outweigh this single benefit.

Shagayda [102] stated that a respective shift of current density maxima is proportional to the grid shift and that observed deviations at edge apertures probably result from the upstream state. However, Fig. 5.24a shows that exactly those deviations also occur with a constant discharge plasma, for which shifts exist even for perfectly aligned grids (here, 0.04 mm in the second most outer position of aperture centers). This illustrates that the erosion pattern is highly dependent on the position inside the aperture pattern, since the impingement positions of CEX ions depend on both their creation places and the complex, highly local electric fields inside the downstream plasma. Thus, a direct relation between single values for grid shift, deflection angle and erosion pattern displacement cannot be found. Nevertheless, it is expected that when considering the erosion pattern of the complete grid as a whole, inferences about the occurred grid shift could be drawn, but a corresponding analysis would require several more simulations.

6 Conclusion

6.1 Summary

The importance of electric propulsion as spacecraft technology has significantly increased in recent decades. Numerical simulation gives valuable insight into the associated, complex physical phenomena and can help in the industrial development process, e.g., in terms of performance optimization. In the course of this study, the coupled PIC-DSMC code *PICLas* was extended and applied for the ion optics simulation of gridded ion thrusters. The required simulation method is challenging due to the complex plasma flow with charge separation and a high degree of rarefaction, but acceptable simulation times can be realized by using high performance computing systems and the efficient framework of *PICLas*. The effects of the finite size of a real system can only be investigated by simulating the complete, three-dimensional thruster, which requires a relatively large computational domain, including the whole radial extent of the grids and a sufficient distance in downstream direction. Hence, the corresponding simulations can already be seen as the first steps towards considering both the actual optic and the plume domain.

To reduce the computational costs, the electrostatic characteristic of ion optics was utilized by using an implementation of the newly developed HDGSEM field solver. In contrast to the original, fully electrodynamic PIC approach of *PICLas*, in which particles and fields are advanced in time concurrently, the electrostatic case leads to a time-independent solution for the field, based on a given charge distribution. This enables significantly increased time step sizes, now only defined by the particle motion. However, the corresponding PIC cycle changes considerably and, additionally, the necessity for an accurate modeling of the particle motion is increased, especially at domain boundaries. Therefore, the conducted code extensions include electrostatic PIC schemes with different temporal integration orders as well as inflow conditions which are compatible with both increased time steps and reservoir states near to the free molecular flow regime. Higher order shape functions were used throughout the study for particle-mesh interpolation to consistently retain the higher order HDGSEM approach. Due to their extent across several cells, corrections were required to be implemented for all boundaries of open and symmetric type. Furthermore, the collision models were extended to include specific charge and momentum exchange reactions between ions and neutral atoms.

The correct numerical behavior of the extended models of *PICLas* was verified and showed good agreement with reference solutions. In the case of an electrostatic plasma sheath, it was shown that the drop towards the applied electric wall potential is always well approximated, independently of the charge correction at solid walls. This simplifies the simulation of complex wall geometries. For the HDGSEM-based PIC method applied to ion optics simulations, it was investigated how the both temporal and spatial discretization influences the three-dimensional distribution of charge density. It is important to note that the accumulated error cannot drop below the statistical uncertainty from the Monte Carlo nature of the particle simulation. For the higher order temporal integration schemes it was shown that, first, they are limited in their numerical degree of accuracy for cases with significant forces onto the inflow particles. Secondly, their higher accuracy must compensate for the higher computational cost per total time step to gain any actual benefit compared to lower order schemes.

The 4 cm diameter, radio frequency ion thruster RIT-μX EBB of ArianeGroup GmbH was chosen as the subject for the numerical simulations because its two-grid system with 37 apertures already features a geometrical complexity comparable to larger thrusters. Furthermore, experimental measurements are available which were the basis for validation. It was shown that the Boltzmann relation is applicable as an electron fluid model for the simulations of interest, even near the electron back-streaming (EBS) limit. The spatial distributions of electric potential and number densities matched well between fully kinetic and hybrid fluid simulations which was additionally confirmed by the velocity distribution functions of electrons corresponding to thermal equilibrium at most positions. Also, a quantitative evaluation of the EBS current based on the fluid assumption agreed well with the fully kinetic determination and it was shown that even an infinite grid domain is a very good approximation for numerical EBS investigations when the same homogeneous inflow condition is assumed for all beamlets. However, the EBS-defining inflow characteristics are highly dependent on the local plasma parameters of the discharge process in the chamber, which excluded EBS measurements as validation approach.

Instead, validation was achieved by grid current simulations based on charge exchange ions impinging onto the completely modeled, second grid. The neutral gas distributions were determined separately by DSMC and used as temporally constant background for the sampling of collision partners in the coupled PIC-DSMC simulations. Furthermore, an under-relaxation approach for charge densities enabled a delay of the steady time of the beam ions towards the value based on scattered ions, but with much less intensive time steps resulting in a total computation time of 1.5 hours on 2400 cores of a Cray XC40. The experimental erosion pattern of the thruster could be reproduced by the simulations. The results show an inverse proportionality of the grid currents to the square root of the assumed neutral gas temperature.

Setting this value to reasonable 300 K results, in the case of the newly implemented scattering-based charge exchange model, in an excellent agreement with the measured grid currents of all considered operating conditions. The other varied parameters were shown to have only insignificant influence on the simulation results.

Eventually, the validated simulation set-up was applied to grid geometries changed by a homogeneous expansion of radial positions of the screen apertures, by which the aperture positions are misaligned between the first and second grid. Those shifts result in a deflection of the beamlets which needs to be prevented during actual thruster operation. Different geometrical expansions were considered so that the same shift could be analyzed for different positions inside the finite grid pattern, which has not been investigated numerically before. It was shown that the deflection angles and the corresponding displacement in the erosion pattern increase not only with the grid shift but also with its respective radial position inside the pattern. The radial dependence of the deflection angle was related to the repulsion between the individual, positively charged beamlets on the downstream side of the grids. Due to the associated complex, highly local electric fields, a direct relation between aperture-independent values for grid shift, deflection angle and erosion pattern displacement cannot be found. However, it is expected that relations could be deduced for the grid as a whole, but this requires several more simulations.

6.2 Outlook

The conducted ion optics simulations of a complete grid geometry were a novelty within the field of research, especially in combination with the parameter studies comparing different models as well as various numerical and physical parameters. Together with the application to grid shifts, a new insight into the physical relationships defining the ion optics of real ion thrusters was provided. The simulation of further operating conditions is expected to be easily possible. Nevertheless, future extensions are also possible due to the utilization of the flexible framework of *PICLas* instead of a tailor-made solution.

A logical next step would be to loosen the two domain restrictions: the upstream discharge chamber and the downstream (as quasi-neutral approximated) plume region. The radial profile of the upstream plasma parameters could be modeled either by given relations, extracted from separate numerical models, or by a direct coupling with the discharge simulation. Once the local, beamlet-dependent plasma parameters, which define the electron characteristics, are set, a more realistic plume neutralization can also be included, e.g., by considering a larger respective domain and an actual source of fully kinetic electrons.

Additionally, more elaborate physical and numerical models could be utilized for the simulations. The presented comparisons between experimental erosion patterns and current densities can only be seen as rough, qualitative evaluations since the actual erosion process depends, besides the ion flux, on the so-called sputter yield. A future implementation of a sputtering model with its dependence on the respective angle and energy of the impact would, therefore, allow a quantitative evaluation and enable a more detailed comparison between the influences of the scattering-based model and the isotropic ion-neutral collisions. The scattering model itself could be extended to a variable soft sphere (VSS) model which represents a more generic, anisotropic model that would also be suitable for other application cases.

In order to decrease the computation times, the parallelization concept of the HDGSEM field solver should be further optimized. The support of non-conformal unstructured meshes would not only speed-up the mesh generation but also allow the utilization of fewer elements, which in turn would accelerate the simulation at the same accuracy if higher geometrical and field polynomial orders were used.

Zusammenfassung

Elektrische Raumfahrtantriebe haben in den letzten Jahrzehnten als Technologie für Raumfahrzeuge stark an Bedeutung gewonnen. Numerische Simulationen geben wertvolle Einblicke in die damit verbundenen, komplexen physikalischen Phänomene und können im industriellen Entwicklungsprozess (z.B. im Hinblick auf Leistungsoptimierung) helfen. Im Rahmen dieser Arbeit wurde der gekoppelte PIC-DSMC-Code *PICLas* erweitert und für die Ionenoptik-Simulation von Gitter-Ionentriebwerken angewendet. Die benötigte Simulationsmethode ist aufgrund der komplexen Plasmaströmung mit Ladungstrennung und einem hohen Grad an Verdünnung eine Herausforderung. Doch relativ kurze Simulationszeiten können durch die Verwendung des bereits bestehenden Frameworks des gekoppelten PIC-DSMC-Codes *PICLas* in Kombination mit Höchstleistungscomputersystemen realisiert werden. Die Auswirkungen, die sich aus der endlichen Größe eines realen Systems ergeben, können nur durch die Simulation des vollständigen dreidimensionalen Triebwerks untersucht werden. Diese Simulationen erfordern einen relativ großen Berechnungsbereich, einschließlich der gesamten radialen Gitterausdehnung und einer ausreichenden Entfernung stromab. Daher stellen die entsprechenden Modelle einen ersten Schritt dar, um sowohl das eigentliche Optik- als auch Plume-Gebiet zu berücksichtigen.

Die Ionenoptik wurde in ihrer elektrostatischen Charakteristik betrachtet und ein neu entwickelter HDGSEM-Feldlöser verwendet. Dadurch wurde der Rechenaufwand reduziert. Im Gegensatz zum ursprünglichen, vollständig elektrodynamischen PIC-Ansatz von *PICLas*, bei dem Partikel und Felder gleichzeitig propagiert werden, führt der elektrostatische Fall, basierend auf einer gegebenen Ladungsverteilung, zu einer zeitunabhängigen Lösung des Feldes. Dies ermöglicht eine wesentlich größere Zeitschrittweite, die jetzt nur noch durch die Partikelbewegung bestimmt wird. Der entsprechende PIC-Zyklus ändert sich jedoch erheblich. Zusätzlich verstärkt sich, insbesondere an Rechengebietsgrenzen, die Notwendigkeit einer genauen Modellierung der Partikelbewegung. Daher umfassen die durchgeführten Code-Erweiterungen elektrostatische PIC-Schemata mit unterschiedlichen zeitlichen Integrationsordnungen sowie Einströmbedingungen, die sowohl mit erhöhtem Zeitschritt als auch mit Reservoir-Zuständen nahe zur freien Molekularströmung kompatibel sind. In der gesamten Arbeit wurden Formfunktionen höherer Ordnung für die Partikel-Rechengitter-Interpolation verwendet, um den HDGSEM-Ansatz höherer Ordnung konsistent aufrechtzuerhalten. Aufgrund ihrer Ausdehnung über mehrere Zellen mussten Korrekturen für alle offenen und symmetrischen Gebietsgrenzen implementiert werden. Darüber hinaus wurden die Kollisionsmodelle um spezielle Ladungs- und Impulsaustauschreaktionen zwischen Ionen und neutralen Atomen erweitert.

Die erweiterten Modelle von *PICLas* wurden in ihrem korrekten numerischen Verhalten überprüft und zeigen eine gute Übereinstimmung mit Referenzlösungen. Für den Fall einer elektrostatischen Plasmarandschicht wurde gezeigt, dass der Abfall in Richtung des angelegten elektrischen Wandpotentials unabhängig von einer Ladungskorrektur an festen Wänden stets gut approximiert wird. Dies vereinfacht die Simulation komplexer Wandgeometrien. Für die HDGSEM-basierte PIC-Methode wurde für Ionenoptik-Simulationen untersucht, wie die sowohl zeitliche als auch die räumliche Diskretisierung die dreidimensionale Verteilung der Ladungsdichte beeinflusst. Es ist wichtig festzuhalten, dass der akkumulierte Fehler die statistische Unsicherheit der Partikelsimulation aufgrund ihrer Monte-Carlo-Charakteristik nicht unterschreiten kann. Für die zeitlichen Integrationsschemata höherer Ordnung wurde gezeigt, dass sie zum einen für Fälle mit großen Kräften auf die einströmenden Partikel in ihrem numerischen Genauigkeitsgrad begrenzt sind. Zum anderen muss ihre höhere Genauigkeit den größeren Rechenaufwand pro Gesamtzeitschritt ausgleichen, um einen tatsächlichen Nutzen im Vergleich zu Verfahren mit niedrigerer Ordnung zu erzielen.

Der Radiofrequenz-Ionenantrieb RIT-μX EBB der ArianeGroup GmbH mit einem Durchmesser von 4 cm wurde für die numerischen Simulationen ausgewählt, da das Zwei-Gitter-System mit 37 Öffnungen bereits eine geometrische Komplexität aufweist, die mit größeren Triebwerken vergleichbar ist. Darüber hinaus sind experimentelle Messungen verfügbar, die die Grundlage für die Validierung waren. Es wurde gezeigt, dass die Boltzmann-Beziehung als Elektronenfluidmodell für die untersuchten Fälle anwendbar ist, und dies sogar nahe der EBS (Electron Backstreaming) Grenze. Die räumlichen Verläufe des elektrischen Potentials und der Teilchendichte stimmten gut zwischen vollkinetischen und Hybrid-Fluidsimulationen überein. Zusätzlich wurde gezeigt, dass die Geschwindigkeitsverteilungsfunktionen der Elektronen an den meisten Positionen dem thermischen Gleichgewicht entsprechen. Auch eine quantitative Bewertung des EBS-Stroms, basierend auf der Fluidannahme, stimmte gut mit der vollständig kinetischen Bestimmung überein. Es zeigte sich, dass selbst ein unendliches Gittergebiet für numerische EBS-Untersuchungen eine sehr gute Näherung darstellt, wenn derselbe homogene Einströmzustand für alle Beamlets angenommen wird. Die EBS-bestimmenden Einströmungsmerkmale hängen jedoch stark von den lokalen Plasmaparametern des Entladungsprozesses in der Kammer ab, weshalb EBS-Messungen als Validierungsansatz ausgeschlossen wurden.

Die Validierung wurde stattdessen durch Gitterstrom-Simulationen erreicht, die auf Ladungsaustausch-Ionen basieren, welche auf das vollständig modellierte zweite Gitter treffen. Die Neutralgasverteilungen wurden separat per DSMC bestimmt und als zeitlich konstanter Hintergrund für die Generierung von Kollisionspartnern in den gekoppelten PIC-DSMC-Simulationen verwendet. Darüber hinaus ermöglichte ein Unterrelaxationsansatz der Ladungsdichten, die stationäre Zeit der Strahl-Ionen in Richtung des auf den gestreuten Ionen basierenden Werts

zu verzögern. Aufgrund der weniger rechenintensiven Zeitschritte führte dies zu einer Gesamtrechenzeit von nur 1,5 Stunden auf 2400 Kernen einer Cray XC40. Das experimentelle Erosionsmuster des Triebwerks konnte durch die Simulationen reproduziert werden. Die Ergebnisse zeigen eine umgekehrte Proportionalität der Gitterströme zur Quadratwurzel der angenommenen Neutralgastemperatur. Ein Setzen dieses Wertes auf realistische 300 K führt für das neu implementierte, streuungsbasierte Ladungsaustauschmodell zu einer hervorragenden Übereinstimmung mit den gemessenen Gitterströmen aller betrachteten Betriebspunkte. Es wurde gezeigt, dass die anderen variierten Parameter die Simulationsergebnisse nur unwesentlich beeinflussen.

Schließlich wurde der validierte Simulationsaufbau auf Gittergeometrien angewendet, die durch eine homogene Ausdehnung der radialen Gitteröffnungspositionen verändert wurden, wodurch die Öffnungspositionen zwischen dem ersten und zweiten Gitter versetzt sind. Diese Verschiebungen führen zu einer Ablenkung der Beamlets, die während des realen Triebwerkbetriebs verhindert werden muss. Es wurden verschiedene geometrische Ausdehnungen betrachtet, sodass dieselbe Verschiebung für unterschiedliche Positionen innerhalb des endlichen Gittermusters analysiert werden konnte, was zuvor noch nicht numerisch untersucht wurde. Es wurde gezeigt, dass die Ablenkwinkel und der daraus folgende Versatz im Erosionsmuster nicht nur mit der Gitterverschiebung zunehmen, sondern auch mit ihrer jeweiligen radialen Position innerhalb des Musters. Die radiale Abhängigkeit des Ablenkwinkels hing mit der Abstoßung zwischen den einzelnen positiv geladenen Beamlets auf der stromabwärtigen Seite der Gitter zusammen. Aufgrund der damit verbundenen komplexen, lokalen elektrischen Felder kann jedoch kein direkter Zusammenhang zwischen positionsunabhängigen Werten für Gitterverschiebung, Ablenkwinkel und Erosionsmusterversatz gefunden werden. Jedoch wird erwartet, dass Beziehungen für das Gesamtgitter abgeleitet werden könnten, dies erfordert jedoch mehrere weitere Simulationen.

Ausblick

Die durchgeführten Ionenoptik-Simulationen einer vollständigen Gittergeometrie waren eine Neuheit innerhalb des Forschungsgebietes, insbesondere in Kombination mit den Parameterstudien, bei denen unterschiedliche Modelle sowie verschiedene numerische und physikalische Parameter miteinander verglichen wurden. Zusammen mit der Anwendung auf Gitterverschiebungen wurde ein neuer Einblick in die physikalischen Beziehungen gegeben, die die Ionenoptik von realen Ionentriebwerken definieren. Es wird erwartet, dass die Simulation weiterer Betriebspunkte auf einfache Weise durchzuführen sein wird. Dennoch ist auch die Möglichkeit für zukünftige Erweiterungen durch die Nutzung des flexiblen Rahmens von

PICLas anstelle einer maßgeschneiderten Lösung gegeben.

Ein logischer nächster Schritt wäre die Auflösung der beiden Gebietsbegrenzungen: die Entladungskammer stromauf und die (als quasi-neutral angenäherten) Plume-Region stromab. Das radiale Profil der stromaufwärtigen Plasmaparameter könnte entweder durch gegebene (aus separaten numerischen Modellen extrahierten) Beziehungen modelliert werden oder durch eine direkte Simulationskopplung mit der Entladung. Sobald die lokalen, Beamlet-abhängigen Plasmaparameter, die die Elektroneneigenschaften definieren, bestimmt sind, kann auch eine realistischere Plume-Neutralisation berücksichtigt werden. Dies kann beispielsweise durch die Betrachtung eines entsprechend größeren Rechengebiets und einer tatsächlichen Quelle vollkinetischer Elektronen erfolgen.

Zusätzlich könnten ausgefeiltere physikalische und numerische Modelle für die Simulationen verwendet werden. Die dargestellten Vergleiche zwischen experimentellen Erosionsmustern und Stromdichten können nur als grobe qualitative Bewertung angesehen werden, da der tatsächliche Erosionsprozess neben dem Ionenfluss von der sogenannten Sputterausbeute abhängt. Eine zukünftige Implementierung eines Sputtermodells, das auch die Abhängigkeit von dem jeweiligen Winkel und der Energie des Aufpralls berücksichtigt, würde daher eine quantitative Auswertung erlauben. Zusätzlich ermöglicht sie einen detaillierteren Vergleich zwischen den Einflüssen des streuungsbasierten Modells und der isotropen Ionen-Neutralgas-Kollisionen. Das Streuungsmodell selbst kann auf ein Variable Soft Sphere (VSS) Modell erweitert werden, das ein allgemeineres anisotropes Modell darstellt, welches auch für andere Fälle eine Anwendung finden könnte.

Um die Rechenzeiten zu verkürzen, sollte das Parallelisierungskonzept des HDGSEM Feldlösers weiter optimiert werden. Die Unterstützung von nicht-konformen unstrukturierten Rechengittern würde nicht nur die Gittergenerierung vereinfachen, sondern auch die Verwendung weniger Elemente ermöglichen, was wiederum die Simulation bei gleicher Genauigkeit beschleunigen würde, wenn höhere geometrische und Feld-Polynomordnungen verwendet werden.

Bibliography

[1] J. R. Anderson, I. Katz, and D. M. Goebel. Numerical Simulation of Two-Grid Ion Optics Using a 3D Code. *Proceedings of the Joint Propulsion Conference and Exhibit*, **40**, 2004.

[2] Y. Arakawa and K. Ishihara. A numerical code for cusped ion thrusters. *Proceedings of the International Electric Propulsion Conference*, **22**, 1991.

[3] Y. Arakawa and M. Nakano. An efficient three-dimensional optics code for ion thruster research. *Proceedings of the Joint Propulsion Conference and Exhibit*, **32**, 1996.

[4] S. J. Araki. *Multi-Scale Multi-Species Modeling for Plasma Devices*. PhD Dissertation, University of California, LA, 2014.

[5] S. J. Araki. Fast computation of high energy elastic collision scattering angle for electric propulsion plume simulation. *AIP Conference Proceedings*, **1786**(1), 2016.

[6] D. Baganoff and J. McDonald. A collision-selection rule for a particle simulation method suited to vector computers. *Physics of Fluids A: Fluid Dynamics*, **2**(7):1248–1259, 1990.

[7] J. Barnes and P. Hut. A hierarchical O (N log N) force-calculation algorithm. *Nature*, **324**(6096):446, 1986.

[8] R. Becker and W. Herrmannsfeldt. IGUN - A program for the simulation of positive ion extraction including magnetic fields. *Review of scientific instruments*, **63**(4):2756–2758, 1992.

[9] P. L. Bhatnagar, E. P. Gross, and M. Krook. A Model for Collision Processes in Gases. I. Small Amplitude Processes in Charged and Neutral One-Component Systems. *Physical Review*, **94**:511–525, 1954.

[10] F. Bin Baharudin, T. Miyasaka, K. Asato, H. Sugiyama, and T. Kobayashi. Study on Electron Distributions in a Three Dimensional Particle Simulation of an Ion Engine. *Transactions of the Japan Society for Aeronautical and Space Sciences, ISTS-28*, **10**, 2012.

[11] T. Binder, P. Boldini, F. Romano, G. Herdrich, and S. Fasoulas. Transmission probabilities of rarefied flows in the application of atmosphere-breathing electric propulsion. *AIP Conference Proceedings*, **1786**(1), 2016.

[12] T. Binder, M. Pfeiffer, and S. Fasoulas. Validation of Grid Current Simulations Using the Particle-In-Cell Method for a Miniaturized Ion Thruster. *Proceedings of the International Symposium on Rarefied Gas Dynamics*, **31**, 2018.

[13] T. Binder, M. Pfeiffer, S. Fasoulas, and H. Leiter. High-fidelity Particle-In-Cell simulations of ion thruster optics. *Proceedings of the International Electric Propulsion Conference*, **35**, 2017.

[14] G. A. Bird. *Molecular Gas Dynamics and the Direct Simulation of Gas Flows*. Oxford, 1994.

[15] C. K. Birdsall. Particle-in-cell charged-particle simulations, plus Monte Carlo collisions with neutral atoms, PIC-MCC. *IEEE Transactions on Plasma Science*, **19**(2):65–85, 1991.

[16] C. K. Birdsall and A. B. Langdon. *Plasma Physics via Computer Simulation*. Hilger, Bristol, 1991.

[17] C. D. Bogart and E. A. Richley. A space-charge-flow computer program, NASA-TN-D-3394. Technical report, Lewis Research Center, 1966.

[18] L. Boltzmann. Weitere Studien über das Wärmegleichgewicht unter Gasmolekülen. *Sitzungsberichte Akademie der Wissenschaften*, **66**:275–370, 1872.

[19] R. Bond and P. Latham. Ion thruster extraction grid design and erosion modelling using computer simulation. *Proceedings of the Joint Propulsion Conference and Exhibit*, **31**, 1995.

[20] I. D. Boyd and R. A. Dressler. Far field modeling of the plasma plume of a Hall thruster. *Journal of Applied Physics*, **92**(4):1764–1774, 2002.

[21] G. R. Brewer. *Ion Propulsion: Technology and Applications*. Gordon and Breach Science Publishers, 1970.

[22] C. Buet. A discrete-velocity scheme for the Boltzmann operator of rarefied gas dynamics. *Transport Theory and Statistical Physics*, **25**(1):33–60, 1996.

[23] H. Cao, Y. Chu, E. Wang, Y. Cao, G. Xia, and Z. Zhang. Numerical Simulation Study on Barrel Erosion of Ion Thruster Accelerator Grid. *Journal of Propulsion and Power*, **31**(6):1785–1792, 2015.

[24] M. H. Carpenter and A. Kennedy. Fourth-Order 2N-Storage Runge-Kutta Schemes. *NASA Technical Memorandum*, **109112**, 1994.

[25] P. Chabert and N. Braithwaite. *Physics of radio-frequency plasmas*. Cambridge University Press, 2011.

[26] V. H. Chaplin, J. E. Polk, I. Katz, G. Williams, G. C. Soulas, J. Yim, and J. R. Anderson. 3D Simulations of Ion Thruster Accelerator Grid Erosion Accounting for Charge Exchange Ion Space Charge. *Proceedings of the Joint Propulsion Conference*, **54**, 2018.

[27] M. Chen, A. Sun, C. Chen, and G. Xia. Particle simulation of grid system for krypton ion thrusters. *Chinese Journal of Aeronautics*, **31**(4):719–726, 2018.

[28] A. J. Christlieb, R. Krasny, J. P. Verboncoeur, J. W. Emhoff, and I. D. Boyd. Grid-free plasma simulation techniques. *IEEE Transactions on Plasma Science*, **34**(2):149–165, 2006.

[29] B. Cockburn, B. Dong, J. Guzmán, M. Restelli, and R. Sacco. A hybridizable discontinuous Galerkin method for steady-state convection-diffusion-reaction problems. *SIAM Journal on Scientific Computing*, **31**(5):3827–3846, 2009.

[30] M. Crofton and I. Boyd. The origins of accelerator grid current-Analysis of T5-grid test results. *Proceedings of the Joint Propulsion Conference and Exhibit*, **35**, 1999.

[31] R. Cybulski, D. Shellhammer, R. Lovell, E. Domino, and J. Kotnik. Results from SERT I ion rocket flight test. Technical report, Lewis Research Center, Cleveland, 1968.

[32] R. Eckhardt. Stan Ulam, John von Neumann, and the Monte Carlo method. *Los Alamos Science*, **15**(131-136):30, 1987.

[33] J. W. Emhoff. *Simulation of ion optics using particle-in-cell and treecode methods*. PhD Dissertation, University of Michigan, 2005.

[34] G. Farin. *Curves and Surfaces for CAGD: A Practical Guide*. Morgan Kaufmann Publishers Inc., San Francisco, CA, USA, 5th edition, 2002. ISBN 1-55860-737-4.

[35] C. C. Farnell. *Performance and lifetime simulation of ion thruster optics*. PhD Dissertation, Colorado State University, 2007.

[36] C. C. Farnell and J. D. Williams. Ion Thruster Grid Design Using an Evolutionary Algorithm. *Journal of Propulsion and Power*, **26**(1):125–129, 2010.

[37] C. C. Farnell, J. D. Williams, and P. J. Wilbur. Numerical Simulation of Ion Thruster Optics. *Proceedings of the International Electric Propulsion Conference*, **28**, 2003.

[38] S. Fasoulas. *Experimentelle und theoretische Charakterisierung einer hochenthalpen Stickstoffströmung zur Wiedereintrittssimulation*. PhD Dissertation, University of Stuttgart, 1995.

[39] I. Funaki, M. Nakano, Y. Kajimura, T. Miyasaka, Y. Nakayama, T. Hyakutake, M. Wada, T. Kenmotsu, T. Muramoto, H. Kuninaka, and I. Shinohara. A Numerical Tool for Lifetime Evaluation of Ion Thruster Ion Optics. *Proceedings of the Joint Propulsion Conference and Exhibit*, **47**, 2011.

[40] A. L. Garcia and W. Wagner. Generation of the Maxwellian inflow distribution. *Journal of computational physics*, **217**(2):693–708, 2006.

[41] P. N. Giuliano and I. D. Boyd. Particle simulation of collision dynamics for ion beam injection into a rarefied gas. *Physics of Plasmas*, **20**(3):033505, 2013.

[42] R. H. Goddard. An autobiography of Robert H. Goddard (notebook dated September 6, 1906). *Astronautics*, **4**:24, 1959.

[43] D. M. Goebel and I. Katz. *Fundamentals of electric propulsion: ion and Hall thrusters*, volume 1. John Wiley & Sons, 2008.

[44] L. Greengard and V. Rokhlin. A fast algorithm for particle simulations. *Journal of computational physics*, **73**(2):325–348, 1987.

[45] V. Hamza and E. Richley. Numerical Solution of Two-Dimensional Poisson Equation: Theory and Application to Electrostatic-Ion-Engine Analysis, NASA-TN-D-1323. Technical report, Lewis Research Center, 1962.

[46] Y. Hayakawa. Three dimensional numerical analysis of ion beam trajectories. *Proceedings of the International Electric Propulsion Conference*, **21**, 1990.

[47] N. R. G. headed by Prof. Claus-Dieter Munz. Flexi: High Perfomance Open Source CFD. `https://www.flexi-project.org/`, 2018. [Online; accessed 06-December-2018].

[48] R. Henrich. *Development of a plasma simulation tool for Radio Frequency Ion Thrusters*. PhD Dissertation, Justus Liebig University Gießen, 2013.

[49] W. B. Herrmannsfeldt. Poisson Equation Solving Program (SLAC-51). Technical report, Stanford Linear Accelerator Center, 1965.

[50] J. Hesthaven and T. Warburton. *Nodal Discontinuous Galerkin Methods: Algorithms, Analysis, and Applications*. Texts in Applied Mathematics. Springer, 2008. ISBN 9780387720654.

[51] F. Hindenlang, T. Bolemann, and C.-D. Munz. Mesh Curving Techniques for High Order Discontinuous Galerkin Simulations. In *IDIHOM: Industrialization of High-Order Methods-A Top-Down Approach*, pages 133–152. Springer, 2015.

[52] F. Hindenlang, G. J. Gassner, C. Altmann, A. Beck, M. Staudenmaier, and C.-D. Munz. Explicit discontinuous Galerkin methods for unsteady problems. *Computers & Fluids*, **61**:86–93, 2012.

[53] A. C. Hindmarsh. ODEPACK, a systematized collection of ODE solvers. *Scientific computing*, pages 55–64, 1983.

[54] R. W. Hockney and J. W. Eastwood. *Computer simulation using particles*. CRC Press, Boca Raton, 1988.

[55] G. B. Jacobs and J. S. Hesthaven. High-order Nodal Discontinuous Galerkin Particle-in-cell Method on Unstructured Grids. *Journal of Computational Physics*, **214**(1):96–121, 2006.

[56] R. Kafafy. *Immersed finite element particle-in-cell simulations of ion propulsion*. PhD Dissertation, Virginia Tech, 2005.

[57] R. Kafafy, T. Lin, and J. Wang. 3-dimensional ion optics simulations using an IFE-PIC code. *Proceedings of the Joint Propulsion Conference and Exhibit*, **39**, 2003.

[58] R. Kafafy and J. Wang. Whole ion optics simulations of a subscale gridlet using a hybrid-grid IFE-PIC code. *Proceedings of the Joint Propulsion Conference and Exhibit*, **40**, 2004.

[59] R. Killinger, R. Kukies, M. Surauer, A. Tomasetto, and L. van Holtz. ARTEMIS orbit raising inflight experience with ion propulsion. *Acta Astronautica*, **53**(4-10):607–621, 2003.

[60] H.-C. Kim, Y. Feng, and J. P. Verboncoeur. Algorithms for accurate collection, ejection, and loading in particle simulations. *Journal of Computational Physics*, **223**(2):629–642, 2007.

[61] D. A. Kopriva. *Implementing Spectral Methods for Partial Differential Equations: Algorithms for Scientists and Engineers*. Mathematics and Statistics. Springer, 2009. ISBN 9789048122615.

[62] D. A. Kopriva and G. Gassner. On the Quadrature and Weak Form Choices in Collocation Type Discontinuous Galerkin Spectral Element Methods. *Journal of Scientific Computing*, **44**:136–155, 2010.

[63] M. Laux. *Direkte Simulation Verdünnter, Reagierender Strömungen*. PhD Dissertation, University of Stuttgart, 1995.

[64] W. S. Lawson. Particle simulation of bounded 1D plasma systems. *Journal of Computational Physics*, **80**(2):253–276, 1989.

[65] H. Leiter. Personal communication, 2019.

[66] H. Leiter, B. Lotz, D. Feili, M. Tartz, H. Neumann, and D. M. Di Cara. Design Development and

Test of the RIT-μX Mini Ion Engine System. *Proceedings of the International Electric Propulsion Conference*, **31**, 2009.

[67] D. Lev, R. Myers, K. Lemmer, J. Kolbeck, M. Keidar, H. Koizumi, H. Liang, D. Yu, T. Schönherr, J. Gonzalez, W. Choe, R. Albertoni, A. Hoskins, S. Yan, W. Hart, R. R Hofer, I. Funaki, A. Lovtsov, K. Polzin, and O. Duchemin. The Technological and Commercial Expansion of Electric Propulsion in the Past 24 Years. *Proceedings of the International Electric Propulsion Conference*, **35**, 2017.

[68] M. A. Lieberman and A. J. Lichtenberg. *Principles of plasma discharges and materials processing*. John Wiley & Sons, 2005.

[69] C. Liu, H. Tang, Z. Zhang, Z. Gu, and Y. Liu. Estimate of Lifetime of Ion Thruster Optics Based on Particle Simulation. *Plasma Science and Technology*, **10**(1):46, 2008.

[70] H. Löb. *Die Verwendungsmöglichkeit der Hochfrequenzionenquelle in elektrostatischen Raketentriebwerken*. PhD Dissertation, Justus Liebig University Gießen, 1967.

[71] H. W. Loeb, K.-H. Schartner, S. Weis, D. Feili, and B. K. Meyer. Development of RIT-Microthrusters. *Proceedings of the International Astronautical Congress*, **55**, 2004.

[72] C. Lu, T. Zhang, P. Qiu, J. Chen, Y. Cao, and L. Zheng. Barrel Erosion of Ion Thruster Accelerator Grid Under Different Operating Conditions. *IEEE Transactions on Plasma Science*, **46**(12):4065–4077, 2018.

[73] S. Malone and G. C. Soulas. Computational Ion Optics Design Evaluations. *Proceedings of the Joint Propulsion Conference and Exhibit*, **40**, 2004.

[74] J. Miller, S. Pullins, D. Levandier, Y.-h. Chiu, and R. Dressler. Xenon charge exchange cross sections for electrostatic thruster models. *Journal of Applied Physics*, **91**(3):984–991, 2002.

[75] A. Mirza. *Entwicklung eines partikelbasierten Kontinuumsverfahrens zur bidirektionalen Kopplung mit der Direct Simulation Monte Carlo Methode*. PhD Dissertation, University of Stuttgart, 2018.

[76] O. Moeschlin (editor). *Experimental stochastics*. Springer, Berlin, 1998. ISBN 3-540-14619-9.

[77] B. Moon, H. V. Jagadish, C. Faloutsos, and J. H. Saltz. Analysis of the clustering properties of the Hilbert space-filling curve. *IEEE Transactions on knowledge and data engineering*, **13**(1):124–141, 2001.

[78] C.-D. Munz, M. Auweter-Kurtz, S. Fasoulas, A. Mirza, P. Ortwein, M. Pfeiffer, and T. Stindl. Coupled Particle-In-Cell and Direct Simulation Monte Carlo method for simulating reactive plasma flows. *Comptes Rendus Mécanique*, **342**(10-11):662–670, 2014.

[79] V. Muravlev and A. A. Shagayda. Numerical modeling of extraction systems in ion thrusters. *Proceedings of the International Electric Propulsion Conference*, **26**, 1999.

[80] M. Nakano. Three-dimensional simulations of grid erosion in ion engines. *Vacuum*, **83**(1):82–85, 2008.

[81] M. Nakano, K. Nakamura, Y. Nakagawa, D. Tomita, Y. Takao, and H. Koizumi. Numerical simulation of full-aperture-pair ion optics in a miniature ion thruster. *Physics of Plasmas*, **25**(1), 2018.

[82] J. Neudorfer. *Computational Strategies for Particle-In-Cell Simulations of Large Scale Engineering Applications*. PhD Dissertation, Rheinisch-Westfälische Technische Hochschule Aachen, 2012.

[83] P. Nizenkov. *Numerical simulation of rarefied, high-enthalpy gas flows around complex three-dimensional bodies during atmospheric entry*. PhD Dissertation, University of Stuttgart, 2018.

[84] P. Nizenkov, M. Pfeiffer, A. Mirza, and S. Fasoulas. Modeling of chemical reactions between polyatomic molecules for atmospheric entry simulations with direct simulation Monte Carlo. *Physics of Fluids*, **29**(7):077104, 2017.

[85] D. Oh. *Computational modeling of expanding plasma plumes in space using a PIC-DSMC algorithm*. PhD Dissertation, MIT, 1997.

[86] Y. Okawa, Y. Hayakawa, K. Miyazaki, and S. Kitamura. Ion thruster thrust vectoring by grid translation. *Proceedings of the International Electric Propulsion Conference*, **28**, 2003.

[87] Y. Okawa and H. Takegahara. Numerical Study of Beam Extraction Phenomena in an Ion Thruster. *Japanese Journal of Applied Physics*, **40**(1):314–321, 2001.

[88] P. Ortwein, S. M. Copplestone, C.-D. Munz, T. Binder, W. Reschke, and S. Fasoulas. A particle localization algorithm on unstructured curvilinear polynomial meshes. *Computer Physics Communications*, **235**:63 – 74, 2019.

[89] X. Peng, W. M. Ruyten, V. J. Friedly, D. Keefer, and Q. Zhang. Particle simulation of ion optics and grid erosion for two-grid and three-grid systems. *Review of Scientific Instruments*, **65**(5):1770–1773, 1994.

[90] X. Peng, W. M. Ruyten, and D. Keefer. Three-Dimensional Particle Simulation of Grid Erosion in Ion Thrusters. *Proceedings of the International Electric Propulsion Conference*, **22**, 1991.

[91] D. Petkow. *Modellierung von Teilchenkollisionen zur Berechnung hochverdünnter Plasmaströmungen*. PhD Dissertation, University of Stuttgart, 2011.

[92] M. Pfeiffer. *Simulation elektromagnetischer Wechselwirkungen in Plasmaströmungen großer Skalengradienten unter Verwendung eines gekoppelten Particle-In-Cell und Direct Simulation Monte Carlo Verfahrens*. PhD Dissertation, University of Stuttgart, 2015.

[93] M. Pfeiffer. Particle-based fluid dynamics: Comparison of different Bhatnagar-Gross-Krook models and the direct simulation Monte Carlo method for hypersonic flows. *Physics of Fluids*, **30**(10):106106, 2018.

[94] M. Pfeiffer, F. Hindenlang, T. Binder, S. Copplestone, C.-D. Munz, and S. Fasoulas. A Particle-in-Cell solver based on a high-order hybridizable discontinuous Galerkin spectral element method on unstructured curved meshes. *Computer Methods in Applied Mechanics and Engineering*, **349**:149 – 166, 2019.

[95] M. Pfeiffer, A. Mirza, and S. Fasoulas. A grid-independent particle pairing strategy for DSMC. *Journal of Computational Physics*, **246**:28–36, 2013.

[96] M. Pfeiffer, P. Nizenkov, A. Mirza, and S. Fasoulas. Direct simulation Monte Carlo modeling of relaxation processes in polyatomic gases. *Physics of Fluids*, **28**(2):027103, 2016.

[97] J. Polk, J. Brophy, and J. Anderson. Numerical simulations of ion thruster accelerator grid erosion. *Proceedings of the Joint Propulsion Conference and Exhibit*, **38**, 2002.

[98] Program Development Corporation Inc, P. Eiseman, S. Ebenezer, V. Sudharshanam, and V. Anbumani. GridPro. `https://www.gridpro.com/`, 2017.

[99] M. Quandt. *High Order Particle Transport for PIC Simulations of Plasma Flows*. PhD Dissertation, University of Stuttgart, 2010.

[100] A. Reeh, U. Probst, and P. J. Klar. 3D Ion Extraction Code incorporated self-consistently into a numerical Model of a Radio-Frequency Ion Thruster. *Proceedings of the International Electric Propulsion Conference*, **35**, 2017.

[101] K.-U. Riemann. The Bohm criterion and sheath formation. *Journal of Physics D: Applied Physics*, **24**(4):493, 1991.

[102] A. A. Shagayda, V. Nikitin, and D. Tomilin. Three-dimensional analysis of ion optics with misalignments of apertures. *Vacuum*, **123**:140–150, 2016.

[103] X. Shan and X. He. Discretization of the velocity space in the solution of the Boltzmann equation. *Physical Review Letters*, **80**(1):65, 1998.

[104] T. Shiraishi, H. Kuninaka, S. Satori, and K. Kuriki. Numerical Simulation of Grid Erosion for Ion Thruster. *Proceedings of the International Electric Propulsion Conference*, **24**, 1995.

[105] P. Spädtke. Model for the description of ion beam extraction from electron cyclotron resonance ion sources. *Review of Scientific Instruments*, **81**(2):3–6, 2010.

[106] L. Stewart, J. Kim, and S. Matsuda. Beam focusing by aperture displacement in multiampere ion sources. *Review of Scientific Instruments*, **46**(9):1193–1196, 1975.

[107] T. Stindl. *Entwicklung und Untersuchung eines Partikelverfahrens zur Simulation elektromagnetischer Wechselwirkungen in verdünnten Plasmaströmungen*. PhD Dissertation, University of Stuttgart, 2015.

[108] T. Stindl, J. Neudorfer, A. Stock, M. Auweter-Kurtz, C. Munz, S. Roller, and R. Schneider. Comparison of coupling techniques in a high-order discontinuous Galerkin-based particle-in-cell solver. *Journal of Physics D: Applied Physics*, **44**(19):194004, 2011.

[109] A. Stock. *A High-order Particle-in-Cell Method for Low Density Plasma Flow and the Simulation of Gyrotron Resonator Devices*. PhD Dissertation, University of Stuttgart, 2013.

[110] A. Stock, J. Neudorfer, M. Riedlinger, G. Pirrung, G. Gassner, R. Schneider, S. Roller, and C.-D. Munz. Three-Dimensional Numerical Simulation of a 30-GHz Gyrotron Resonator With an Explicit High-Order Discontinuous-Galerkin-Based Parallel Particle-In-Cell Method. *IEEE Transactions on Plasma Science*, **40**(7):1860–1870, 2012.

[111] A. Sun, G. Mao, J. Yang, G. Xia, M. Chen, and C. Huo. Particle Simulation of Three-Grid ECR Ion Thruster Optics and Erosion Prediction. *Plasma Science and Technology*, **12**(2):240, 2010.

[112] M. Tartz, E. Hartmann, R. Deltschew, and H. Neumann. Experimental validation of a grid erosion simulation. *Proceedings of the Joint Propulsion Conference and Exhibit*, **35**, 1999.

[113] M. Tartz, E. Hartmann, R. Deltschew, and H. Neumann. Effects of aperture displacement in broad-beam ion extraction systems. *Review of Scientific Instruments*, **73**(2 II):928, 2002.

[114] M. Tartz, E. Hartmann, and H. Neumann. Validated simulation of the ion extraction grid lifetime. *Review of Scientific Instruments*, **79**(2):02B905, 2008.

[115] E. Turkoz, F. Sik, and M. Celik. A Study of Ion Thruster Optics through Particle Simulations and Evaluation of the Near Plume Plasma Properties. *Proceedings of the Joint Propulsion Conference*, **50**, 2014.

[116] M. W. Tysanner and A. L. Garcia. Non-equilibrium behaviour of equilibrium reservoirs in molecular simulations. *International Journal for Numerical Methods in Fluids*, **48**(12):1337–1349, 2005.

[117] A. A. Vlasov. The vibrational properties of an electron gas. *Physics-Uspekhi*, **10**(6):721–733, 1968.

[118] P. J. Wilbur, J. Miller, and C. C. Farnell. A Study of High Specific Impulse Ion Thruster Optics. *Proceedings of the International Electric Propulsion Conference*, **27**, 2001.

[119] R. E. Wirz, J. R. Anderson, I. Katz, and D. M. Goebel. Time-Dependent Erosion of Ion Optics. *Proceedings of the Joint Propulsion Conference and Exhibit*, **44**, 2008.

[120] R. E. Wirz, L. Chu, M. Patino, H.-S. Mao, and S. Araki. Well-characterized plasma experiments for validation of computational models. *Proceedings of the International Electric Propulsion Conference*, **32**, 2011.

[121] R. E. Wirz, I. Katz, D. M. Goebel, and J. R. Anderson. Electron Backstreaming Determination for Ion Thrusters. *Journal of Propulsion and Power*, **27**(1):206–210, 2011.

[122] M. Yadollahi, A. S. Taleghani, and V. Esfahanian. Extractor Grid Effects on Beam Characteristics of Dual-Stage Ion Thruster. *IEEE Transactions on Plasma Science*, **47**(3):1–7, 2018.

A Appendix

A.1 Reservoir method as ARM for the flux velocity distribution

The reservoir method (see 3.3.1) can be interpretated as ARM (see 2.5.2) for sampling from f_{flux} with $f_{\mathcal{N}(\mu,\sigma^2)}(v_{\perp in})$ as envelope $g(R_1)$:

1. Sample first random number $v \in \mathcal{N}(\mu,\sigma^2)$ by $g(R_1)$.
2. Sample second random number $x_{-1} = -R_2 L$ with $R_2 \in \text{unif}(0,1)$ and $L = v_{max}\Delta t$. Accept v only if $x_{-1} + v\Delta t = -R_2 v_{max}\Delta t + v\Delta t \overset{?}{>} 0 \Rightarrow v/v_{max} \overset{?}{>} R_2$.

The final acception condition in the second ARM-step (see Fig. 2.3b) is $f(v)/k\cdot g(v) \overset{?}{>} R_2$, thus:

$$\frac{v}{v_{max}} \overset{!}{=} \frac{f_{flux}(v)}{k\cdot g(v)} \quad \Rightarrow \quad f_{flux}(v) = \frac{k}{v_{max}} v g_{\mathcal{N}(\mu,\sigma^2)}(v) \propto v g_{\mathcal{N}(\mu,\sigma^2)}(v)\,, \tag{A.1}$$

When scaling all velocities with $\hat{v}$ (e.g., $\tilde{v} = v/\hat{v}$, see Eq. 3.14), the normalized $f_{flux}(\tilde{v})$ and envelope $g_{\mathcal{N}}(\tilde{v}, \mu = a, \sigma = \sqrt{1/2})$ become:

$$f_{flux}(\tilde{v}) = C\tilde{v}e^{-(\tilde{v}-a)^2}\,, \quad C = \frac{2}{e^{-a^2} + \sqrt{\pi}a\,[1+\text{erf}\,(a)]}\,, \quad g(\tilde{v}) = \frac{1}{\sqrt{\pi}} e^{-(\tilde{v}-a)^2}\,. \tag{A.2}$$

For the ARM, $k\cdot g(\tilde{v}) \geq f_{flux}(\tilde{v})$ must apply which results with $k = C\sqrt{\pi}\tilde{v}_{max}$ in $\tilde{v}_{max} \geq \tilde{v}$ and holds because the latter was set by definition. The high rejection rate of the reservoir method is based on the limited fraction of reservoir particles reaching the domain (see Fig. 3.5a). However, the rejections decrease for larger mean velocities directed into the domain, as also depicted in Fig. A.1 in terms of an envelope adapted more to $f(\tilde{v})$ with increasing a.

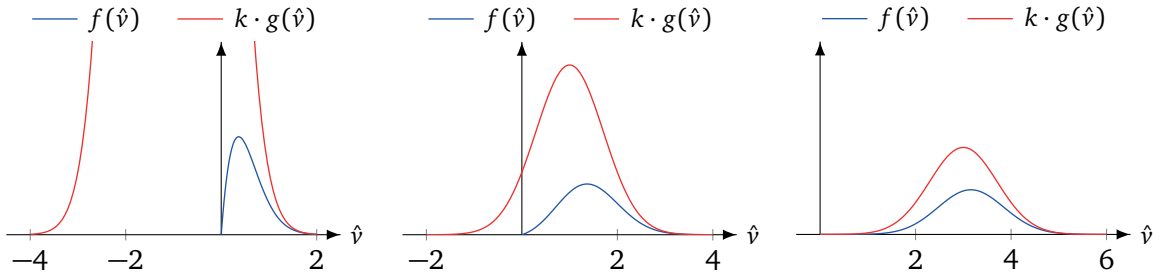

(a) speed ratio $a = -1$. **(b)** speed ratio $a = 1$. **(c)** speed ratio $a = 3$.

Figure A.1: Reservoir method as ARM for different speed ratios a with $\tilde{v}_{max} = a + 3$.

A.2 Algorithms implemented in PICLas.

Algorithm 1: Surface flux.

foreach i_{side} **do**
  $a_{side} \leftarrow a_{in} \frac{\vec{v}_{in}}{|\vec{v}_{in}|} \cdot \vec{n}_{BC}(i_{side})$
  $N_{part}(i_{side}) \leftarrow$ `RoundingRoutine`$(i_{side}, \Gamma_{in}(a_{side}, \text{Eq. 3.14}))$
  foreach $i_{part} \leq N_{part}(i_{side})$ **do**
    `placeOnSide`(i_{part}, i_{side})
  end
  if $T_{in} > 0$ **then**
    `SetMaxwellianFluxVelocities`(i_{side})
  end
end
if $T_{in} = 0$ **then**
  $\vec{v}(1 : N_{part}(i_{side})) \leftarrow \vec{v}_{in}$
end

SetMaxwellianFluxVelocities (i_{side})
  foreach $i_{part} \leq N_{part}(i_{side})$ **do**
    if $\vec{v}_{in} \cdot \vec{n}_{BC}(i_{side}) = 0$ **then**
      $R \leftarrow$ `random number` $\in \text{unif}(0,1)$
      $z^* \leftarrow -\sqrt{-\ln(R)}$
    else
      $z^* \leftarrow$ `optimal sample procedure` (dependent on a_{side})
    end
    $\vec{v}(i_{part}) \leftarrow \vec{n}_{BC}(i_{side})\hat{v}_{in} \cdot (a_{side} - z^*)$
    $v_{t1} \leftarrow$ `random number` $\in \mathcal{N}(\mu = 0, \sigma = 1)$
    $v_{t2} \leftarrow$ `random number` $\in \mathcal{N}(\mu = 0, \sigma = 1)$
    $\vec{v}(i_{part}) \leftarrow \vec{v}(i_{part}) + \vec{t}_{1,BC}(i_{side}) \cdot (\vec{v}_{in} \cdot \vec{t}_{1,BC}(i_{side}) + v_{t1}\sigma_{in})$
    $\vec{v}(i_{part}) \leftarrow \vec{v}(i_{part}) + \vec{t}_{2,BC}(i_{side}) \cdot (\vec{v}_{in} \cdot \vec{t}_{2,BC}(i_{side}) + v_{t2}\sigma_{in})$
  end

Algorithm 2: Divide integer value into sub-values based on their weights.

$X_{side}(0:N_{sides}) \leftarrow 0$
foreach i_{side} **do**
  $E(N_{part}(i_{side})) \leftarrow N_{part}^{total} W_{side}^{total}(i_{side}) / \sum_{i_{side}=1}^{N_{sides}} W_{side}^{total}(i_{side})$
  $N_{part}(i_{side}) \leftarrow \lfloor E(N_{part}(i_{side})) \rfloor$
  $W_{side}^{remain}(i_{side}) \leftarrow E(N_{part}(i_{side})) - N_{part}(i_{side})$
  $X_{side}(i_{side}) \leftarrow X_{side}(i_{side}-1) + W_{side}^{remain}(i_{side})$
end
$N_{part}^{remain} \leftarrow N_{part}^{total} - \sum_{i_{side}=1}^{N_{sides}} N_{part}(i_{side})$
foreach $i_{part} \leq N_{part}^{remain}$ **do**
  $R \leftarrow$ `random number` $\in \mathrm{unif}(0, X_{side}(N_{sides}))$
  foreach i_{side} **do**
    if $X_{side}(i_{side}-1) < R \leq X_{side}(i_{side})$ **then**
      $N_{part}(i_{side}) \leftarrow N_{part}(i_{side}) + 1$
    end
  end
end

Algorithm 3: Deposition of particle identity I by planes A and B "linked" to a corner.

`depositOnDOFs`(I)
foreach i_{link} **do**
  $tmp \leftarrow I$
  foreach $i_{mirror} \leq n_{180} - 1$ **do**
    $plane \leftarrow (B(i_{link}), A(i_{link}), B(i_{link}), ...)$
    $tmp \leftarrow$ `mirror`$(tmp, plane)$
    `depositOnDOFs`(tmp)
  end
  $plane \leftarrow A(i_{link})$
  $tmp \leftarrow$ `mirror`$(I, plane)$
  `depositOnDOFs`(tmp)
  foreach $i_{mirror} \leq n_{180} - 1$ **do**
    $plane \leftarrow (B(i_{link}), A(i_{link}), B(i_{link}), ...)$
    $tmp \leftarrow$ `mirror`$(tmp, plane)$
    `depositOnDOFs`(tmp)
  end
end